Probing of Reaction Mechanisms, and Development of Polymeric Materials for Lithium-Air Batteries

By

Chibueze Vincent Amanchukwu

Bachelor of Science, Chemical Engineering

Texas A&M University, College Station, Texas (2012)

SUBMITTED TO THE DEPARTMENT OF CHEMICAL ENGINEERING IN PARTIAL FULFILLMENT OF THE REQUIREMENTS FOR THE DEGREE OF

DOCTOR OF PHILOSOPHY IN CHEMICAL ENGINEERING

AT THE

MASSACHUSETTS INSTITUTE OF TECHNOLOGY

June 2017

Signature of Author..... Signature redacted .....
Department of Chemical Engineering
May 5, 2017

Certified by..... Signature redacted .....
Paula T. Hammond
David H. Koch (1962) Professor in Engineering
Thesis Supervisor

Accepted by..... Signature redacted .....
Daniel Blankschtein
Professor of Chemical Engineering
Chairman, Committee for Graduate Students

Probing of Reaction Mechanisms, and Development of Polymeric Materials for Lithium-Air Batteries

By

Chibueze Vincent Amanchukwu

Submitted to the Department of Chemical Engineering on May 5, 2017, in partial fulfillment of the requirements for the Degree of Doctor of Philosophy in Chemical Engineering

Abstract

Limiting the use of fossil fuels is vital to stemming climate change. Incorporation of renewable energy technologies into the grid, and the shift to electric vehicles for transportation increases the need for better energy storage media. Lithium-air (O_2) batteries are of great interest because they have high theoretical energy densities. However, conventional Li–O_2 batteries face challenges such as the use of volatile and flammable liquid electrolytes, side reactions between the electrolyte/electrode with oxygen reduction products, and high charging overpotentials that lead to poor cycle life. We address these challenges by developing non-flammable polymeric-based electrolytes and electrodes, and investigate their performance and stability in Li–O_2 batteries.

In this thesis, we synthesized and studied the properties of a nonvolatile and nonflammable siloxane solid polymer electrolyte that can support Li–O_2 discharge, but show it is vulnerable to reaction with the desired Li_2O_2 discharge product. We developed a screening tool that involves mixing commercial Li_2O_2 with various polymers of interest for Li–O_2 batteries, and formulate polymer reactivity rules where the presence of electron-withdrawing groups on the polymer and adjacent hydrogen atoms make the polymer vulnerable to degradation.

Of the polymers studied in contact with Li_2O_2, poly(methyl methacrylate) was found to be stable, and then used as part of a gel polymer electrolyte with an ionic liquid (IL) and lithium salt. The Li/IL molar ratio in the GPE was shown to allow for a switch from a 2 e^- to 1e^- oxygen reduction chemistry, and the formation of ionic liquid-superoxide complexes as the discharge product. Exploiting this understanding of the influence of a bulky ionic liquid cation on the oxygen electrochemistry, we incorporate ammonium salts in a Li–O_2 battery and show it can also support discharge and lead to > 0.5 V reduction in charging overpotential when compared to lithium salts. Finally, we explore an electron conducting polymer electrode poly(3, 4-ethylenedioxythiophene) (PEDOT) as a Li–O_2 electrode and show the polymeric surface allows for oxygen reduction and Li_2O_2 formation. Coupling fundamental understanding with material selection can empower the design of next generation Li–O_2 batteries.

Thesis Supervisor: Paula T. Hammond

Title: Department Head, David H. Koch (1962) Professor in Engineering

Acknowledgments

Thank you God for the opportunity of a lifetime.

It is true that one's PhD experience is determined by their advisor, and Paula allowed me to mature personally and professionally as an independent researcher. I am forever indebted for her guidance, support, and for always having my best interest. I want to thank my thesis committee members Professors Yang Shao-Horn, Timothy Swager, and Martin Bazant for their critical feedback during my thesis committee meetings, and especially Yang for allowing me to use her laboratory, and essentially making me an honorary member of her lab.

I want to thank my family for their love; my parents for bringing me to the US and allowing me to pursue my MIT adventure. My lovely siblings Chiamaka, Chisom, and Chimaobi for loving me and my idiosyncrasies, and for being my best friends. My family members back in Nigeria: Florence Okoli for having been there for my siblings and I since birth, Aunty Atinuke for always keeping up with me, and Uncle Ifeanyi for constantly pushing me to think bigger.

I want to thank friends that are always available to hear me babble about any and everything. To Dirgh Rabadia and Johnson Asi, I know I can always count on you. To Brooke Wages, Seyi Lapite, Olamide Ajadi, Bukky Onanuga, Nnenna Akaronu, Carlos De La Torre, Steven Cisar, Chapman Lai, Ryan Pesek, Huong Pesek, and Cole Kohut, thank you for always been there. I want to thank my MIT classmates especially Manish, Sue Zanne, Abel, Ankur, Karthick, Andong, Mikhil, and Rohit for making the MIT experience more rewarding, and for surviving the first year together. I also want to thank Jonathon Harding for helping me get started on my research and for being an excellent mentor, and also my frequent collaborators Hao-Hsun Chang, Shiyu Zhang, Magali Gauthier, Shuting Feng, and Thomas Batcho. My fellow African MIT brothers Tunde Alawode, Kosi Aroh, Nwike Iloeje, Chidube Ezeozue, Abiodun Olaoye, David Kwabi, Koffi Pierre Yao, Julius Adebayo, Ekene Umeike, and Julius Arop made MIT seem like home, especially through all the events/moments we shared.

I also want to thank my church family, especially Aunty Marleen Palmer who basically adopted me as her own, Mr. Melbourne, Maran Wallace, the Joseph family, the Tellis family, and especially Michelle Tellis who has truly been a blessing.

Finally, without the personal financial resources provided by the GEM Fellowship, MIT-Lemelson Fellowship, National Defense Science and Engineering Graduate Fellowship (NDSEG), and the Alfred P. Sloan Minority PhD Program, my MIT experience may not have been truly fulfilling. In addition, the Office of the Dean for Graduate Education (ODGE) and MIT-MISTI through programs such as the MIT Global Fellows Program and the Global Teaching Labs allowed me to travel internationally and truly broaden my perspective.

Table of Contents

List of Figures

Chapter 1

Introduction

1.1 Climate Change

Climate change is the most significant challenge facing mankind. There is scientific consensus that burning of fossil fuels for industrial use, electricity generation, and transportation has led to a rise in the atmospheric concentration of greenhouse gases.[1] Carbon dioxide (CO_2) – a greenhouse gas – is a product of fossil fuel combustion, and its atmospheric concentration has increased by at least 90 ppm in the past fifty years.[2] Greenhouse gases trap heat in the atmosphere and are responsible for rising global temperatures. The 2015 United Nations Climate Change Conference held in Paris served to address this by collating agreements from over 190 countries to curtail fossil fuel use and limit the temperature rise to no more than 1.5 °C above pre-industrial levels.[1]

1.2 Multiple Approaches to Dealing with Climate Change

There are numerous approaches to dealing with climate change, and a multifaceted approach will be vital. Researchers work on developing media to remove CO_2 from the atmosphere, sequester and convert to commodity chemicals such as methanol.[3,4] Others have focused on developing renewable energy technologies that are 'carbon free.'[5,6]

1.3 Renewables and Need for Energy Storage

Renewable technologies that exploit sunlight and wind are becoming important factors in energy generation. But, solar and wind are intermittent, and cannot alone serve as the backbone of an electric grid. Energy storage is needed, and coupled with solar and wind can revolutionize the electric grid.[7]

Beyond the integration of renewable technologies into the grid, energy storage is vital for current electric grids. Electric grids are currently sized to meet peak demand, even though peak demand varies significantly between hours of the day.[8] This is inefficient and wasteful as gas plants or 'peakers' run at minimal flow rates so that when needed, they can ramp up quickly.[8] Electricity generation is an on-demand system: when more electricity is needed, it is immediately generated. In contrast to other commodities such as food, oil, and water where storage is a vital cog in the

supply chain, energy storage is virtually nonexistent.[8] Hence, rolling blackouts are common as number of severe weather events increase, and as population densities increase, peak demand will grow and more 'peakers' will be needed.[8] This is despite the relative stability in energy demand due to more efficient devices.[8] Hence, incorporating energy storage into the grid will make it more reliable, efficient, and less costly.

1.4 Batteries

Energy storage media are wide-ranging. Options range from batteries and flywheels to compressed air energy storage and pumped hydro storage.[8] Batteries are exciting because they are energy dense, compact, and portable. Not only can they be used to stabilize the grid, they can be used to transform transportation by accelerating a shift from internal combustion engines that burn fossil fuels to electric motors. Transportation is one of the dominant sources of CO_2 emissions in the US; hence, the use of battery-powered electric vehicles will play an important role in reducing greenhouse gas emissions.

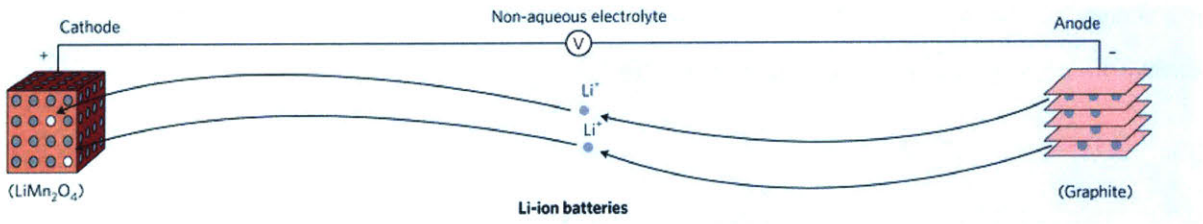

Figure 1-1. Typical setup for an intercalation chemistry-based Li-ion battery. Reproduced with permission from ref (9). © 2017 Macmillan Publishers Ltd.

Batteries have three components; anode: where oxidation occurs; electrolyte: medium that supports ionic transport; cathode: where reduction occurs.[10] The most energy-dense batteries commercially available are lithium-ion batteries commonly found in portable electronic devices and electric vehicles.[10] Lithium-ion batteries are based on intercalation chemistry where lithium ions are shuttled between two chemical hosts (Figure 1-1). The Li-ion battery anode is typically graphite, cathode varies between $LiFePO_4$ and lithium transition metal oxides (e.g., $LiCoO_2$), and the electrolyte consists of a lithium salt dissolved in carbonate solvents (e.g., propylene

carbonate).[11] These batteries have energy densities about 250 Wh/kg (Table 1-1). However, in their current format, lithium-ion batteries are believed to have reached their practical energy densities.[12,13] This is due to multiple reasons: current graphite anode requires roughly 6 carbon atoms for each intercalated lithium, and the transition metal cathode hosts feature heavy atoms like Co and Ni, that do not contribute to the generated current.[14] These factors limit the energy density where 'inert' compounds like graphite and the cathode host contribute weight and volume but not energy.

Table 1-1. Theoretical and Practical Energy Densities for Commonly-Studied Non-aqueous Battery Systems

Battery Chemistry	**Theoretical Specific Energy (Wh/kg)[12]**	**'Practical' Specific Energy (Wh/kg)[15]**
Li-ion	~387	~250
Li metal battery (with LMO)	~1070 (ref. 11)	~440
Li-sulfur	~2,567	~650
Li-air	~3,505	~950

*LMO = lithium transitional metal oxide.

1.5 Beyond Li-ion Chemistries

Interest has skyrocketed in what are termed 'beyond Li-ion chemistries' that can provide energy densities greater than current Li-ion batteries.[12,16] For example, switching to a silicon anode or lithium anode, while maintaining current cathode architectures.[15] More interestingly, chemistries such as lithium-air or lithium-sulfur batteries necessitate a change to a lithium metal anode and the use of oxygen or sulfur as the active specie. Lithium-air and lithium-sulfur exploit the energy density that can be gained by reducing oxygen and sulfur, and yield an order of magnitude greater theoretical energy density compared to commercial Li-ion batteries (Table 1-1).[12] My work has focused on lithium-air batteries (Figure 1-2).

1.6 Lithium-air (O_2) Batteries

Lithium-air batteries (or Li–O_2 because oxygen is the active specie) are governed by two fundamental reactions: the oxygen reduction reaction (ORR) and oxygen evolution reaction (OER).[16] During discharge, oxygen is reduced to superoxide and peroxide to yield Li_2O_2 as the desired discharge product.[14] During charge, lithium peroxide product is oxidized to release O_2. These reactions occurs at the cathode. At the lithium metal anode, lithium ions are stripped during discharge and deposited during charge.[14] The electrolyte facilitates oxygen solubility and Li^+ and O_2 transport. The aforementioned are idealities. The inner workings of a Li–O_2 cell are much more complex and numerous challenges abound.[14,16]

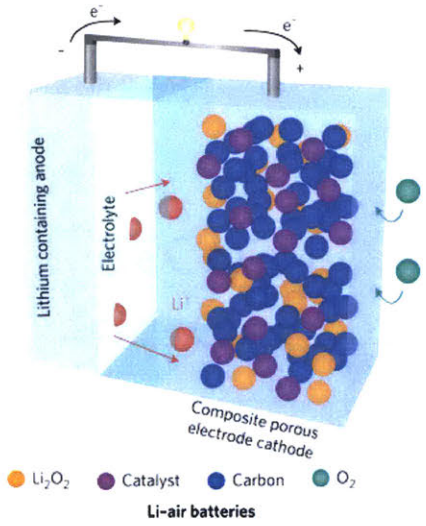

Figure 1-2. Typical setup for a lithium-air (O_2) battery where O_2 serves as the active specie. Reproduced with permission from ref (9). © 2017 Macmillan Publishers Ltd.

1.7 Challenges with Li–O_2 Batteries

1.7.1 Anode

Lithium metal is used as the anode because it is vital for the high energy density that can be obtained with Li–O_2 batteries. Lithium stripping and deposition occur, but nonuniform lithium deposition leads to dendritic growth.[17] This phenomenon is well known for lithium metal batteries (LMB). Li–O_2 researchers expect that once a solution (or solutions) are found to

address/suppress dendritic growth in lithium metal batteries, the solution can be replicated in lithium-air batteries. Hence, the lithium-air community has not addressed any unique behavior of the metal anode for Li-air batteries. One cannot necessarily expect a 1:1 technological transfer from LMB to Li-air systems because of the different chemistries. For example, not much is known about how superoxide intermediates interact with the lithium metal surface during cycling or the nature of the generated solid electrolyte interface. In addition, how will the presence of reduced oxygen intermediates affect dendritic growth? The dominant theme in the Li–O_2 community has been first and foremost understanding the ORR and OER reactions that occur at the cathode, and the influence of electrolytes.

1.7.2 Electrolyte

Most of the electrolytes studied are nonaqueous, volatile, and flammable.[16] Some of these include carbonates,[18] ethers,[19] sulfoxides,[20] amides etc.[14] For a system where O_2 is present, and may be operated in an open configuration, these batteries will be inherently unsafe. Solid electrolytes are therefore needed, and polymer electrolytes are an alternative.

Solid polymer electrolytes can be nonvolatile, nonflammable, and inherently safe. Polymers that are amorphous, and can solubilize salt can support ionic conduction.[21] Polyethylene oxide (PEO) with ether functionality that can solubilize lithium salt and is semi-crystalline can support ionic conduction through its amorphous phase. PEO has been studied in Li-air batteries by our group[22] and others,[23] and has been shown to support Li–O_2 discharge and charge, but can be susceptible to auto-oxidation in oxygen.[22] In **Chapter 2**, we address these concerns by synthesizing a siloxane polymer that is completely amorphous, hence we can afford high ionic conductivities, and reduce the fraction of ether groups present by moving from a linear ether chain as in PEO to a siloxane where the ether chain is short and is grafted onto a siloxane main chain. Ours was the first study of siloxane polymers for lithium-air batteries. We show that the siloxane polymer has high ionic conductivities, can support lithium-air discharge and appears more stable than PEO. We also evaluate the susceptibility of the siloxane polymer to understand the functional groups vulnerable to degradation.

Instability of electrolytes has plagued all Li–O_2 batteries.[14,16] Carbonates are the primary electrolyte medium for Li-ion batteries,[13] but when used in Li–O_2 batteries undergo ring opening reactions with superoxide and peroxide.[18] In addition, lithium carbonate, lithium formate among other products are observed after discharge instead of the desired Li_2O_2 discharge product.[18] Dimethylsulfoxide (DMSO) has been studied, and been shown to be more stable than carbonates,[20] but still react with Li_2O_2 to form LiOH and dimethylsulfone.[24] Amides such as dimethylformamide (DMF) and N-methyl pyrrolidone (NMP) have been studied as electrolyte candidates and although they support Li_2O_2 on the first discharge, electrolyte decomposition is also observed.[25] Ethers have been shown to be the more stable electrolyte class.[19] Dimethoxyethane (DME), diglyme, tetraglyme have been used to support Li-air cycling; however, like PEO, these ethers are susceptible to auto-oxidation in O_2 that leads to hydrogen abstraction and the formation of esters and formate decomposition products.[19]

Although the stability of small molecule electrolytes have been studied, the literature was lacking in an understanding of the vulnerabilities of polymers for Li–O_2 use. Nazar *et al.*[26] examined the stability of poly(vinylidene fluoride) (PVDF) and proposed a dehydrofluorination decomposition pathway. However, they studied the stability of only one polymer. Nasybulin *et al.*[27] studied multiple polymers, but using x-ray diffraction (XRD) as a post-reaction characterization tool does not provide insight into the polymeric functional groups that are responsible for degradation, and limited decomposition mechanisms are presented. In **Chapter 3**, we study the chemical stability of a group of polymers that have previously been used for Li-ion batteries, and may hold promise for Li–O_2 systems as a part of the electrolyte or as binder for the electrode. We use a chemical mixture of Li_2O_2 with the polymer and use spectroscopic tools such as nuclear magnetic resonance (NMR), ultraviolet-visible (UV-Vis) and Fourier transform infrared (FTIR) to determine unstable functional groups and polymers. Among the polymers studied, we found poly(methyl methacrylate) (PMMA), and fully fluorinated polymers such as poly(tetrafluoroethylene) and Nafion to be stable in contact with Li_2O_2. This study allowed us to develop a set of reactivity rules that can help in the selection and synthesis of new polymers for lithium-air batteries.[28]

The susceptibility of ethers to degradation renders almost all current solid polymer electrolytes inadequate for Li-air use because SPEs need the ether unit for ionic conduction.[21] This prompted

an interest in gel polymer electrolytes (GPEs) where one can decouple desired mechanical stability from ionic conductivity.[29] Using knowledge gained from **Chapter 3**, we explored a GPE consisting of PMMA, a lithium salt, and a number of ionic liquids (**Chapter 4**). Ionic liquids are nonflammable and ionically conducting, and some families such as pyrrolidinium, imidazolium, and ammonium among others have been studied in Li–O_2 and been shown to support Li–O_2 discharge and charge.[30] In our work,[31] we show that a GPE can remarkably modify the discharge mechanism from a 2 e^- process to a 1 e^- process as a function of the lithium/ionic liquid molar ratio in the GPE. This switching is in contrast to typical nonaqueous Li–O_2 batteries that utilize a 2 e^- ORR during discharge. Other metal-air batteries such as Na-air[32] and K-air[33] utilize a 1 e- oxygen reduction process and can sustain higher discharge capacities and currents, and have lower charging overpotentials during charge. We further characterize the Li–O_2 GPE discharge process, and show that ionic liquid-superoxide complexes are the discharge product. To further probe the mechanism, we fabricated Li–O_2 cells where the lithium salt is replaced by a tetrabutylammonium (TBA) salt. **Chapter 5** shows the ability of non-lithium cations to support a discharge process in Li–O_2 batteries; a behavior not previously studied.

My thesis focused heavily on the electrolyte medium because it was relatively unexplored, and we sought to engineer the electrolyte to control the discharge behavior, understand electrolyte stability, and degradation.

1.7.3 Cathode

Numerous cathodes have been studied for Li–O_2 batteries. Carbon electrodes (super P, vulcan carbon) are the most studied because they are cheap, electron conducting, and can have high surface area.[16] These electrodes support Li_2O_2 discharge,[34] but degrade above 3.5 V during charge when Li_2O_2 is present.[35] Alternative such as titanium carbide (TiC),[36] nanoporous gold[20] have been studied and shown to be stable, but these electrodes are heavier than carbon, have lower surface area, and in the case of gold, more expensive. Electron-conducting polymers are interesting because they can be synthesized with high surface area, have high electron conductivities and can be cheap.[37] Poly(pyrrole) was studied by Cui *et al.*[38] and shown to support

Li_2O_2 discharge product formation and oxidation. Others[39,40] evaluated poly(3, 4-ethylenedioxythiophene)-polystyrene sulfonate (PEDOT-PSS) as an additive in the presence of carbon to modify the discharge capacities. In **Chapter 6**, we show that free-standing PEDOT films can support ORR in non-aqueous solvent, allow for Li_2O_2 growth, and limited cycling.[41] However, spectroscopic results show that the PEDOT backbone can be destabilized in the presence of nucleophilic species.

Studies of Li_2O_2 oxidation during charging on the cathode focus on reducing the high overpotential that occurs because of the insulating nature of Li_2O_2. Metal catalysts such as Cr, and Mo,[42] etc have been shown to reduce charge overpotential, and redox mediators that can be dissolved in the electrolyte, can also oxidize Li_2O_2 during charge.[43] In **Chapter 5**, we show that TBA dissolved in an ether or sulfoxide electrolyte can also reduce the charging overpotential by > 0.5 V compared to lithium salts. Using spectroscopic tools, we propose a mechanism that involves the electrochemical transformation of tetrabutylammonium to tributylamine at > 3.55 V, and the conversion of tributylamine to a tributylamine oxide intermediate that reacts with and oxidizes Li_2O_2.

1.8 Thesis Scope

My PhD thesis focused on developing polymer electrolytes and electrode for lithium-air batteries, studying the influence of these polymeric materials on the discharge and charge behavior, understanding polymeric stability, and formulating mechanisms that can account for the observations. The knowledge gained from the work will guide design of better polymers for metal-air use.

In **Chapter 2**, we synthesize a siloxane polymer and study its thermal properties and ionic conductivity as a function of salt type, salt and silica additive content. The siloxane polymer was then incorporated as a solid polymer electrolyte in a lithium-air battery to study the discharge capacity as function of discharge current rate. After discharge, nuclear magnetic resonance (NMR) spectroscopy was used to study the stability of the polymer, and combined with chemical stability tests, the polymer was shown to degrade in the presence of Li_2O_2. This work showed that chemical stability tests with Li_2O_2 can serve as a good proxy for understanding polymer stability in actual lithium-air cells.

Using this knowledge, in **Chapter 3**, we select a number of polymers heavily used in the Li-air/Li-ion battery literature, and examine their stability, and the changes in molecular structure in the presence of commercial Li_2O_2. Of the polymers studied, poly(acrylonitrile) (PAN), poly(vinyl chloride) (PVC), poly(vinylidene fluoride) (PVDF), poly(vinylidene fluoride-co-hexafluoropropylene) (PVDF-HFP), and poly(vinyl pyrrolidone) (PVP) are reactive and unstable in the presence of Li_2O_2. The presence of the electrophilic nitrile group in PAN allows for nucleophilic attack by Li_2O_2 at the nitrile carbon, before further degradation of the polymer backbone. For the halogenated polymers, the presence of the electron-withdrawing halogens, and adjacent alpha and beta hydrogen atoms that become electron-deficient due to hyperconjugation makes PVC, PVDF, and PVDF-HFP undergo dehydrohalogenation reactions with Li_2O_2. PVP is also reactive, but with much slower kinetics. On the other hand, the polymers poly(tetrafluoroethylene) (PTFE), Nafion®, and poly(methyl methacrylate) (PMMA) appear stable against nucleophilic Li_2O_2 attack. The lack of labile hydrogen atoms and the poor leaving nature of the fluoride group allows for the stability of PTFE and Nafion®, while the methyl and methoxy functionalities in PMMA reduce the number of potential reaction pathways for Li_2O_2 attack in PMMA.

Since PMMA was shown to be stable in the presence of Li_2O_2 at room temperature, **Chapter 4** explores gel polymer electrolytes (GPEs) fabricated with PMMA serving as the mechanical framework. The GPE consisted of a polymer, ionic liquid, and lithium salt. We studied the thermal properties and ionic conductivity of the free-standing GPEs, fabricated lithium-air cells using this electrolyte, and show that the lithium/ionic liquid molar ratio in the GPE can control the oxygen reduction chemistry in a Li–O_2 cell (switching from a 2 e^- to a 1 e^- oxygen reduction chemistry). Using spectroscopic tools, we confirm the 1 e^- superoxide chemistry and show the formation of ionic liquid-superoxide complexes as the discharge product. Based on the observation of the importance of the lithium/ionic liquid molar ratio, we explored if a similar behavior can be observed when a tetrabutylammonium (TBA) salt is used in the electrolyte.

In **Chapter 5**, we show that TBA salts dissolved in ether or dimethyl sulfoxide (with no lithium salt present) can be used as a Li–O_2 electrolyte with a lithium metal anode to support Li_2O_2 formation, lead to > 500 mV reduction in charging overpotentials at low current rates compared to that with lithium salt, and support the oxidation of Li_2O_2 during charge. Furthermore, based on results from several spectroscopic techniques, we propose a mechanism that involves electrochemical transformation of TBA to tributylamine at ~ 3.55 V, and the formation of a tributylamine oxide intermediate in the presence of O_2 or Li_2O_2 that is responsible for Li_2O_2 oxidation during charging.

Finally, **Chapter 6** explores the use of a polymeric cathode for lithium-air batteries. We study the electron-conducting polymer poly(3, 4-ethylenedioxythiophene) (PEDOT) and show it can support oxygen reduction to form Li_2O_2 in a nonaqueous environment. We also propose a degradation mechanism, and show that the formation of sulfone functionalities on the PEDOT surface and cleavage of the polymer repeat unit impairs electron conductivity, and leads to poor cycling.

Chapter 2

Solid Siloxane Polymer Electrolyte for Lithium-air Batteries

Adapted and reproduced with permission from Chibueze V. Amanchukwu, Audrey V. Eshun, Robert B. Zabala, and Paula T. Hammond. "Solid siloxane polymer electrolyte for lithium-air batteries." (2017) *Manuscript in preparation.*

2.1 Introduction

Majority of CO_2 emissions are a result of fossil fuel use in electricity generation and transportation. Transitioning from fossil fuels to abundant renewable energy technologies is a path forward, but new technologies such as solar and wind are intermittent and require energy storage.[16] Energy storage media such as batteries are compact and can fulfill this need.[13] However, current commercial lithium-ion (Li-ion) batteries are expensive and in their current format involving a graphitic anode have reached their practical energy densities. Lithium-air batteries are promising because their theoretical energy densities are an order of magnitude greater than Li-ion, and have spurred intense research interest.[12,16] Lithium-air (O_2) chemistry is governed by oxygen reduction to form lithium peroxide as the discharge product, and oxygen evolution from Li_2O_2 oxidation during charge.[14] Nucleophilic species such as superoxide and peroxide that form during cycling degrade the electrolyte and electrode,[28,41] and insulating Li_2O_2 and the generated side reaction products such as Li_2CO_3 lead to high charging overpotentials.[24,44,45] These challenges have led to poor capacity retention with cycling and limited cycle life.[14,16] In addition, most Li–O_2 batteries studied in literature, and commercial Li-ion batteries are unsafe because they use non-aqueous volatile and flammable electrolytes. Solid polymer electrolytes (SPEs) are of interest because they are nonflammable and inherently safe. A recent review has been published on polymer electrolytes for Li-air use.[46] Some researchers have studied polymer electrolytes for Li–O_2 batteries, primarily focusing on polyethylene oxide (PEO), where Harding *et al.*[22] and Balaish *et al.*[23] show that ether functionality in PEO is susceptible to auto-oxidation and hydrogen abstraction in the presence of oxygen to form esters and formates. In addition, PEO auto-oxidation increases at higher voltages leading to a loss of mechanical stability of the PEO electrolyte. The high density of ethers in PEO and PEO instability prompted interest in studying SPEs with high ionic conductivity, but lower density of ether groups. Siloxane polymers with short ether side chains are of interest because of their low glass transition temperature (T_g), high ionic conductivity, and lower density of ether groups.[47,48] We chose to study silicon-tripodand (Si-trip) siloxane electrolyte previously synthesized by Walkowiak *et al.*[49] because it forms free-standing flexible films when lithium salt is incorporated. One can then obtain a SPE without addition of another polymer for mechanical stability[50] or need for crosslinker.[47,51] In this work, we synthesize Si-trip electrolytes and expand their parameter space by characterizing their thermal and conductivity properties as a function of

salt type, salt and silica content. We also explore these electrolytes in Li–O_2 batteries and characterize their performance and electrochemical/chemical stability.

2.2 Experimental Methods

2.2.1 Materials used

Poly(methylhydrosiloxane) (M_n ~1700-3200), Polymethylhydrosiloxane (trimethylsilyl terminated, Mn ~ 390), mesoporous silica, lithium triflate, lithium bis(trifluoromethane)sulfonamide salt, tris(2-methoxyethoxy)(vinyl)silane (98%), toluene (anhydrous, 99.8%), N-methyl pyrrolidone, tetrahydrofuran (anhydrous), Platinum(0)-1,3-divinyl-1,1,3,3-tetramethyldisiloxane complex solution (in xylene, Pt~2%) [Karstedt's catalyst], deuterated chloroform, were purchased from Sigma-Aldrich. Lithium metal was obtained from Chemetall (Germany).Vulcan carbon (Vulcan XC72) was obtained from Premetek Inc. Celgard C480 was obtained from Celgard. Carbon paper (TGP-H-60 PTFE treated) was obtained from Alfa Aesar. Teflon dish was obtained from VWR. Nitrogen gas (UHP 300) was obtained from Airgas. Benzoylated dialysis membrane tubing was obtained from Spectrum Labs. 13 mm syringe filter with a 0.45 μm PTFE membrane was obtained from VWR International.

2.2.2 Synthesis procedure for Si-trip polymer

Typical synthesis procedure: All glassware were dried in a 100 °C oven for at least four hours. In a 2-arm 250 mL round bottom flask, repeated vacuum and nitrogen purge was performed using a Schlenk line. The PMHS (MW of 1700 – 3200) is then added to the flask (10 grams). Then, vacuum is pulled for about 1 hour. The flask is flushed with nitrogen. Then, tris(2-methoxyethoxy)(vinyl)silane is added using a volumetric pipette to obtain a 1.2:1 molar ratio of vinyl silane:PMHS (54.2 mL). The molar ratio was often varied between 1:1 to 1.2:1. See Table A-3 in Appendix A for calculations used to obtain the amounts. About 15 μL of the Karstedt catalyst is added. The amount of catalyst was typically varied between 7.5 to 15 μL. About 10 mL of toluene is then added to the mixture. Using an oil bath, the flask is heated at 50 °C at 800 rpm under a nitrogen atmosphere for about 3 days. The viscosity of the mixture increases significantly. The mixture is transferred to a 100 mL round bottom flask and rotavapped at 50 °C and vacuum to remove the toluene solvent (the polymer product can look translucent or cloudy).

For some batches, the product can be further purified using dialysis with acetone as the solvent and a 32 mm benzoylated dialysis bag. The acetone bath was changed at least twice. The purified polymer is then transferred to a nitrogen glovebox (MBRAUN, $H_2O < 0.1$ ppm, $O_2 < 10$ ppm).

2.2.3 Synthesis procedure for silicon-tripodand oligomer

The synthesis procedure is similar to that for the silicon-tripodand polymer. Here, PMHS (M_n = 190) is used. Once PMHS is added to the flask, no vacuum is pulled. Instead, 3 mL of toluene is added. Then the vinyl silane is added followed by addition toluene addition. Finally, the platinum catalyst is added (7.5 μL). More toluene (3 mL) is added. The mixture is heated at 50 °C and stirred at 500 rpm under a nitrogen atmosphere. Cryo-distillation was performed on the product to remove toluene. The purified Si-tripodand oligomer product was clear and transparent, and was stored in a nitrogen glovebox. The Si-tripodand oligomer was not used to make films.

2.2.4 Si-tripodand film fabrication

The entire film fabrication was performed in a nitrogen glovebox (MBRAUN, $H_2O < 0.1$ ppm, $O_2 < 10$ ppm). In a 20 mL vial, an amount of salt is dissolved in anhydrous tetrahydrofuran (THF). This solution serves as the stock salt solution.

In a 20 mL vial, about 1 gram of the polymer is added. Then, a predetermined volume of the stock salt solution is added to the vial to obtain the desired salt weight percentage (weight by mass). For films containing silica, a predetermined amount of silica powder is added to the vial to obtain the desired silica weight percentage. About 4 mL of pure anhydrous THF is added to the vial and it is stirred to obtain a clear transparent solution (when no silica is present). For films containing silica, the vial is stirred overnight to obtain a uniform dispersion of silica in the solution. The solution is then poured into a Teflon dish. The Teflon dish is allowed to sit in the glovebox for at least 2 days until the THF has evaporated. The films are cut into disks (12 mm for ionic conductivity measurements and 16 mm for battery testing) outside the glovebox. The cut disks are then transferred immediately to a vacuum oven and dried overnight at 50 °C under vacuum. The vacuum-dried films are stored in an Argon glovebox (MBRAUN, $H_2O < 0.1$ ppm, $O_2 < 0.1$ ppm) until they are used.

2.2.5 Vulcan carbon electrode fabrication

Vulcan carbon-based electrodes were prepared by mixing Vulcan carbon (80 wt%), silicon-tripodand polymer (16 wt%), and lithium salt (4 wt%) in 20 mL vial. NMP solvent was added and the contents was sonicated for at least 30 minutes to obtain a fine ink. The uniform black ink was transferred onto a PTFE-treated TGP-H-60 carbon paper substrate, and a doctor blade was used to create a film on the carbon paper substrate. The film was allowed to sit on the benchtop overnight before it was cut into 12.7 mm disks. The electrode disks were then vacuum-dried at 75 °C overnight before being transferred and stored in an Argon glovebox (MBRAUN, H_2O < 0.1 ppm, O_2 < 0.1 ppm)

2.2.6 Li–O_2 cell with Si-tripodand polymer film

For these cells, a "viscous polymer cream" was used to reduce the interfacial resistance between the anode-SPE and the cathode-SPE. In a 5 mL vial, Si-tripodand polymer was added and a salt solution was added to obtain 20 wt% lithium triflate in the Si-tripodand polymer. The solution was stirred, and then the vial was left opened in the glovebox to allow for THF evaporation. Then, the vial was held under high vacuum to remove all the THF. As expected, the viscosity was much higher than the pristine polymer.

Li–O_2 fabrication was performed in an Argon glovebox (MBRAUN, H_2O < 0.1ppm, O_2 < 0.1 ppm). Li–O_2 cell setup: Li metal (15 mm diameter) | one thin layer of "viscous polymer cream" on the lithium anode | Si-trip film 20 wt% Li-triflate and 4 wt% silica (16 mm diameter) | one thin layer of viscous polymer cream on the SPE | vulcan carbon electrode (12.7 mm). A paint brush was used to apply one layer of coating on the lithium metal anode and on the side of the SPE facing the cathode. The cells were transferred to another Argon glovebox (MBRAUN, H_2O < 0.1ppm, O_2 < 1%) without ambient exposure and filled with pure oxygen gas. The Li–O_2 cell was allowed to rest for 15 hours at 60 °C before it was also discharged at 60 °C.

For the Si-trip cell at OCV where the data is shown in Figure 2-3a, the cathode was a 15 mm diameter 316 stainless steel mesh instead of a Vulcan carbon cathode.

2.2.7 Li–O_2 cell with Si-tripodand oligomer

Li–O_2 cell fabrication was performed in an Argon glovebox (MBRAUN, H_2O < 0.1ppm, O_2 <0.1 ppm). Li metal was used as the anode. Two Celgard C480 separators were used. About 120 µL to 150 µL volume of Si-tripodand electrolyte was used. For the electrolyte, 10 wt % lithium triflate

was dissolved in the silicon-tripodand oligomer (no THF was added to aid the dissolution). A vulcan carbon electrode was used as the cathode. The cells were transferred to another Argon glovebox (MBRAUN, H_2O < 0.1ppm, O_2 < 1%) without ambient exposure and filled with pure oxygen gas. The electrochemical tests were performed at 60 °C. The Li–O_2 cells were usually allowed to rest at 60 °C for 15 hours before discharge began.

After the Li–O_2 cells were discharged, they were transferred into an Argon glovebox without air exposure (MBRAUN, H_2O < 0.1ppm, O_2 <0.1 ppm). NMR sample preparation was also done in the glovebox. The electrolyte soaked Celgard separator was placed in a 20 mL vial. Then, anhydrous deuterated chloroform was added to the vial and manually stirred. The solution was transferred to an NMR tube and ^1H NMR experiment was performed. The sample was never exposed to ambient at any time.

2.2.8 Mixture of Li_2O_2 with Si-tripodand oligomer

The following procedure was performed in a nitrogen glovebox (MBRAUN). In a 20 mL vial, about 80 mg of Li_2O_2 was added. Then, the corresponding amount of Si-tripodand oligomer was added to the vial. The vial was then stirred for 5 days at room temperature. No solvent was added. The following procedure was performed for the NMR measurement: About 10 µL of the Li_2O_2/Si-trip oligomer mixture was deposited in a 3 mL vial. Anhydrous deuterated chloroform was added. The vial was manually stirred to solubilize the contents. Then, the vial was allowed to rest to allow the Li_2O_2 particle to settle. Using a 0.45 µm PTFE filter, the solution was filtered and transferred to an NMR tube for NMR experiment.

2.2.9 Ionic conductivity measurements

Using a Swagelok setup, the 12 mm silicon-tripodand films were sandwiched between two 12 mm stainless steel disks. A Solartron 1470 (Solartron Analytical, UK) was used.

2.2.10 Battery fabrication

Lithium metal (15 mm diameter) was used as the anode, the silicon-tripodand film as the separator and electrolyte, and the Vulcan-carbon electrode as the cathode. A VMP3 potentiostat (BioLogic Inc.) or Solartron 1470 (Solartron Analytical, UK) was used for all electrochemical tests. The Li–O_2 cells were allowed to rest at 60 °C for 10 hours before discharge was performed.

2.2.11 Differential scanning calorimetry (DSC)

A DISCOVERY DSC (TA Instruments) was used, and 2-6 mg of the silicon-tripodand films were placed in hermetically sealed aluminum pans (TA instruments). Heating and cooling rates of 10 °C/min was used under a nitrogen flow rate of 50 mL/min. Two heating and cooling runs were performed for each sample to remove any thermal history. The second heating/cooling run is reported in the Results/Discussion section.

2.2.12 Nuclear magnetic resonance (NMR) spectroscopy

A Bruker AVANCE or AVANCE III-400 MHz spectrometer was used for the NMR experiments.

2.2.13 X-ray diffraction

XRD experiments was performed using a Rigaku Smartlab (Rigaku, Salem, NH, USA) in the parallel beam configuration with a Cu Kα radiation source. After the Li–O_2 cells were discharged, they were transferred into an Argon glovebox without air exposure (MBRAUN, H_2O < 0.1ppm, O_2 <0.1 ppm). The electrode was sealed in an airtight XRD sample holder (Antor Paar, Austria) for XRD measurement.

2.3 Results and Discussion

The silicon-tripodand siloxane polymer was synthesized using the hydrosilyation reaction catalyzed by Karstedt platinum catalyst.[48,49] The reaction scheme is shown in Figure 2-1a, and ^1H nuclear magnetic spectroscopy (NMR) data in Figure A-1 shows the expected disappearance of the vinyl functionality of tris(2-methoxyethoxy)(vinyl)silane (~5.8 – 6.15 ppm) and the Si–H bond (~4.7 ppm) of polymethylhydrosiloxane (PMHS). The obtained polymer was viscous (Mn = 13,444 Da; Mw = 32,000 Da).

Flexible free-standing films are generated when a lithium salt is dissolved in the polymer because of physical crosslinks that form when the lithium cation is coordinated by ether groups across different repeat units. As the salt content is increased, the films become more mechanically robust. However at a salt concentration of 20 wt% or more, the films may be

brittle. In SPEs, ionic conduction is believed to occur in the amorphous region. Hence, polymers capable of dissolving salt and have low glass transition temperature (T_g) are of interest. Differential scanning calorimetry (DSC) was used to study the thermal behavior of the generated films. As the DSC spectra in Figure 2-1b shows, the generated films are non-crystalline as there is no peak in the spectra. The T_g for the 10 wt% lithium bis(trifluoromethane)sulfonimide (LiTFSI) film is remarkably low (< −90 °C) and was beyond the cooling capacity of the DSC equipment used. As lithium salt concentration is increased, the mechanical stability increases, and the T_g increases. Changing the lithium salt from LiTFSI to lithium triflate, where triflate has a higher donor number (DN = 16.9)[52] than TFSI (DN = 5.4)[52] leads to higher T_g for the triflate films compared to LiTFSI at similar salt concentrations (Figure A-2). The anion donor number is a gauge of the electron-donating ability of the anion and hence ion-ion interactions and binding to the lithium will be stronger for higher donor number salts. Therefore, the type of lithium salt modulates the thermal properties of the films. The increased interaction may be responsible for the observed higher T_g in Figure A-2. Interestingly, films reported by Walkowiak *et al.*[49] incorporated $LiPF_6$ salt (DN = 2.5)[52], but had T_g close to room temperature. This discrepancy might be due to the fact that their starting Si-trip polymer has a much higher T_g than we measure in our work for our starting polymer.

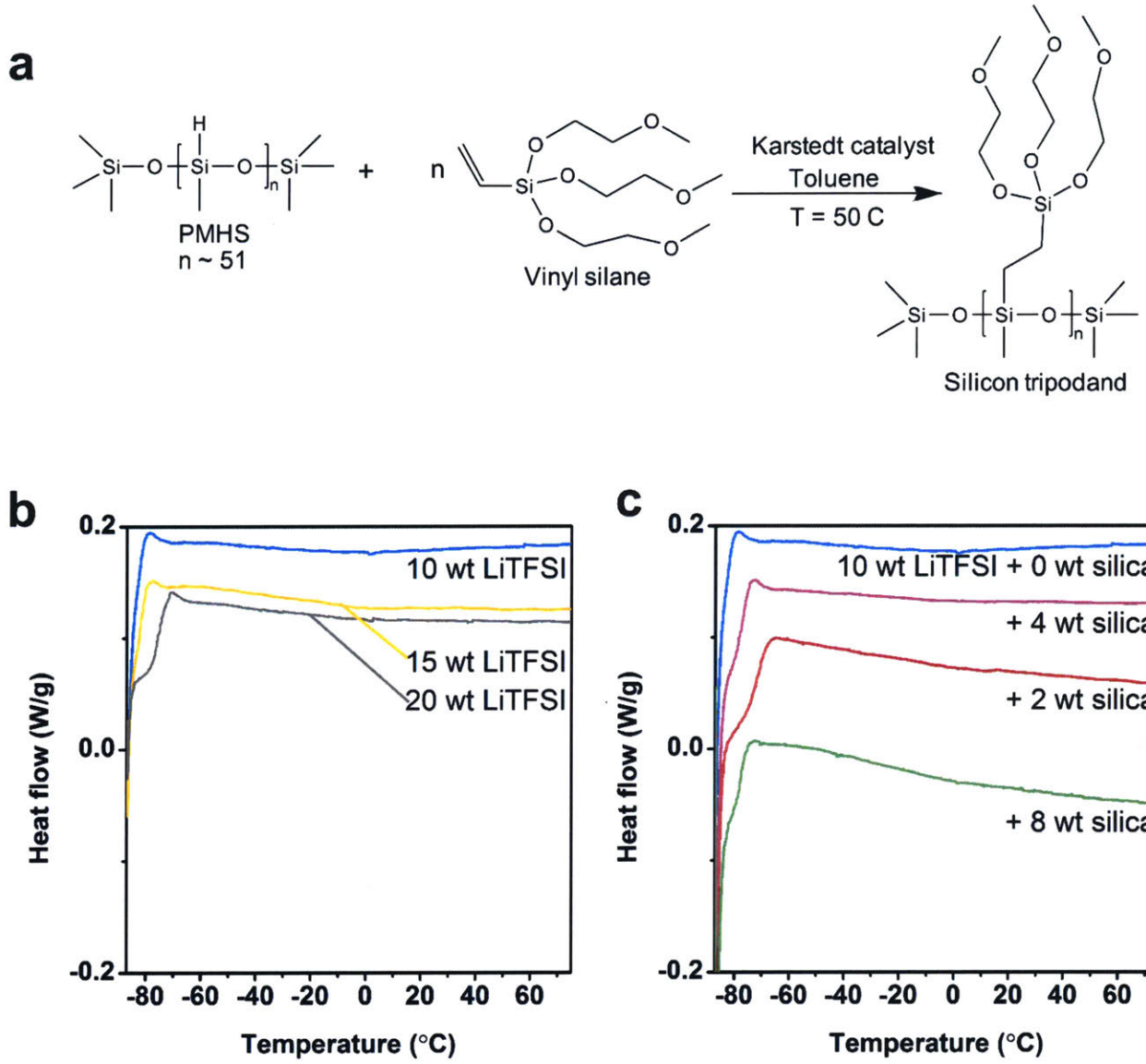

Figure 2-1 | Synthesis and characterization of siloxane polymer. (a) Hydrosilylation reaction between polymethylhydrosiloxane (PMHS) and tris(2-methoxyethoxy)(vinyl)silane ("vinyl silane" in the presence of Karstedt catalyst. Differential scanning calorimetry (DSC) spectra of siloxane/LiTFSI films as a function of (b) LiTFSI weight percentage, and as function of (c) silica weight percentage where all films contain 10 wt% LiTFSI. Numerical values for the glass transition temperature (T_g) can be found in Table A-1.

Additives have been explored in PEO-based electrolytes to inhibit PEO crystallization at room temperature, increase room temperature ionic conductivity while increasing mechanical

stability.[53-56] Furthermore, additives like silica (SiO_2) have been shown to limit ion-ion interaction of lithium salts in PEO to increase number of free lithium cations.[53] But, SiO_2 alone does not appear to support Li ion transport. Hence, an optimal amount of SiO_2 is needed to suppress crystallization and ion-ion interactions, but not lead to a high volume fraction of nonconductive SiO_2.[54] Since the Si-trip films are non-crystalline, SiO_2 addition may only aid in limiting ion-ion interactions. The DSC spectra in Figure 2-1c shows that silica addition can also modulate T_g. When 2 – 8 wt% silica is added to a 10 wt% LiTFSI film, the 4 wt% silica addition gives the lowest T_g value and is optimal among the silica compositions studied. However, silica addition does not lead to T_g lower than when no silica is present. This may be due to the already low T_g of the 10 wt% film and the low donor number of LiTFSI where ion-ion interactions are expected to be limited. The influence of silica content is more pronounced when films containing a salt of higher donor number where ion-ion interactions are more prominent. When 4 wt% silica is added to a film containing 20 wt% lithium triflate, the T_g reduces significantly, showing that silica can improve the thermal property of the films (Figure A-3).

The amorphous nature of these films, low T_g, and lithium ion solubility leads to high ionic conductivities. Figure 2-2a shows ionic conductivities as function of salt and silica content. 10 wt% Si-trip films shows the highest conductivities at all temperatures, where an ionic conductivity of ~10^{-4} S/cm is obtained at 60 °C. However, the 10 wt% films are fragile. The addition of silica does improve mechanical stability, but leads to conductivities ~ 10^{-5} S/cm at 60 °C.

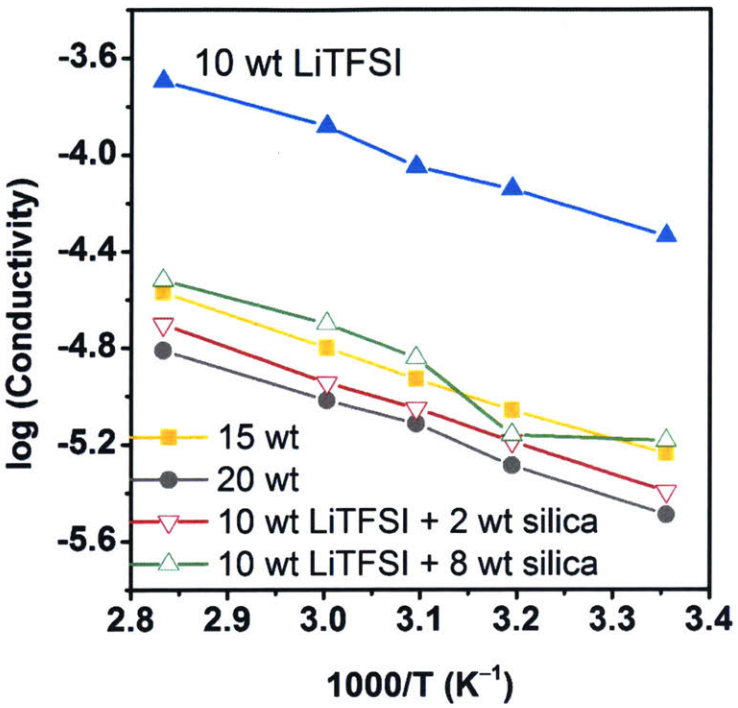

Figure 2-2 | Ionic conductivity of generated films. Average ionic conductivity of siloxane/LiTFSI films as a function of LiTFSI salt and silica content.

The Si-trip electrolytes were explored in actual Li–O_2 batteries. PEO electrolytes have been explored in Li–O_2 batteries, and work by Harding *et al.*[22] shows that holding a PEO electrolyte in O_2 at open circuit voltage (OCV) leads to a rise in the voltage as a function of time. The voltage rise was a result of oxygen-induced decomposition of PEO to form formates, esters even in the absence of any induced electrochemistry. The Si-trip electrolyte contains ether side chains for ionic conductivity, but the fraction of ether in Si-trip is lower compared to PEO. Figure 2-3a shows that when Si-trip is also held at OCV, a steady voltage is observed for 100 hours. All Li–O_2 batteries were operated at 60 °C to increase the reaction kinetics and access high ionic conductivities. With this result, we studied the discharge capacities of Li–O_2 cells containing a lithium metal anode, Si-tripodand electrolyte, and a Vulcan-carbon electrode at 60 °C. Despite the high ionic conductivities of the films, when cells were fabricated, the anode-SPE and cathode-SPE interfaces were very resistive. Hence, a 20 wt% salt was dissolved in Si-trip polymer to generate a viscous "polymer cream". A paint brush was then used to apply a thin coating to both the anode-SPE and cathode-SPE interfaces (more information in the experimental section). Figure 2-3b shows discharge capacities as a function of current rate. At 10 mA/g_c, a 2.8

V_{Li} plateau is observed that is similar to voltages observed using PEO electrolyte and organic liquid electrolytes. However, as the current rate is increased, lower discharge capacities are observed. This capacity reduction is often attributed to poor oxidation reduction kinetics, limited oxygen diffusion in the electrode, insulating Li_2O_2 film growth that prevents further oxygen reduction among others. Although we show that Li–O_2 discharge is supported, the desired Li_2O_2 discharge product is not observed after discharge. This could be due to low capacities that do not generate high amount of Li_2O_2 that can be observed using x-ray diffraction (XRD), or possible reaction between Li_2O_2 and the electrolyte that leads to Li_2O_2 disappearance after discharge.

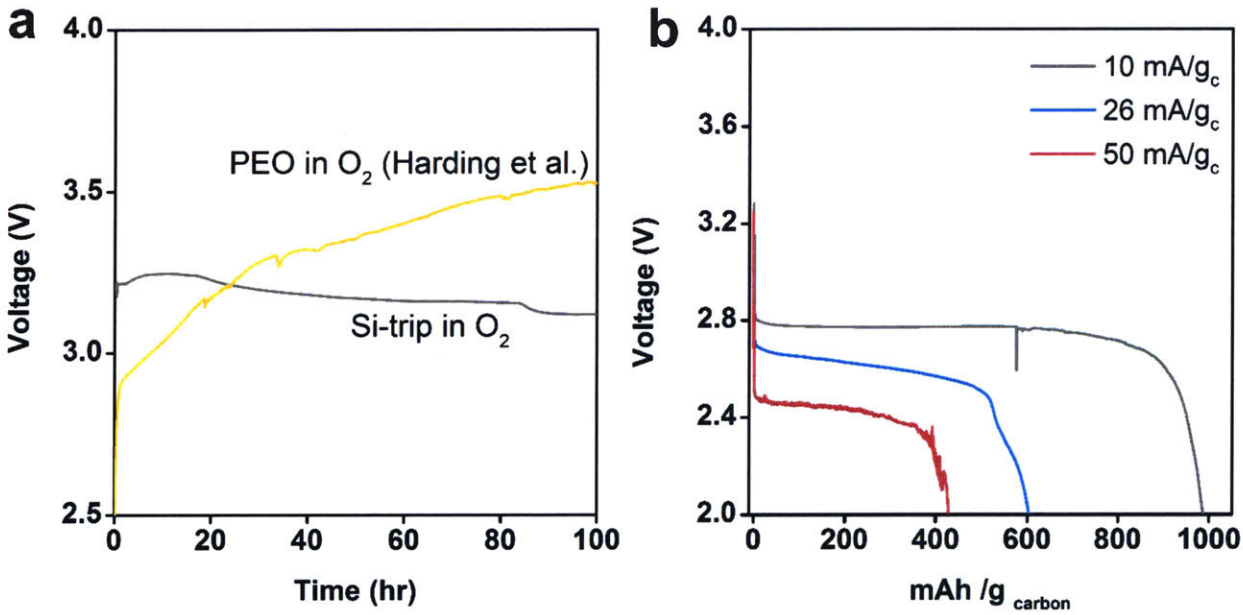

Figure 2-3 | Li–O_2 batteries using siloxane films. (a) Open-circuit voltage (OCV) of Li–O_2 cells in oxygen as a function of time with a stainless steel mesh cathode. (b) Discharge capacity as a function of current rate of Li–O_2 cells in oxygen with a Vulcan carbon cathode. All cells held at 60 °C during electrochemistry. PEO data was obtained from Harding *et al.*[22] (Copyright American Chemical Society). Electrolyte for (a): 20 wt% lithium triflate in Si-tripodand. (b): 20 wt% lithium triflate with 4 wt% silica.

Post-discharge characterization of these films is difficult because the films are solid, but a yellowish color was observed on the electrolyte films. To understand the stability of the Si-trip

chemical structure, Si-trip oligomers were fabricated (see Experimental Section) so that when lithium salt is dissolved, the Si-trip oligomer/salt mixture is still liquid. Li–O_2 cells were then fabricated using these liquid Si-trip oligomer electrolytes. The discharge curves can be found in Figure A-4. Similarly to the Si-trip films, a yellowish side reaction product was also formed after discharge using the Si-trip oligomer electrolyte. Using ^{1}H NMR, Figure 2-4 shows the Si–O–CH_2 is unstable during Li-air discharge as new proton peaks at 3.7 – 3.8 pm are in different chemical environments and appear adjacent to the Si–O–CH_2 peak at 3.85 ppm. This is unsurprising as the Si–O–CH_2 bond has been shown by others to be labile. A number of nucleophilic species (superoxide, peroxide) present could be responsible for the degradation. For a rechargeable Li–O_2 battery, the electrolyte must be stable in the presence of Li_2O_2 and support Li_2O_2 formation and oxidation. Therefore, we studied the stability of the Si-trip structure in the presence of commercial Li_2O_2.

Using a previously published technique, a chemical mixture of Li_2O_2 and Si-trip (1:1 molar ratio of Li_2O_2:Si-trip repeat unit) was made and stirred for five days.[28] ^{1}H NMR was then performed on the mixture, and Figure 2-4b shows that Li_2O_2 is capable of reacting with the Si–O–CH_2 bond on the Si-trip electrolyte yielding the same decomposition products observed electrochemically. Therefore, the silicon-tripodand structure is unstable for Li–O_2 use. Modified Si-trip structures can be synthesized that avoid the Si–O–CH_2 bond (Figure A-5), but the ether side group may still be susceptible to degradation as in PEO[22] and glyme solvents.[19] Finally, although the Si-trip structure may degrade in Li–O_2, it may show promise in lithium-ion batteries where nucleophilic species like superoxide and peroxide are not present. Therefore, more work should be done to explore these electrolytes in lithium and sodium-ion batteries.

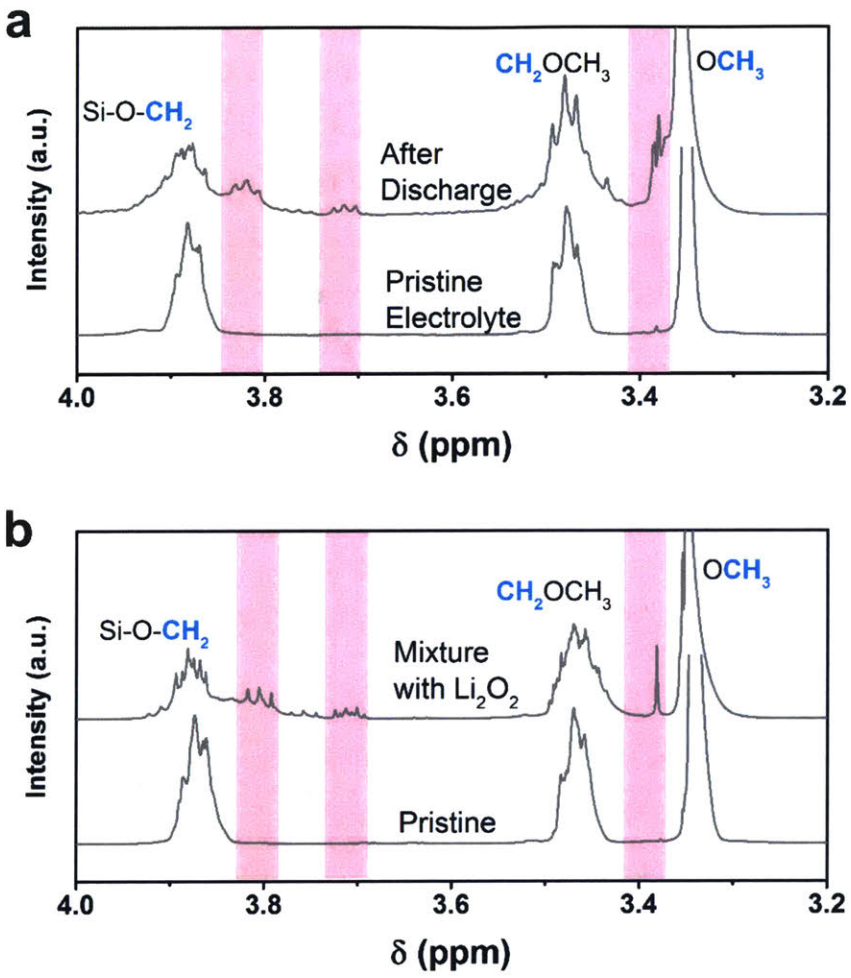

Figure 2-4 | NMR characterization to probe stability of Si-trip structure. ^{1}H NMR characterization (a) after discharge in oxygen in a Li–O_2 cell using a liquid Si-trip oligomer electrolyte and (b) after chemically mixing Li_2O_2 with the Si-trip oligomer for five days. The highlighted region are where new peaks arise in the spectra. ^{1}H NMR (400 MHz; $CDCl_3$; residual $CHCl_3$ reference)

2.4 Conclusions

In this work, we show that salt and silica dissolution in the synthesized silicon-tripodand polymer can lead to flexible ionically conducting free-standing films where salt type, salt and silica content can modulate the thermal and conductivity properties. We show that the siloxane polymer can support Li–O_2 discharge, but the Si–O–CH_2 bond is susceptible to degradation in

the presence of Li_2O_2. By exploring the parameter space for this electrolyte, and incorporating in a battery, we can better understand electrolyte properties, and their chemical vulnerabilities. Knowledge gained from this work will guide the use of these electrolytes for other battery chemistries such as Li and Na-ion.

2.5 Acknowledgments

This work was partially supported by the Samsung Advanced Institute of Technology, and facilities at the Koch Institute for Integrative Cancer Research. CVA was supported by the GEM Fellowship and by the US Department of Defense through the National Defense Science and Engineering Graduate Fellowship (NDSEG). AS was supported by the MIT Summer Research Program (MSRP), and RBZ was supported by the MIT Undergraduate Research Opportunities Program (UROP).

Chapter 3

Understanding the Chemical Stability of Polymers for Lithium-air Batteries

3.1 Introduction

Innovations in portable electronic devices such as smart phones and laptops, and electrical vehicles, can be partly attributed to lithium-ion batteries; the most energy-dense batteries commercially available.[12,13] Lithium-ion battery use in electric vehicles has allowed for the gradual electrification of transport, but the current format–graphitic negative electrode and transition metal oxide positive electrode–has reached its practical limits in gravimetric energy density.[12,13,57] To allow future electric vehicles to effectively compete with gasoline-powered cars in driving range per charge, newer battery chemistries with much higher energy densities are being explored. In recent years, lithium-air (O_2) batteries have emerged as a possible lithium-ion replacement because their theoretical gravimetric capacity (3861 mAh/g_{Li}) is an order of magnitude greater than lithium-ion (372 mAh/g_C) if a lithium metal negative electrode is utilized as opposed to a graphitic intercalation electrode.[12,14,16,58-60] Although this difference has spurred intense research and commercial interest, several challenges such as electrolyte instability,[18,19,44] low rate-capability,[34] poor round-trip efficiency,[18,34,61] and limited cycle life[61,62] must be addressed before possible commercialization.

In its current configuration, lithium-air (O_2) battery technology uses lithium metal as the negative electrode, a porous high surface area material (e.g., carbon) as the positive electrode, and oxygen as the active material.[12,57] During cell discharge, oxygen is reduced to form superoxide radical anions ($O_2^{\cdot-}$)[63] that can combine with lithium ions to form lithium superoxide (LiO_2)[63,64] before the formation of the desired discharge product, lithium peroxide (Li_2O_2).[14,63-65] During charging, lithium peroxide is then oxidized to evolve oxygen.[20,43,63,64] The reversible formation and oxidation of lithium peroxide is therefore vital to the rechargeable nature of a lithium-air cell.[20,36,62]

Reduced oxygen species such as the superoxide radical anion are highly reactive species,[66] and the desired discharge product, lithium peroxide, is a strong base[67] that can participate in unwanted side reactions detrimental to cell performance.[44] These superoxide and peroxide species readily decompose carbonate-based electrolytes, such as ethylene and propylene carbonate, that are widely used in commercial lithium-ion batteries,[68] and even prevent the formation of Li_2O_2, instead leading to side products such as lithium carbonate and lithium

formate.[18,45,68] Ether-based electrolytes (e.g., 1, 2-dimethoxyethane and tetraglyme) have proven more stable than their carbonate counterparts and allow for the formation of Li_2O_2 during the first discharge; however these ether-based electrolytes also decompose upon further cell cycling.[19,44] Other electrolyte systems such as amides[25] and DMSO[69] have been explored, but they too decompose during cell cycling and on exposure to Li_2O_2 and KO_2,[70] highlighting the importance of developing stable electrolytes.

In addition to Li-air battery research into liquid aprotic electrolytes, Li-air cells with polymer electrolytes have been explored.[12,71,72] Some of the widely used polymer electrolytes are stable in contact with lithium metal, and like their ceramic counterparts, can help suppress lithium dendrite formation.[73] In addition, polymers have been widely used as binder for the oxygen electrode.[19,25,34,36,62,72] Therefore, the ubiquity of polymers in lithium-air research, and the technological potential of new roles for polymers as solid state electrolytes are developed, necessitates a thorough study to carefully evaluate their stability when exposed to the discharge and charge cell reactions.

Recent work by several researchers have highlighted the importance of evaluating the stability of polymers for lithium-air use. Black *et al.* studied the decomposition of the common binder poly(vinylidene fluoride), and reported on the dehydrofluorination of the polymer backbone in the presence of chemically generated LiO_2, and the formation of lithium fluoride (LiF) during cell discharge.[26] Nasybulin *et al.* studied a wider range of polymers, and characterized their stability in the presence of KO_2/Li_2O_2 based on the formation of inorganic decomposition products such as K_2CO_3.[74] However, indicating the formation of inorganic decomposition products like K_2CO_3 does not give insight into how the polymer chemical structure reacts. Therefore, it is unknown how the polymeric structure of PAN, PVC, PVP etc. react or are affected by the presence of Li_2O_2. Are the resultant carbonates observed using X-ray diffraction (XRD) due to a degrading polymeric backbone or the polymeric functional group? Although the mechanism of PVDF degradation in lithium-air has been studied by some researchers,[26,72] there is a dearth in knowledge about the mechanism of degradation for other polymers. Despite these previous works, it is not known what functional groups should be avoided to prevent reactivity with lithium peroxide, and in turn how to inhibit reactivity of these polymers. This work strives to address these issues. There remains a need for greater insights into how and why the polymers

react with Li_2O_2, the functional groups and polymer backbones that are especially susceptible to attack, the extent and time frame (days, weeks etc.) of polymer degradation, and some controlling trends and principles that govern polymer reactivity and instability that can inspire new stable polymer binders and electrolytes.

In this work, we aim to address some of these questions by evaluating the reactivity and stability of a subset of polymers in the presence of commercial lithium peroxide powder. Since the desired discharge product of a lithium-air cell is lithium peroxide, it is vital that the polymer used be stable in contact against Li_2O_2. Using commercial Li_2O_2 affords us a quick screening tool to deduce the chemical stability of a polymer or small organic molecule before complete lithium-air cells are fabricated. In addition, it isolates the polymer, and eliminates the influence of lithium metal and carbon in the oxygen electrode as it pertains to reactivity against products formed upon discharge and charge in Li-air batteries.[44,61,75] For this paper, we chose to examine a set of polymers that have been thoroughly studied in the lithium-ion and lithium-air literature; the structures of which are shown in Figure 3-1.[73,74,76,77] These polymers have aliphatic C–C backbones (except polyethylene oxide), and their side-chain functionalities were chosen to understand the influence of the side-chain functional groups on the reactivity and stability of the polymer and its backbone. In addition to determining the stability of each polymer tested, we establish reactivity trends across all evaluated polymers with regard to the electron-withdrawing/ electron-donating nature of their functional groups, the influence of α and β-hydrogen atoms in the hydrocarbon polymer backbone, and how these factors contribute to the polymers' chemical stability in lithium-air. Knowledge and reactivity patterns gained from this work should prove critical in the bottom-up design of new polymers to serve as binders and mechanical supports, or as solid-state/gel polymer electrolytes for future lithium-air batteries.

3.2 Experimental Methods

3.2.1 Materials used

All polymers used in this work are shown in Figure 3-1, and an explanation of the abbreviations is listed in the Abbreviations section. The polymers PAN, PMMA, PTFE, PVC, PVDF, and

PVDF-HFP were obtained from Sigma-Aldrich. PEO was obtained from Polysciences, Inc. Nafion® was obtained from Ion Power Inc. as a 7.2 wt% lithiated Nafion® in isopropanol solution. Drops of the Nafion® solution were drop-cast onto a polystyrene weigh-boat and allowed to slowly evaporate overnight. The resultant film was vacuum-dried at 50 °C for at least 24 hours. Lithium peroxide (Li_2O_2) powder (technical grade, 90%), anhydrous N, N-dimethylformamide (DMF), and N, N-dimethylacetamide (DMAc) were purchased from Sigma-Aldrich, and used as obtained. Deuterated DMSO (D, 99.9%), and deuterated DMSO with tetramethylsilane (D, 99.9% + 0.05% v/v TMS) were obtained from Cambridge Isotope Laboratories, Inc.

3.2.2 Chemical reactivity tests

All chemical reactivity tests were performed in a dry-nitrogen glove box (MBRAUN, $H_2O < 0.1$ ppm, $O_2 < 10$ ppm). The following describes a typical experiment. In a 20 mL vial, about 132 mg of polymer was dissolved in 4 mL of DMF. Since no solvent has been proven to be completely stable in lithium-air, we chose DMF to serve as our reaction medium. While DMF can be unstable when used in a lithium-air cell,[25] we use DMF for our studies because its FTIR and UV-Vis peaks mostly do not interfere with the peaks of interest in the studied polymers (Figure B-1), and allows for the use of a DMF-based gel permeation chromatography (GPC) instrument. For PVDF only, DMAc was used as the solvent since PVDF is insoluble in DMF. The polymer/solvent mixture was stirred to allow the polymer to dissolve. In another 20 mL vial, about 85 mg of Li_2O_2 was added to allow for an excess mass concentration of Li_2O_2 compared to the polymer mass concentration. Then, 1.5 mL of the polymer/solvent solution was added to the vial containing Li_2O_2. The mixture was stirred throughout the course of the experiment.

3.2.3 FTIR characterization

In the glove box, 10 µL of the polymer/Li_2O_2/solvent mixture was placed on a transparent IR card (International Crystal Laboratories, 19 mm KBr aperture IR card). The IR card containing sample was allowed to rest in the glove box to allow for solvent evaporation until there was no visible trace of solvent. However, some of the samples were also transferred to the glove box ante-chamber, where it was allowed to vacuum dry at room temperature for at least two days for effective solvent removal. The IR card was then transferred out of the glove box, and the IR

spectra obtained immediately. A JASCO 4100 Fourier transform infrared (FTIR) spectrometer was used for data collection. All spectra were obtained in absorbance mode with a resolution of 1 cm^{-1}, using 100 accumulation scans. The spectrometer was flushed with dry nitrogen before and during sample measurement.

3.2.4 UV-Vis characterization

In a 20 mL vial, a polymer was dissolved in DMF (or DMAc for PVDF) to obtain a 10.5 mg/mL mass concentration of polymer. 100 µL of the polymer/solvent solution was removed to later serve as a control. Then, Li_2O_2 powder was added to the polymer solution to obtain a Li_2O_2 concentration of 16.4 mg/mL. The mixture was thoroughly stirred throughout the course of the experiment. At different time points, stirring was stopped and the mixture allowed to rest for about 15 minutes to ensure that the dispersed Li_2O_2 fall out of solution. For example, for the '1 hour' time point, stirring was stopped at 45 minutes. Carefully, a volumetric pipette was used to collect 25 µL of the topmost part of the mixture (to ensure Li_2O_2 particles are also not collected), and deposited in an empty 3 mL vial. Then, 1 mL of pure DMF was added to dilute the contents of the 3 mL vial. The vial was vigorously shaken to ensure full dissolution. A Pasteur pipette was then used to transfer the diluted mixture to a UV-Vis cuvette. The pure solvent (DMF or DMAc) was used as a blank. A Beckman Coulter DU 800 ultraviolet-visible (UV-Vis) spectrophotometer was used for data collection. For data analysis, the CTRL data, which corresponded to the polymer/solvent control, was subtracted from each polymer/Li_2O_2/solvent time point to better illustrate the accumulation of decomposition species as a function of time. In addition, the CTRL data was also subtracted from itself leading to the straight line that corresponds to zero in the UV-Vis spectra.

3.2.4.1 Details: a) For PAN, 5 µL of the PAN/Li_2O_2/DMF mixture was used (instead of 25 µL) because of the very high concentration of decomposition species, and diluted with 1 mL of DMF. b) For PVDF-HFP and PVC, 25 µL of the polymer/Li_2O_2/DMF mixture was used and diluted with 1 mL of DMF. c) For PVDF, a syringe was used to collect about 0.2 mL of the PVDF/Li_2O_2/DMAc mixture and filtered using a 0.45 µm Teflon® filter into a polystyrene well plate. Then, 25 µL of the contents of the well plate were then transferred to a 3 mL vial and

diluted with 1 mL DMAc. The PVDF mixture was filtered because of the interference of Li_2O_2 particles during data collection. d) For Nafion® and PVP, the polymer/Li_2O_2/DMF mixture was also filtered in the same manner as PVDF, and 25 µL of the mixture diluted with 1 mL DMF. e) For the CTRL data for each polymer, the same volume used for the polymer/Li_2O_2 mixture was used. For example, 5 µL of the PAN/DMF mixture (without Li_2O_2) was diluted with 1 mL DMF to obtain the CTRL data.

3.2.5 NMR characterization

In a 5 mL vial, about 16 mg of polymer was dissolved in 1 mL of deuterated DMSO with TMS (D, 99.9% + 0.05% v/v TMS). Then, 0.5 mL of the polymer solution was transferred to a NMR tube for ^1H NMR analysis. This served as the control. In another 5 mL vial, about 30 mg of Li_2O_2 was dissolved in 0.7 mL deuterated DMSO without TMS (D, 99.9%). Then, 0.4 mL of the Li_2O_2/DMSO dispersion was added to the NMR tube containing the polymer solution. The NMR tube was sonicated throughout the experiment to keep the Li_2O_2 particles dispersed in solution. At different time points, the NMR tube was removed from the sonication bath and taken for ^1H NMR analysis. The maximum temperature reached in the sonication bath was 50 °C. Although the temperature in the sonication bath can go as high as 50 °C, it was not held at 50 °C throughout the course of sonication. Since the results obtained using NMR are consistent with the FTIR and UV-Vis data, the temperature rise in the sonication bath is not believed to affect the interpretation of our results. All measurements (except ^1H NMR and sonication bath) were performed in a nitrogen-filled glove box (H_2O < 0.1 ppm, O_2 < 10 ppm). The contents of the NMR tube were never exposed to the atmosphere. A Bruker AVANCE and Bruker AVANCE III-400 MHz nuclear magnetic resonance (NMR) spectrometer was used.

3.2.6 GPC characterization

A DMF-based Waters® gel permeation chromatography (GPC) instrument was used to determine the polymer molecular weight before and after reaction with Li_2O_2. The polymer/Li_2O_2/DMF mixture was filtered using a 0.45 µm Teflon® filter before GPC analysis. A poly(methyl methacrylate) calibration standard was used.

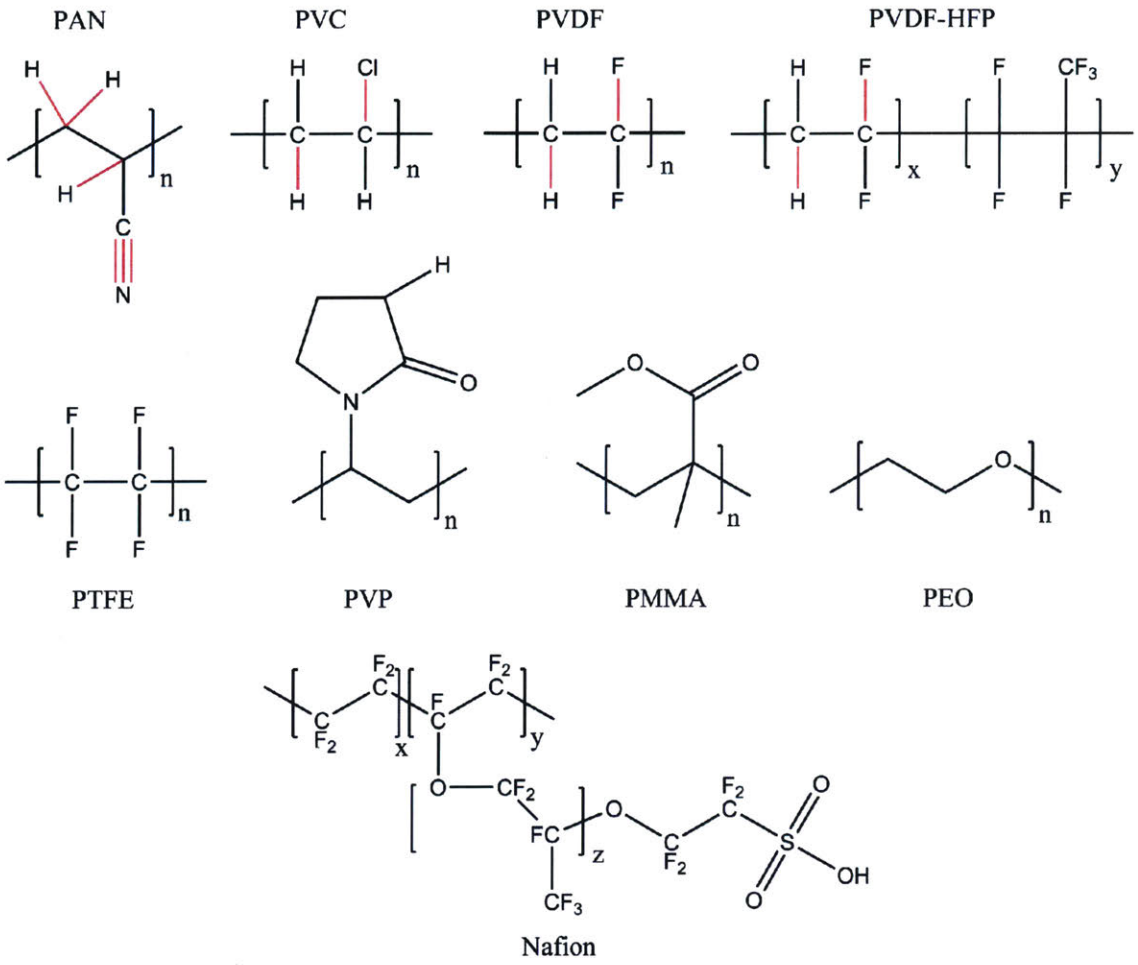

Figure 3-1 | Polymers studied in this work. List of polymers studied for this work. The red lines represent bonds that are cleaved during reaction with Li_2O_2.

3.3 Results and Discussion

3.3.1 Poly(acrylonitrile)

Poly(acrylonitrile) (PAN) has been a widely used mechanical support for gel polymer electrolytes, and PAN support/electrolyte systems have had some of the highest reported ionic conductivities.[78] In addition, PAN was the polymer of choice for the first lithium-air cell developed by Abraham *et al.*[77] In our work, PAN was found to be highly unstable, and reacted readily with Li_2O_2. Using procedures detailed in the Experimental Section, commercial lithium peroxide was added to a PAN/dimethylformamide (DMF) solution, and within minutes, the

previously clear and transparent solution turned yellow (Figure 3-2). After one day, the solution deepened to an orange color, and finally to a permanent dark red hue after about two days. The color changes are an obvious indication of a chemical reaction between PAN and Li_2O_2. Several characterization techniques such as ultraviolet-visible (UV-Vis) spectroscopy, Fourier transform infrared (FTIR) spectroscopy, nuclear magnetic resonance (NMR), and gel permeation chromatography (GPC) were used to characterize the decomposition products and elicit the mechanism and rate of PAN reaction.

Since the solution color changes are due to resultant soluble decomposition species, absorption in the ultraviolet-visible (UV-Vis) region can be particularly helpful in monitoring the reaction. Therefore, the reaction mixture of PAN/Li_2O_2/DMF was carefully studied using UV-Vis, and Figure 3-2a shows an increase in the absorbance of the soluble decomposition species as a function of Li_2O_2 exposure time. Beer's law allows for the correlation of absorbance with concentration;[79] therefore the absorbance increase corresponds to an increase in concentration of soluble decomposition species with time. Although Beers law does have a concentration limitation, the overall trends discussed here are still valid within the absorbance range of 0-1, for which Beers law is most accurate. These decomposition species could only result from the chemical degradation of PAN by Li_2O_2. After about three days, the saturation or completion of the reaction was reached, and the concentration of decomposition species approached steady state in solution. In addition, the loss of the absorbance peak at 310 nm corresponds to the conversion of an intermediate decomposition species to another, and there were slight shifts of the wavelength of maximum absorbance (λ_{max}) as the reaction proceeded. We further used FTIR and NMR to understand the molecular changes in the PAN structure to provide valuable information that can be used to devise methods to mitigate reaction or avoid the functionality responsible for reaction.

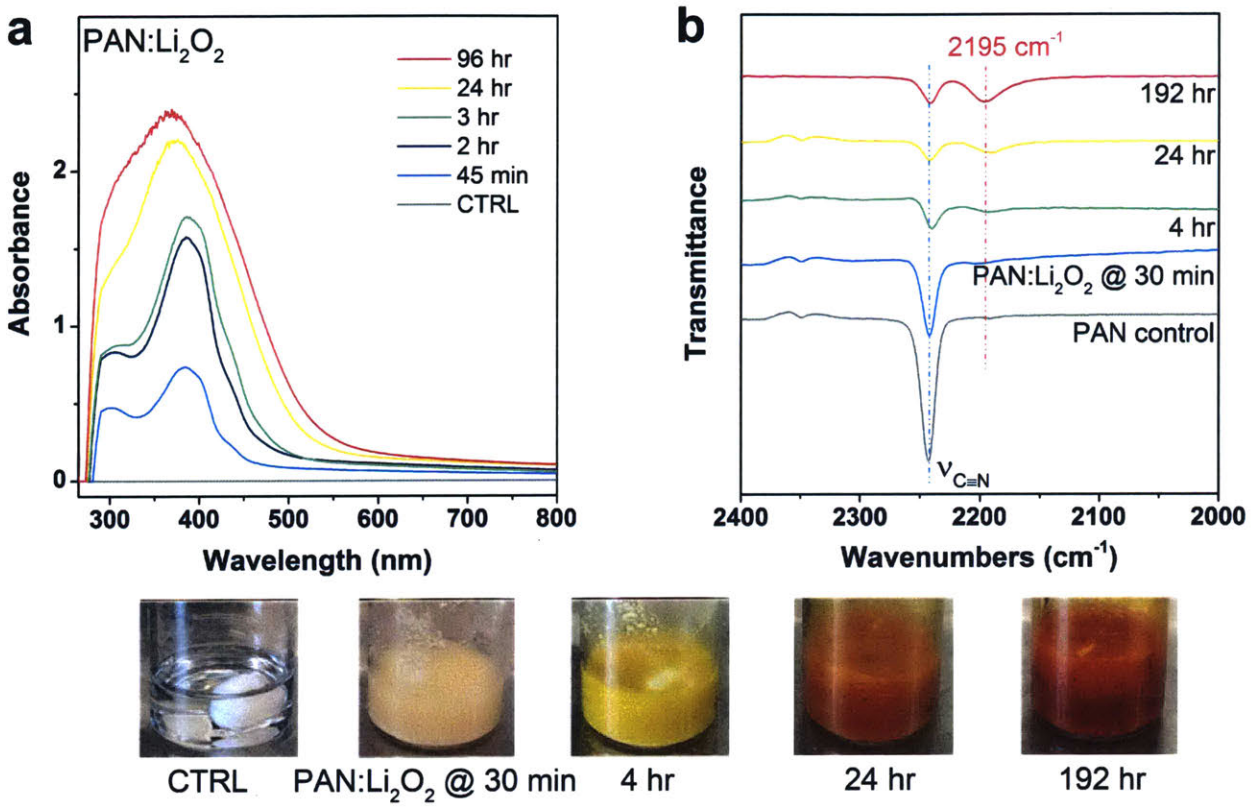

Figure 3-2 | Reaction of poly(acrylonitrile) with Li_2O_2. (a) UV-Vis spectra for the reaction of PAN with Li_2O_2.The rise in absorbance in (a) corresponds to the rise in the concentration of soluble decomposition species due to PAN degradation. (b) FTIR spectra for the reaction of PAN with Li_2O_2 which shows a decrease in the nitrile stretching vibration (2242 cm^{-1}) and the rise of a new peak at 2195 cm^{-1} due to PAN reaction that has previously been attributed to a β-amino nitrile.[80] The reaction pictures correspond to the same samples used to obtain the FTIR spectra.

We propose that the reactive chemical functionality in PAN is the nitrile functional group (−C≡N). The nitrile functional group is highly polarized, meaning the carbon directly attached to the nitrogen has a partial positive character (δ^+), and is electrophilic.[79] Fortunately, this functional group has a separate and highly definitive stretching vibration at 2242 cm^{-1}, making FTIR[81] an easy technique for characterization and possible delineation of the reaction mechanism. This hypothesis is supported by FTIR measurements in Figure 3-2b, which show a consistent decrease in the intensity of the nitrile functional group as Li_2O_2 exposure time

increases. This observation suggests that Li_2O_2 attacks the nitrile functionality, which leads to imine-like conjugated soluble species (−C=N−C=N−) that are responsible for the marked color changes observed visually and monitored in UV-Vis.[80,82,83] The observed wavelength of these imine species are dependent on the cause of PAN decomposition. For thermolysis of PAN under vacuum at 150°C, and thermo-oxidation in the presence of atmospheric O_2, two absorption bands attributed to polyimine appear in the UV-Vis spectra at 270 and 360 nm (thermolysis), and 270 and 385 nm (thermo-oxidation), respectively.[84] At early decomposition times (at least three hours), two absorption bands are present at 310 and 385 nm that may be due to these polyimine species. For much later decomposition times, the absorption spectra widens, consolidating the two maxima, and the λ_{max} shifts to lower wavelengths, an indication of a variation in the level of conjugation and/or oxidation of the polyimine species.[84] As a result of the electrophilic carbon atom in the nitrile functional group, nitriles can undergo nucleophilic addition and are susceptible to oxygen radical attack from radicals generated by Li_2O_2.[79]

Interestingly, when a stoichiometric excess of Li_2O_2 was used (excess mole ratio of peroxide to nitrile repeat unit), a new IR absorption peak at 2195 cm^{-1} appeared after about 4 hours and increased in intensity as the reaction proceeded.[80] The observed color changes, the decrease in nitrile functionality, and subsequent increase in the new functional group at 2195 cm^{-1} (attributed by Coleman *et al.* to be a β-amino nitrile)[80] has previously been observed during the thermal degradation of PAN at 200°C and reduced pressure,[80] and also during benzoic acid treatment at 170°C.[82] Therefore, it is interesting to note that we observed similar changes during Li_2O_2 exposure at room temperature, suggesting that the reaction with free radicals derived from peroxide yields some degree of nitrile oligomerization at much lower temperatures than previously reported. Although excess Li_2O_2 concentration was used, the nitrile functional group was not completely eliminated based on FTIR (which could be due to the presence of short nitrile oligomers), and it took about three days for the reaction to equilibrate and reach saturation. In addition, if the PAN/Li_2O_2/DMF mixture was not stirred thoroughly, a highly viscous dark red gel was found, possibly resulting from crosslinking due to the generated imine groups and the formation of conjugated ladder-like structures often observed as precursors to graphitization.[85]

To determine the extent of reaction on the polymer backbone, we used ^{1}H NMR to monitor the aliphatic CH_2 hydrogen atoms in the main polymer backbone and the α-CH hydrogen directly attached to the nitrile group. Figure 3-3 shows the ^{1}H NMR spectra chronicling the reaction of PAN. After about four hours, new proton peaks arose, whose source can only be from the protons available in the polymer backbone. After three days, the α-CH (δ = 3.2 ppm) and β-CH_2 (δ = 2.1 ppm) proton signals were almost nonexistent, implying they were cleaved and the polymer backbone significantly degraded. Also, there was the rise of a new peak at δ = 2.95 ppm that has previously been observed in colored PAN (obtained through thermal treatment or treatment with base),[83] and ascribed to methylene and/or methine protons resulting from cyclic ladder-like decomposition species or azomethine structures.[83] Incomplete PAN reaction, the presence of protons in very different chemical environments along the chemical backbone, and other smaller oligomers that may form during degradation led to the conglomeration of peaks from δ = 0.5–2.4 ppm. In addition, these new proton peaks could also be due to protons on the end groups of polymers that have been cleaved. Gel permeation chromatography (GPC) data allowed us to monitor the changes in the polymer molecular weight, and we observed a 65 percent decrease in the weight average molecular weight of the polymer, further supporting polymer degradation and breakdown.[82]

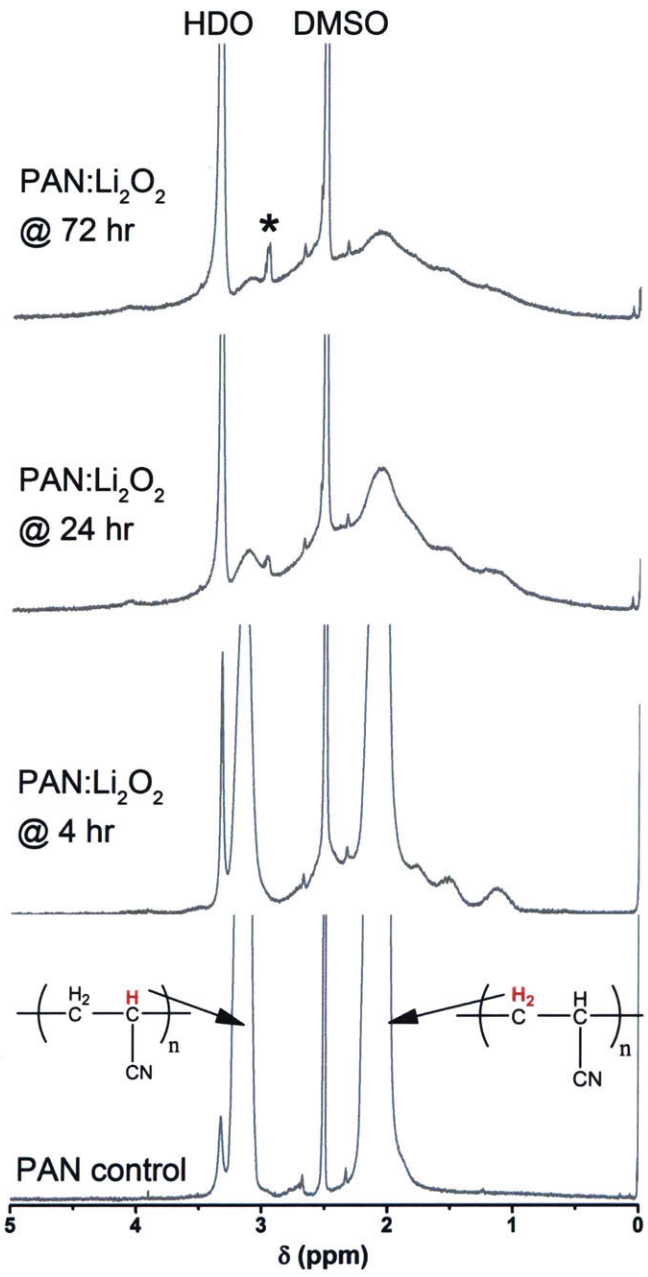

Figure 3-3 | ^{1}HNMR analysis of reaction between poly(acrylonitrile) and Li_2O_2. ^{1}H NMR (400 MHz; DMSO; Me4Si) spectra of PAN reaction with Li_2O_2. As reaction time increases, there is a loss of the α-CH (δ = 3.2 ppm) and β-CH_2 protons (δ = 2.1 ppm) in the molecular structure of PAN due to reaction with Li_2O_2. The HDO peak is present because pure deuterated DMSO contains H_2O residue which can exchange protons with DMSO. The rise in the HDO concentration can be due to the reaction of Li_2O_2 with DMSO which several authors have

postulated can lead to the formation of water.[69,70] *New peak at $\delta = 2.95$ ppm that has been previously observed in colored PAN.[83]

Several researchers have proposed decomposition mechanisms for the degradation of PAN, and the mechanism that best correlates with our experimental results is that by Coleman *et al.*[80] for thermal degradation of PAN. The mechanism is adapted and reproduced in Figure 3-4. Firstly, as shown in the FTIR spectra (Figure 3-2b), reaction begins by nucleophilic attack at the carbon of the nitrile functional group by dispersed Li_2O_2 particles or the peroxide anion (if Li_2O_2 slightly dissociates in DMF). There is a subsequent decrease in nitrile functionality within 4 hours, and formation of imine-like (−C=N) ionic species responsible for the yellowish color, further confirmed by the two absorption bands in the UV-Vis spectra as mentioned previously. The nitrile functional group is highly electron-withdrawing, meaning that the α-CH carbon atom becomes electron deficient due to an inductive electron withdrawing effect, and more importantly, the α-CH hydrogen atom becomes electron deficient due to hyperconjugation.[79] Hence, the α-CH hydrogen atoms are acidic and vulnerable to nucleophilic attack from O_2^{2-} or more probably, the newly formed and more nucleophilic imine ions.[80] Therefore, after 4 hours of reaction, the α-CH proton signals (using ^1H NMR) begin to decrease in intensity, leading to a different conjugated species (−C=C−N) that is responsible for the second color change from yellow to orange, and possibly responsible for the disappearance of the ultraviolet peak at 310 nm, and the distinct difference between the UV-Vis spectra at 3 hours and the UV-Vis spectra at 19 hours (Figure 3-2a). Finally, once the electron-deficient β-CH_2 protons and α-CH protons are cleaved, the final solution becomes dark red. Based on these results, PAN is unsuitable for use in Li-air batteries due to its high reactivity and almost complete degradation in the presence of Li_2O_2.

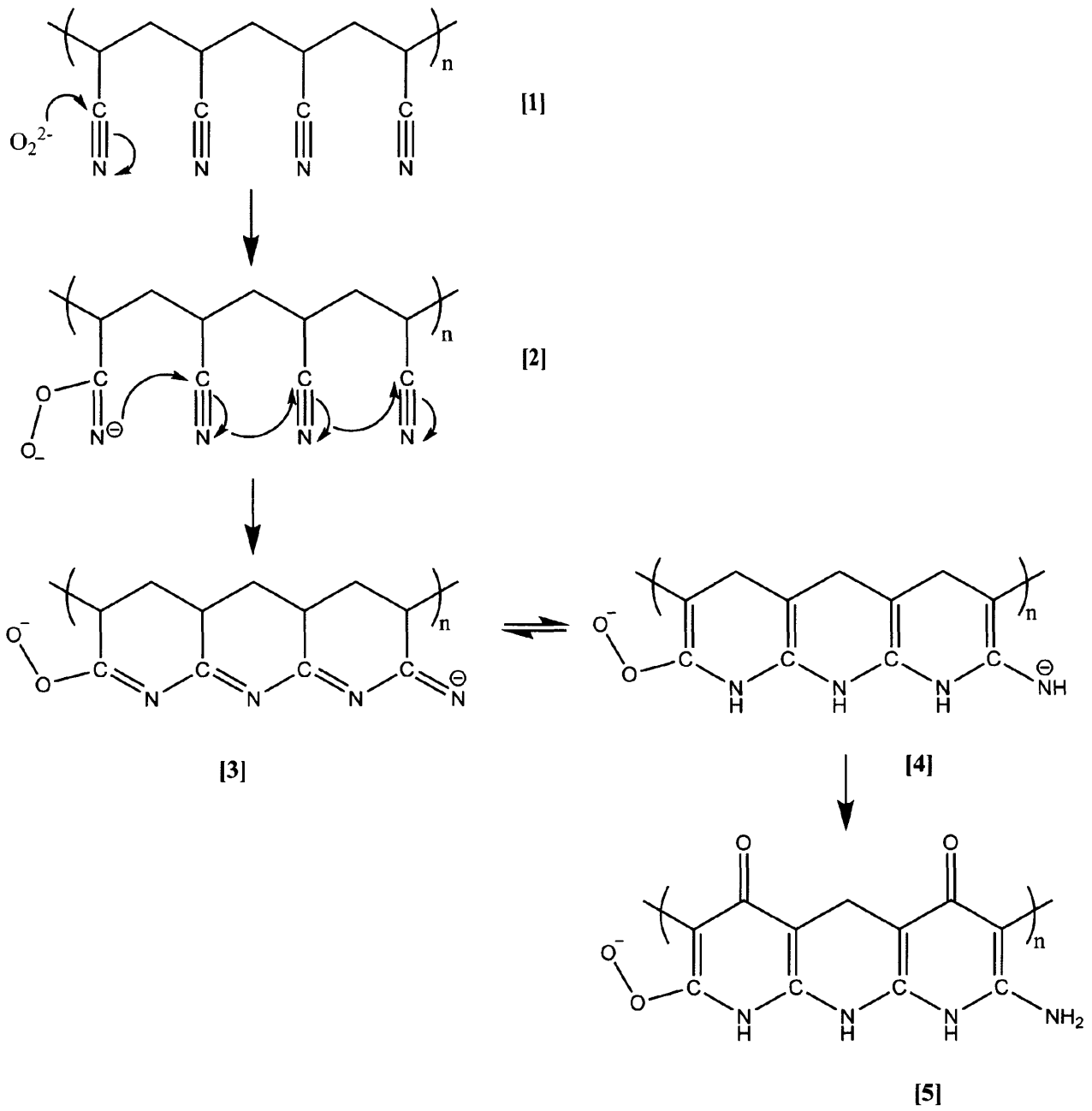

Figure 3-4 | Proposed PAN reaction mechanism. Mechanism for the reaction of poly(acrylonitrile) with Li_2O_2. This figure is adapted from reference [80]. We do not fully observe structure [5] above since no new carbonyl peaks in the PAN degradation products are observed in FTIR. However, the loss of the β-CH_2 protons is observed as shown in the NMR data in Figure 3-3. Another mechanism may be responsible for the abstraction of the β-CH_2 protons without the formation of a carbonyl moiety.

3.3.2 Halogenated polymers

Of the polymers heavily utilized in the battery literature, halogenated polymers are often at the forefront with some like poly(vinylidene fluoride) (PVDF), sold under the trademark Kynar®, that are commercially marketed for battery applications. Similar to poly(acrylonitrile), halogenated polymers such as poly(vinyl chloride) (PVC), PVDF, poly(vinylidene fluoride-co-hexafluoropropylene) (PVDF-HFP), and Nafion® have been used as mechanical supports for gel polymer electrolytes,[72,73] but even more so as binders for the positive electrode.[19,34,62] In contrast, poly(tetrafluoroethylene) (PTFE), commonly known as Teflon®, is almost exclusively used as a binder for lithium-battery applications.[25,36] These halogenated polymers are mechanically robust,[73] but despite the presence of the strong carbon-halogen bonds, PVC, PVDF, and PVDF-HFP are unstable and react readily with Li_2O_2. On the other hand, Nafion® and PTFE are stable and do not appear to react with Li_2O_2.

When Li_2O_2 powder was added to the PVC/DMF solution, the solution color changed immediately from transparent to slight orange, before becoming a dark mixture within three days (Figure 3-6b). Similar color changes occurred for PVDF and PVDF-HFP when Li_2O_2 powder was added with both changing from clear solutions to black within three days (Figures 3-5c-d), indicative of the instability of these polymers. This finding is in good agreement with recent work by Black *et al.*[26] and others studying PVDF,[74,86] and past work that has shown strong bases such as potassium hydroxide (KOH) can act as a dehydrochlorination agent.[87,88] For lithium-air, these bases can be $O_2^{\cdot-}$, LiO_2, Li_2O_2, etc.; for this work, we have focused primarily on Li_2O_2.

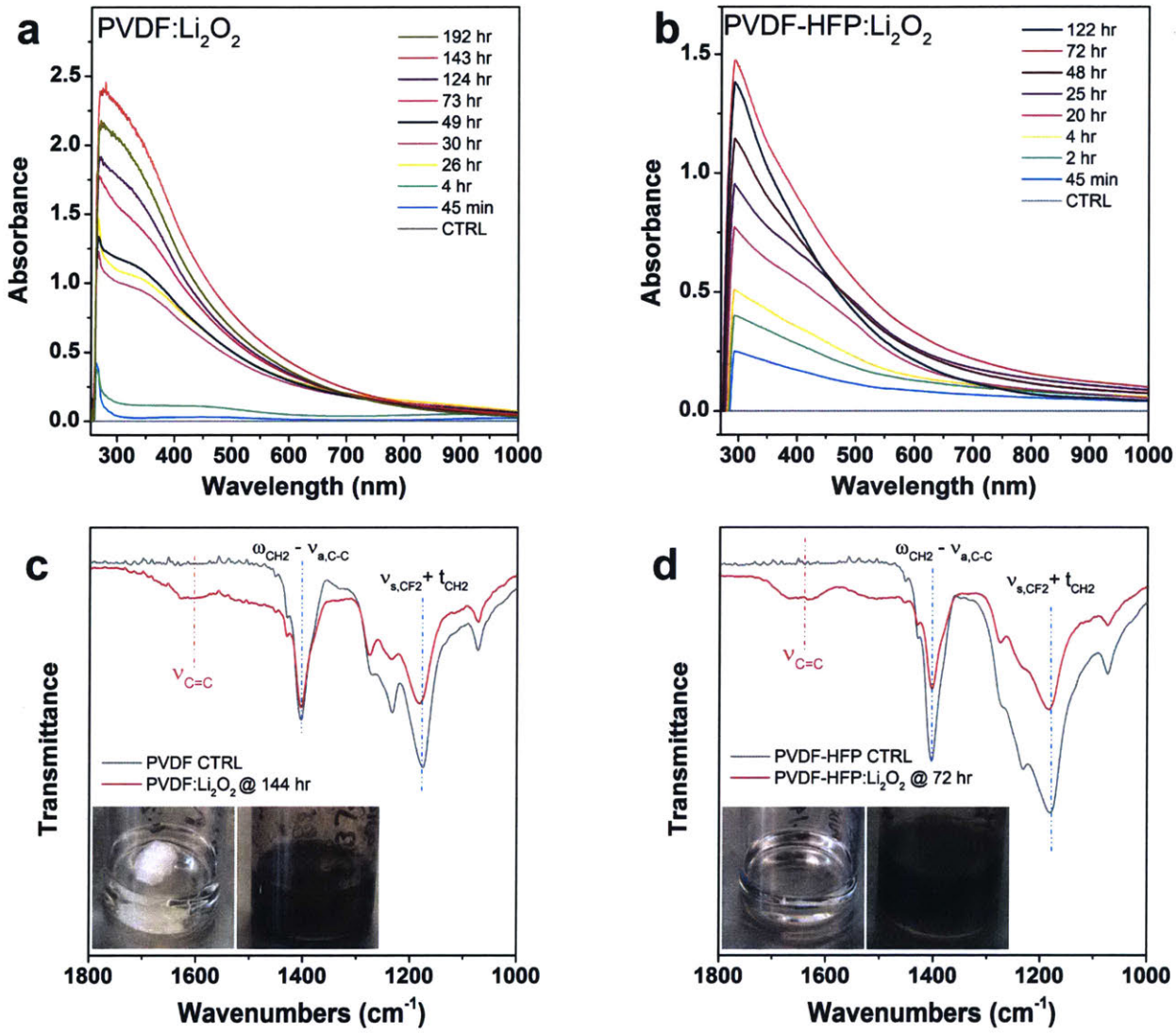

Figure 3-5 | Reaction of PVDF and PVDF-HFP. UV-Vis spectra of the reaction of (a) PVDF and (b) PVDF-HFP with Li_2O_2 as a function of time. The absorbance increase in the UV-Vis spectra show the rise in concentration of soluble decomposition species resulting from PVDF and PVDF-HFP degradation. (c) FTIR spectra of the PVDF: Li_2O_2 reaction after 144 hours and (d) the PVDF-HFP: Li_2O_2 reaction after 72 hours. The rise of the C=C stretching vibrations around 1650 cm-1 confirm the formation of conjugated alkene-like degradation products whose formation is tracked in the UV-Vis spectra. The inset pictures in (c) and (d) correspond to the PVDF and PVDF-HFP solutions after reaction with Li_2O_2, respectively. Peak assignments and vibration descriptors consistent with ref [89].

The changes in color, and formation of possible π-conjugated species again allowed for the use of UV-Vis spectroscopy to track the reactivity of PVC, PVDF, and PVDF-HFP in contact with Li_2O_2 (Figures 3-5a-b, 3-6a).[79] As the polymer/Li_2O_2 exposure time increased, so did the absorption in the UV-Vis spectra, corresponding to an increase in the concentration of soluble conjugated decomposition species resulting from PVC, PVDF, and PVDF-HFP degradation. Possible precipitation of these species led to a decrease in concentration (and absorbance). This is most evident in Figure 3-6a for the decomposition of PVC as the peak area first increased, and then decreased after longer exposure periods. Interestingly, the UV-Vis spectra for the degradation of PVC indicates a range of conjugated species that form, which absorb over most of the UV-Vis region.

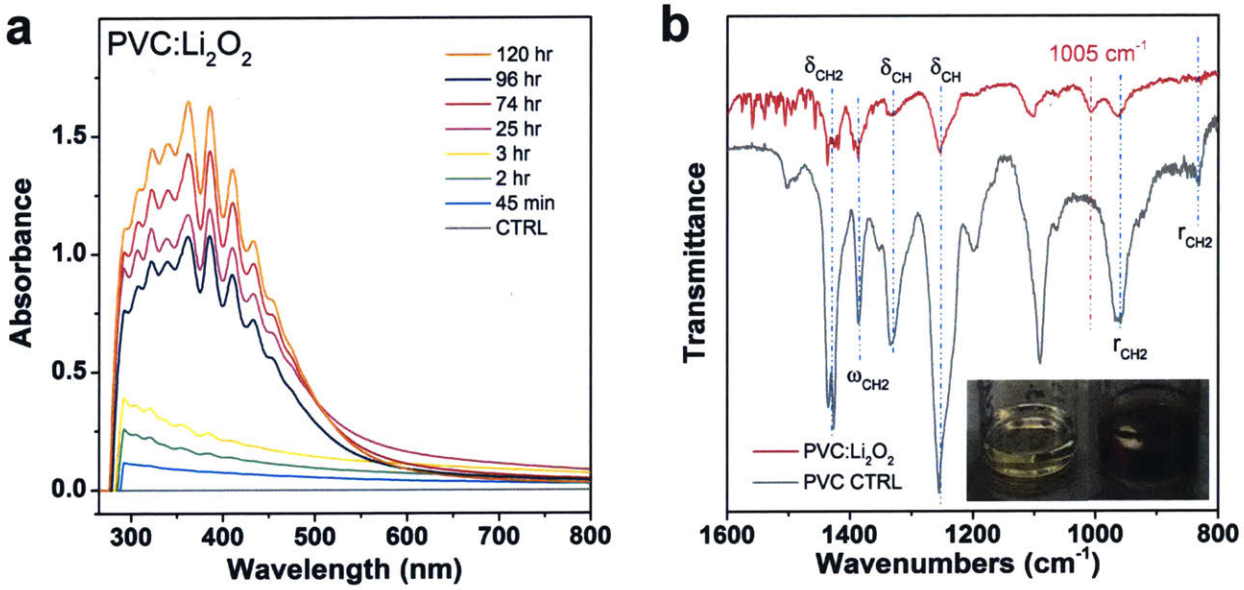

Figure 3-6 | Reaction of PVC with Li_2O_2. (a) UV-Vis spectra of the PVC reaction with Li_2O_2 as a function of time. The soluble decomposition species that result from PVC degradation increase with time, and absorb over most of the ultraviolet-visible region. (b) FTIR spectra of the PVC: Li_2O_2 reaction after 72 hours. Inset picture in (b) shows the corresponding color change after reaction. Peak assignments obtained from ref [90], while vibration descriptors are consistent with the notation given in ref [89].

In the analysis of these halogenated polymers, it is helpful to reference the well-known reactions of alkyl halides. The carbon-halogen (C–Cl, C–F) bond is highly polar due to the significant difference in electronegativity between carbon and the halogens, and this results in an electron-deficient α-C atom.[79] Alkyl halides often act as electrophiles and are capable of undergoing two different reactions: (i) nucleophilic substitution at the α-C, and (ii) elimination of the β-H and the halogen to yield an alkene.[79] For PVDF and PVDF-HFP, where fluorine is the halogen, a bimolecular (S_N2) substitution of peroxide or any nucleophile at the α-C is unfavorable because F is a very poor leaving group. Alkyl fluorides typically do not undergo these S_N2-type reactions.[79] In addition, a unimolecular (S_N1) substitution is also unlikely because of the poor leaving nature of F, the secondary nature (2°) of the α-C, and because the nucleophile Li_2O_2 is a strong base.[79] Therefore, an elimination mechanism would be preferred for the reaction of PVDF with Li_2O_2, and the PVDF component of PVDF-HFP. A unimolecular (E1) elimination mechanism would be uncompetitive because the first step, which involves F leaving the chain, would be too slow. Therefore, a bimolecular elimination (E2) reaction is favored because of the presence of a strong nucleophile and the highly electron deficient protons; and as shown in Figure 3-7 begins with the abstraction of a β-CH_2 proton, followed by the formation of an alkene, and then expulsion of the fluorine.[26,79] FTIR spectra[89] of the decomposition products of PVDF and PVDF-HFP in Figures 3-5c-d support this elimination mechanism and shows the rise of the aforementioned alkene C=C stretching vibrations at 1650 cm^{-1} that result from the dehydrofluorination of the PVDF backbone.[26] These C=C vibrations and the formation of the resultant LiF has also been reported by several authors.[26,72,91] The resultant conjugated alkene species is responsible for the observed blackening of the solution, and for the discoloration some have observed when PVDF and PVDF-HFP are used in lithium-air cells.[26,72] It must be mentioned that the presence of two fluorine groups on the polymer's α-carbon will make the β-H protons more electron deficient as compared to, for example poly(vinyl fluoride) with just one fluorine in its repeat unit.

For PVC, the decomposition mechanism is slightly different. Although the α-C of PVC is secondary and also contains a halogen functionality, an S_N2-type substitution is possible because Cl is a good leaving group.[79] However, for secondary alkyl halides where a strong base is used, an E2 mechanism dominates like in the fluorinated PVDF and PVDF-HFP, and leads to the elimination of H-Cl (Figures 3-7, S8), and the formation of alkene species along the polymer

backbone.[79,87] Again, these alkene conjugated species are responsible for the color changes, and the FTIR spectra[90] in Figure 3-6 shows the stretch at 1005 cm^{-1} that is specific for long all-trans polyene conjugate species, also observed during the dehydrochlorination of PVC by KOH.[87,92] The UV-Vis spectra in Figure 3-6a are similar to those obtained for PVC that has been degraded thermally and degraded by exposure to potassium tert-butoxide, and the general absorption over the UV-Vis region is attributed to these long polyene-like moieties.[88] Therefore, it is proposed that PVC, PVDF, and PVDF-HFP undergo dehydrohalogenation processes upon exposure to Li_2O_2.

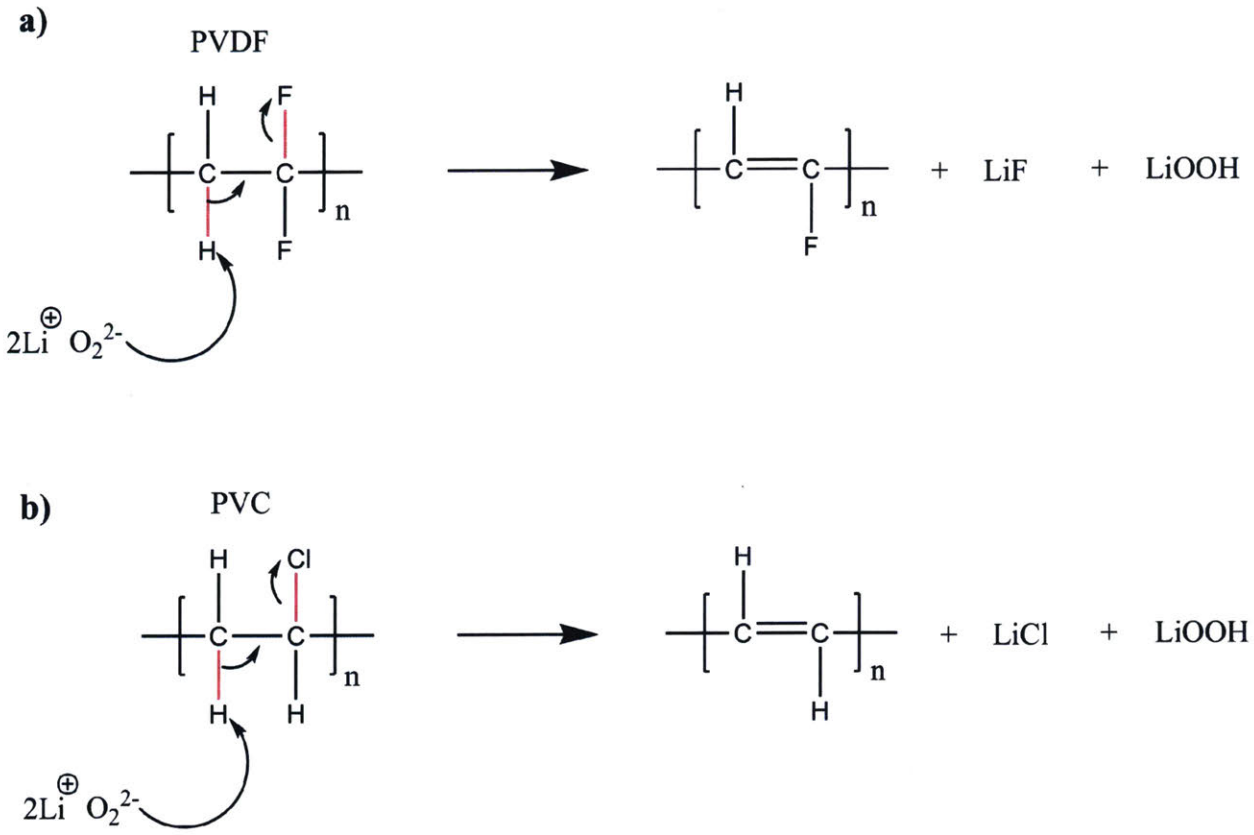

Figure 3-7 | Proposed mechanism for PVDF and PVC reaction. Mechanism for the degradation of (a) PVDF and (b) PVC. These polymers both undergo dehydrohalogenation degradation processes in the presence of peroxide.

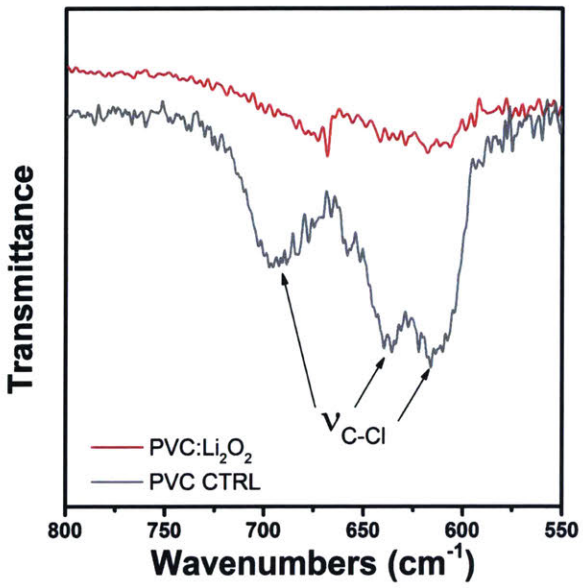

Figure 3-8 | FTIR analysis of PVC and Li_2O_2 reaction. FTIR spectra of the reaction of PVC with Li_2O_2. This is the extended fingerprint region of the same spectra shown in Figure 3-6b. It shows a significant intensity decline in the C-Cl stretching vibrations, further confirming the dehydrochlorination process that involves a loss of H-Cl from the polymer backbone to yield conjugated polyenes.

When polymers devoid of hydrogen atoms in their backbone like fully fluorinated PTFE and Nafion® were examined, no reaction with Li_2O_2 was observed (Figure 3-9). The elimination reactions responsible for the degradation of PVC, PVDF, and PVDF-HFP are no longer possible due to the absence of hydrogen atoms that can be abstracted on the polymer chain, and any bimolecular or unimolecular substitutions of peroxide are unfavorable.[79] The FTIR spectra[93] in Figures 3-9a-b did not show any decomposition products (either alkene or other) for Nafion® and PTFE, and no color changes were observed. The new broad peak that did appear in Figure 3-9a for the PTFE mixture with Li_2O_2 was also present in the Li_2O_2/DMF control. Nafion® was also examined using UV-Vis (Figure B-2), which revealed no soluble decomposition species. It is important to mention that although the backbone of commercially sold Nafion® often remains the same, the end group varies because of different functional groups introduced to impart solubility properties. If the end-group is reactive with Li_2O_2, it is possible for the stability of Nafion® to be adversely affected.

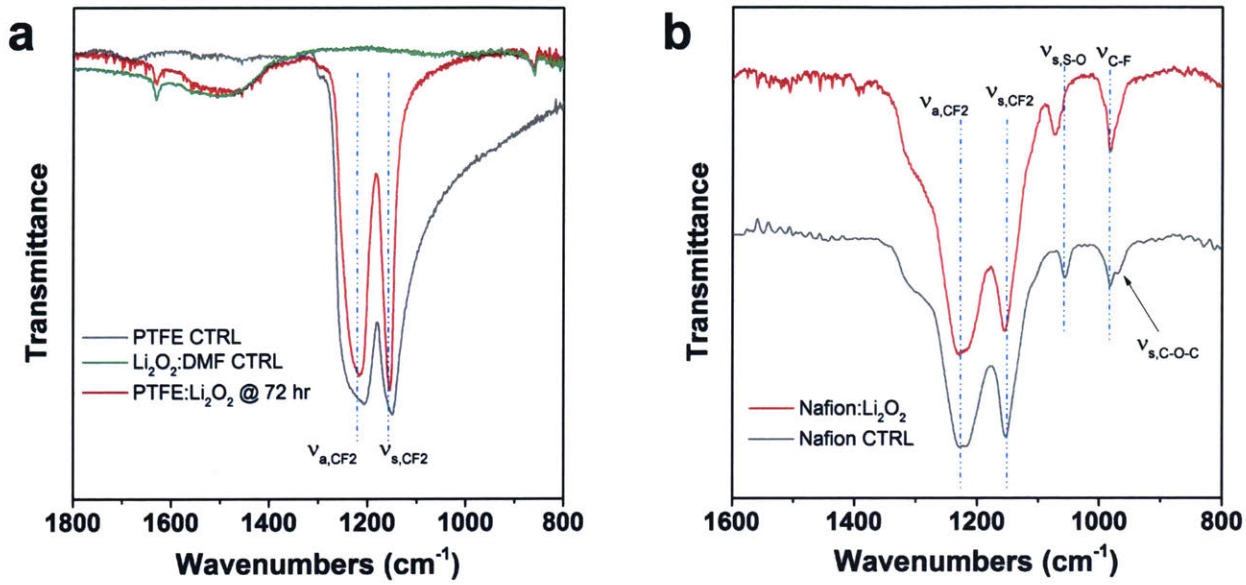

Figure 3-9 | FTIR analysis of PTFE and Nafion mixture with Li_2O_2. FTIR spectra of the mixture of (a) PTFE and (b) Nafion® with Li_2O_2 after 72 hours. Neither PTFE nor Nafion® appear reactive with Li_2O_2. Peak assignments for 6a and 6b obtained from ref [93], while vibration descriptors are consistent with the notation given in ref [89].

Since the fully fluorinated polymers do not appear to react with Li_2O_2, the reactive component of the PVDF-HFP copolymer is presumed to be PVDF and not HFP, as HFP is fully fluorinated with no protons on the polymer backbone. As Figures 3-5a-b show, the concentration of soluble decomposition species was higher for PVDF than PVDF-HFP, suggesting PVDF can be more reactive than PVDF-HFP due to the higher fraction or relative concentration of PVDF units in the homopolymer.

3.3.3 Poly(vinyl pyrrolidone)

Poly(vinyl pyrrolidone) is another polymer that has been explored for electrolyte systems.[94,95] It has a pyrrolidone side chain on the aliphatic backbone of the polymer. When this polymer was exposed to Li_2O_2, a light yellow solution resulted (Figure B-3). UV-Vis data showed an increase in soluble decomposition species as a function of time, but as compared to the reactive polymers discussed previously, the concentration of soluble decomposition species was much lower (Figure B-3). Therefore, although PVP reacts with Li_2O_2, it is a slow reaction, and when the

decomposition species were analyzed, no significant changes appeared in the NMR and FTIR spectra (Figures B-3).[96] Although the carbonyl group is highly polar, the presence of the nitrogen atom in the ring with its lone pair electrons donate electron density to the carbonyl and reduce the electron deficiency of the α-CH_2 protons adjacent to the carbonyl.[79] Nucleophilic attack is still possible at the α-CH_2 position and the carbonyl carbon, and the slight reaction with Li_2O_2 may be due to this attack, but the reaction rate is significantly lower than those discussed above.

3.3.4 Poly(methyl methacrylate)

Another polymer that has found common utility in gel polymer electrolyte systems for lithium-based batteries is poly(methyl methacrylate) or PMMA.[73,97] A gel can be formed by mixing PMMA powder with organic liquids (or ionic liquid) or polymerizing the monomer MMA in the presence of the ionically conducting organic liquid/ ionic liquid.[98] Remarkably, when PMMA was exposed to Li_2O_2, it appeared stable, and no discoloration was observed. FTIR (Figure 3-10a)[99] and NMR (Figure 3-11)[100] data showed no appearance or disappearance of peaks, and the molecular structure of the polymer before and after Li_2O_2 exposure remained intact. However, in the NMR data in Figure 3-11, an unassigned proton peak at $\delta = 3.16$ ppm appeared, which may be due to a reactive impurity in PMMA since the polymer backbone and side-chain functionality appear stable.

We can consider the stability of PMMA by simplifying the polymer into an ester-like small molecule that affords us different reaction mechanisms for possible nucleophilic attack by Li_2O_2. Firstly, the carbonyl functional group (C=O) is highly polar due to the difference in electronegativity between oxygen and carbon, and like the nitrile carbon and the α-C in an alkyl halide, the carbonyl carbon has a partial positive character (δ^+), is acidic, and capable of reacting with nucleophiles.[79] For carbonyl-containing compounds, there are four general reactions that can be anticipated for these systems: (i) alpha substitution at the carbon α to the carbonyl, (ii) carbonyl condensation between two carbonyls, (iii) nucleophilic addition at the carbonyl carbon, and (iv) nucleophilic acyl substitution at the carbonyl carbon.[79]

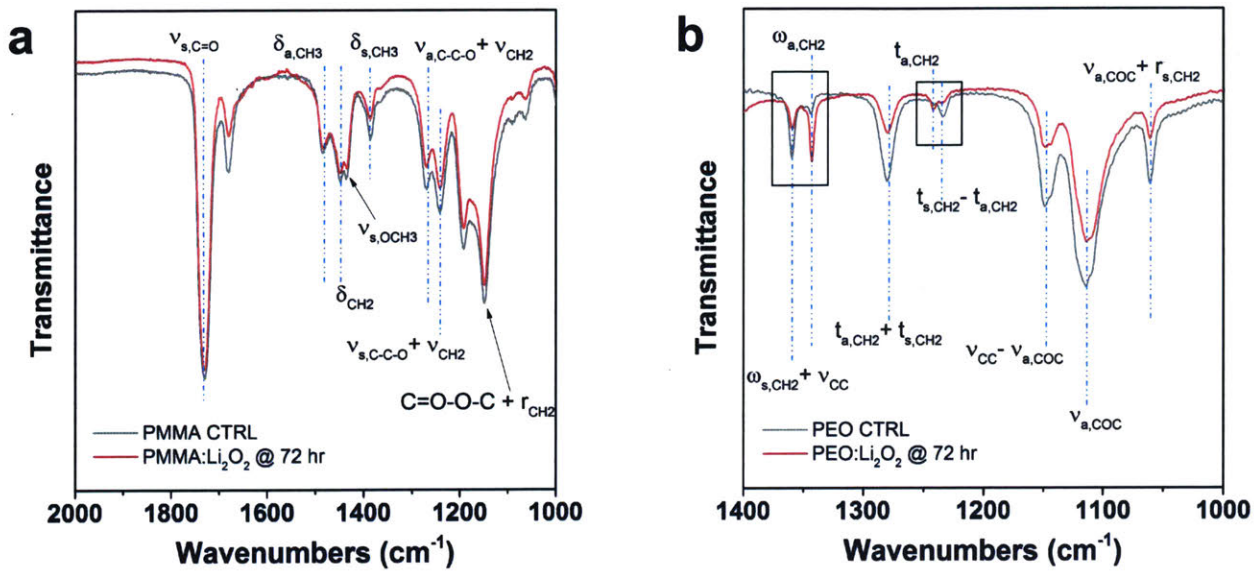

Figure 3-10 | FTIR analysis of Li_2O_2 with PMMA and PEO. FTIR spectra of the mixture of (a) PMMA and (b) PEO with Li_2O_2. PMMA appears stable while the intensity of the CH_2 vibrations of PEO changes, hinting at a degree of crosslinking within the PEO chains induced by Li_2O_2 (boxed section in 3-10b). Peak assignments for 3-10a and 3-10b obtained from refs [99] and [101] respectively, while vibration descriptors are consistent with the notation given in ref [89]

At the α-C position of PMMA that is attached to the polymer backbone, there is no hydrogen atom present. Instead, the α-C is substituted with a methyl group that donates electron density to the α-C, essentially shutting off any potential reaction mechanism that can occur at that quaternary carbon. Since no α-CH is present, the first two reactions listed above are unlikely in PMMA.

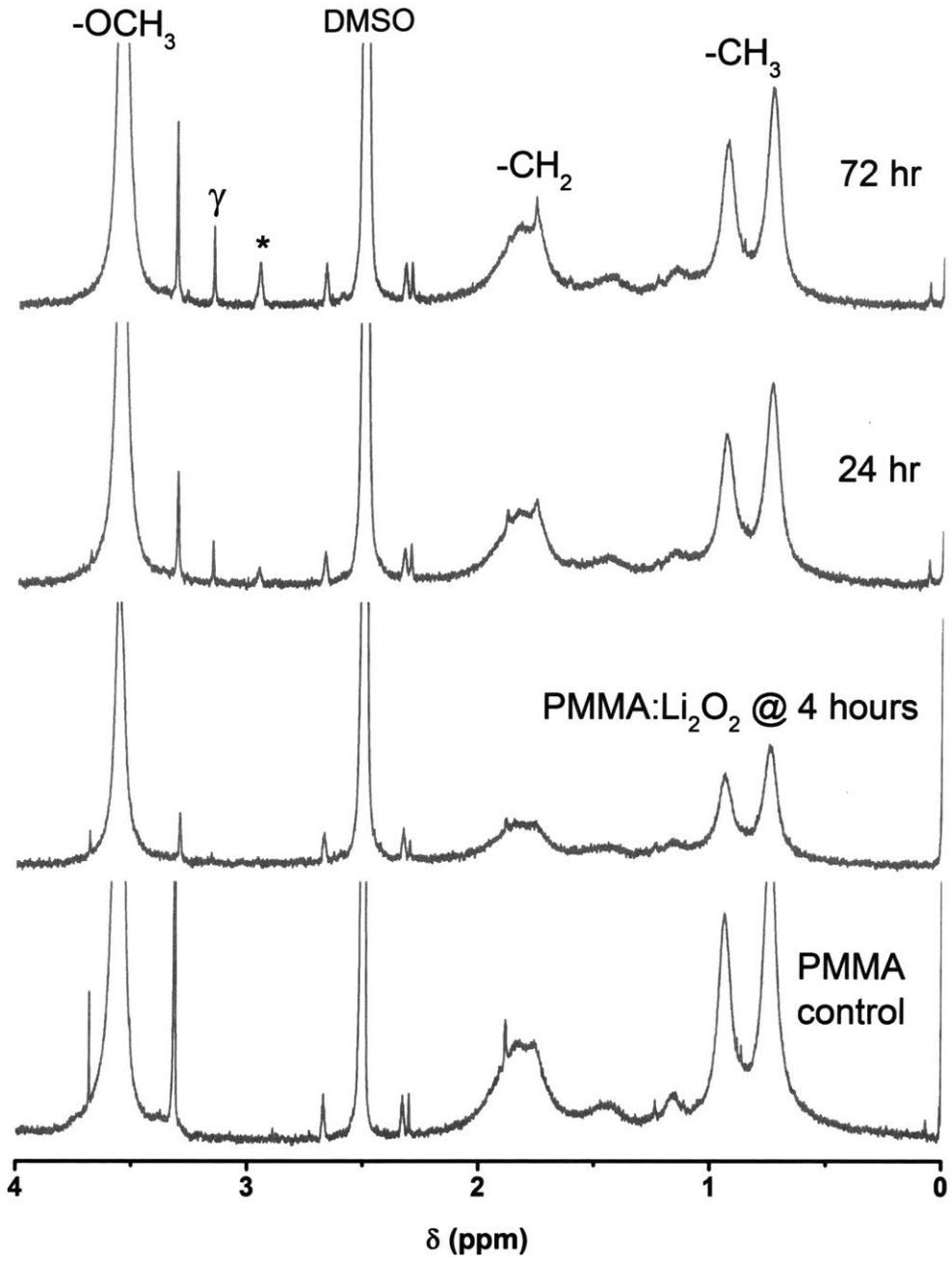

Figure 3-11 | H NMR analysis of PMMA with Li_2O_2. 1H NMR (400 MHz; DMSO; Me4Si) spectra of the PMMA mixture with Li_2O_2 as a function of time. * – peak due to Li_2O_2 reacting with DMSO (see Figure 3-8). γ – Unassigned peak.

Theoretically, the last two reactions listed are possible. Despite the fact that our data shows that PMMA is stable, we cannot rule out possible nucleophilic addition (rxn iii) or substitution (iv) at

the carbonyl carbon. If PMMA is used in a Li-air cell, strong bases like the superoxide radical anion can possibly add to the carbonyl center, and although this addition is reversible, any impurity such as water present in the cell could lead to further decomposition.[79] This might explain why Nasybulin *et al.* reported the formation of Li_2CO_3 in the mixture of PMMA/Li_2O_2/KO_2.[74] Also, nucleophilic substitution by a strong base at the carbonyl carbon that leads to elimination of a methoxy anion is possible, but the methoxy anion is a poor leaving group—much worse than fluorine—making this reaction route unfavorable.[79] It is for these reasons we consider PMMA to be stable in the presence of Li_2O_2 alone.

3.3.5 Poly(ethylene oxide)

Unlike the aliphatic (C–C, C–H) backbone polymers such as PAN and PMMA discussed above, whose stability is heavily influenced by the presence and type of functional group, polyethylene oxide (PEO) has an ether backbone with no side-chain functionalities. It is the only polymer studied in this work that, when complexed with a lithium salt, is capable of acting as a good solid-state electrolyte in the absence of liquids. For current lithium-air cells, ether solvents such as dimethoxyethane (DME) and tetraethylene glycol dimethyl ether (TEGDME) have become the solvent of choice,[59,62,102] despite widely varying conclusions regarding their stability.[19,44,103] PEO is essentially a macromolecule of DME, and when exposed to Li_2O_2 appears relatively stable (Figure 3-10b).

Ethers are often highly stable compounds, and except for possible C–O bond cleavage by strong acids or highly oxidative conditions, are unreactive in the presence of bases, nucleophiles, and many other reagents.[79] This is consistent with our observation that PEO is relatively stable in the presence of Li_2O_2. As the FTIR spectra[101] in Figure 3-10b shows, no new functional groups are observed after addition of Li_2O_2 to the PEO/DMF mixture. However, the change in the ratio of the peaks at 1242 cm^{-1}/1234 cm^{-1} and 1360 cm^{-1}/1343 cm^{-1} (highlighted in Figure 3-10b) that correspond to the CH_2 stretches indicate that some crosslinking of PEO may have occurred in the presence of Li_2O_2. In addition, GPC data showed a 15 percent increase in the weight average molecular weight, an increase in the number average molecular weight by a factor of 3, and a reduction in the polydispersity index by a factor of 2.5, confirming crosslinking of the PEO chains. The NMR spectra shows very minor signs of degradation (Figure 3-12) where a peak associated with lithium formate is observed, an occurrence previously noted in small molecule

ethers.[19,102]. Furthermore, we must note that ethers can also react with oxygen to form peroxide species.[79] Therefore, future studies would be needed to examine the effect of possible PEO crosslinking on the performance of a lithium-air cell.

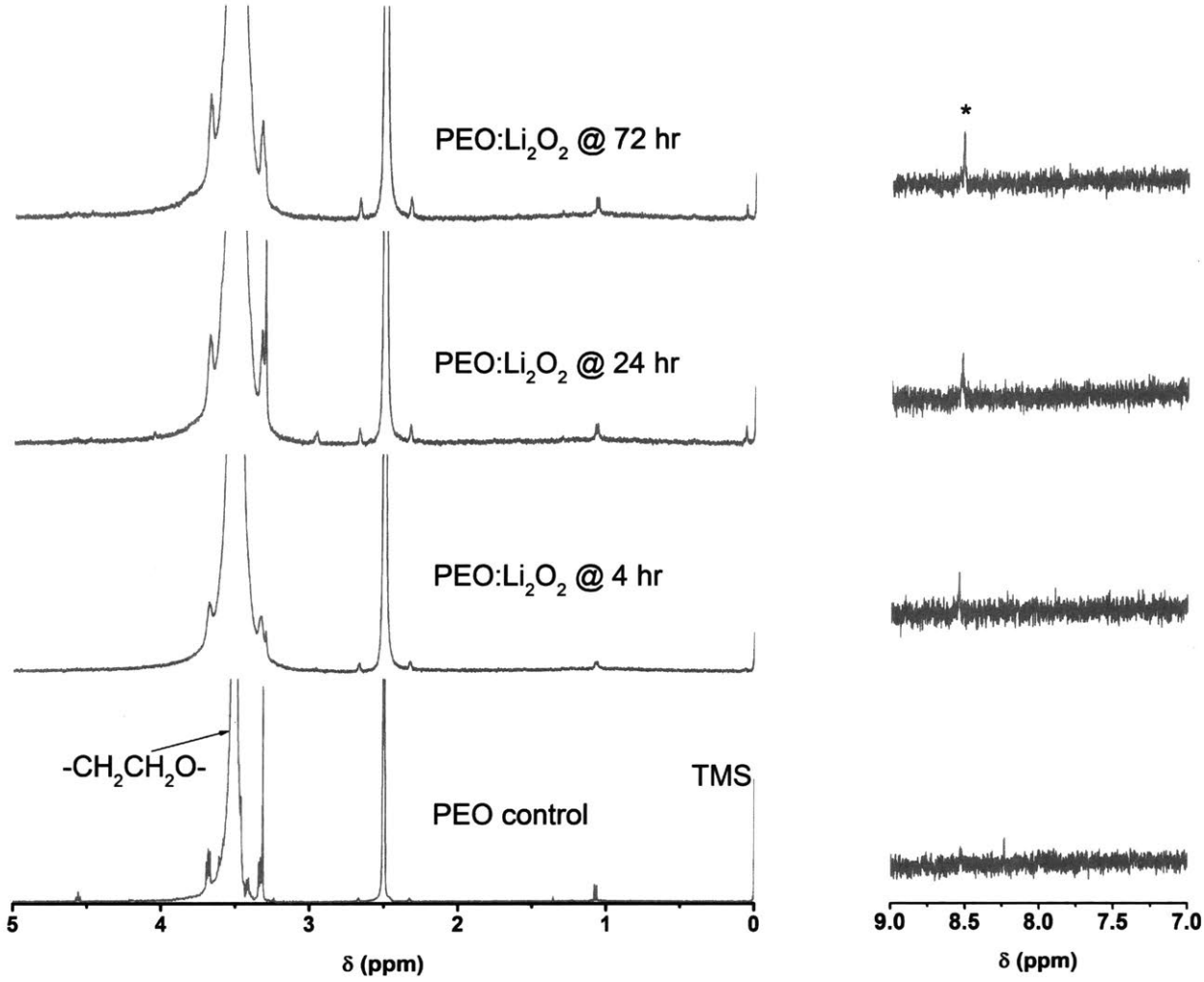

Figure 3-12 | ^{1}H NMR analysis of PEO with Li_2O_2. ^{1}H NMR (400 MHz; DMSO; Me4Si) spectra of the PEO mixture with Li_2O_2 as a function of time. The plot on the right hand side is a zoomed-in section of the left-hand plot. *-indicates the possible formation of lithium formate as a minor decomposition product of PEO in the presence of Li_2O_2. The formation of formate as an ether decomposition product has been reported previously.[19,102]

3.3.6 Establishing reactivity trends

The polymers discussed in this work were examined to determine their stability and possible reactivity in the presence of the desired discharge product in a lithium-air cell. However, the goal of this work encompasses more than the study of a small number of polymers; rather, it would be helpful to use the knowledge gained from this subset of polymers to predict the stability of other polymers. This subset of polymers listed in Figure 3-1 allows us to develop reactivity trends that can prove useful in the selection and utilization of new polymers for lithium-air applications.

UV-Vis spectroscopy makes it possible to understand the relative rates of reactivity for the unstable polymers studied. To compare the reactivities of PAN, PVC, PVDF, PVDF-HFP, and PVP, equivalent polymer and Li_2O_2 mass concentrations were used (see Experimental section for more details). Using the absorbance value at λ_{max}, which corresponds to the concentration of soluble species from polymer degradation, a plot of absorbance versus reaction time (Figure 3-13) yields a form of kinetic degradation rate curve for each of the polymers. PAN appears to be the most reactive of the polymers studied, and PVP the least. Despite the fact that the aliquot used for the other polymers (PVC, PVDF, PVDF-HFP, and PVP) was five times more concentrated than PAN (see Experimental Section), the concentration of PAN decomposition species is still much higher. The order of polymer reactivity with Li_2O_2 appears to be as follows: PAN >> PVC ~ PVDF > PVDF-HFP >> PVP. At initial reaction times, PVC reacts similarly to PVDF but, at longer reaction times, PVDF appears more reactive than PVC because the protons in PVDF are more electron-deficient (due to the two fluorine functionalities in each repeat unit) as compared to the protons in PVC. In addition, as mentioned previously, PVDF is more reactive than PVDF-HFP because of the higher PVDF fraction in the homopolymer.

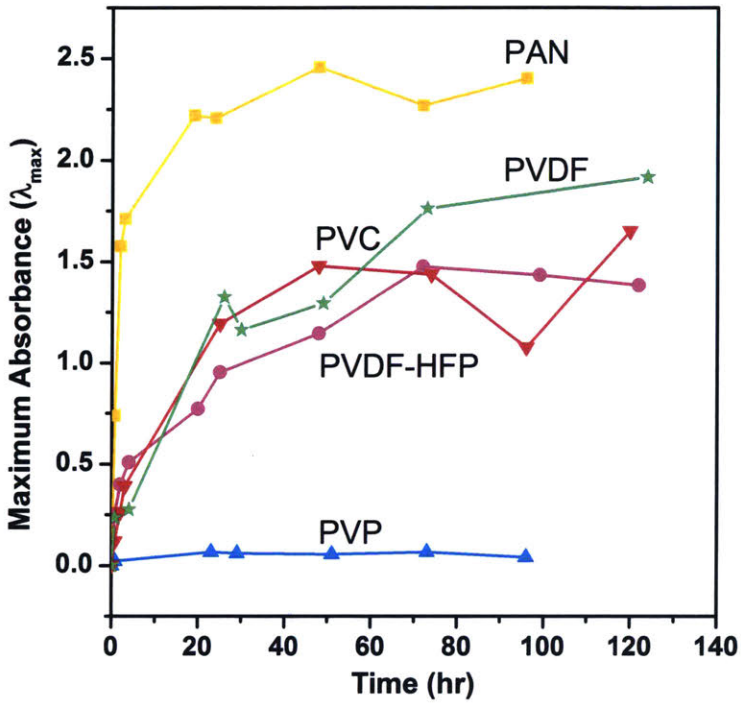

Figure 3-13 | Reactivity trends across studied polymers. Plot of the maximum absorbance (λmax) at each time point for the different unstable polymer/Li_2O_2 mixtures studied. The maximum absorbance corresponds to the soluble decomposition species resulting from polymer degradation. Of the polymers studied, PAN appears to be the most reactive with Li_2O_2, while PVP the least. The halogenated polymers have similar reactivity with Li_2O_2, although at longer times, PVDF appears more reactive than PVC and PVDF-HFP.

Not surprisingly, at short reaction times, this order of reactivity closely corresponds to the Hammett constants for the different functional groups: PAN (0.56) > PVC (0.37) ~ PVDF (0.34) > PVP (0.05).[104] This trend is reasonable because it correlates with the electrophilic nature of the functional groups. The higher the Hammett constant, the more electrophilic and electron withdrawing the functional group, the more electron-deficient the polymer chain, and the more reactive the polymer will be with the nucleophilic and electron-rich Li_2O_2.[79] However, the electrophilic nature of the functional group on the polymer is not the only parameter that governs reactivity with Li_2O_2, especially since PTFE and Nafion® share the same functional group as PVDF and PVDF-HFP, but still appear stable. A second parameter, the presence of an α or β-

hydrogen atom adjacent to the electron-withdrawing/electrophilic functional group, also contributes to the polymer's instability.[26] The two parameters that appear to govern reactivity with Li_2O_2, and in turn polymer stability in the nucleophilic lithium-air cell environment are summarized as follows:

I. The presence of highly electron-withdrawing functional groups on the polymer side chain [$-C\equiv N$, $-X$ (F, Cl), $-NO_2$, $-CF_3$] AND

II. If the polymer backbone is aliphatic, the presence of a hydrogen atom that is α or β to the electron-withdrawing group.

We propose that these two parameters are important for the stability of the fluorinated polymers (PTFE and Nafion® vs. PVDF and PVDF-HFP), where the only difference between the two classes is parameter II. For PAN, the presence of the electrophilic nitrile group (parameter I) seems sufficient enough for PAN to react with Li_2O_2, especially since nucleophilic attack begins at the nitrile carbon. Replacing the α-CH – which is cleaved during PAN reaction with Li_2O_2 (Figure 3-3) – with a methyl group might reduce the reactivity of PAN, but will be insufficient to entirely thwart the reaction of PAN. For PVC, the presence of the halide functionality (parameter I) and the adjacent α and β hydrogens (parameter II) make the dehydrochlorination of PVC in the presence of Li_2O_2 possible. PVP is much less reactive because the nitrogen donates electron density to the carbonyl side group, while PEO is relatively stable despite possible crosslinking in the presence of Li_2O_2 because of the electron-donating nature of the ether functional group.[79]

These guidelines can be used to examine numerous other polymers. For example, a polymer with a nitro functional group ($-NO_2$) or a trifluoromethyl functional group ($-CF_3$) adjacent to an α-CH proton will lead to an electron-deficient proton and almost-certain reactivity with Li_2O_2. Knowledge of the reactions of small molecules in the presence of bases and nucleophiles should provide additional insight with regards to the chemical stability of polymers for lithium-air.

It is important to note that although Li_2O_2 is used for these polymer screening tests, it may not be the only source of nucleophilic species in a lithium-air cell. It is believed that during cell discharge, superoxide radical anions are formed[14,65] and they could serve as either a nucleophile or a source of radical species that can propagate polymer decomposition. Therefore, the polymer

reactions that occurred in the presence of Li_2O_2 may be accelerated in the presence of O_2^- in an actual lithium-air cell. In addition, it will be important to examine the polymers that do appear chemically stable (PTFE, Nafion®, PMMA, and PEO) in a lithium-air cell to determine their electrochemical stability in a reduced oxygen environment.

Finally, lithium peroxide size variations[70] and different surface chemistry[105] can also lead to differences between the chemical stability that this work has examined, and what occurs in a fully operating lithium-air cell. Although commercial lithium peroxide is used for this screening study, electrochemically generated lithium peroxide species may be in the form of particles with much smaller dimensions (dependent on discharge capacity)[106] that may increase their surface area and thus reactivity with the polymers studied, and accelerate polymer degradation. In addition, the stability of these polymers upon charging in lithium-air is also of importance and further studies will be needed to elucidate potential degradation pathways. Continued degradation of the polymer that serves as an electrolyte or as a binder will contribute to poor rate capabilities of lithium-air cells, poor round-trip efficiencies, and a much shorter cell lifetime.[72]

3.4 Conclusions

Using commercial lithium peroxide as a screening tool, we have examined the stability of polymers that have been commonly used for lithium-based battery applications. The polymers PAN, PVC, PVDF, PVDF-HFP, and PVP react with Li_2O_2 and are unstable. The polymers PMMA, PTFE, and Nafion® appear chemically stable in the presence of Li_2O_2. PEO appears relatively stable, but may undergo some chemical crosslinking. Using tools such as UV-Vis, NMR, FTIR, and GPC, the decomposition species were characterized to determine the modes of degradation. Two parameters seem to govern the stability of the polymers studied: (i) the presence of highly electron-withdrawing/electrophilic functional groups on the polymer side chain, and (ii) the presence of hydrogen atoms that are adjacent to the aforementioned electron-withdrawing groups. Lithium peroxide or any oxygen free-radical species or nucleophile in a lithium-air cell can attack these unstable polymers, leading to polymer decomposition that will negatively affect the chemistry and long-term performance of a lithium-air cell. Finally, these studied polymers provide invaluable insight into the general stability of polymers and the correlation between polymers and their small organic molecule counterparts. Understanding the

general reactivity of functional groups with bases and nucleophiles will be important in the selection and development of new polymers for lithium-air applications.

3.5 Acknowledgments

This work was supported by the Samsung Advanced Institute of Technology (SAIT), and the facilities at the Koch Institute for Integrative Cancer Research at MIT. The authors also thank the Institute for Soldier Nanotechnologies (ISN) at MIT for use of their GPC. C.V.A. would like to acknowledge the GEM Fellowship, and support by the Department of Defense (DoD) through the National Defense Science & Engineering Graduate (NDSEG) Fellowship Program.

Chapter 4

One-Electron Mechanism in a Gel-Polymer Electrolyte Li–O_2 Battery

Adapted and reproduced with permission from Chibueze V. Amanchukwu, Hao-Hsun Chang, Magali Gauthier, Shuting Feng, Thomas P. Batcho, and Paula T. Hammond, "One electron process in a gel polymer electrolyte Li-O_2 battery." *Chem. Mater.* 2016, 28, 7167-7177.

4.1 Introduction

The need to address climate change and decrease the carbon output generated from fossil fuels has spurred rapid development and fervent commercial implementation of renewable energy technologies such as solar and wind. These energy generation technologies require the development of cheaper and more energy-dense storage media to make them viable large scale or mobile energy solutions.[12] Therefore, newer battery chemistries such as metal-air and metal-sulfur have been explored.[12,13,57] Among the metal-air chemistries, lithium-air (O_2) has the highest theoretical gravimetric energy density (~3500 Wh/kg_{Li2O2}),[12] and involves oxygen as the active species in combination with lithium metal.[14] Discharge of Li–O_2 batteries typically involves a two-electron process, where oxygen is first reduced to superoxide $O_2^{\bullet-}$ (equation (1)), and further to lithium peroxide through disproportionation of lithium superoxide (a reactive free radical), (equation (3a)) or an additional electrochemical reduction step (equation (3b)).[14,20,45,64,107-110] On charge, it is believed that oxidation of Li_2O_2 yields Li^+ and O_2 gas.[20,43,110]

$$O_2 + e^- \rightarrow O_2^- \quad (1)$$

$$Li^+ + O_2^- \rightarrow LiO_2 \quad (2)$$

$$LiO_2 + LiO_2 \rightarrow Li_2O_2 + O_2 \quad (3a)$$

$$LiO_2 + Li^+ + e^- \rightarrow Li_2O_2 \quad (3b)$$

Controlling the discharge chemistry in Li–O_2 cells is vital, and solvent type, catalysts, and other additives have been explored to improve the discharge capacities, current rate, and O_2 solubility, but have not yielded a 1 mol e^-/mol O_2 process.[58,109,111,112] During the writing of this work, Lu *et al.* reported a 1 mol e^-/mol O_2 process in the presence of iridium nanoparticles on a reduced graphene oxide electrode in a liquid electrolyte.[113] The 2 mol e^-/mol O_2 reduction process has been suggested to be partially responsible for the kinetically-limited oxygen reduction and evolution reactions, low current rates, poor capacity retention, and low cycle life typically observed in Li–O_2 cells.[12,14,32] In addition, conventional Li–O_2 batteries use non-aqueous liquid electrolytes, and their chemical and electrochemical instability,[18,19,24] volatility and flammability preclude their use in an oxygenated environment.

Ionic liquids (IL) and bulky cations such as tetrabutylammonium (TBA) have been shown to support a 1 mol e^-/mol O_2 process using cyclic voltammograms (CVs), but never in an actual Li–O_2 cell. Instead, a 2 mol e^-/mol O_2 process to form Li_2O_2 is observed when ionic liquid/salt systems based on 1-butyl-1-methylpyrrolidinium bis(trifluoromethanesulfonyl)imide ($Pyr_{14}TFSI$) and 1-ethyl-3-methylimidazolium bis(trifluoromethanesulfonyl)imide (EMITFSI) are used as the electrolyte in a Li–O_2 cell.[30] In this work, we incorporate ionic liquids into a gel polymer electrolyte (GPE), and show that the Li^+/IL^+ molar ratio in the GPE controls the oxygen reduction process, switching from 2 mol e^-/mol O_2 in the presence of Li^+ to 1 e^- in the absence of Li^+ (and only presence of ionic liquid cation). Spectroscopic tools such as ultraviolet-visible (UV-Vis) and electron paramagnetic resonance (EPR) spectroscopy were used to confirm the formation of a ionic liquid-superoxide complex not previously observed in Li–O_2 batteries. This discharge behavior is observed only when the ionic liquid (either ammonium, pyrrolidinium or imidazolium) is incorporated in a GPE, and not in the pure ionic liquid.

The GPE contains a polymer and an ionic liquid/lithium salt mixture, where the polymer provides mechanical support and impacts barrier and diffusion properties in the membrane, and the ionic liquid/lithium salt provides the necessary ionic conductivity. DFT calculations and Pearson's Hard Soft Acid Base (HSAB) theory[114] are used to explain the observed oxygen reduction phenomena, and a non-aqueous battery prototype that uses an anion-exchange membrane to simulate the GPE Li–O_2 cell environment is developed to demonstrate the broad scope of this work. A one electron discharge process could prove vital in alleviating the slow kinetics, poor cycle life, and reactivity concerns of standard Li–O_2 batteries. Moreover, the mechanism observed here could be of great interest in other metal-air and metal-sulfur batteries where controlling intermediate type and solubility is paramount.

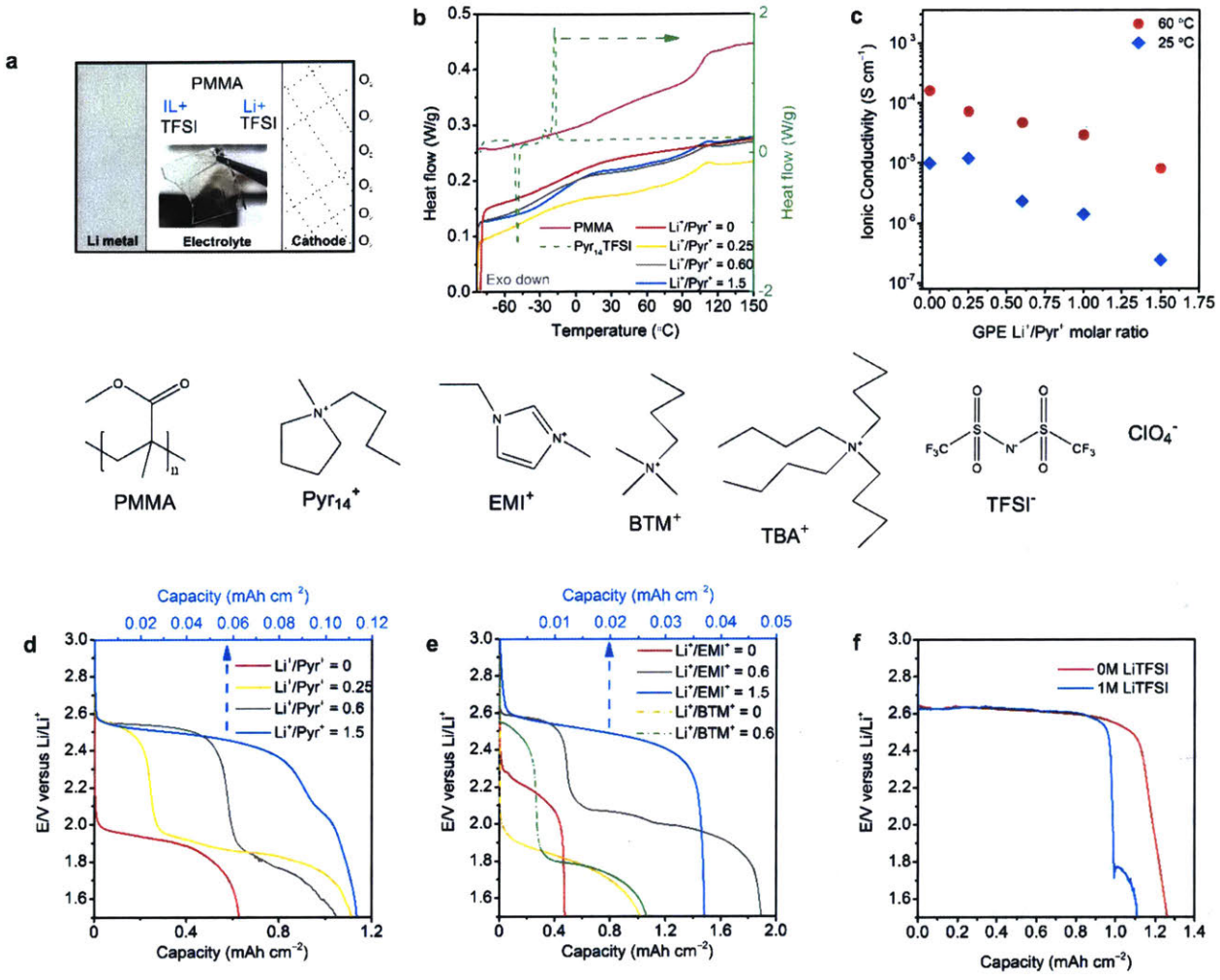

Figure 4-1 | Physical and electrochemical characterization as function of Li+/IL+ content in the GPEs and in pure ionic liquid systems (without polymer). a, Configuration of the gel polymer electrolyte Li–O_2 cell. (1a inset = flexible GPE film with Li^+/Pyr^+ molar ratio of 0); b, Differential Scanning Calorimetry (DSC) plot of PMMA, $Pyr_{14}TFSI$, and varying GPE content; c, Ionic conductivity of different GPE formulations at 25 and 60 °C; Discharge curves of Li–O_2 cells in O_2 of varying Li^+/Pyr^+ (d) Li^+/EMI^+ and Li^+/BTM^+ (e) GPE formulations; f, Discharge curves of Li–O_2 cells in O_2 using a salt-free or 1 M LiTFSI in $Pyr_{14}TFSI$ ionic liquid electrolyte (no PMMA present in electrolyte). (d)–(f) Current rate = 10 μA cm^{-2} (based on geometric surface area) using a Vulcan carbon/PMMA electrode (4:1 mass ratio) at 60 °C. The ratios indicate the molar ratio of Li^+/Pyr^+ or Li^+/EMI^+ in the GPE. Chemical structures of the polymer,

salt, and ionic liquids are shown. PMMA: poly (methyl methacrylate); Pyr14: 1-butyl-1-methylpyrrolidinium; EMI: 1-ethyl-3-methylimidazolium; BTM: Butyl-trimethyl ammonium; TBA: tetra-n-butyl ammonium; TFSI: bis(trifluoromethanesulfonyl)imide. IL+ = ionic liquid cation

4.2 Experimental Methods

4.2.1 Materials used

Poly(methyl methacrylate) (Mw = 120, 000), lithium bis(trifluoromethane)sulfonimide (LiTFSI) salt (99.95 % trace metals basis), tetra-n-butylammonium perchlorate (> 99.0 %, for electrochemical analysis), diethylene glycol dimethyl ether (anhydrous, 99.5%), acetonitrile (anhydrous, 99.8 %), dimethyl formamide (anhydrous, 99.8 %), deuterated dimethylsulfoxide (DMSO) (99.9 atom % D), poly(tetrafluoroethylene) (free-flowing, 1 μm particle size), deuterated chloroform (99.8 atom % D), and isopropanol were obtained from Sigma-Aldrich. Diethylene glycol dimethyl ether (diglyme) and dimethylsulfoxide (DMSO) were stored in 3 Å molecular sieves before use. Teflon evaporating dishes (65 mm diameter x 12 mm height) were obtained from VWR. 1-butyl-1-methylpyrrolidinium bis(trifluoromethanesulfonyl)imide ($Pyr_{14}TFSI$, ultrapure, 99.5%), Butyltrimethylammonium bis(trifluoromethylsulfonyl)imide (BTMTFSI, 99%), and 1-ethyl-3-methylimidazolium bis(trifluoromethansulfonyl)imide (EMITFSI, ultrapure, 99.5%) were obtained from IOLITEC Inc (Tuscaloosa, AL). Carbon paper (TGP-H-60, PTFE and non-PTFE treated) and lithium metal (0.75 mm thick, 99.9 %) were obtained from Alfa Aesar. Titanium carbide (nanopowder, 99+%, 40–60 nm, cubic) was obtained from US Research Nanomaterials (Houston, TX). Nafion was obtained as a 7.2 wt % lithiated Nafion in isopropanol solution from Ion Power Inc. Celgard C480 was obtained from Celgard. Spin trap 5-tert-butoxycarbonyl 5-methyl-1-pyrroline N-oxide (BMPO) was obtained from Cayman Chemical. The anion exchange membrane (Neosepta AHA) was obtained as a free sample from Ameridia (New Jersey, USA). Vulcan carbon (Vulcan XC72, 100 m^2/g) was obtained from Premetek Inc.

4.2.2 Gel polymer electrolyte film fabrication

Bohnke *et al.*[29] showed that in a PMMA/propylene carbonate (PC)/$LiClO_4$ GPE, a PMMA weight percentage less than 30 wt% is sufficient to retain an ionic conductivity regime similar to

pure PC solvent, and also generate mechanically stable films. Therefore, unless otherwise stated, PMMA content in the PMMA/Pyr_{14}TFSI/LiTFSI GPEs was maintained at around 30 wt% in this study. PMMA (at least 500 mg), LiTFSI, and Pyr_{14}TFSI were added to a 20 mL vial in the desired amounts. Sample amounts shown in Table C-2. About 4.5 mL of acetonitrile was then added to the vial and stirred until a clear transparent solution was obtained. The solution was drop-casted onto a Teflon dish, and allowed to sit in a Nitrogen glovebox for at least two nights to allow for evaporation of acetonitrile. Then, the Teflon dish was moved to a vacuum oven, where it was heated at 70 °C under vacuum for two more days. The films (average thickness 350–400 μm) were moved to an argon glovebox (MBRAUN, $H_2O < 0.1$ ppm, $O_2 < 0.1$ ppm), where they are stored until use. The same procedure was used for EMITFSI-based GPEs. The GPE film was cut into the desired disk diameter in the glovebox just before Li–O_2 cell fabrication.

4.2.3 Electrode fabrication

Several electrodes were used during this study. Vulcan carbon-based electrodes were prepared as follows: Vulcan carbon and other components, 4–5 mL of acetonitrile and 5 mm zirconia beads were added to a ball mill jar, and the contents mixed in a planetary ball mill for at least 4 hours at 500 rpm. The uniform black ink was transferred onto a PTFE-treated TGP-H-60 carbon paper substrate, and a Meyer rod (RDS 60) was used to create a film. Titanium carbide (TiC) electrodes were fabricated by dispersing 90 wt% TiC and 10 wt% PTFE in iso-propanol in a mortar and grinding with a pestle. The paste was then coated on nickel foam. Free-standing vertically aligned few-walled CNT carpets were fabricated as previously reported.[61] All electrodes were vacuum-dried at 75 °C before being transferred and stored in an Argon glovebox (MBRAUN, $H_2O < 0.1$ ppm, $O_2 < 0.1$ ppm).

4.2.4 Ionic conductivity measurements

Ionic conductivity measurements were made by sandwiching the GPE between two 15 mm stainless steel disks (Stainless steel disk | GPE | Stainless steel disk). The setup was heated at 60 °C for 10 hours before electrochemical impedance spectroscopy (EIS) measurement was performed. This exact setup was allowed to rest at room temperature for 5 hours before the 25 °C data point was collected. The thickness of the GPE film was determined after the EIS measurements were completed. This is because the GPE film flows during heating, leading to a

different thickness before and after heating. The thickness after heating is the true thickness contributing to ionic conductivity, and is used for the calculations. The thicknesses listed in Table C-1 are not the typical thickness of free-standing films which are 350–400 μm. EIS measurements were performed in the frequency range of 1 MHz to 0.1 Hz with a signal level of 10 mV. 15 mm was used as the film diameter. The ionic conductivity values are in Table C-1.

4.2.5 GPE Li–O_2 cell fabrication

Using a Li–O_2 cell setup developed in our laboratory,[22] lithium metal (15 mm diameter) was used as the anode, the free-standing GPE (16 mm diameter) as the electrolyte and separator, and the corresponding electrode (12.7 mm diameter for Vulcan carbon-based electrodes). The electrode was 80 wt% Vulcan carbon and 20 wt% PMMA. For cells using CNT (1 cm x 1 cm) as the electrode, a stainless steel mesh (12.7 mm diameter) was added as the current collector. The TiC electrodes (90 wt% TiC and 10 wt% PTFE) were square pieces (12.7 mm x 12.7 mm). The cells were prepared in an Argon glovebox (MBRAUN, $H_2O < 0.1$ ppm, $O_2 < 0.1$ ppm) and moved to another Argon glovebox (MBRAUN, $H_2O < 0.1$ ppm, $O_2 < 0.3$ %) – without air exposure—and filled with oxygen gas. A VMP3 potentiostat (BioLogic Inc.) was used for all electrochemical tests. The Li–O_2 cells were allowed to rest at 60 °C for 10 hours before discharge or charge tests were performed.

For the DEMS setup, a 15 mm Li metal anode, 18 mm GPE, and 15 mm electrode (for $Li^+/Pyr^+ = 0.6$) or 12.7 mm electrode (for $Li^+/Pyr^+ = 0$) was used. The electrode was 78wt% Vulcan carbon, 7 wt% $Pyr_{14}TFSI$, 5 wt% LiTFSI, and 10 wt% lithiated nafion on carbon paper.

4.2.6 Non-aqueous Li–O_2 cell fabrication

Preparation of anion exchange membrane: The anion exchange membranes were cut into 18 mm disks and soaked in a 1 M $LiClO_4$ solution for two nights to allow for anion exchange. Then, the AEM disks were rinsed for 5 minutes with copious amounts of milliQ water. The AEM disks were soaked again in fresh 1 M $LiClO_4$ solution for 1 night. After rinsing again with milliQ water, the disks were washed with acetone before vacuum-drying at 75 °C.

The same Li–O_2 cell setup was used. Lithium metal (15 mm diameter) was used as the anode, two Celgard C480 membranes were used as porous separators (18 mm diameter), and a pristine TGP-H-60 (no PTFE treatment) carbon paper electrode was used for these experiments. 0.1 M

$TBAClO_4$ in diglyme or 0.1 M $LiClO_4$ in diglyme or the mixture were used as stated in the main text. For cells containing the anion exchange membrane, the 18 mm AEM was sandwiched between two Celgard C480 separators. About 90 μL of electrolyte was used. Filling the cell with oxygen and testing was done as stated in the GPE Li–O_2 cell fabrication.

4.2.7 Li–O_2 fabrication with ionic liquid (no polymer present)

The same procedure for the 'non-aqueous Li–O_2 cell fabrication' was used. For the 0 M LiTFSI configuration, pure $Pyr_{14}TFSI$ was used as the electrolyte. An 80 wt% Vulcan carbon/20 wt% PMMA electrode on carbon paper was used. The Li–O_2 cell was allowed to rest at 60 °C for 10 hours before discharge.

4.2.8 Differential Scanning Calorimetry (DSC)

2–6 mg of PMMA, $Pyr_{14}TFSI$, and the electrolyte films were placed in hermetically sealed aluminum pans (TA Instruments). A 10 °C/min cooling and heating rate was used under a nitrogen flow rate of 50 mL/min. Two heating and cooling runs were performed on each sample to remove any thermal history. Only the second heating/cooling run is reported. A DISCOVERY DSC (TA Instruments) was used.

4.2.9 Scanning electron microscopy (SEM)

SEM was performed using a ZEISS Merlion (Carl Zeiss Microscopy GmbH, Germany). Sample preparation was done in an Argon glovebox ($O_2 < 0.1$ ppm, $H_2O < 0.1$ ppm). For samples that were washed, the samples (Li | GPE| CNT) were placed in a 20 mL and 2 mL of dimethoxyethane was added. The vial was shaken for less than five minutes until the CNT delaminated from the GPE and lithium metal. In the Argon glovebox, samples were placed in an aluminum foil bag and the bag was heat sealed. The sealed foil bag was removed from the glovebox and moved to the SEM room. The sample was removed from the foil bag and in less than 5 seconds was transferred into the SEM chamber where high vacuum was then pulled. All images were taken with an in-lens detector at 5 kV and 68 pA. An integrated Energy Dispersive Spectroscopy (EDAX, Ametek) was used to probe the composition of the products.

4.2.10 Differential Electrochemical Mass Spectrometry (DEMS)

The same DEMS setup as described in reference (22).

4.2.11 Ultraviolet-visible (UV-Vis) spectroscopy

After the CNT electrode was discharged using a GPE Li^+/BTM^+ molar ratio of 0, the Li |GPE| CNT piece was placed in a 20 mL vial. Then, 0.3 mL of dimethyl sulfoxide was added. After 0.2 mL of the solution was removed, 0.5 mL of pure DMSO was added to the vial. Finally, 0.3 mL was removed from the vial and added to a clean 3 mL vial where it was diluted with 1 mL DMSO. 0.01 mL of the solution in the 3 mL vial was then used for the UV-Vis measurement. For the control, a Li–O_2 cell was made with lithium metal, a GPE Li^+/BTM^+ molar ratio of 0.6 and a CNT. The cell was heated at 60 °C for over 10 hours, but was not discharged. The cell components were then stored in an Argon glove box for over two weeks. This is to ensure that the control has the same exposure with lithium metal as the discharged electrode. The cell components (Li |GPE| CNT) were then placed in a 20 mL vial. 0.3 mL DMSO was added. 0.01 mL of the solution was then used for UV-Vis measurement. These sample preparations were done in an Argon glove box. A Nano Drop ND-1000 Spectrophotometer was used in the UV-Vis module and a 1 mm path. Pure DMSO was used as the blank.

4.2.12 Electron paramagnetic resonance (EPR) spectroscopy

Fragments of the cell setup (either discharged or control) were added to a 3 mL vial. Then, 0.3 mL of pure DMSO was added and the vial was allowed to sit for over 4 hours. 0.2 mL of the solution was removed and placed in a 1 mL vial. Then, 0.1 mL of a BMPO/dimethylformamide solution was added. The contents of the vial were mixed for a few seconds before the content was transferred to a capillary tube for EPR measurements. Sample preparations were done in an Argon or Nitrogen glovebox. The discharged sample and control are as described in the UV-Vis spectroscopy section. Both sample and control solutions were made and characterized at the same time. EPR measurements were performed using a glass capillary tube inside a quartz tube. Spectrum was recorded on a Bruker EMS spectrometer, an ER 4199HS cavity, and a Gunn diode microwave source producing X-band radiation. Measurements were performed at room temperature with a 9.861 GHz radiation, 0.201 mW power, 100 kHz modulation frequency, and 20.48 ms time constant.

Spectral simulation was performed using the program QCMP 136 by Prof. Frank Neese from the Quantum Chemistry Program Exchange as used by Neese *et al.* in J. Am. Chem. Soc. 1996, 118, 8692-8699. Simulation parameters for the BMPO-superoxide adduct were obtained using a 1N,

1H model; $g_1=g_2=g_3=2.0055$ with ^{14}N (a_N = 57 MHz) and ^{1}H (a_H = 38 MHz), Gaussian line shape line broadening $W_1=W_2=W_3=2$ mT. Simulation parameters for the broad peak (originating from the control) were obtained with $g_1=g_2=g_3=2.002$ and a Gaussian line shape line broadening $W_1=W_2=W_3=6$ mT.

4.2.13 X-ray Photoelectron Spectroscopy (XPS) characterization

To avoid any exposure to air, samples were transferred from the glovebox to the XPS chamber using a sample transfer vessel (ULVAC-PHI, INC.) Spectra were collected with a PHI 5000 VersaProbe II (ULVAC-PHI, INC.) using a monochromatized Al K_α source, a pass energy of 23.5 eV and a charge neutralizer. All spectra were calibrated with the C1s photoemission peak of adventitious carbon at 285 eV. Photoemission lines were fitted using combined Gaussian-Lorentzian functions after subtraction of a Shirley-type background.

4.2.14 Density Functional Theory (DFT) calculations

All calculations were performed using the Gaussian 09 computational package. The ground state molecular structures were fully optimized in the solvent environment at the B3LYP/6-311++G(d, p) level of theory and verified by absence of any imaginary frequencies. The CPCM solvation model was used, and N, N-dimethylformamide was used as the solvent.

4.2.15 Fourier Transform Infrared (FTIR) characterization

FTIR characterization of discharged electrolyte films involve placing the film on a transparent IR card (International Crystal Laboratories, KBr aperture IR card). A JASCO 4100 FTIR spectrometer was used for data collection. Spectra were obtained in absorbance mode with 1 cm^{-1} resolution, using at least 100 accumulation scans.

4.2.16 Nuclear Magnetic Resonance (NMR) characterization

For discharged cells, films were removed from the Li–O_2 cell. The films were submerged in deuterated chloroform or deuterated dimethylsulfoxide. The supernatant was then placed in a NMR tube. A Bruker AVANCE and Bruker AVANCE III-400 MHz nuclear magnetic resonance (NMR) spectrometer was used for characterization.

4.3 Results and Discussion

Poly(methyl methacrylate) (PMMA) was selected as the polymer for the GPE because it was found to be stable in contact with lithium peroxide based on our finding at room temperature,[28] although a previous study reported formation of Li_2CO_3 in mixtures with KO_2. Jung *et al.*[72] incorporated $Pyr_{14}TFSI$ in a PVDF-HFP-based GPE in a Li–O_2 battery, but their films contain residual flammable N-methyl-2-pyrrolidone (NMP) solvent from the film fabrication process (see Appendix C). Furthermore, PVDF-HFP undergoes extensive elimination reactions upon exposure to peroxide.[28,72] Ionic liquids with or without LiTFSI salt are incorporated within the PMMA matrix (Figure 4-1a) to obtain ionically conductive free-standing films with no solvent impurities (Figure C-1). Although $Pyr_{14}TFSI$[115] and EMITFSI[116] are susceptible to reactions with superoxide, $Pyr_{14}TFSI$ and butyl-trimethylammonium (BTM)TFSI are among the more stable ionic liquids commercially available.[116]

The Li^+/IL^+ molar ratio in the GPE affects the thermal properties and ionic conductivity of the GPEs. As Figure 4-1b shows, the amorphous PMMA prevents ordering of the ionic liquid at lower temperatures. The glass transition temperature of pure PMMA is approximately 105 °C, whereas the blends examined here show a clear suppression of this glass transition, with a small inflection appearing at approximately 20 to 30 °C instead, closer to room temperature. As lithium salt is added to the GPE, two inflections appear, one at the lower temperature and one closer to pure PMMA, implying separation of the mixture into PMMA-rich and ionic liquid/salt rich blend phases. Furthermore, the GPE content affects the net ionic conductivity where films with a Li^+/Pyr^+ molar ratio of 1.5 have much lower ionic conductivities (~10^{-6} S/cm) than films with Li^+/Pyr^+ molar ratios < 1 (~10^{-4} S/cm) at 60 °C (Figure 4-1c and Table C-1). As the Li^+/Pyr^+ molar ratio is reduced, more free volume is generated that can allow for ionic transport, leading to GPE conductivities that approach the conductivity of the pure ionic liquid. Although the PMMA content is similar across the films, the decrease in ionic conductivity and the brittle nature of the $Li^+/Pyr^+ = 1.5$ films are due to interactions between the PMMA carbonyl group and the lithium ions that limit ion transport.

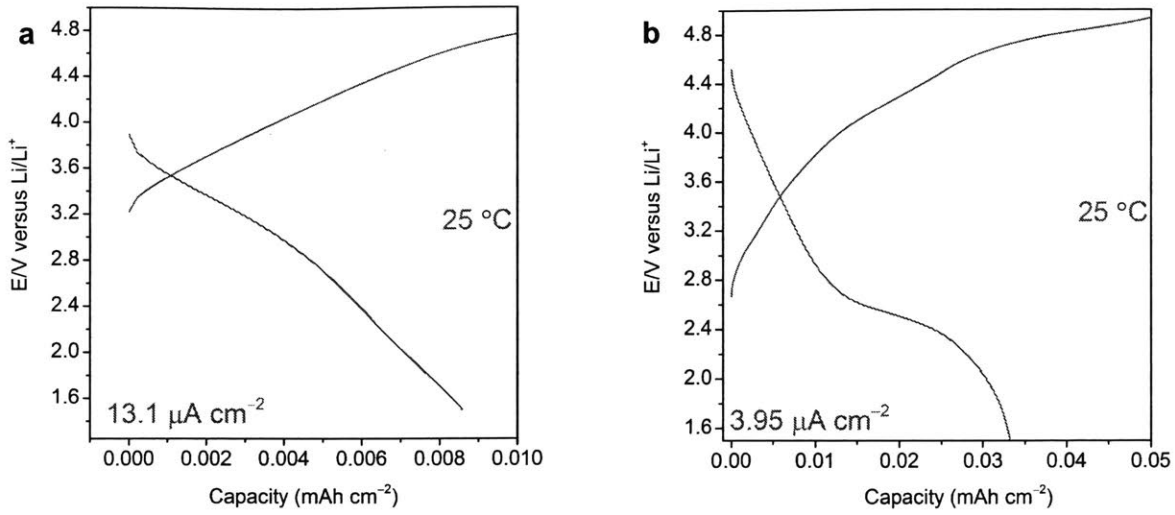

Figure 4-2 | Effect of temperature on the cell behavior. Li–O_2 cell discharged and charged at 25 °C first at a current rate of 13.1 μA cm^{-2} (a) and then at 3.95 μA cm^{-2} (b) with a GPE Li^+/Pyr^+ molar ratio of 0.6. The capacity obtained is an order of magnitude lower than that obtained at 60 °C with the same GPE electrolyte content (Figure 4-1). A cell with a Li^+/Pyr^+ molar ratio of 0.6 was cycled at two different current rates at room temperature. Firstly, the cell was held at 60 °C for 24 hours to generate an interconnected electrolyte/electrode interface. Then, the cell was allowed to rest at room temperature for 4 hours before discharge and charge begun. Electrode: 70 wt% Vulcan carbon, 15 wt% lithiated nafion, 7.5 wt% LiTFSI, and 7.5 wt% Pyr_{14}TFSI on carbon paper.

The GPEs were incorporated in Li–O_2 batteries as a dual separator and electrolyte with a Vulcan carbon electrode and Figure 4-1d shows that GPEs can support Li–O_2 discharge. All Li–O_2 cells discussed in this work – unless otherwise stated – were tested at 60 °C. Discharge at room temperature leads to poor discharge capacities (Figure 4-2). At a Li^+/Pyr^+ molar ratio > 1, when lithium ions are in excess (compared to Pyr^+) in the GPE, a single discharge plateau at 2.5 V is observed. All voltages mentioned in this work are versus Li/Li^+. Li–O_2 batteries with conventional non-aqueous liquid electrolytes show similar discharge voltages.[14] Interestingly, when 0 < Li^+/Pyr^+ molar ratio < 1, two discharge plateaus appear at 2.5 V and 1.9 V. Furthermore, reduction of the Li^+ content when going from Li^+/Pyr^+ molar ratios of 0.6 down to 0.25 decreases the capacity obtained from the 2.5 V plateau. When the Li^+/Pyr^+ molar ratio = 0

(no lithium salt in GPE), the 2.5 V plateau disappears and only the 1.9 V plateau is observed. Therefore, the 2.5 V plateau is a function of lithium-ion content in the electrolyte; as the Li^+ content increases from 0 to 0.25 to 0.6, the width (capacity) of the 2.5 V plateau increases; however, once the Li^+/Pyr^+ ratio is greater than one, the 1.9 V plateau is absent, and the obtained capacities are an order of magnitude lower. The 1.9 V plateau appears kinetically limited and is not observed at high current rates (Figure 4-3).

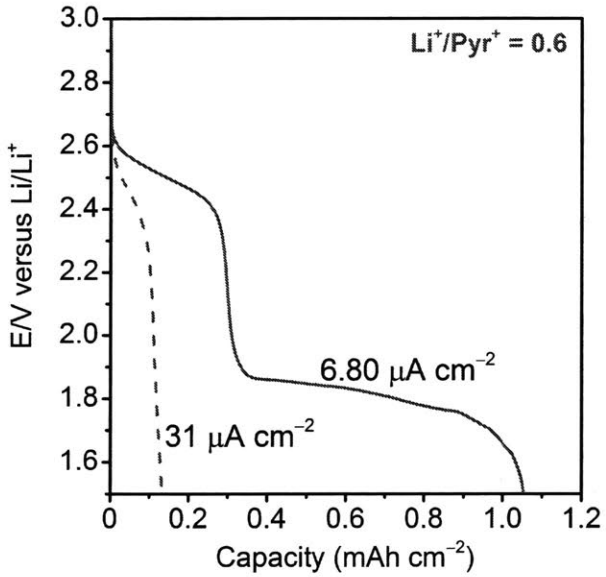

Figure 4-3 | Effect of current rate on discharge. Discharge curves at different current rates for a Li–O_2 cell using a GPE molar ratio of 0.6. Electrode: 70 wt% Vulcan carbon, 15 wt% lithiated nafion, 7.5 wt% LiTFSI, and 7.5 wt% Pyr_{14}TFSI on carbon paper.

The same qualitative discharge behavior as a function of Li^+/IL^+ molar ratio observed with Pyr-based GPEs is also seen with EMI-based and BTM-based GPEs (Figure 4-1e). However, the second plateau voltage is dependent on the ionic liquid cation (1.9 V for Pyr^+, ~1.85 V for BTM^+, and ~2.1 V for EMI^+). The same discharge behavior as in Figure 4-1d is also observed in Li–O_2 cells even with Vulcan carbon electrodes formulated with lithium salt and ionic liquid (Figure 4-4). Although this discharge mechanism seems to be irrespective of the type of ionic liquid cation present in the GPE, it is not observed in a pure ionic liquid (without polymer) Li–O_2 cell (Figure 4-1f).[30] When pure Pyr_{14}TFSI (no salt or polymer) or 1 M LiTFSI in Pyr_{14}TFSI are

used as the electrolyte with a Vulcan carbon electrode using the same current rates and conditions as the GPEs, the same discharge mechanism is observed irrespective of lithium salt content. The transport of Li^+ from the oxidized anode is responsible for the discharge plateau in the 0 M LiTFSI in $Pyr_{14}TFSI$ system. Therefore, the incorporation of the ionic liquid into a polymeric matrix can change the voltage where the oxygen reduction reaction occurs (discussed later).

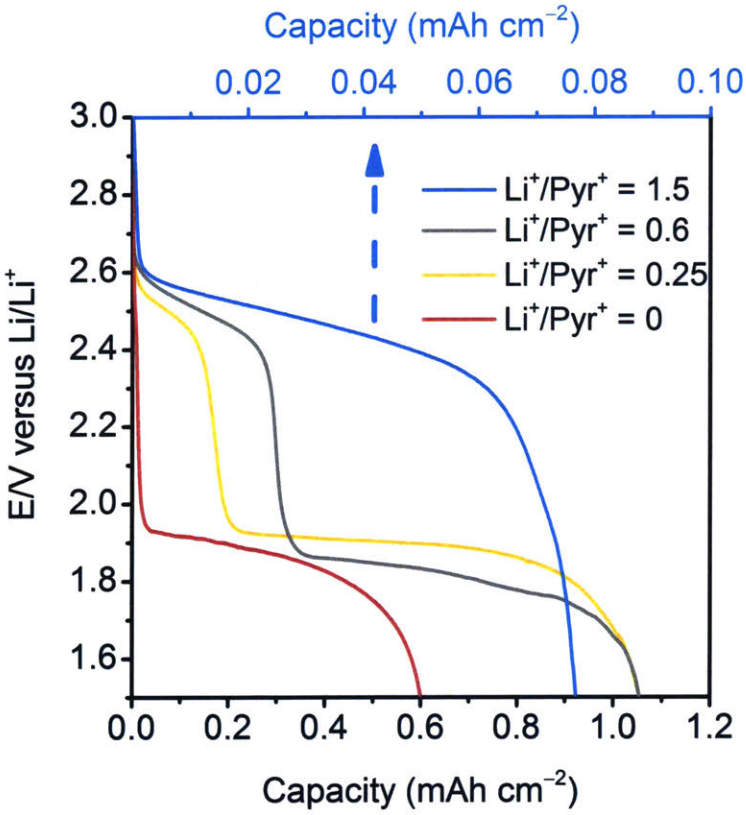

Figure 4-4 | Discharge curves with varying GPE Li^+/Pyr^+ molar ratio. Discharge curves at 10 mA g_{vc}^{-1} obtained using a Vulcan carbon electrode containing LiTFSI and $Pyr_{14}TFSI$ (Li^+/Pyr^+ molar ratio = 1.4). This shows that the Li^+/Pyr^+ content originally in the GPE governs the observed chemistry. Electrode: 70 wt% Vulcan carbon, 15 wt% lithiated nafion, 7.5 wt% LiTFSI, and 7.5 wt% $Pyr_{14}TFSI$ on carbon paper. The behavior observed with an electrode containing lithium salt and ionic liquid (figure above) is the same as that shown in Figure 4-1 with a Vulcan carbon and PMMA electrode. Therefore, the Li^+/Pyr^+ molar ratio in the electrolyte dictates the mechanism observed because the electrolyte has to infiltrate the electrode for discharge to occur.

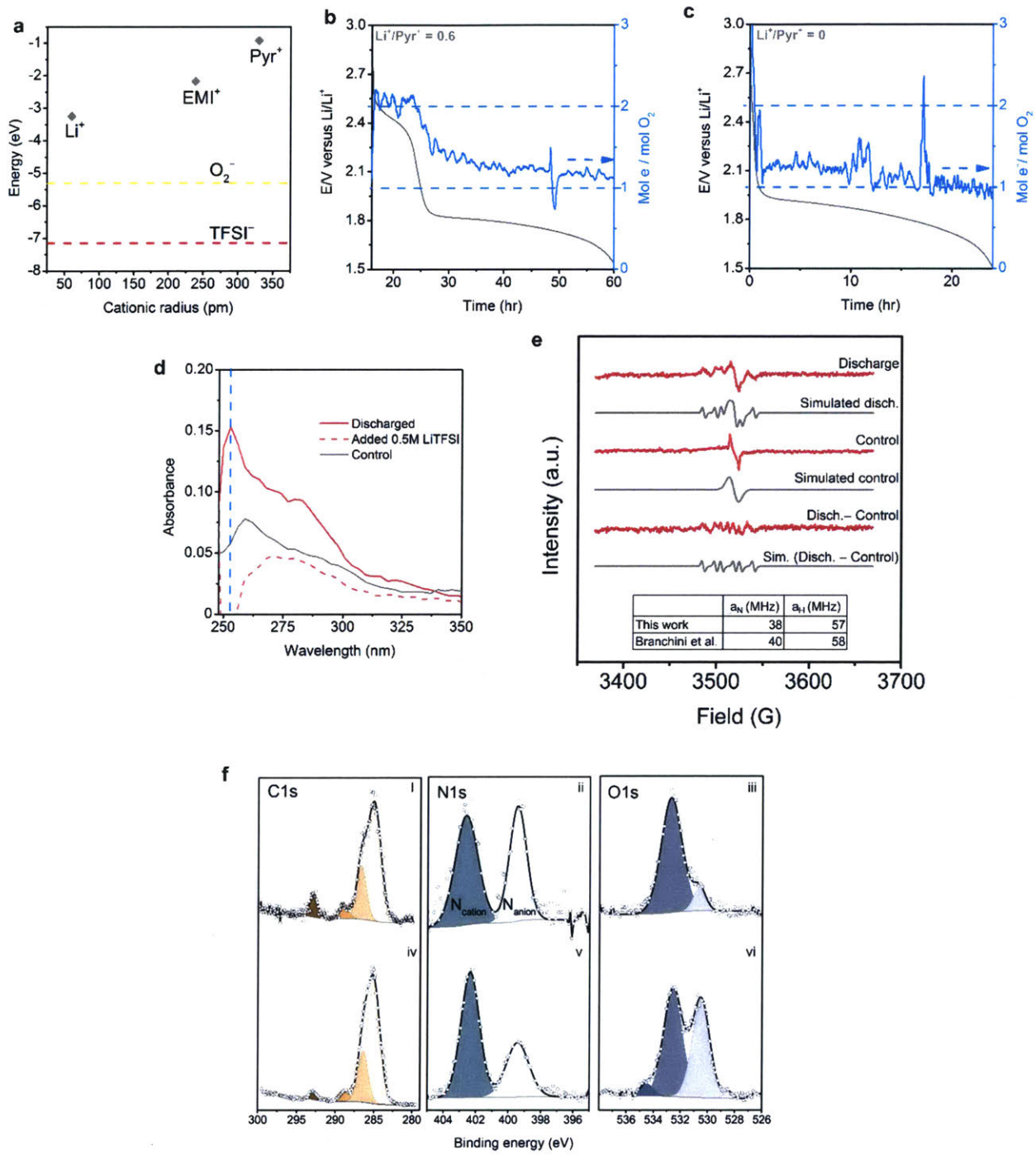

Figure 4-5 | Electrochemical and spectroscopic characterization during and after the first discharge. a, Highest Occupied Molecular Orbital (HOMO) of superoxide and TFSI, and Lowest Unoccupied Molecular Orbital (LUMO) of respective cations as a function of cationic radius; Differential Electrochemical Mass Spectrometry (DEMS) of Vulcan carbon/Pyr14TFSI/LiTFSI/Nafion electrode (7.8:0.7:0.5:1 mass ratio) with GPE Li^+/Pyr^+ molar

ratio of 0.6 (b) and 0 (c) at 11.3 and 15.8 μA cm^{-2} respectively (based on geometric surface area); d, Ultraviolet-visible (UV-Vis) spectra of the supernatant of a discharged CNT electrode (first discharged at 10 mA gc^{-1} and then at 5 mA gc^{-1}) with a GPE Li^+/BTM^+ molar ratio of 0 that was later soaked in dimethylsulfoxide (DMSO), 0.5 M LiTFSI added to the discharged supernatant solution, and a control consisting of a CNT (not discharged) with a GPE Li^+/BTM^+ molar ratio of 0.6; e, Electron paramagnetic resonance (EPR) spectra at room temperature of the discharged CNT electrode (5 mA gc^{-1})/DMSO supernatant as in (d) with added BMPO, control as in (d) with BMPO addition. Discharge–control involves subtracting the control spectrum from the discharged spectrum. Simulated parameters are in the Methods section; figure 4-5e inset = Hyperfine coupling constants for the BMPO-superoxide adduct simulated from the discharged spectra compared to the literature (ref. [117]) ; (f) XPS data chronicling the change in the C1s, N1s, and O1s in the pristine (i–iii) and after 1 discharge for a CNT electrode discharged with a Li+/Pyr+ molar ratio of 0 (iv–vi). BMPO = 5-tert-butoxycarbonyl 5-methyl-1-pyrroline N-oxide.

In the GPEs studied here, the ionic liquid provides a supplementary cationic source to Li^+ cations and thus can alter the discharge mechanism. Allen *et al.*[118] postulate through cyclic voltammetry (CV) that oxygen reduction in pure ionic liquid (no Li^+) occurs at 1.96 V and 2.1 V for $Pyr_{14}TFSI$ and EMITFSI-based cells respectively, and is associated with ionic liquid-superoxide complexation. These reduction potentials are similar to those obtained in the GPE cells when Li^+/Pyr^+ or Li^+/EMI^+ molar ratio < 1. Therefore, we hypothesize that the 1.9 V plateau for Pyr^+ and the 2.1–2.2 V for EMI^+ in GPE-based Li–O_2 cells is due to ionic liquid-superoxide complexation. When lithium ions originally present in the GPE become depleted at the cathode, a second plateau appears when the ionic liquid cation itself becomes the active cationic species. This lithium ion exhaustion occurs in the GPEs because the lithium transference number is much lower than the pristine ionic liquid.[119,120] This suggests that, coupled with the voltage change, the oxygen reduction chemistry changes when Li^+ is substituted with IL^+ in an actual Li–O_2 cell. In the absence of Li^+, the ionic liquid cation (either Pyr^+, EMI^+ or BTM^+) can act as a Li^+ substitute and is capable of complexing the superoxide oxygen reduction products,[118] thus explaining why discharge can occur when there is no lithium salt present in the GPE. Other metal-air chemistries such as Na–air and K–air have shown rechargeable chemistries based on stable superoxide

formation and oxidation, providing lower charging overpotentials, and faster one-electron oxygen reduction kinetics.[32,33] Furthermore, the ability of the GPE to sequester the superoxide intermediate may prove interesting in limiting the solubility of polysulfides and prevent their shuttle in lithium-sulfur batteries. Ionic liquid-superoxide complexation is not observed in the pure ionic liquid Li–O_2 cells because lithium ions can easily migrate from the anode; but is observed in the GPE-based Li–O_2 cells because the PMMA acts as a diffusion barrier to actively limit the transport of Li^+ from the oxidized anode at least on the first discharge (allowing the ionic liquid to become the active cationic specie).

In the GPE where lithium and ionic liquid cations are present, the lithium reaction with $O_2^{\bullet-}$ (high-lying HOMO) to yield Li_2O_2 is energetically favored (over other ionic liquid cations) because of lithium's polarizing nature, high charge density, and low-lying LUMO (Figure 4-5a). Density Functional Theory (DFT) was used to calculate the LUMO of the ionic liquid cations. Coupled with the reported lithium LUMO[109], the trend where Li^+ (−3.25 eV)[109] < EMI^+ (−2.17 eV) < Pyr^+ (−0.93 eV) corroborates the observed oxygen complexation voltage where Li–O_2 (2.5 V) > EMI–O_2 (~2.1 V) > Pyr–O_2 (1.9 V).

To explain why the oxygen reduction chemistry changes when lithium ions become unavailable, we apply Pearson's HSAB reasoning provided by Laoire *et al.*,[64,108] where the small lithium cation (radius = 60 pm)[121] with high charge density is a hard acid and the charge stabilized bulky cations such as EMI^+ (239 pm),[122] Pyr^+ (330 pm),[123] TBA^+ (494 pm)[121] are soft acids. Moreover, while peroxide anion is a hard base, superoxide anion is a soft base.[64,108] Hard acids prefer to bind with hard bases, and soft acids prefer to bind with soft bases.[114] If lithium cations are present when oxygen is reduced to superoxide, the oxygen reduction process does not stop at superoxide, but continues to yield peroxide (Li_2O_2) (Schematic 4-1a). This is an overall 2 e^- process (hard acid-hard base). If lithium cations are absent when oxygen is reduced to superoxide, the reduction process does not proceed to peroxide; instead the superoxide complexes with the ionic liquid cation. This is an overall 1 e^- process (soft acid-soft base).

To confirm the hypothesis of a 2 e^- versus 1 e^- process, Differential Electrochemical Mass Spectrometry (DEMS) was performed with two electrolyte configurations (Li^+/Pyr^+ = 0.6 and 0). As Figure 4-5b shows, the first plateau at 2.5 V corresponds to a 2 mol e^-/mol O_2 process

(peroxide formation). As lithium ions become unavailable at the cathode, the second plateau appears and corresponds to a ~ 1.2 mol e^-/mol O_2 process (superoxide formation) at the end of discharge. This imperfect ratio (1.2 vs. 1 expected) could be due to concurrent superoxide and peroxide formation, although superoxide formation is dominant. For an electrolyte with no lithium salt, a 1 mol e^-/mol O_2 process is solely observed (Figure 4-5c). To our knowledge, this is the first time that a superoxide-dominated discharge mechanism is demonstrated in a gel polymer Li–O_2 battery. Schematic 4-1b shows a summary of the proposed discharge mechanism for a $Li^+/Pyr^+ = 0$ GPE Li–O_2 cell.

a)

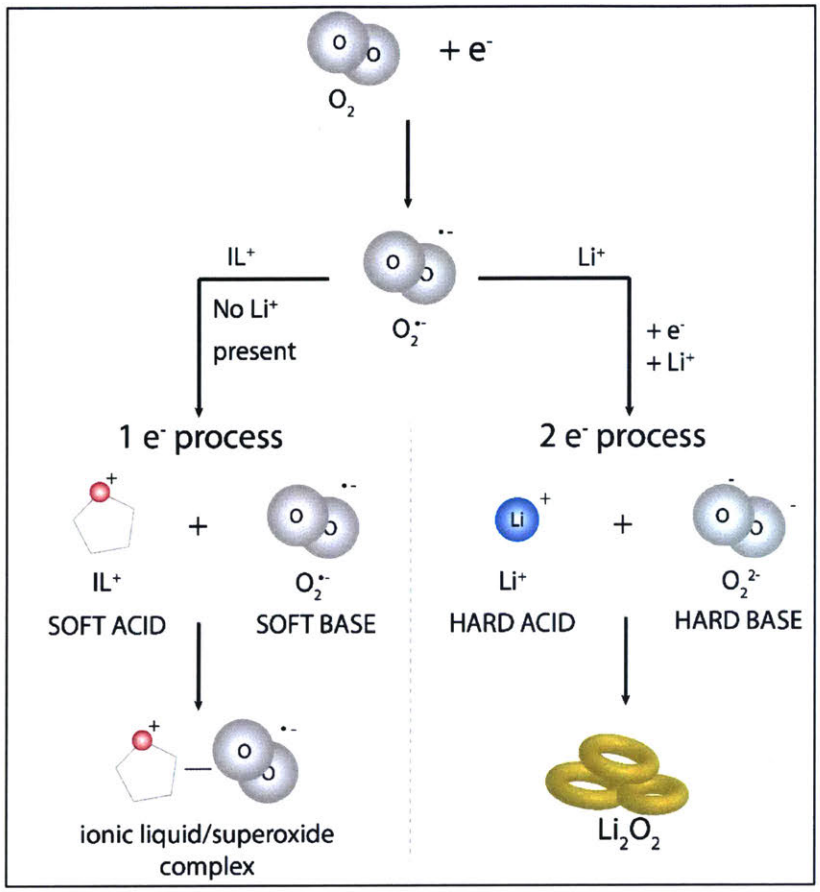
+ e⁻
O2
IL+
No Li+
present
Li+
O2•-
+ e⁻
+ Li+
1 e⁻ process
2 e⁻ process
IL+
SOFT ACID
O2•-
SOFT BASE
Li+
HARD ACID
O2 2-
HARD BASE
ionic liquid/superoxide
complex
Li2O2

b)

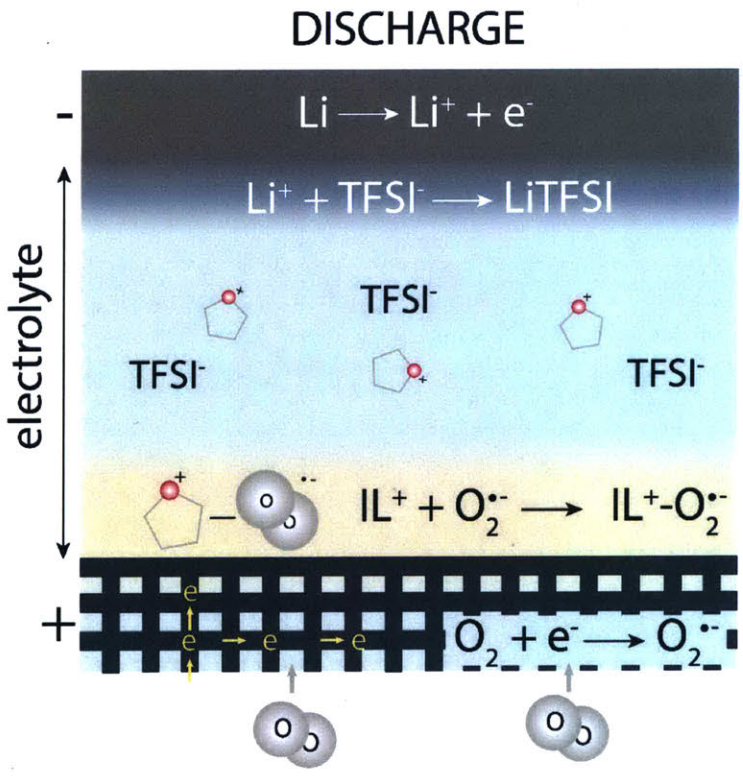
DISCHARGE
-
+
electrolyte
Li ⟶ Li+ + e⁻
Li+ + TFSI⁻ ⟶ LiTFSI
TFSI⁻
TFSI⁻
TFSI⁻
IL+ + O2•- ⟶ IL+-O2•-
e⁻
e⁻ → e⁻ → e⁻
O2 + e⁻ ⟶ O2•-

Schematic 4-1 | Proposed discharge mechanism for varying GPE Li^+/Pyr^+ molar ratio. a, Application of HSAB theory and the overall oxygen reduction process in the presence of Li^+ (2 e− process) and the absence of Li^+ (1 e− process in presence of IL+); b, overall superoxide discharge mechanism when GPE Li^+/Pyr^+ molar ratio = 0 showing that charge neutrality is maintained. IL+= ionic liquid cation (EMI^+, Pyr^+, BTM^+)

Other spectroscopic tools were used to further confirm the presence of superoxide in the discharge product. Carbon nanotubes (CNTs) were used as the electrode to provide higher surface area for the discharge reaction. CNT electrodes display similar discharge behavior to Vulcan carbon electrodes (Figure 4-6). After a CNT electrode with a $Li^+/BTM^+ = 0$ GPE was discharged, the GPE/electrode was removed from the Li–O_2 cell and soaked in dry dimethyl sulfoxide (DMSO). DMSO is known to solubilize superoxide.[111] The supernatant was removed from the soaked solution and then analyzed through Ultraviolet-visible (UV-Vis) spectroscopy. The UV-Vis data in Figure 4-5d show maximum absorbance at 253 nm typically associated with the $1\pi_u \rightarrow 1\pi_g$ transition of superoxide[115,124]; supporting the 1 e^- superoxide reduction process. Furthermore, when excess 0.5 M lithium salt is intentionally added to the UV-Vis solution, the superoxide peak diminishes because of quick disproportionation to lithium peroxide.[111] Electron paramagnetic resonance (EPR) is also typically used to unambiguously detect paramagnetic species like superoxide.[117,125] The addition of a 5-tert-butoxycarbonyl 5-methyl-1-pyrroline N-oxide (BMPO) spin trap to the supernatant from a discharged CNT electrode soaked in DMSO yields EPR signal with the "doublet of triplet" feature typically observed for a BMPO-superoxide radical adduct (Figure 4-5e).[117] These hyperfine coupling features are not observed in the control solution (CNT not discharged). Simulating the observed spectrum yields hyperfine interactions from ^{14}N and ^{1}H of $a_N = 38$ MHz and $a_H = 57$ MHz (Figure 4-5e) that are similar to previously reported BMPO-superoxide coupling constants of $a_N = 40$ MHz and $a_H = 58$ MHz,[117] further confirming the presence of superoxide in the discharged electrode.

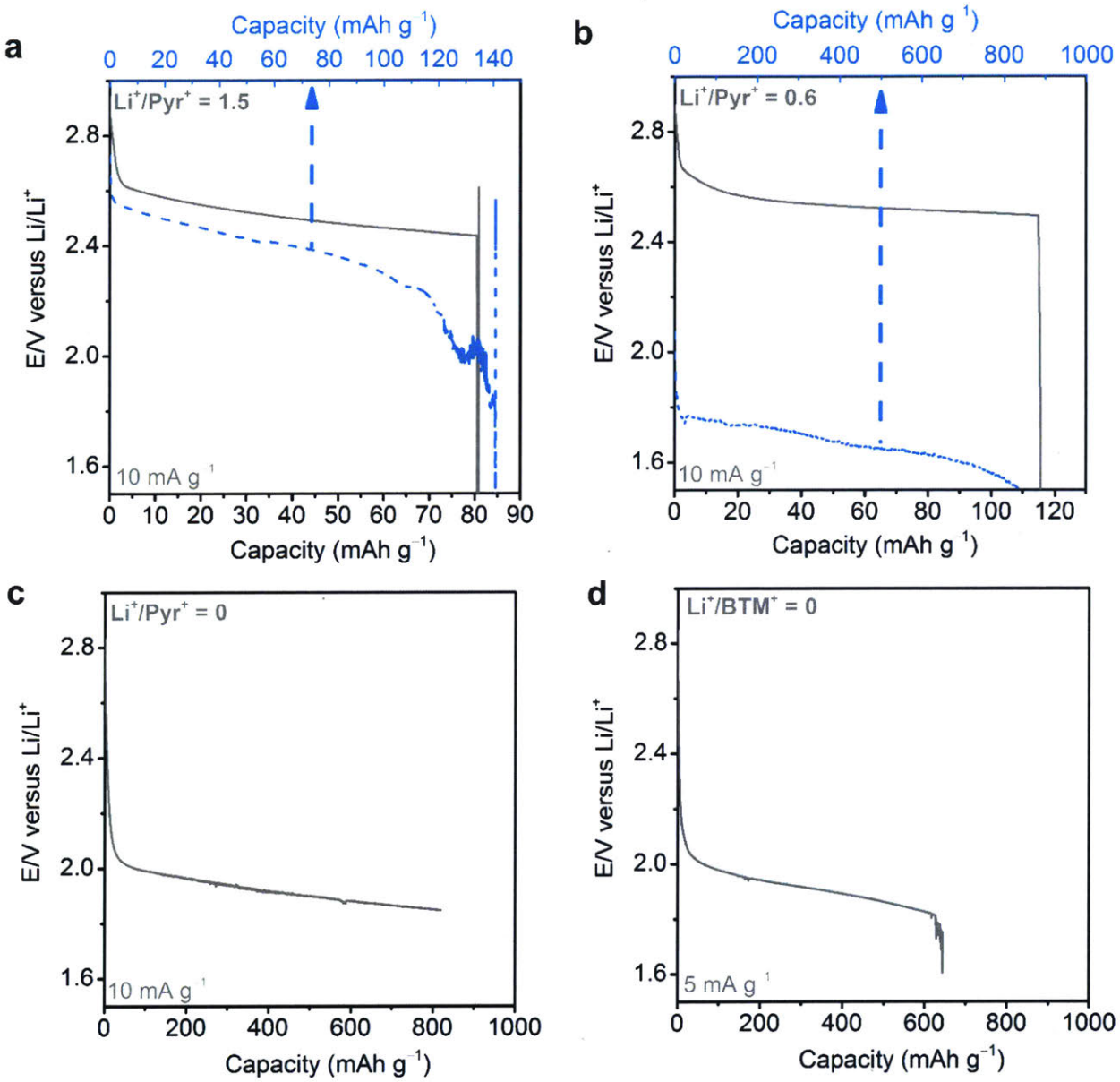

Figure 4-6 | Discharge profiles using GPEs and carbon nanotube (CNT) electrodes. Discharge at 10 mA g_c^{-1} using a GPE Li^+/Pyr^+ molar ratio of 1.5 (a), 0.6 (b), and 0 (c); d, Discharge at 5 mA g_c^{-1} using a GPE Li^+/BTM^+ molar ratio of 0. For figures (a) – (b), the dashed blue spectra was obtained by restarting the cell after the sudden drop in voltage. We attribute the sudden drop in voltage to a loss of lithium ions present in the cathode. Subsequent discharge continues until a gradual voltage decrease. (c) cell was manually stopped to reduce the number of discharge products and allow for better visualization with SEM. These discharge profiles in (c) and (d) correspond to the SEM images shown for the discharged electrodes in Figure 4-7.

Figure 4-5f shows XPS spectra that further supports the formation of a Pyr^+–$O_2^{\bullet-}$ complex. As expected, no changes are visible in the C1s spectra from the pristine (2f i) to the discharged electrode (Figure 4-5f iv). However, the Nitrogen 1s peak associated with the TFSI anion[126] (binding energy = 399 eV, Figure 4-5f v) reduces compared to the Pyr^+ cationic Nitrogen 1s peak[126] (B.E. = 403 eV, Figure 4-5f v), implying that the anion coordinated to the Pyr^+ cation has been replaced. Unsurprisingly, the O1s spectra shows the rise of peaks at 530 eV and 534 eV. Several authors have attributed the peak at ~ 534 eV to superoxide.[127,128] Assignment of the O1s peak at ~ 530 eV has been difficult and it has been attributed to superoxide[129] by some and hydroxide[130] by others. The XPS data shows that the Pyr^+–$O_2^{\bullet-}$complex has broken the original Pyr^+–$TFSI^-$ coordination. Superoxide reaction with Pyr^+ can occur as observed by Schwenke *et al.*,[115] and is observed in XPS data obtained on another location of the same CNT electrode (Figure C-2).

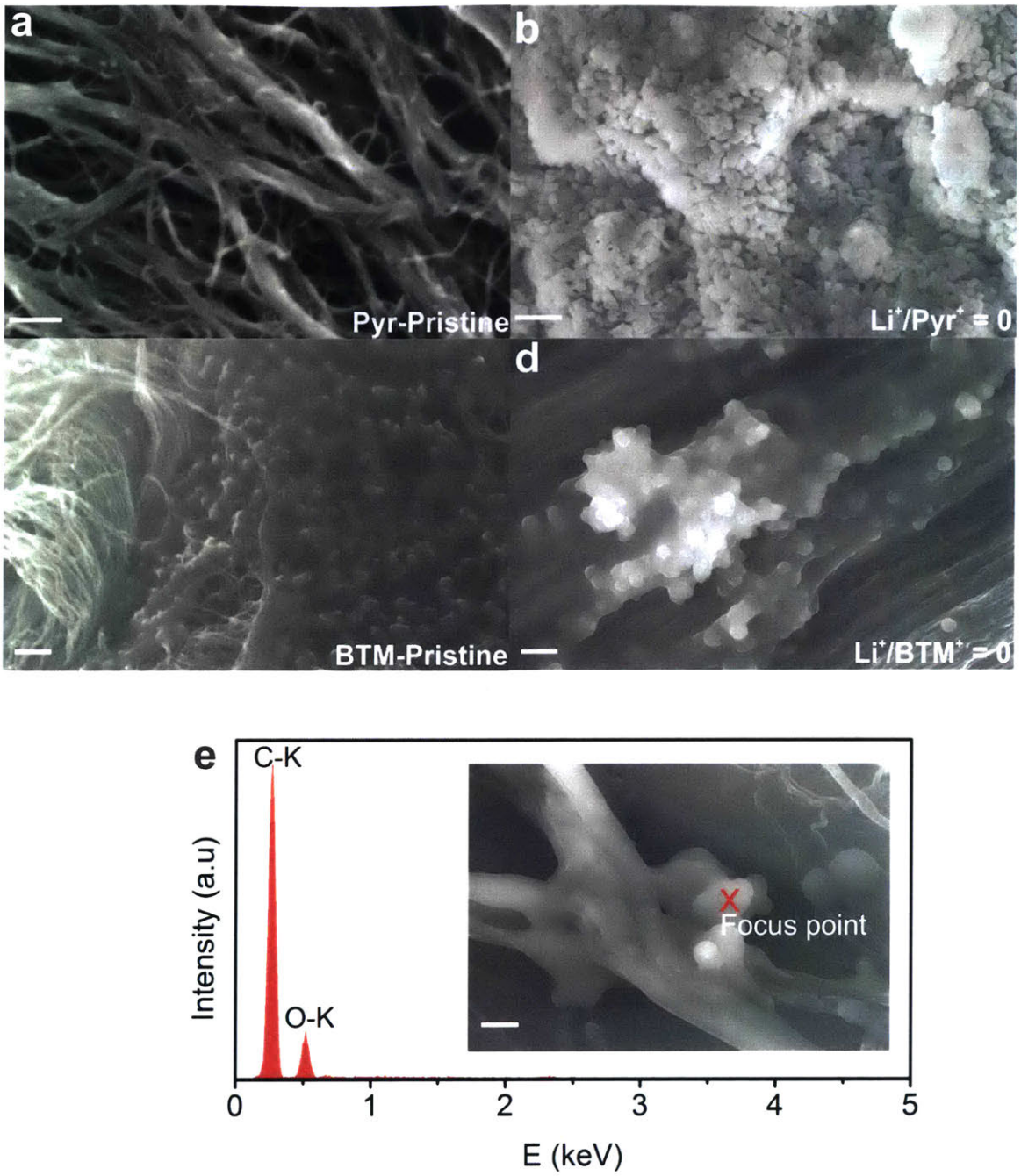

Figure 4-7 | Morphology of discharged Li–O_2 cells using different GPE formulations. Scanning Electron Microscopy (SEM) images of a pristine CNT electrode sandwiched with a GPE Li^+/Pyr^+ (a) or GPE Li^+/BTM^+ (c) molar ratio of 0.6; discharged CNT electrodes with a GPE Li^+/Pyr^+ (b) or GPE Li^+/BTM^+ (d) molar ratio of 0; e, Energy Dispersive Spectrum (EDS) of one of the particles (shown in inset) using the same electrode in (d). The discharged electrode in (d) and (e) was washed with dimethoxyethane (DME) before the SEM images were taken.

The stated ratios are the molar ratio of Li^+/Pyr^+ or Li^+/BTM^+ in the GPE. CNT electrode in (b) was discharged at 10 mA gc^{-1}, (d) and (e) were discharged first at 10 mA gc^{-1} and then at 5 mA gc^{-1}. (a, c: scale bar = 200 nm; b, d: scale bar = 500 nm; Inset in (e) scale bar = 1 μm)

Scanning electron microscopy (SEM) was used to study the discharge product morphology with CNT electrodes in a GPE Li–O_2 cell. The pristine CNT electrodes mixed with a GPE show a coating on the CNT walls (Figures 4-7a and 4-7c). However, when a GPE Li^+/Pyr^+ molar ratio of 0 is used to support discharge, products with cuboid morphology are formed on the CNT walls (Figure 4-7b). These cuboids (sensitive to SEM beam damage in Figure 4-8) are a result of the discharge plateau below 2 V, and are reminiscent of the cubic morphology of Na–O_2 discharge products.[32] Similar discharge products are observed when a GPE Li^+/BTM^+ molar ratio of 0 is used and the observed particles grow from the CNT surface (Figure 4-7d). These particles in the Pyr and BTM–based cells are not present in the pristine GPE/CNT set-up (Figures 4-7a and 4-7c), and lack the toroidal/flake-like features associated with lithium-based discharge products such as Li_2O_2, LiOH or Li_2CO_3.[24,59,131] Knowing that DEMS, UV-Vis, EPR, and XPS confirms superoxide formation, and the voltage at which this superoxide complexation occurs has been verified by CV in the pure ionic liquid,[118] the cuboids observed after discharge in Figure 4-7b are $Pyr^+–O_2^{\bullet-}$ complexes, and the particles observed in Figure 4-7d-e are $BTM^+–O_2^{\bullet-}$ complexes. The Energy Dispersive Spectrum (EDS) in Figure 4-7e showing C and O as the primary atomic components of the particles further supports ionic liquid-superoxide formation. The nitrogen peak is typically adjacent to the O and difficult to separate. Additional tools to spatially determine the chemical identity of the solid particles are certainly needed. The observation of these solid complexes is reminiscent of $TBA^+–O_2^{\bullet-}$ complexes that have been previously synthesized.[125] The particles are not the ionic liquid or lithium-based salts (no typical F and S anion peaks at 0.67 and 2.31 keV respectively in Figure 4-7e), and are not PMMA because PMMA is amorphous (Figure 4-1b) and should not form highly ordered particles/cuboids as observed in the SEM images. These complexes are observed using GPE-based Li–O_2 cells partly because limited solubility of the complex in the solid-like GPE architecture may lead to supersaturation.

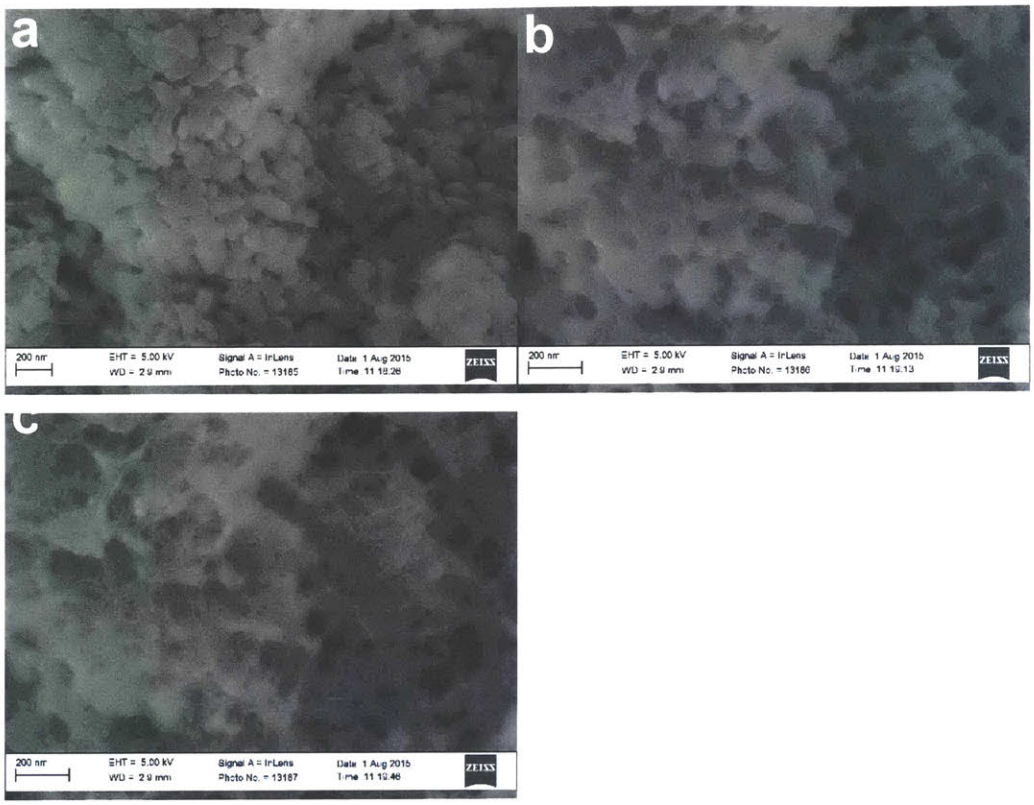

Figure 4-8 | Sensitivity of the Pyr^+–superoxide complexes to beam damage from the SEM beam. The same electrode area is imaged, and with further exposure to the electron beam, the CNT underneath the Pyr^+–$O_2^{\bullet-}$ particles is revealed. The same beam intensity is used, and the time stamp in the images reveals the exposure time length. (a) was the first SEM image taken; (b) SEM image was taken 87 seconds later; (c) SEM image was taken 1 minute and 20 seconds after image (a).

When a GPE Li^+/Pyr^+ molar ratio of 1.5 is used, no product is observed (Figure 4-9) and the CNT walls are similar to the pristine (not discharged) CNT electrode (Figure 4-7a). This lack of discharge products is unsurprising because lower discharge capacities are obtained with a GPE molar ratio of 1.5 (Figure 4-6). The lower capacity is attributed to poor wetting and utilization of the cathode because of the brittle nature of the $Li^+/Pyr^+ = 1.5$ films, and the limited ionic conductivity. Reduction of the PMMA content in the $Li^+/Pyr^+ = 1.5$ GPEs should allow for more flexible films and better electrode utilization.

Figure 4-9 | Morphology of a discharged electrode. CNT electrode after discharge at 10 mA g_c^{-1} using a Li^+/Pyr^+ molar ratio of 1.5. Typical discharge profile is in Figure 4-6.

$Li–O_2$ cells using the PMMA-based GPEs were cycled to study their rechargeability. Figure 4-10 shows a $Li–O_2$ battery including a Vulcan carbon electrode cycled with Li^+/Pyr^+ ratios < 1 and a 1.5 V cutoff, where the cell with a GPE Li^+/Pyr^+ ratio of 0.6 shows poor charging, and oxidation of products formed in the 1.9 V plateau does not occur. Increasing the ionic liquid content, and depressing the Li^+/Pyr^+ ratio to 0.25 allows for a better coulombic efficiency (84 % compared to 32 %) by facilitating transport of the formed superoxide complexes to the electrode when charging begins.

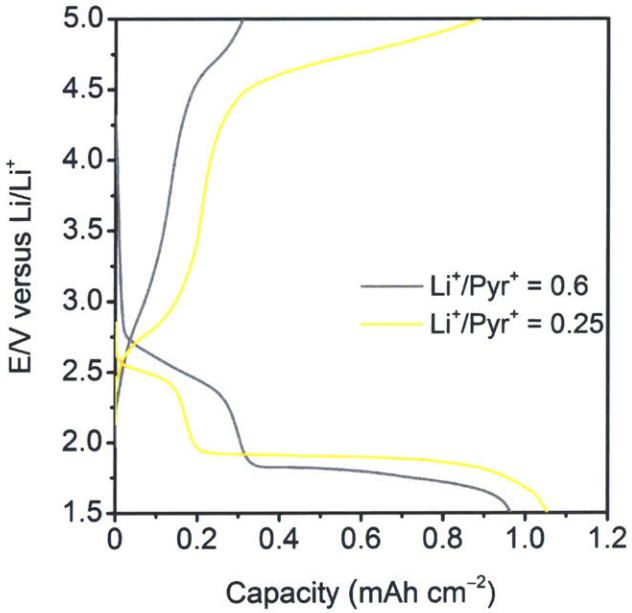

Figure 4-10 | Effect of GPE molar ratio on cycling. First cycles of Li–O_2 cells with GPE Li^+/Pyr^+ molar ratios of 0.25 and 0.6. Current rate of 10 mA g_{vc}^{-1} or 9.3 and 12.5 μA cm^{-2} for GPE Li^+/Pyr^+ ratio of 0.25 and 0.6 respectively. Electrode: 70 wt% Vulcan carbon, 15 wt% lithiated nafion, 7.5 wt% LiTFSI, and 7.5 wt% Pyr_{14}TFSI on carbon paper.

To directly compare the effect of a 2 e^- process versus a 1 e^- process, a 2 V cutoff was used for the Li^+/Pyr^+ = 0.6 Li–O_2 cells, and a 1.5 V cutoff was used for the Li^+/Pyr^+ = 0 Li–O_2 cells. Figure 4-11a shows the first and fifth cycles of Li–O_2 cells with a GPE molar ratio of 0.6 and 0 with Vulcan carbon electrodes, and for Li^+/Pyr^+ = 0.6 cells, charging is reversible and mostly accomplished below 4 V. For a cell with no salt present (Li^+/Pyr^+ = 0), the first discharge shows a plateau just below 2 V and the charging voltages are much lower compared to the Li^+/Pyr^+ = 0.6 cells even at the first and fifth cycles. The second discharge plateau increases, possibly due to lithium-ion encroachment of the cathode from the oxidized anode (Figure C-3). Although this Li^+/Pyr^+ =0 GPE can support cycling, coulombic efficiency at 4.5 V is 39 % (first cycle); the low efficiency could be due to poor charge transfer kinetics and limited accessibility of the ionic liquid-superoxide complexes to the electrode. A Li^+/Pyr^+ = 1.5 GPE content was also used to show cycling for at least five cycles, and Electrochemical Impedance Spectroscopy was used to show reversible formation and oxidation of resistive discharge products for this 2 mol e^-/O_2 process (Figure C-4). Upon extensive cycling, regardless of the initial Li^+/Pyr^+ molar ratio, the cycling profiles look similar because infiltration of lithium ions from oxidized anode changes the molar balance in the GPE. The same cycling behavior observed with Li^+/Pyr^+ based cells was also observed with Li^+/BTM^+ based Li–O_2 cells (Figure C-3).

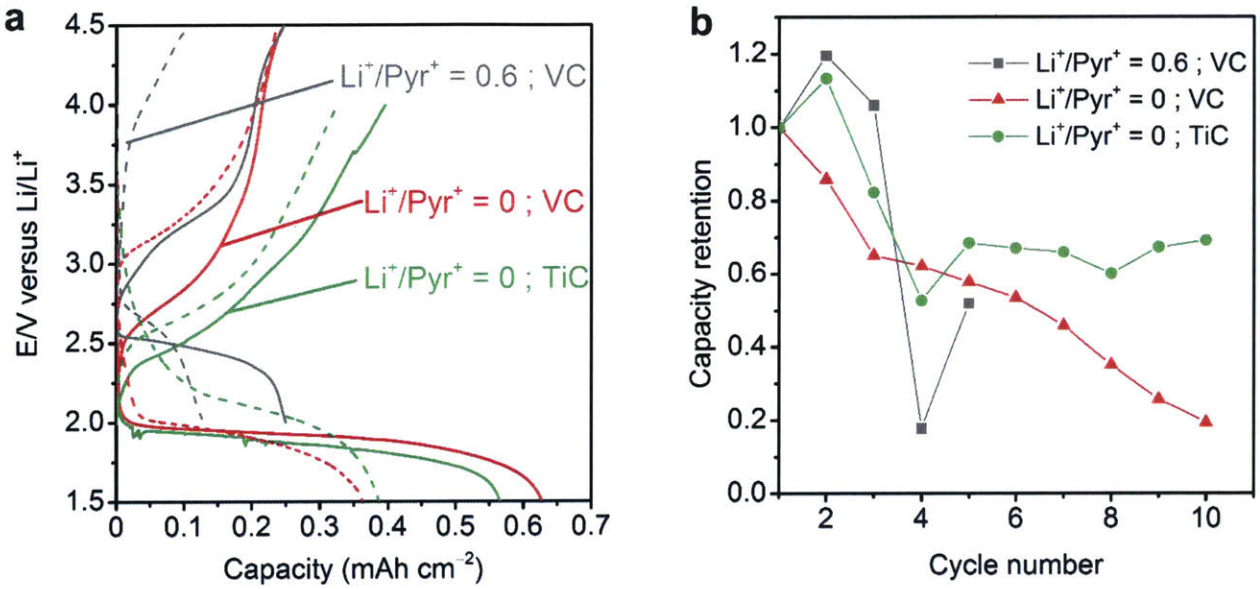

Figure 4-11 | Cycling performance using different GPE formulations with different electrodes. a, First (bold lines) and fifth cycles (dashed lines) of Vulcan carbon/PMMA electrode (4:1 mass ratio, 10 μA cm^{-2}) or TiC electrodes (12.4 μA cm^{-2}) with varying Li^+/Pyr^+ molar ratios; b, Capacity retention versus cycle number for the same Li–O_2 cells in (a). A discharge cutoff of 1.5 V was used for $Li^+/Pyr^+ = 0$ cells, and a 2 V cutoff was used for $Li^+/Pyr^+ = 0.6$. Cycling performed at 60 °C and current rates based on geometric surface area.

The instability of carbon-based electrodes during Li–O_2 cycling[35,44,75] prompts the use of titanium carbide (TiC) to support Li–O_2 discharge and charge with different GPE formulation.[110] Similarly to the Vulcan carbon electrode in Figure 4-11a, the first discharge for a cell with Li^+/Pyr^+ molar ratio of 0 is below 2 V with a TiC electrode, and the 5th discharge shows a higher discharge voltage due to Li^+ infiltration from the oxidized anode. The charging voltages are lower compared to the Vulcan carbon electrodes, and the capacity retention even at 4 V is much better with TiC than the Vulcan carbon electrodes (Figure 4-11b). This electrode-dependent behavior may be due to the instability of Vulcan carbon or different electrode charge-transfer kinetics.

One benefit of this one-electron discharge mechanism is the ability to limit the number of nucleophilic species to $O_2^{\bullet-}$, and possibly prevent formation of additional reactive species like O_2^{2-}, LiO_2, and Li_2O_2; therefore, making the GPE Li–O_2 cell less prone to electrolyte

degradation at least on the first cycle. GPEs recovered after multiple cycles at 60 °C show no changes in the PMMA carbonyl functionality (1700 cm^{-1}) in the infrared spectra, and minor decomposition products/impurities were observed in the ^1H NMR spectra (Figure C-5). Yellow coloration of the GPE – attributed to $Pyr_{14}TFSI$ reduction on lithium metal[132] – was observed after discharge/cycling in Li–O_2 cells with GPE Li^+/Pyr^+ molar ratios < 1 or when only ionic liquid was used (without polymer), but not when GPE $Li^+/Pyr^+ > 1$.

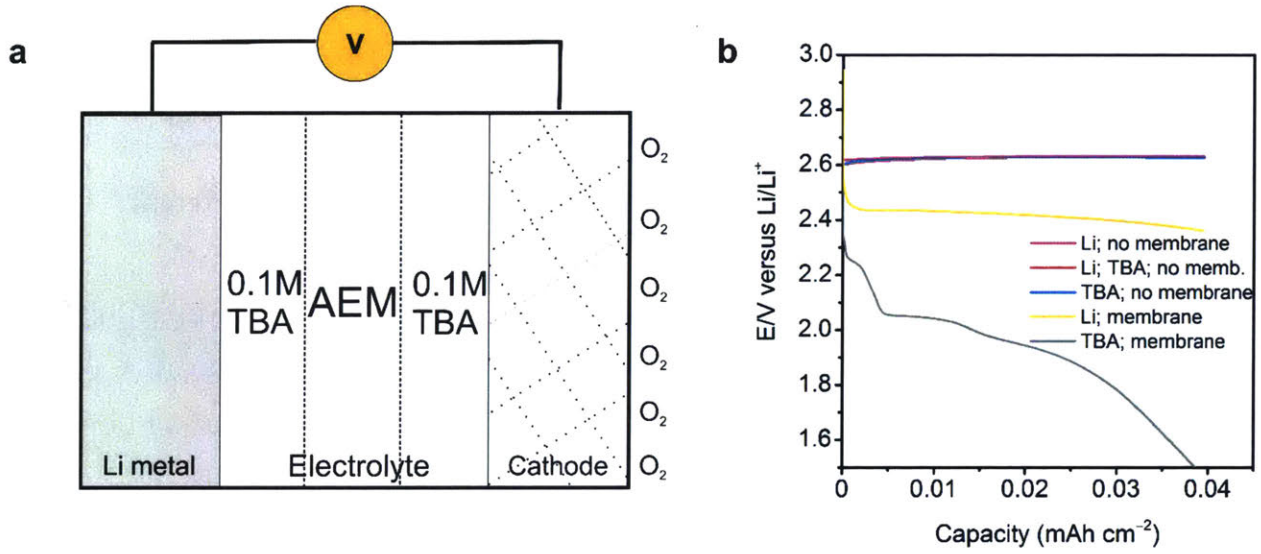

Figure 4-12 | Non-aqueous Li–O_2 cells to mimic GPE Li–O_2 behavior. a, Configuration of a Li–O2 cell with an anion exchange membrane (AEM) present in a 0.1 M $TBAClO_4$ in diglyme electrolyte. b, Discharge curves at 3.94 μA cm^{-2} with different electrolyte configurations at room temperature: 'Li; no membrane,' 'TBA; no membrane,' and 'Li; TBA; no memb.' = electrolyte containing only 0.1 M $LiClO_4$ in diglyme, 0.1 M $TBAClO_4$ in diglyme, and a 1:2 molar mixture of $LiClO_4$:$TBAClO_4$ in diglyme, with no AEM present, respectively. 'Li; membrane' and 'TBA; membrane' = electrolyte containing 0.1 M $LiClO_4$ and 0.1 M $TBAClO_4$ in diglyme respectively and an AEM. Further descriptions of the legend can be found in Appendix C.

Finally, a prototype non-aqueous liquid Li–O_2 cell (Figure 4-12a) was developed to replicate the discharge mechanism observed in the GPE Li–O_2 cells. This set-up is a corollary to the GPE Li–O_2 cell with an anion-exchange membrane (AEM) mimicking the function of the PMMA GPE

by reducing free lithium-ion transport across the electrolyte, and TBA^+ mimicking the ionic liquid cation ($TBAClO_4$ is dissolved in diglyme solvent). At low current rates, Figure 4-12b (TBA + membrane) shows that the first discharge has a plateau at around 2 V, a voltage similar to that observed for TBA^+–$O_2^{\bullet-}$ complex formation.[108] The plateau at around 2.2 V is due to Li^+ from the membrane (the anion for the AEM was exchanged with $LiClO_4$ prior to incorporation in the Li–O_2 cell; see Experimental Section). However, when no membrane is present, irrespective of the type of salt (either $LiClO_4$ or $TBAClO_4$), a single plateau at 2.6 V is observed. Even when the membrane is used with a $LiClO_4$ electrolyte, a 2.4 V plateau is observed, further suggesting that the plateau at 2 V is not merely due to kinetic losses from membrane addition. The membrane is thus needed to limit Li^+ transport from the anode to enable TBA–superoxide complexation to occur and mimic the effects of the GPE. This further supports our observation in the PMMA GPE system, where superoxide complexation only occurs when lithium-ions are unavailable. Moreover, like the GPE system, only about 30 % of the TBA^+ cations are used for superoxide complexation, resulting in low discharge capacity (see Appendix C). Furthermore, with cycling (Figure C-6), lithium ions cross the AEM, leading to higher discharge plateaus after the first discharge, again similar to the PMMA GPE-based Li–O_2 cells.

4.4 Conclusions

In this work, we demonstrate for the first time the use of an amorphous polymeric matrix, in combination with an ionic liquid, to control the oxygen reduction chemistry across multiple electrodes in a Li–O_2 cell. In the presence of Li cations, a 2 mol e^-/O_2 process is observed, but when Li^+ are absent – and ionic liquid cations are present – the ionic liquid becomes the active cationic specie, leading to a 1 mol e^-/O_2 process and the formation of solid ionic liquid-superoxide complexes.

The ability to obtain a 1 mol e^-/O_2 chemistry through a gel polymer electrolyte – without the addition of expensive catalysts – can allow for remediation of the sluggish kinetics, significant reactivity, high charging overpotentials, and poor capacity retention typically attributed to the 2 mol e^-/O_2 process in Li–O_2 batteries. Furthermore, this approach reduces the stringency of requiring high lithium-ion conductivity in electrolytes (any bulky cationic source can be used),

and could be explored in other metal-air batteries, and metal-sulfur systems where the limitation of intermediate polysulfide solubility is vital. Further optimization of this system, development of more stable ionic liquids, an investigation of a broader set of stable polymer systems with differing glass transition, ionic liquid compatibility, and molecular transport properties can allow for higher ionic liquid utilization, higher capacities, and longer cycle life.

4.5 Acknowledgments

This research was supported by the Samsung Advanced Institute of Technology (SAIT), and the facilities at the Koch Institute for Integrative Cancer Research. This work made use of the Shared Experimental Facilities supported in part by the MRSEC Program of the National Science Foundation under award number DMR-1419807. C.V.A. would like to acknowledge support by the Department of Defense (DoD) through the National Defense Science and Engineering Graduate (NDSEG) Fellowship, and the GEM Fellowship. H-H.C. is in part supported by the Ministry of Science and Technology of Taiwan (102-2917-I-564-006-A1). T.P.B. was supported by the Skoltech Center for Electrochemical Energy Storage. The authors also thank Professor Yang Shao-Horn for fruitful discussion and help with reviewing the Chapter, Dr. Sang Bok Ma for help in fabricating the TiC electrodes, Shiyu Zhang for help with EPR measurements and analysis, and Jonathon Harding for constructing the Differential Electrochemical Mass Spectrometer (DEMS).

Chapter 5

A Non-lithium Cation Additive for Solution-mediated Li–O_2 Electrochemistry: Influence of Ammonium Salts on Discharge and Charge of Li–O_2 Batteries.

Adapted from Chibueze V. Amanchukwu, Hao-Hsun Chang, and Paula T. Hammond. "A Non-lithium Cation Additive for Solution-mediated Li–O_2 Electrochemistry: Influence of Ammonium Salts on Discharge and Charge of Li–O_2 Batteries." 2017 (Submitted)

5.1 Introduction

Energy storage media such as batteries and fuel cells are vital in the drive to reduce fossil fuel use in transportation and electricity generation.[12,13,57] Newer energy-dense battery chemistries are being explored[12] and of these, Li-air (O_2) batteries with a theoretical gravimetric energy density of 3500 Wh/kg_{Li2O2} compared to 200 Wh/kg for Li-ion have shown great promise.[12,13,16] Li–O_2 chemistry is governed by oxygen reduction and evolution during discharge and charge, respectively.[14,20] During discharge, oxygen is reduced at the cathode to produce superoxide (Schematic 5-1).[14,108] Once formed, superoxide is a soft base that according to Hard Soft Acid Base (HSAB) theory prefers stabilization by a bulky cation (soft acid).[31,64] However, the presence of Li^+ in the electrolyte leads to LiO_2 (lithium superoxide);[109] a highly reactive and unstable intermediate.[26] Disproportionation of LiO_2 or a further electron transfer step leads to Li_2O_2 (lithium peroxide).[14,108] Charging of Li–O_2 cells involve decomposition of Li_2O_2 to release Li^+ and O_2.[20] Because Li_2O_2 is an insulator with high bandgap and low electronic conductivity,[133] high overpotentials are observed during charging. Side reactions between LiO_2 (or Li_2O_2) with the electrolyte solvent,[24] salt,[91] and electrodes[41] lead to unwanted side products such as LiOH,[24] Li_2CO_3,[44] LiF[26] among others that also require much higher charging overpotentials to oxidize, leading to low energy efficiencies, poor capacity retention with cycling, and limited cycle life.[14,28]

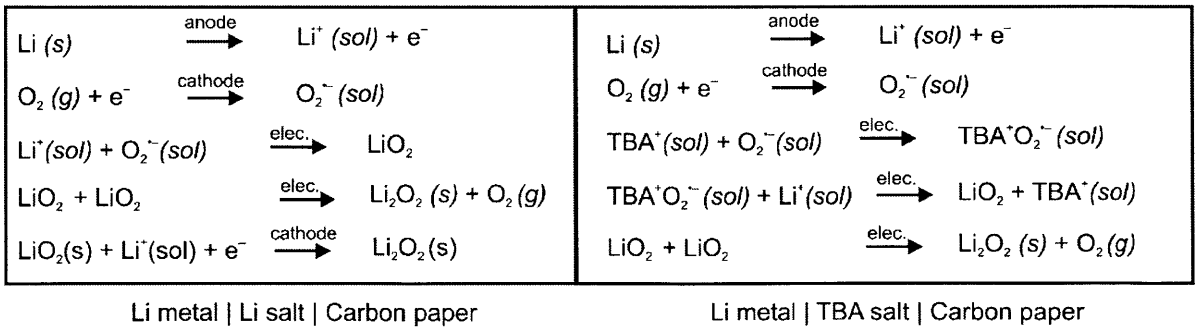

Schematic 5-1. Li–O_2 cell discharge mechanisms. Proposed discharge reaction mechanism when lithium salt is dissolved in the electrolyte compared to when $TBAClO_4$ salt dissolved in the electrolyte. The anion (e.g., ClO_4^-) is omitted in the schematic for clarity. Anode and cathode are

lithium metal and carbon paper respectively. TBA= tetrabutylammonium; "elec." = electrolyte; "s" = solid; "g" = gas; "sol" = solution.

Several strategies have been pursued to mediate the discharge and charge processes to improve discharge capacity and capacity retention with cycling. For charging, metal/metal oxide catalysts[42] and redox mediators such as LiI[106] and tetrathiafulvalene (TTF)[43] have been added to the electrode or electrolyte to reduce the charging voltages below 4 V. Reducing charging hysteresis is vital to improve energy efficiencies, but also because the most stable family of solvents for Li–O_2 batteries are glymes, which are electrochemically unstable above 4 V.[134] For discharge, a solution-mediated formation of Li_2O_2 discharge product, where toroids are formed lead to better utilization of the cathode and higher discharge capacities[135,136] whereas a surface-driven formation leads to film growth on the electrode. Since Li_2O_2 is an insulator, it blocks further O_2 reduction and lowers the discharge capacity. Compared to toroids, Li_2O_2 films are easier to remove during charge because of their proximity to the electrode.[111,137] The Li_2O_2 growth mechanism is typically rate-dependent with low current rates favoring a solution-based mechanism, and a high current rate favoring surface formation, but other parameters such as solvent type,[111] salt anion,[136] additives (H_2O etc.)[135] have been explored to modulate Li_2O_2 growth.

The ability of a solvent to support the solution-mediated formation of Li_2O_2 is correlated with its susceptibility to nucleophilic attack.[135,138] For example, as one increases the solvent donor number (ability of solvent to donate electron density to an acceptor or Lewis acid)[139] from acetonitrile, DME to DMSO, the vulnerability of the solvent to nucleophilic attack increases.[138] Therefore, it is important to modulate the solution-based mechanism by varying additives in one solvent (instead of changing solvents), preferably in glyme solvents.[136] Burke *et al.*[136] varied anion (NO_3^-) concentration in DME to improve Li^+ solvation and induce solution-mediated Li_2O_2 formation, but solubility of $LiNO_3$ in ethers is limited, and nitrate will be irreversibly consumed in creating a solid electrolyte interface (SEI) layer on the lithium metal anode.[140,141] Other researchers have shown that added H_2O in the electrolyte directs toroidal and crystalline Li_2O_2 growth through a solution-driven process,[135,142] but LiOH formation or other side reactions with lithium metal limits the utility of added H_2O. However, cation type has not been evaluated

because it has been widely assumed (as expected) that a lithium salt was required for Li–O_2 discharge. The larger a cation, the 'softer' it is, and the more stable the cation-superoxide complex, where cations such as pyrrolidinium[143] and ammonium[125] can coordinate and stabilize superoxide at longer time scales than lithium.[118] Therefore, investigating the influence of the presence of bulkier cations as an additional knob for controlling Li–O_2 battery chemistry is vital.

The oxygen reduction and evolution process in nonaqueous systems has been heavily studied using ammonium-based salts as supporting electrolytes.[64,108]. Tetrabutylammonium (TBA) salts can form stable TBA-superoxide complexes[125] during oxygen reduction, and these complexes can be reversibly oxidized without external catalysts.[108] Although TBA-influenced oxygen reduction and evolution has been investigated using cyclic voltammetry,[64,108] the influence of TBA on the electrochemical performance of actual Li–O_2 batteries has not been explored.

In this work, we study the ability of a non-lithium salt to support a solution-driven formation of Li_2O_2 in Li–O_2 batteries. We exploit the ability of TBA to sequester superoxide, and fabricate Li–O_2 cells using $TBAClO_4$ (Figure 5-1a inset) as the only dissolved salt. Similar to the use of viologen[144] and 2,5-di-tert-butyl-1,4-benzoquinone[137], TBA supports a solution-driven formation of Li_2O_2; a discharge product formed despite the lack of lithium salt present (Schematic 5-1). The influence of current rate, TBA concentration, and solvent type on the ability of TBA to support Li–O_2 discharge and charge was also explored. Interestingly, we observe that the presence of TBA in the electrolyte leads to much lower charging overpotentials (500 mV difference) than when a lithium salt is used. Using Li_2O_2-preloaded cells, we further show that the presence of TBA at potentials below 4 V is capable of oxidizing Li_2O_2, unlike typically-used lithium salts like $LiClO_4$. Given the results from several spectroscopic tools, we propose a mechanism that involves the electrochemical induced transformation of TBA to tributylamine, and the formation of a tributylamine oxide intermediate in the presence of O_2 or Li_2O_2 that can oxidize Li_2O_2 below 4 V. This work shows for the first time the evaluation of a Li–O_2 cell with no added lithium salt present in the electrolyte, the influence of ammonium salts on the discharge/charge behavior of Li–O_2 cells, and the use of amine oxides to oxidize Li_2O_2. Knowledge gained should provide insight into a new class of potential salts for metal-air use, and new pathways to oxidize Li_2O_2 during charge.

5.2 Experimental Methods

5.2.1 Materials used

Tetrabutylammonium perchlorate (>99%), lithium perchlorate, diethylene glycol dimethyl ether (diglyme), 1, 2-dimethoxyethane (anhydrous), acetonitrile, dimethylsulfoxide (anhydrous), lithium peroxide (90%), tributylamine, 1-decene, trimethylamine oxide, and quinine were obtained from Sigma Aldrich. Carbon paper (TGP-H-60, not PTFE treated) and lithium metal (0.75 mm thick, 99.9 %) were obtained from Alfa Aesar. Nafion was obtained as a 7.2 wt % lithiated Nafion in isopropanol solution from Ion Power Inc. Celgard C480 was obtained from Celgard. DMSO-d6 (with or without 0.03 v/v % tetramethylsilane) was obtained from Cambridge Isotope. Whatman GF/A separator was obtained from GE Life Sciences. Vulcan carbon (Vulcan XC72, 100 m^2/g) was obtained from Premetek Inc.

The solvents (DME, diglyme, and DMSO) were stored with molecular sieves (4 Å) in an Argon glovebox (MBRAUN, H_2O <0.1 ppm, O_2 < 0.1 ppm), and the electrolyte (salt dissolved in solvent) was made in the glovebox just before fabricating the Li–O_2 cell to limit exposure to water. Measured water content of the electrolytes was less than 30 ppm (using Karl-Fischer).

5.2.2 Electrode fabrication

The carbon paper electrodes were cut into 12.7 mm diameter disks and vacuumed-dried at 75 °C overnight. The Li_2O_2 preloaded electrodes were fabricated in a 1:1:1 mass ratio of Vulcan carbon: Li_2O_2: Lithiated nafion, and deposited on aluminum foil in the same manner as described in ref ([42]). The electrodes were transferred to the glove box without ambient exposure. The carbon nanotube (CNT) carpets were fabricated as previously reported by Gallant *et al.*,[61] and vacuum-dried at 75 °C overnight before being transferred and stored in an Argon glovebox (MBRAUN, H_2O <0.1 ppm, O_2 < 0.1 ppm) without ambient exposure.

5.2.3 Electrochemical testing

Lithium metal (15 mm diameter) was used as the anode and carbon paper (12.7 mm diameter) as the cathode. 120 µL of 0.1 M $TBAClO_4$ or 0.1 M $LiClO_4$ in DME solution and 0.1 M $TBAClO_4$ or 0.1 M $LiClO_4$ in DMSO was used. For the 2:1 molar ratio $TBAClO_4$/$LiClO_4$ electrolyte mixture, the 0.1 M $TBAClO_4$ in DME and the 0.1 M $LiClO_4$ in DME solutions were not

premixed before making the Li–O_2 cell. 40 μL of the 0.1 M $LiClO_4$ in DME solution was first added to the Li–O_2 cell before 80 μL of 0.1 M $TBAClO_4$ in DME was added. Two Celgard C480 separators were used for all DME Li–O_2 cells, while one Whatman separator was used for the DMSO Li–O_2 cells. Li–O_2 cells were fabricated in an Argon glovebox (MBRAUN, $H_2O < 0.1$ ppm, $O_2 < 0.1$ ppm). Then, the cells were transferred to another Argon glovebox (MBRAUN, $H_2O < 0.1$ ppm, $O_2 < 1\%$) without air exposure and pressurized with either Argon or oxygen. The cells were allowed to rest at open circuit voltage (OCV) for at least four hours before electrochemical measurements were performed. A VMP3 potentiostat (BioLogic Inc.) was used for all electrochemical tests.

Cyclic voltammetry (2-electrode setup) was performed using the same Li–O_2 cell setup as above. Lithium metal (15 mm diameter) served as both reference and counter electrode. Carbon paper (12.7 mm diameter) served as the working electrode. The cell was fabricated in an Argon glovebox (MBRAUN, $H_2O < 0.1$ ppm, $O_2 < 0.1$ ppm) and was pressurized with either Argon or oxygen (without air exposure) in a similar manner as above. The cell was allowed to rest at OCV for at least four hours before electrochemical measurements were performed. A sweep rate of 0.1 mV/s was used from 1.5 V to 4.5 V. The second cycle is shown in the figure in Chapter 5.

5.2.4 Potentiostatic Li_2O_2 preloaded cells

The Li_2O_2 preloaded cells were fabricated in a similar version as the Li–O_2 cells. A lithium metal anode (15 mm diameter) was used as the negative electrode, 90 μL of either $LiClO_4$ or $TBAClO_4$ in diglyme or 120 μL of $TBAClO_4$ in DMSO was used as the electrolyte. The Vulcan carbon/Li_2O_2/Nafion (1:1:1 mass ratio) on aluminum foil was used as the positive electrode. For the cell without Li_2O_2 present, a Vulcan carbon/Nafion (1:1 mass ratio) on Celgard electrode was used. The cells were allowed to rest for at least 5 hours at OCV, before the potentiostatic tests were performed. For cells held at oxidizing voltages (e.g., 3.7 and 3.9 V), the cell was held at 2.9 V for thirty minutes before continuing at the oxidizing voltage for the stated time (100 or 200 hours).

5.2.5 Chemical mixtures with Li_2O_2 or KO_2

All experiments were performed in an inert glovebox atmosphere (Argon or Nitrogen). Vials were stirred for three days.

a. Tributylamine: In a 5 mL vial, 15 mg Li_2O_2 and 0.3 mL of tributylamine
b. 1-Decene: In a 5mL, 15 mg Li_2O_2 and 0.3 mL of 1-decene
c. Trimethylamineoxide: 1:1 molar ratio of TMAO: Li_2O_2 in acetonitrile.
d. $TBAClO_4$: In a 20 mL vial, a 10:10:1 molar ratio of KO_2: Li_2O_2:$TBAClO_4$ was added to acetonitrile and stirred for three days.

The $TBAClO_4/KO_2/Li_2O_2$, tributylamine/ Li_2O_2, and 1-decene/ Li_2O_2 mixtures were allowed to settle and for remaining Li_2O_2 to sediment. About 20 µL of each supernatant was added to DMSO-d6 for ^1H NMR analysis. For the TMAO/ Li_2O_2 mixture, acetonitrile was removed from the vial, and DMSO-d6 was then added for ^1H NMR.

5.2.6 X-ray diffraction (XRD)

XRD data was obtained using a Rigaku Smartlab (Rigaku, Salem, NH, USA) in the parallel beam configuration with a Cu Kα radiation source. Electrochemically-tested samples were opened in an Argon glovebox, and sealed in an airtight XRD sample holder (Anton Paar, Austria) for XRD measurement. The reference code (01-074-0115) was used for all the Li_2O_2 references in the XRD spectra.

5.2.7 Raman spectroscopy

Raman data was obtained using a LabRAM Hr800 microscope (HORIBA) using an external 633 nm laser, with a 50X long working distance lens. A silicon wafer was used for calibration. A sealed custom-designed airtight Raman cell was used for the electrochemically-tested samples.

5.2.8 Scanning electron microscope (SEM)

SEM images were captured using a ZEISS Merlion (Carl Zeiss Microscopy GmbH, Germany) with an in-lens detector at 10 kV and 127 pA. Samples were sealed in aluminum foil bags in an Argon-filled glove box and rapidly transferred into the SEM chamber to minimize air exposure.

5.2.9 Ultraviolet-visible (UV-Vis) spectroscopy

UV-Vis data was collected using a Beckman Coulter DU 800 ultraviolet-visible (UV-Vis) spectrophotometer. In an Argon glovebox, the separator from the electrochemically-tested Li–O_2 cells was removed and placed in a clean 20 mL vial. Then, 1.5 mL of DMSO-d6 was added to the vial to dissolve the components in the separator. 1 mL of the solution was then placed in a

sealed-cuvette. The cuvette was removed from the glovebox and UV-Vis measurement was performed rapidly. The pristine solvent was used as a blank.

5.2.10 Nuclear magnetic resonance (NMR) spectroscopy

NMR experiments were performed on a Bruker AVANCE or AVANCE III-400 MHz spectrometer. After the Li–O_2 cells were cycled, they were transferred into an Argon glovebox without air exposure (MBRAUN, $H_2O < 0.1$ ppm, $O_2 < 0.1$ ppm). The cells were then placed in the glovebox antechamber (again without air exposure) and the cell was held under vacuum for about 10 minutes to remove some of the solvent. The separator and electrode were soaked in deuterated DMSO (DMSO-d6 or DMSO-d6 with TMS). The obtained NMR spectra was calibrated using the residual DMSO peak.

5.2.11 Quadrupole Time of Flight (Q-TOF) Mass Spectrometry

After the electrochemical experiments were performed, the cells were moved to an argon glovebox without ambient exposure. The electrolyte-soaked separator was then removed from the cell and placed in a 5 mL vial. The vial was vacuumed in the glovebox antechamber to remove the DME solvent. Excess methanol was added and Q-TOF analysis was performed on the supernatant. A Waters Q-TOF micro mass spectrometer equipped with an electrospray ionization ion source and a Time of Flight detector was used. The Q-TOF was run in ES+ mode meaning a proton is added to the neutral molecule before it enters the detector. Therefore, all the reported m/z values for neutral molecules are a proton larger than the actual molecular weight of the molecule. The figures were calibrated with respect to the internal standard (Quinine, m/z value of 325.19 and molecular weight of 324.42 g/mol).

5.3 Results and Discussion

5.3.1 Influence on discharge: The influence of TBA on the Li–O_2 discharge chemistry was studied by fabricating Li–O_2 cells with 0.1 M $TBAClO_4$ in 1, 2-dimethoxyethane (DME) as the electrolyte. Figure 5-1a shows that $TBAClO_4$ in the electrolyte can support oxygen reduction at reaction voltages similar to those observed for Li–O_2 cells with $LiClO_4$ (~2.5 V_{Li}). Cyclic voltammetry has shown TBA is capable of complexing oxygen reduction products such as

superoxide, and supporting the oxygen reduction and evolution process.[64,108] However, TBA has not been incorporated and studied in conventional Li–O_2 cells. Although $TBAClO_4$ is the only salt introduced into the Li–O_2 cell, the discharge product obtained here appears to be Li_2O_2; the desired discharge product in conventional Li–O_2 cells. Raman spectroscopy data in Figure 5-1b shows peroxide vibration peaks at 250 and 790 cm^{-1} that are typically associated with lithium peroxide.[145] We hypothesize that TBA complexes the superoxide intermediate (derived from oxygen reduction), bringing the superoxide intermediate into solution before allowing for coordination with lithium ions from the anode (Schematic 5-1). We do not expect to see TBA-superoxide as the final discharge product because lithium ions that originate from lithium metal oxidation during discharge would lead to disproportionation of the superoxide to peroxide (Schematic 5-1). X-ray diffraction (XRD) spectra (Figure 5-1c) shows that the obtained Li_2O_2 discharge product is crystalline,[34] and the scanning electron microscope (SEM) image in Figure 5-1d reveals toroidal features typically associated with Li_2O_2, suggesting solution formation of Li_2O_2.[59] The effect of solvent on TBA-supported discharge was also explored and in Figure 5-2, TBA can also support Li–O_2 discharge in DMSO and lead to Li_2O_2 formation. We cannot currently assign the XRD diffraction peaks at 43.6° and 50.5° 2θ range, but they appear to be a result of discharge as they are observed in DME and DMSO. These results in Figures 5-1a-d and Figure 5-2 indicate that a lithium salt added in the electrolyte is not required to support Li–O_2 discharge. The oxidation of lithium metal during discharge provides the lithium ions that are needed for Li_2O_2 formation. Any salt (e.g., $TBAClO_4$) capable of supporting oxygen reduction in combination with lithium metal can be utilized. Furthermore, the presence of $TBAClO_4$ doesn't appear to have a detrimental effect on the observed reaction voltage at least on the first discharge.

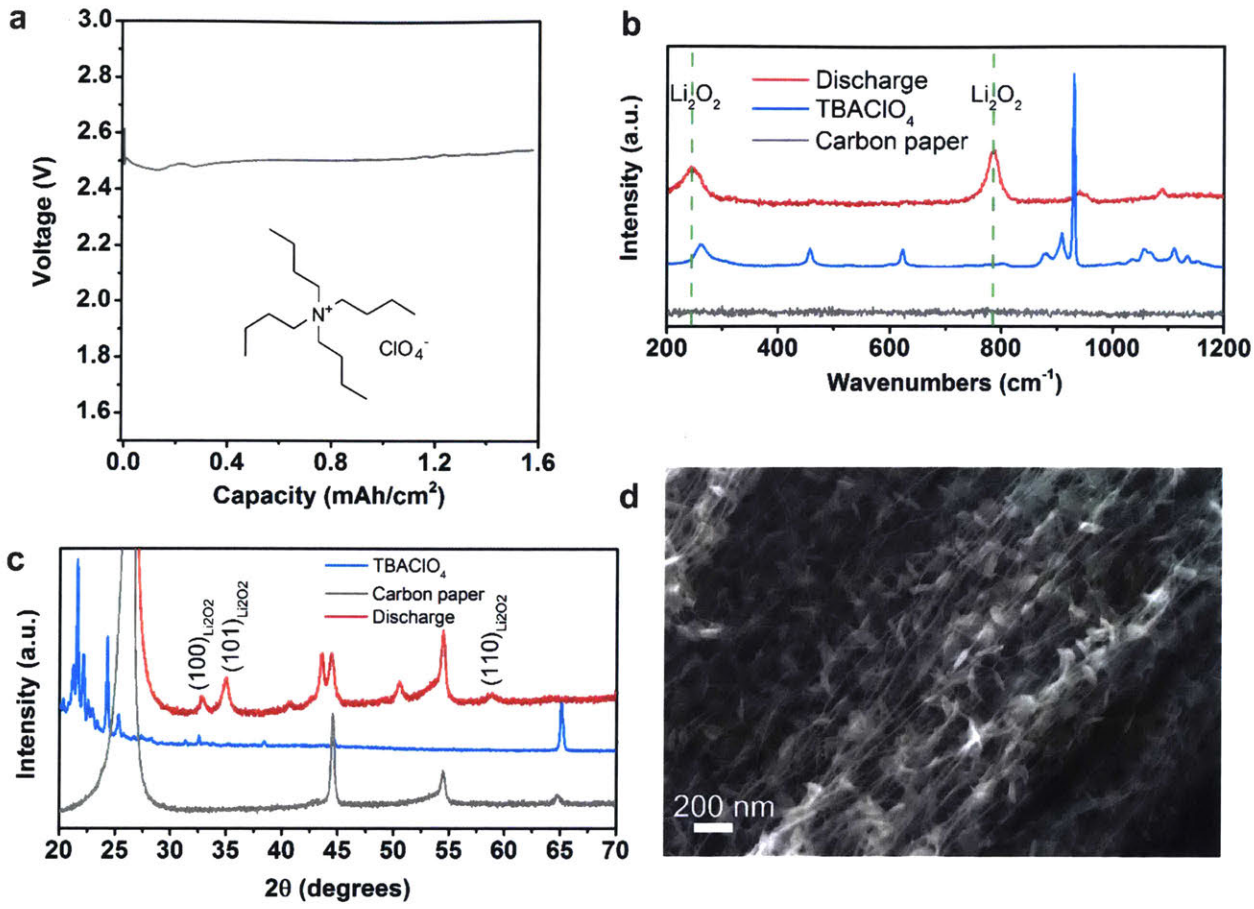

Figure 5-1 | Discharge behavior using a $TBAClO_4$-only electrolyte. (a) Discharge curve, (b) Raman, (c) XRD, and (d) SEM after discharge at 15.7 $\mu A/cm^2$ (geometric surface area) in oxygen using 0.1 M $TBAClO_4$ in DME as the electrolyte. Inset in Figure 5-1a is the chemical structure of tetrabutylammonium perchlorate. Voltage (vs. Li/Li^+). $Li–O_2$ cell setup for (a)-(c): Li metal | 0.1 M $TBAClO_4$ in DME | carbon paper. $Li–O_2$ cell setup for (d): Li metal | 0.1 M $TBAClO_4$ in DME | carbon nanotube.

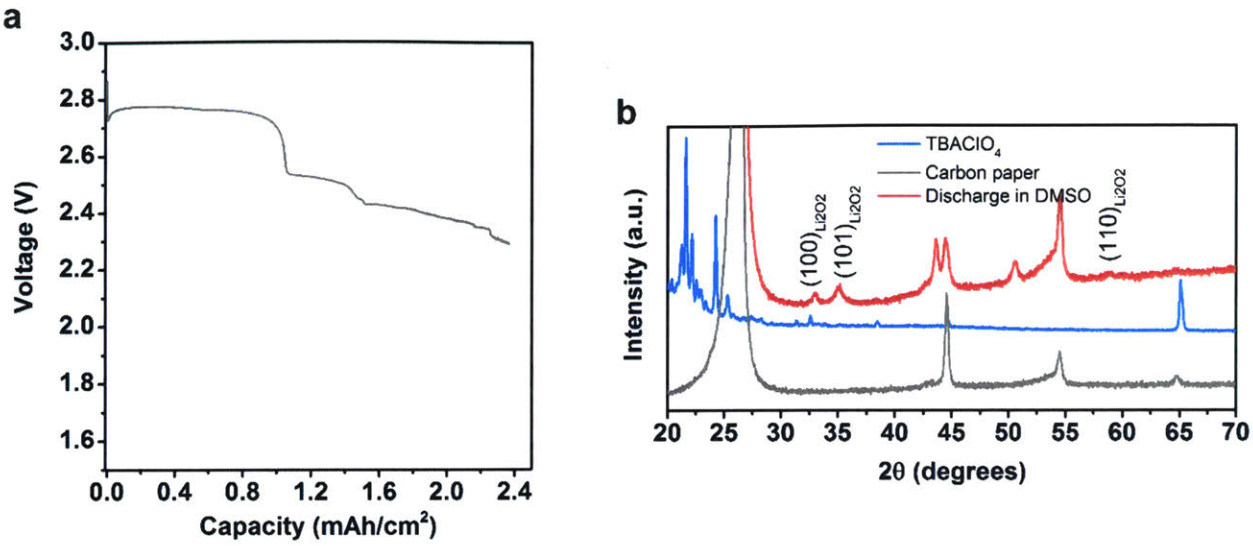

Figure 5-2 | Discharge behavior using a $TBAClO_4$ electrolyte in DMSO (a) Discharge curve of a Li–O_2 cell discharged in O_2 at 15.8 μA/cm^2 with 0.1 M $TBAClO_4$ in DMSO as the electrolyte. (b) XRD spectra of the electrode in (a) after discharge. Li–O_2 cell setup: Li metal | 0.1 M $TBAClO_4$ in DMSO | carbon paper.

5.3.2 Influence on cycling: The effect of cation type ($TBAClO_4$ or $LiClO_4$) and solvent type (DME or DMSO) on cycling were also examined. Figure 5-3a shows the first and fifth cycles of three different electrolyte configurations at a low current rate (3.95 μA/cm^2). Current rates are based on geometric surface area of the carbon paper electrode. When 0.1 M $LiClO_4$ is used as the electrolyte, a discharge voltage at ~2.6 V is observed. However, complete charging requires voltages greater than 4 V, a behavior typically observed in the absence of catalysts[42] or redox-mediator additives.[43] When 0.1 M $TBAClO_4$ is used as the electrolyte, the first discharge is similar to that obtained with 0.1 M $LiClO_4$, but a flat plateau at 3.55 V is observed almost during the entire charge. Furthermore, the charging profile for the 0.1 M TBA Li–O_2 cell remains similar at the fifth charge. When a mixture of $TBAClO_4$: $LiClO_4$ (2:1 molar ratio) is used as the electrolyte, charging behavior similar to a standard $LiClO_4$ cell is observed at the first charge. However, by the fifth cycle, charging occurs at 3.55 V (Figure 5-3a). The $TBAClO_4$:$LiClO_4$ Li–O_2 cell is certainly intermediate between the behavior observed for a $LiClO_4$-only cell or a $TBAClO_4$-only cell. The charging behavior in the presence of 0.1 M $TBAClO_4$ is reminiscent of

redox mediator-like charging where iodide,[106] TEMPO (2,2,6,6-tetramethylpiperidinyloxyl),[146] or TTF[43] can be oxidized during charge, and subsequent chemical reaction with Li_2O_2 leads to Li_2O_2 oxidation and reduction of the oxidized mediator. However, a redox-like mechanism doesn't seem likely for TBA because the nitrogen functionality is already fully oxidized (+1).

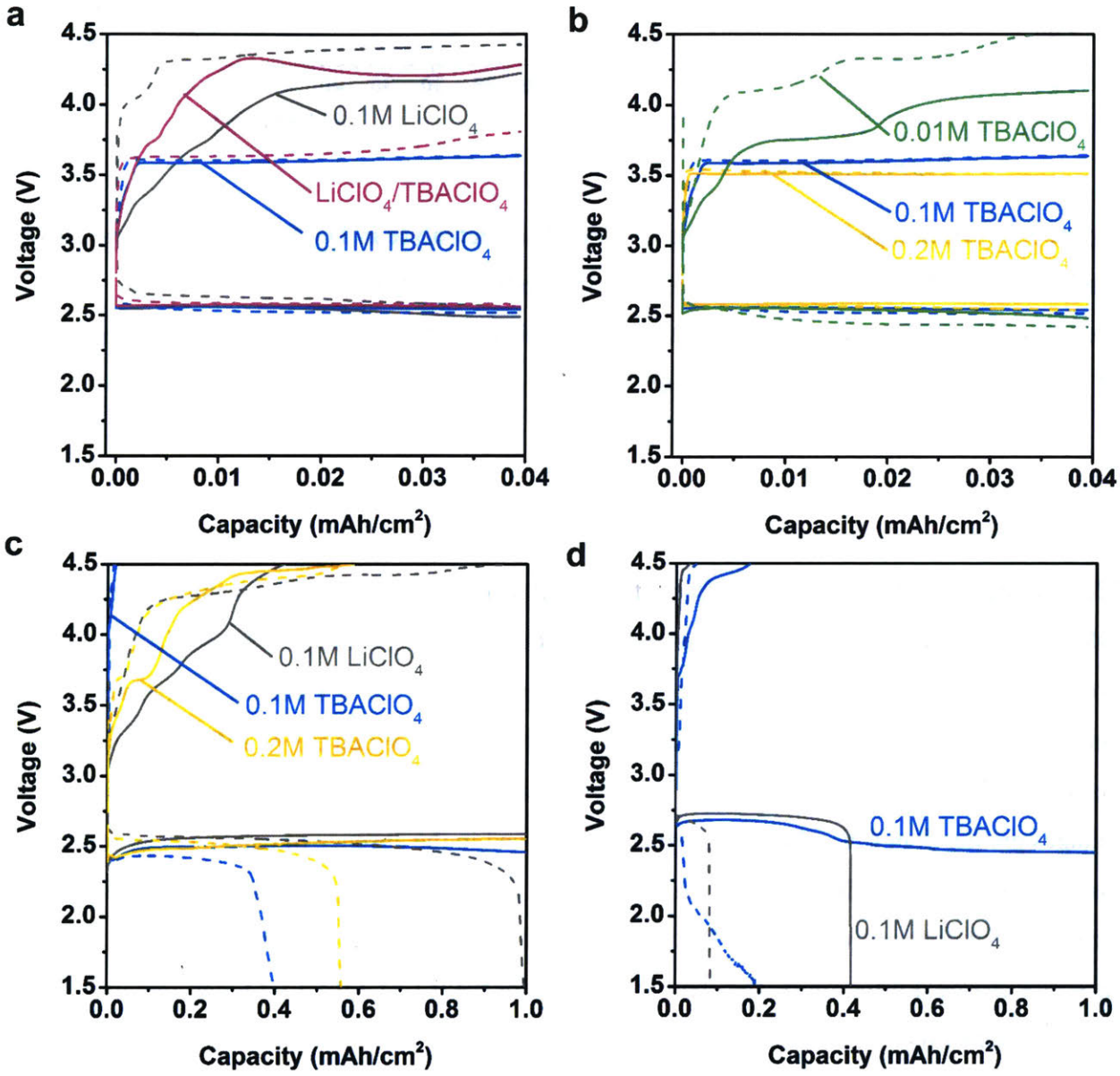

Figure 5-3 | Effect of TBA and Li salt on Li–O_2 cycling in DME and DMSO at different current rates. Cycling of a Li–O_2 cell in oxygen in DME at 3.95 μA/cm^2 to a 0.04 mAh/cm^2 cutoff with (a) different electrolyte salt content and (b) different TBA concentration. The

$LiClO_4$/$TBAClO_4$ electrolyte is a 2:1 molar ratio of $TBAClO_4$: $LiClO_4$ in DME. Cycling in oxygen at 100 $\mu A/cm^2$ to a 1 mAh/cm^2 cutoff with (c) DME and (d) DMSO electrolytes. Concentrations are as shown in the figures in the respective solvents (a–c: DME; d: DMSO). (Bold lines) – First cycle; (Dashed lines) – Fifth cycle. Voltages are vs Li/Li^+. Current rates and capacities are based on the geometric surface area of the carbon paper electrode. Li–O_2 cell setup: Li metal | ($TBAClO_4$ or $LiClO_4$) in DMSO or DME | carbon paper.

When the TBA concentration in the electrolyte is increased, the charging plateau is reduced, and the charging behavior at the fifth charge is improved when comparing 0.01 M to 0.2 M TBA in DME (Figure 5-3b). However, there are limits to this surprising reduction in charging overpotentials in the presence of $TBAClO_4$. Figure 5-3c shows that as the current rate in DME is increased to 100 $\mu A/cm^2$, the ~ 3.55 V plateau is absent, and the charging curve resembles the $LiClO_4$-containing cells.

In DMSO, a different phenomenon is observed. At low current rates (3.95 $\mu A/cm^2$), $TBAClO_4$ can support discharge and charge, but again the ~3.55 V plateau is absent (Figure D-1) and it resembles the $LiClO_4$ cell. The plateau absence is also observed at 100 $\mu A/cm^2$; however, the discharge capacities are higher when $TBAClO_4$ in DMSO is used as the electrolyte at high current rates. The improvement in discharge performance may be due to the ability of DMSO to stabilize superoxide species and solubilize TBA,[111] a superoxide complexing agent.[109] At high current rates, there is a diminishment in discharge capacity observed with cycling that may be due to the inability to completely oxidize the discharge products. In summary, the redox-like charging behavior induced by TBA appears rate and solvent-dependent.

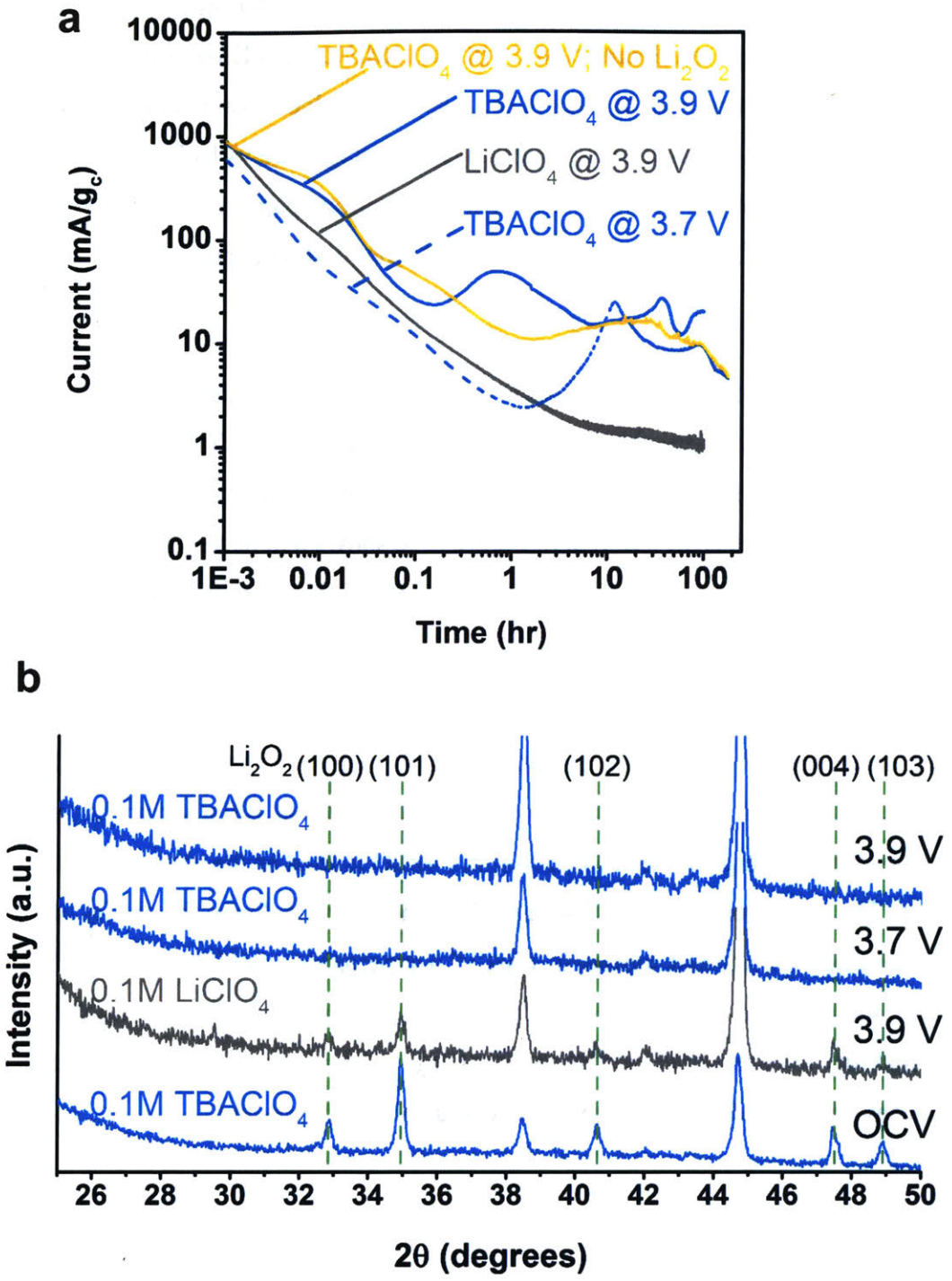

Figure 5-4 | Li_2O_2 oxidation under potentiostatic hold. (a) Current vs. time from potentiostatic holds at 3.7 or 3.9 V with or without Li_2O_2 preloaded in the electrode and with different salts in diglyme (0.1 M salt concentration). (b) Corresponding x-ray diffraction (XRD) spectra at the different voltages in (a). The "OCV" sample was held at open-circuit voltage for 200 hours. Dashed lines in (b) are the (100), (101), (102), (004), and (103) Li_2O_2 diffraction peaks (left to

right). Li–O_2 cell set-up: Li metal | 0.1 M $LiClO_4$ or $TBAClO_4$ salt in diglyme | Vulcan carbon + Nafion + Li_2O_2 (when present) on aluminum foil.

5.3.3 Effect on Li_2O_2 oxidation: Although a stable 3.55 V charging plateau is observed when TBA is used as a salt in an ether solvent, it is important to know if its presence can lead to Li_2O_2 oxidation. To study this, Li_2O_2-preloaded electrodes were fabricated. These electrodes consisted of Li_2O_2: Vulcan carbon: Lithiated Nafion in a 1:1:1 mass ratio with no added catalysts. Other researchers have used these electrodes as a tool to study Li_2O_2 oxidation and eliminate the influence of other side reaction products that may have formed during cell discharge.[42,102] Figure 5-4a shows current-time plots of these Li_2O_2 preloaded electrodes subjected to potentiostatic charging tests in different salt configurations in diglyme. Similar to work reported by Yao *et al.*,[42] when 0.1 M $LiClO_4$ is used as the electrolyte, no oxidation current is observed at 3.9 V for 100 hours. As expected, XRD spectra in Figure 5-4b shows that Li_2O_2 is still present in the LiClO4-containing electrode. However, when 0.1 M $TBAClO_4$ is used as the electrolyte at 3.7 V or 3.9 V (above ~3.55 V), an oxidation current is observed. Remarkably, this corresponds to Li_2O_2 oxidation as Li_2O_2 is no longer observed on the electrode (Figure 5-4b). In addition, the Li_2O_2 is not converted to LiOH as LiOH is not observed on the electrode; no (101) or (110) diffraction peaks at 32.5° and 35.7° 2θ range.[24] A Li_2O_2-preloaded cell is also held at open-circuit with a 0.1 M $TBAClO_4$ electrolyte and crystalline Li_2O_2 peaks are still observed. This further supports the notion that Li_2O_2 oxidation is not a result of chemical reaction with $TBAClO_4$, but needs an oxidizing voltage. Despite the lack of a stable oxidation plateau at around 3.55 V in DMSO (Figure D-1), and the solvent-dependence of the charging profile, the presence of 0.1 M $TBAClO_4$ in DMSO also leads to the removal of Li_2O_2 during charge as the XRD spectrum in Figure D-2 shows. Yao *et al.*[42] showed that catalysts such as Ru and Cr are capable of oxidizing Li_2O_2 only when present in the solid-state electrode, but not when the catalysts are in the electrolyte. Here, TBA appears to act as a redox mediator typically dissolved in the electrolyte (this hypothesis will be evaluated and discussed later).

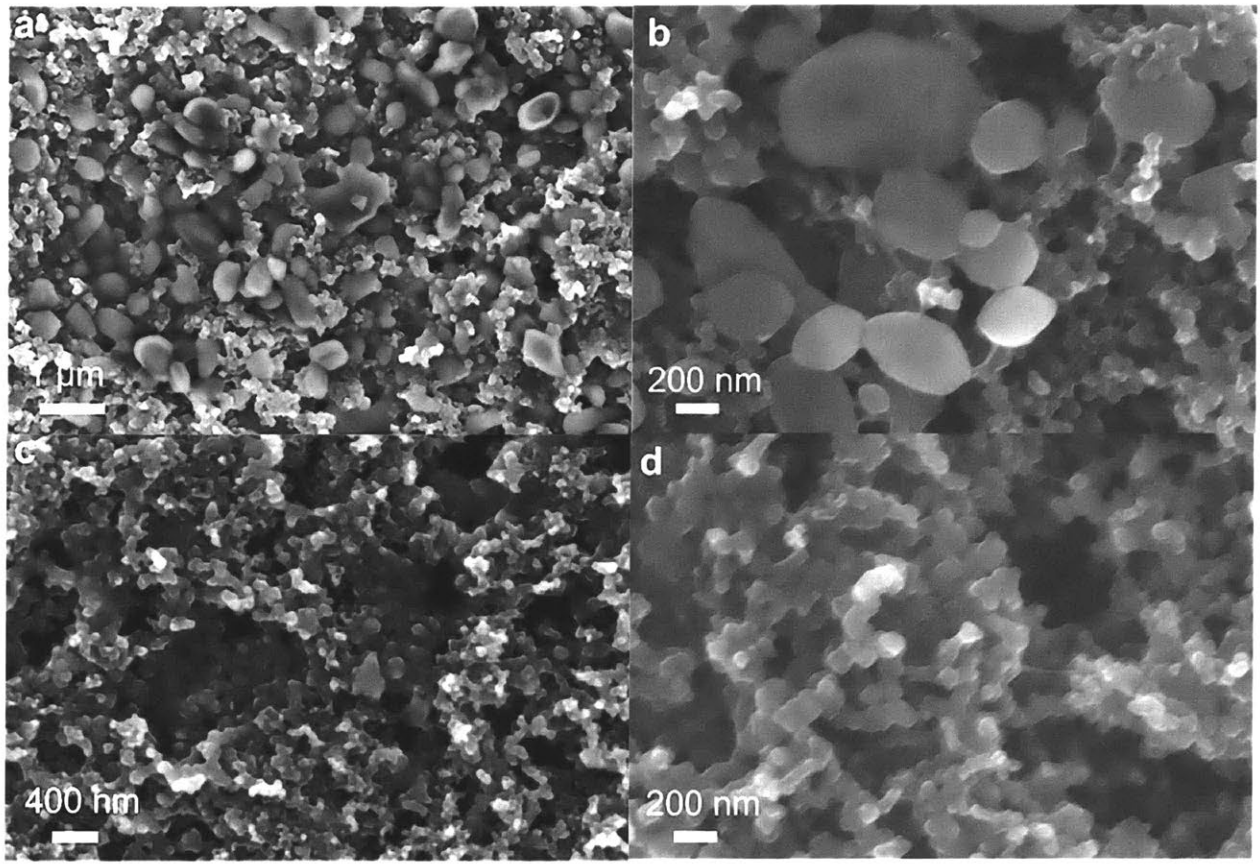

Figure 5-5 | SEM micrographs chronicling the electrochemical changes in Figure 5-4. (a) Li_2O_2-preloaded electrode held at open-circuit voltage (OCV) in 0.1 M $TBAClO_4$ for 200 hours, (b) at 3.9 V in 0.1 M $LiClO_4$ for 100 hours, (c) 3.7 V in 0.1 M $TBAClO_4$ for 200 hours, and (d) 3.9 V in 0.1 M $TBAClO_4$ for 100 hours. Solvent = diglyme. Li–O_2 cell set-up: Li metal | 0.1 M $LiClO_4$ or $TBAClO_4$ salt in diglyme | Vulcan carbon + Nafion + Li_2O_2 on aluminum foil.

The same charged Li_2O_2 electrodes examined by XRD in Figure 5-4 were studied using SEM. Figure 5-5 shows SEM images that further confirm the observations made in Figure 5-4, and show that the disappearance of the Li_2O_2 XRD peaks in Figure 5-4b is not due to phase change between crystalline and amorphous Li_2O_2, but Li_2O_2 oxidation. The large solid particles seen in Figure 5-5a are the preloaded Li_2O_2 and they remain even after seating in a $TBAClO_4$ electrolyte at open-circuit voltage (OCV) for 200 hours. In addition, Figure 5-5b shows that Li_2O_2 particles remain after the 3.9 V potentiostatic hold in 0.1 M $LiClO_4$, corroborating the XRD spectra in Figure 5-4b. When $TBAClO_4$ is used as the electrolyte, holes are observed where presumably

Li_2O_2 particles used to be; further evidence of Li_2O_2 oxidation. Yao *et al.*[102] also used SEM to chronicle Li_2O_2 oxidation in the presence of perovskite and Cr nanoparticle catalyzed Li_2O_2 electrodes, and attributed the disappearance of Li_2O_2 particles and appearance of these holes to be a result of Li_2O_2 oxidation. Since the 3.9 V 0.1 M $TBAClO_4$ cell was held for only 100 hours, remnant partially oxidized Li_2O_2 particles can still be found (Figure D-3), but their quantities are miniscule compared to the OCV and $LiClO_4$-based cells. Furthermore, since the 3.7 V 0.1 M $TBAClO_4$-based preloaded cell was held for 200 hours, no Li_2O_2 particles were found on the electrode after charging was completed.

5.3.4 Electrochemical effect on TBA: TBA was examined in the absence of oxygen to decouple the mechanism of Li_2O_2 and TBA transformation. Figure 5-6a shows that because of the lack of oxygen, no significant discharge plateau is observed as expected, but the ~3.55 V charging plateau is still present. However, the $LiClO_4$-based cells cycled in Argon show no significant discharge or charge plateau (Figure D-4). Furthermore, in Figure 5-4a, when the TBA electrolyte is held at 3.9 V with no Li_2O_2 present, there is a significant oxidation current. The cyclic voltammetry (CV) data in Figure 5-6b corroborates this observation as an oxidation current beginning at 3.5 V is observed when the $TBAClO_4$-containing electrolyte is scanned positively in Argon. Again, no reduction current is observed in Argon even after the TBA decomposition product is formed, indicating that TBA cannot act as a typical redox shuttle. The electrochemical-induced transformation of TBA appears irreversible, and reversibility is a requirement for any true redox shuttle. Therefore, in Argon or O_2, TBA is electrochemically transformed during charge, and the TBA decomposition product leads to the oxidation of Li_2O_2 (when present). The mechanism that explains this behavior will be discussed in the next paragraph.

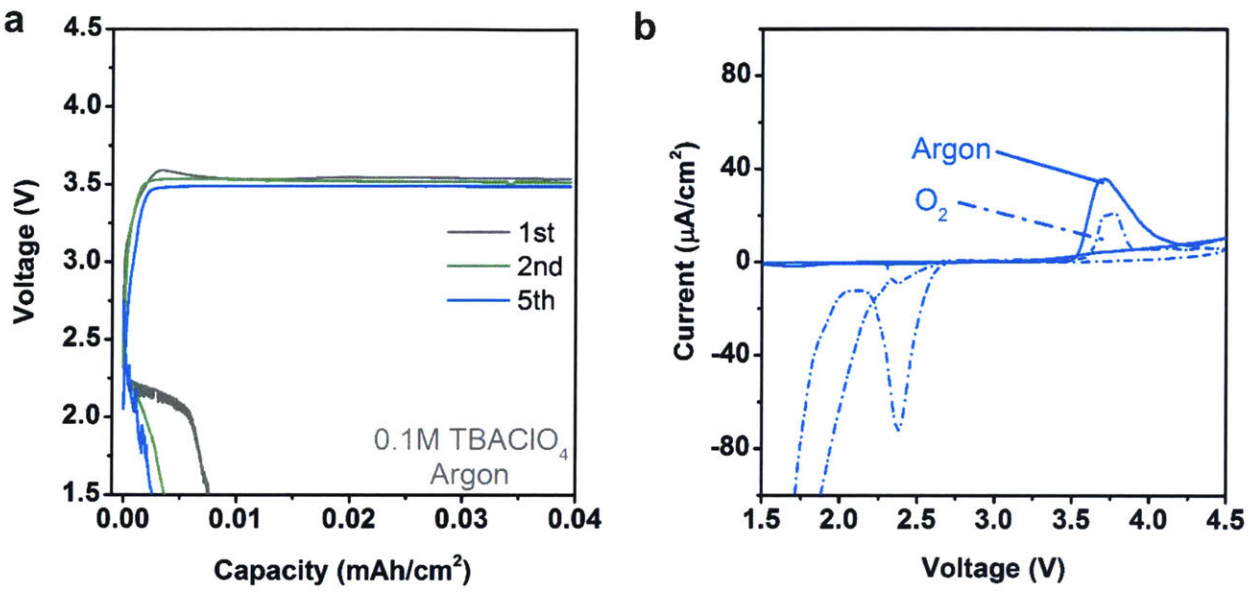

Figure 5-6 | Electrochemical-induced transformation of TBA. (a) Cycling using 0.1 M $TBAClO_4$ in DME at 3.95 $\mu A/cm^2$ to 0.04 mAh/cm^2 in argon. (b) Cyclic voltammetry (2-electrode setup) in argon and O_2 at 0.1 mV/s scan rate with a 0.1 M $TBAClO_4$ in DME electrolyte. Li–O_2 cell setup for (a): Li metal | 0.1 M $TBAClO_4$ in DME | carbon paper. Setup for (b): Working electrode: Carbon paper; Reference and counter electrode: Lithium metal. CV was performed by scanning first to 4.5 V before scanning to 1.5 V. The second cycle for both argon and O_2 is shown in (b).

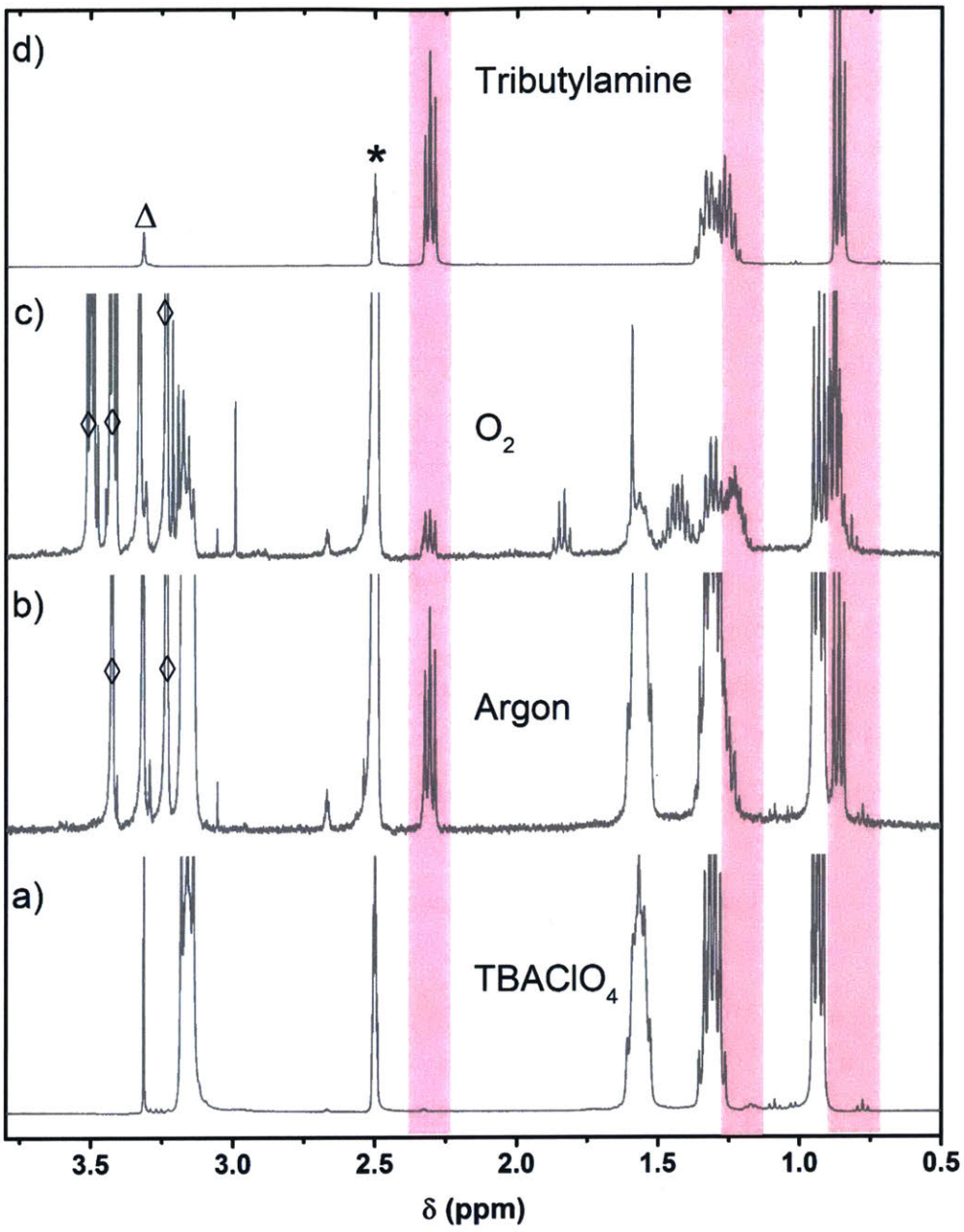

Figure 5-7 | ^{1}H NMR after Li–O_2 cycling in argon and oxygen. ^{1}H NMR (400 MHz; DMSO-d6; H-DMSO) spectrum of (a) $TBAClO_4$ (b) electrolyte of Li–O_2 cell after five cycles in Argon, (c) electrolyte of Li–O_2 cell after fifteen cycles in oxygen, and (d) commercial tributylamine. *= DMSO, Δ=HDO, ◊=solvent. Spectra was calibrated using the residual DMSO ('H-DMSO') peak in DMSO-d6. Integration values for peaks in (b) and (c) are in Table D-2. Li–O_2 cell setup: Li metal | 0.1 M $TBAClO_4$ in DME | carbon paper. The actual cycling profile for (b) is shown in Figure 5-3a, and for (c) is shown in Figure D-5.

5.3.5 Proposed mechanism: ^{1}H NMR was used to determine the changes in the TBA chemical structure during cycling. The electrolyte-soaked separator from cycled Li–O_2 cells using 0.1 M $TBAClO_4$ or $LiClO_4$ in DME-based cells were extracted and soaked in deuterated DMSO for ^{1}H NMR and UV-Vis analysis. In all TBA-based Li–O_2 cells in DME or diglyme where charging was performed, yellow coloration of the electrolyte was observed. UV-Vis spectra in Figure 5-8 chronicles the presence of these light-absorbing species when cycling is performed using a TBA-based electrolyte, and additional species are formed when the cell is cycled in oxygen compared to argon. Figure 5-7 shows ^{1}H NMR characterization of cells cycled with 0.1 M $TBAClO_4$ in argon and oxygen where new peaks related to TBA decomposition are observed. TBA is electrochemically transformed at 3.55 V (Figures 5-3 and 5-6) to form tributylamine (Figure 5-7) and possibly an alkene (Schematic 5-2). We propose an electrochemically-induced transformation of a base (from decomposition of carbon or electrolyte) at > 3.5 V which deprotonates TBA and allows TBA to undergo Hoffman elimination reaction that leads to tributylamine and butene. The ^{1}H NMR peaks of commercial tributylamine match the new observed TBA degradation peaks. Furthermore, quadrupole time-of-flight (Q-TOF) mass spectra in Figure 5-9 shows a peak at an m/z value of 186.2 that corresponds to tributylamine (MW = 185.4 g/mol), and is formed after electrochemical induced degradation in either Argon or O_2. Finkelstein *et al.*[147] have previously shown that a quarternary ammonium salt can degrade to a tertiary amine and a hydrocarbon radical intermediate through a one electron pathway. Assuming a one-electron decomposition pathway, Table D-1 shows that complete decomposition of TBA should occur before 7 charging steps, and Figure D-5 shows evidence that the charging voltage begins to increase at the seventh charge. However, NMR data in Figure 5-7 shows TBA is still present after 15 cycles in O_2. Therefore, it is possible that during charging, TBA decomposition products can also be electrochemically oxidized as well as some direct delithiation of Li_2O_2 that can occur below 4 V.[148]

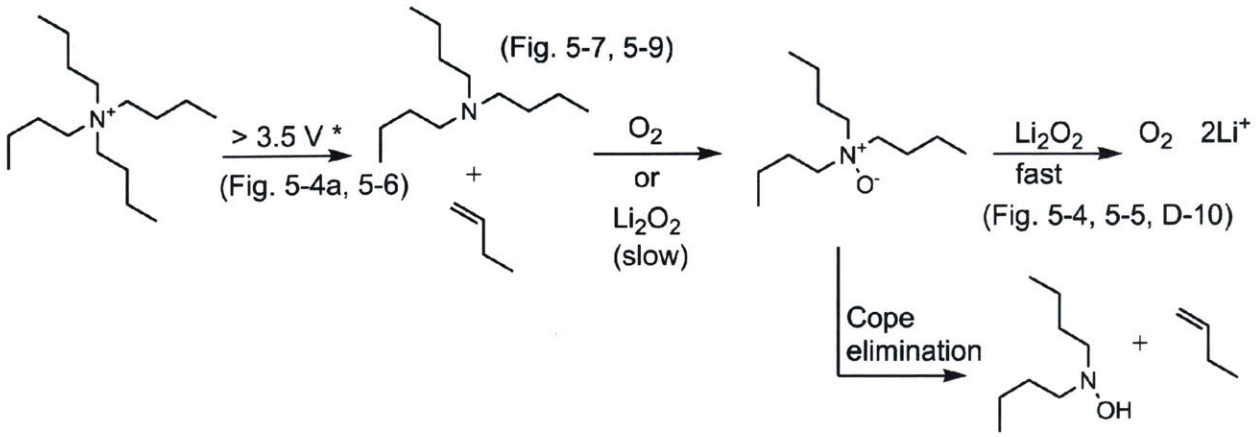

Schematic 5-2 | Mechanism for TBA-supported Li_2O_2 oxidation. Proposed mechanism of electrochemical oxidation of tetrabutylammonium to form tributylamine, and the subsequent oxidation of Li_2O_2 to release oxygen. The figure numbers in parenthesis in the mechanism indicates the figure in this Chapter that provides evidence of the stated pathway. ClO_4^- anion is omitted in the mechanism schematic for clarity. Li–O_2 cell setup: Li metal | 0.1 M $TBAClO_4$ in DME | carbon paper. *At 3.5 V, electrochemical-induced base formation that deprotonates TBA, allowing TBA to undergo Hoffman elimination.

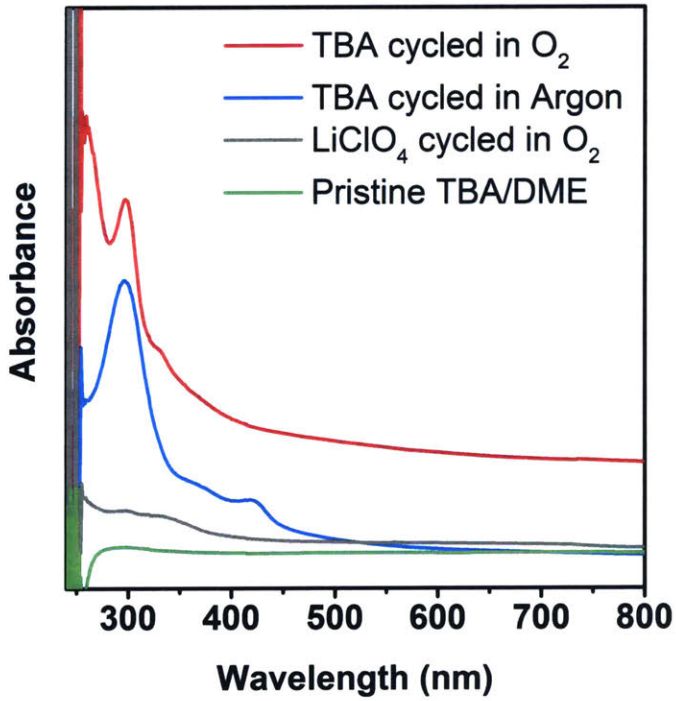

Figure 5-8 | UV-Vis spectroscopy after cycling. Ultraviolet-visible (UV-Vis) spectroscopy data obtained after $TBAClO_4$ or $LiClO_4$ was cycled in either oxygen or Argon. The figures shows additional species are formed when $TBAClO_4$ is cycled in oxygen compared to argon.

The proposed TBA reaction pathway is in Schematic 5-2. The alkene formed here would be butene, but the low boiling point of butene (−6.5 °C) makes post-cycling characterization difficult. OCV experiments in Figure 5-4b, and chemical experiments involving a 10:10:1 molar ratio of Li_2O_2:KO_2:$TBAClO_4$ in Figure D-6 show that TBA does not appear to chemically react with Li_2O_2 to oxidize Li_2O_2. Once tributylamine and butene are formed, they can possibly undergo reactions with Li_2O_2. To examine this, a Li_2O_2-preloaded electrode is held at OCV in commercial tributylamine or decene (chemically similar to butene but is a liquid at room temperature) for 200 hours and perform XRD afterwards (Figure D-7). XRD shows that Li_2O_2 is still present; hence, the oxidation of Li_2O_2 is not due to chemical reaction between Li_2O_2 and tributylamine or butene alone. A stirred chemical mixture of Li_2O_2 with tributylamine or decene also does not reveal any changes in the ^1H NMR spectra (Figures D-8 and D-9), further confirming the XRD observation in Figure D-7. The lack of bulk reaction between tributylamine and Li_2O_2 is surprising because it is known that tertiary amines can react with H_2O_2 to form amine oxides,[149,150] however Hoh *et al.*[150] noted that direct oxidation of tertiary amines with H_2O_2 proceeds slowly. The limited solubility of Li_2O_2 in tributylamine would also diminish an already slow reaction with tributylamine compared with H_2O_2. Other researchers have shown that oxygen can react with tertiary amines to form an amine oxide, and the amine oxide is an intermediate that is difficult to characterize because it undergoes subsequent reactions.[151,152] Some of these possible reactions are shown in Schematic 5-2. One reaction the tributylamine oxide can undergo is Cope elimination,[151,153] an intra or inter molecular reaction that involves the oxygen on the tertiary amine oxide abstracting a hydrogen from a carbon that is beta to the nitrogen to form an olefin. In addition, alkyl radicals and nitroxide can also be formed.[151]

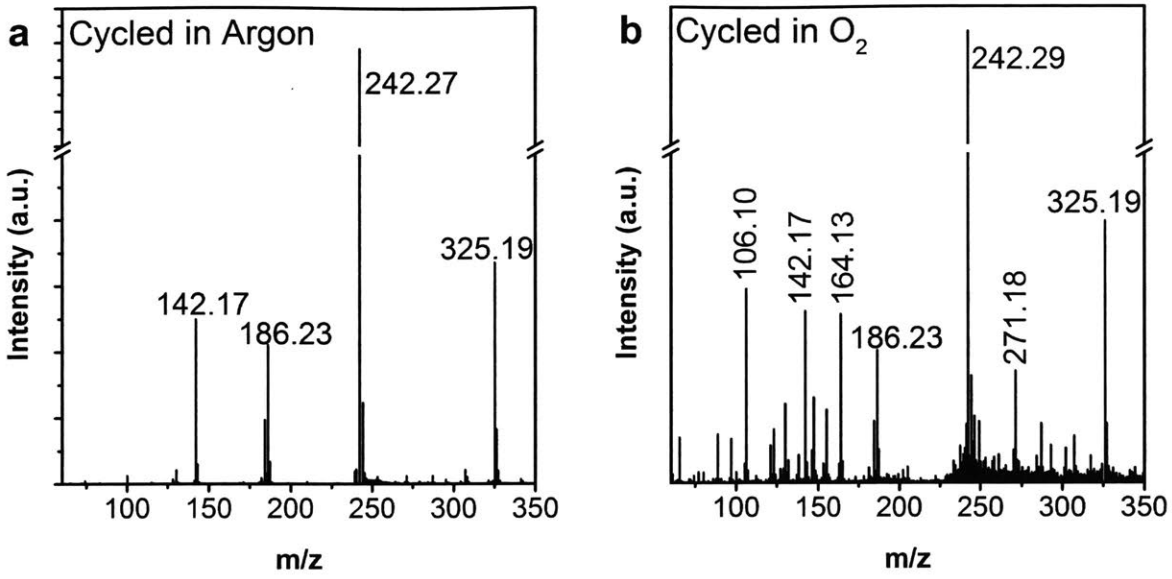

Figure 5-9 | Quadrupole Time of Flight (Q-TOF) mass spectra after Li–O_2 cycling. Spectra obtained after cycling in (a) argon and (b) oxygen. Li–O_2 cell setup: Li metal | 0.1 M $TBAClO_4$ in DME | carbon paper. For neutral molecules, a proton is added to the molecule by the electron source before detection; therefore, MW = m/z value – 1 for neutral molecules. Known assignments: internal standard (Quinine, neutral, m/z = 325.19, MW = 324.42 g/mol), tetrabutylammonium (charged, m/z = 242.3, MW = 242.5 g/mol), tributylamine (neutral, m/z = 186.2, MW =185.4 g/mol). Additional structures that may correspond to the unassigned m/z value shown in this figure are listed in Figure D-11. MW = molecular weight

Therefore, we hypothesize that tributylamine can react with oxygen (or Li_2O_2) to form a tributylamine oxide intermediate. The amine oxide, when formed, can react with Li_2O_2 to release Li^+ and O_2. This reaction between the amine oxide intermediate and Li_2O_2 is responsible for the Li_2O_2 oxidation observed after charging in the XRD and SEM data (Figures 5-4 and 5-5). It is also possible that the generated nitroxide (from alkyl radical loss) can also react with Li_2O_2 to oxidize it as a similar nitroxide – 2,2,6,6-tetramethylpiperidinyloxyl (TEMPO) – has been shown to oxidize Li_2O_2 during charging.[146] The mechanism shown in Schematic 5-2 explains our observations, but cannot encompass all the possible decomposition products formed as tertiary amine oxides are known to structurally rearrange to yield other products.[151] The extra ^1H NMR peaks observed in O_2 (not including the tributylamine peaks) could be due to decomposition

products that result from the amine oxide reaction with Li_2O_2, Cope elimination etc. Whereas in argon, only tributylamine is present, because the lack of O_2 or Li_2O_2 in the argon cells preclude the formation of tributylamine oxide and the presence of additional peaks. To test this hypothesis, we mix trimethylamine oxide (as proxy for tributylamine oxide) with Li_2O_2 in acetonitrile and the characteristic yellow color was observed; a color observed electrochemically (after cycling) in our experiments and by Hoh *et al.*[150] in the mixture of tertiary amine with H_2O_2 at higher temperatures. New peaks also arise in the NMR spectra (Figure D-10). Therefore, next-generation Li–O_2 cells can be fabricated to include amine oxides as a tool to reduce Li_2O_2 charging voltages. Unfortunately, the amine oxide – once formed – cannot revert to the original TBA to make this system an ideal redox mediator.

The electrochemical-induced decomposition of TBA is irreversible, and as Mousavi *et al.*[154] recently reported, changing the chain length, type of branching, and size on the ammonium may not improve the electrochemical stability.

5.4 Conclusions

We have shown that Li–O_2 discharge and charge can occur in the absence of lithium-based salts. Ammonium-based electrolytes in the presence of lithium metal can support the formation of Li_2O_2 during discharge, where TBA can temporarily complex superoxide in solution before Li ions from the oxidized lithium metal anode combines to form Li_2O_2. During charge, TBA-based electrolytes can lead to charging voltages below 4 V at low current rates, leading to a 0.5 V improvement over $LiClO_4$-based electrolytes. TBA concentration and solvent type (ether vs DMSO) was also studied, and shown to influence the observed discharge and charge performance. Furthermore, we proposed a mechanism to explain the ability of TBA to support Li_2O_2 oxidation. Electrochemically-induced degradation of TBA occurs at 3.55 V to form a tertiary amine that can react with oxygen (or Li_2O_2) to form an amine oxide; the amine oxide reacts with Li_2O_2 in a faster reaction to release O_2 and Li^+. Unfortunately, TBA decomposition is irreversible. We have shown TBA can support discharge and charge in Li–O_2 cells, and amine oxides can oxidize Li_2O_2 in Li–O_2 cells. Knowledge gained from this work should allow for development of newer salts and broaden our understanding of Li_2O_2 oxidation mechanisms.

5.5 Acknowledgments

This work was supported in part by the Samsung Advanced Institute of Technology (SAIT), and the facilities at the Koch Institute for Integrative Cancer Research. C.V.A is supported by the US Department of Defense (DoD) through the National Defense Science and Engineering Graduate (NDSEG) Fellowship, and the Alfred P. Sloan Foundation's Minority PhD Program. This work made use of the Shared Experimental Facilities supported by the MRSEC Program of the National Science Foundation under award number DMR- 1419807. The authors also thank Professor Yang Shao-Horn for providing access to her laboratory and equipment, and Li Li for performing the Q-TOF experiment and helpful discussion.

Chapter 6

Evaluation and Stability of PEDOT Polymer Electrodes for Li–O_2 Batteries

Adapted from Chibueze V. Amanchukwu, Magali Gauthier, Thomas P. Batcho, Chanez Symister, Yang Shao-Horn, Julio M. D'Arcy, and Paula T. Hammond. "Evaluation and stability of PEDOT electroactive polymer electrodes for Li-O_2 batteries." *J. Phys. Chem. Lett.* 2016, 7, 3770-3775.

6.1 Introduction

Lithium-air (O_2) batteries have shown promise as one of the energy-dense storage media of the future.[12,16] With a theoretical energy density (3500 Wh kg^{-1}_{Li2O2})[12] an order of magnitude greater than Li-ion, the quest for commercial Li–O_2 batteries has spurred great research interest. Despite their promise, Li–O_2 batteries have been plagued with numerous challenges such as the instability of the electrode and electrolyte, slow oxygen reduction and evolution kinetics, poor capacity retention with cycling and low cycle life.[16,24,28] Commonly used electrodes such as carbon have been shown to be unstable in the presence of lithium peroxide (Li_2O_2) – the desired discharge product – and superoxide intermediates during cycling.[35,44] Decomposition of carbon leads to insulating products such as lithium carbonate (Li_2CO_3) that are difficult to oxidize during charge and require high overpotentials.[35] Other cathodes such as nanoporous gold,[20] carbides[110] and inorganic metal oxides,[155] among others have been studied to replace carbon during Li–O_2 battery operation. Efficient cathodes for Li–O_2 need high surface area, good electronic conductivity, and low cost. Some electrode materials that may present these desirable properties include carbides and inorganic metal oxides; however, the limited surface area of these systems, and the cost of precious relatively inert metals such as gold limit their wide applicability in Li–O_2 batteries. Electron-conducting polymers are attractive as they have the desired electrode properties and are very easily processed into different cathode structures. Despite the numerous cathode types examined for Li–O_2, only few reports examining electron-conducting polymers for Li–O_2 cathodes exist.

Conducting polymers such as poly(3, 4-ethylenedioxythiophene) (PEDOT),[156] poly(pyrrole),[157] and poly(aniline) have been widely explored as electrodes or electron-conducting binders for traditional Li-ion batteries. Typical binders such as poly(vinylidene fluoride) (PVDF) and polytetrafluoroethylene (PTFE) are not electronically conducting, and are used to bind composite electrodes. Poly(pyrrole) served as both binder and electron conductor with a $LiMn_2O_4$ cathode,[157] and PEDOT has been used to eliminate the conventional carbon electron conducting matrix.[158] Furthermore, coating active electrode materials such as lithium cobalt oxide ($LiCoO_2$) and iron oxyfluoride (FeOF) with PEDOT can improve kinetics and limit the degradation and side reactions between the active material and the electrolyte solvent.[159,160] This strategy could be promising for Li–O_2 batteries where most organic insulating polymer binders such as PVDF

have been shown to be unstable, as the ability of these conducting polymeric materials to transport electrons eliminates the need for further additives. [26,28]

Cui *et al.*[38] studied tubular poly(pyrrole) as an electrode for Li–O_2 batteries, and show formation of lithium peroxide and charge/discharge over multiple cycles. Yoon *et al.*[40] recently reported the use of PEDOT:PSS (polystyrene sulfonate) to coat a graphene electrode and claim that PEDOT:PSS can suppress undesirable side reactions in the Li–O_2 cell and improve cycling performance. Nasybulin *et al.*[39] studied a Super P carbon/PEDOT composite as an electrode for Li–O_2 batteries, but the discharge performance and electrochemistry was dominated primarily by the carbon, and their use of a sulfone-containing salt like LiTFSI (lithium bis(trifluoromethane)sulfonimide) prevented a thorough understanding of PEDOT decomposition. The electron-conducting PEDOT was not evaluated as a stand-alone electrode despite its high electronic conductivity; serving primarily as a binder and contributing at most five percent of the obtained capacity.[39] In addition, these aforementioned studies did not explore the stability and mechanisms of degradation of the electron-conducting polymer upon cycling in Li–O_2 cells.

In this work, we examine the performance of a free-standing microstructured PEDOT electrode (with no carbon or binders present) in a Li–O_2 battery and show that it can support lithium peroxide formation and Li–O_2 cycling. Our use of $LiClO_4$ as the electrolyte salt instead of LiTFSI allows for a clear understanding of the changes in the PEDOT structure. We show that the thiophene ring in PEDOT is susceptible to degradation that leads to sulfone formation, loss of conjugation in the polymer chain and diminished electronic conductivity that leads to poor cycling. Knowledge gained from this work can allow for greater understanding of the feasibility of using electron-conducting polymers as stand-alone Li–O_2 cathodes, and devising moieties that can avoid the observed degradation pathway of PEDOT. In addition, electron-conducting polymers could be used to coat cheap carbon particles to direct current and limit carbon reactivity and degradation in Li–O_2 cells.

6.2 Experimental Methods

6.2.1 Synthesis of PEDOT electrode

The free-standing PEDOT electrode was synthesized as previously reported in ref ([161]) using an evaporative vapor-phase polymerization procedure. In a chemical vapor deposition (CVD) chamber, a droplet of $FeCl_3$ aqueous oxidant solution is placed on a gold-coated substrate. An EDOT in chlorobenzene solution is also introduced into the chamber, and the temperature is ramped from 25 °C to 130 °C at 600 °C/h for polymerization to occur. The PEDOT is removed from the chamber, washed with water and methanol to remove excess oxidant, and stored in 6 M HCl. To prepare for Li–O_2 use, the electrodes were washed in copious amounts of milliQ water (18 mΩ cm) before washing with methanol. The electrodes were then vacuum-dried at 75 °C for at least two nights. The PEDOT electrode was soaked in excess 0.1 M $LiClO_4$ in DME electrolyte prior to cell fabrication.

6.2.2 Fabrication of Li–O_2 cell

Li–O_2 cells were fabricated in an Argon glovebox (MBRAUN, H_2O < 0.1 ppm, O_2 < 0.1 ppm). Using Li–O_2 cells fabricated in our laboratory,[22] 15 mm lithium metal (Alfa Aesar, 99.9% metals basis) was used as the anode, a 0.1 M $LiClO_4$ in DME electrolyte (BASF), two 18 mm Celgard C480 separators, and the PEDOT electrode. A stainless steel mesh (12.7 mm diameter) was used as the current collector. After fabrication, the Li–O_2 cell was moved without air exposure to another Argon glovebox (MBRAUN, H_2O < 0.1 ppm, O_2 < 1%) where it was filled with oxygen. The fabricated Li–O_2 cell was allowed to rest for 4 hours before any electrochemical tests were performed. After the electrochemical tests, the Li–O_2 cell was opened in an Argon glovebox without air exposure, and the PEDOT electrodes were stored.

6.2.3 Scanning Electron Microscope (SEM) characterization

Samples were imaged using a Zeiss Supra 55VP and a Zeiss Ultra 55 (Carl Zeiss AG, Germany). The working voltage was 5kV. Samples were mounted and sealed in an Argon glovebox in order to minimize the time (~< 5 sec) of exposure to ambient atmosphere during transfer into SEM.

6.2.4 X-ray diffraction characterization

Electrochemically-tested cells were opened in an Argon glovebox (MBRAUN, H_2O < 0.1 ppm, O_2 < 0.1 ppm) without air exposure. Samples were sealed in an airtight XRD sample holder (Anton Paar, Austria) to minimize air exposure before and during XRD measurement. A Rigaku

Smartlab (Rigaku, Salem, NH) in the parallel beam configuration was used to collect the XRD spectra.

6.2.5 X-ray photoelectron spectroscopic (XPS) characterization

To avoid any exposure to air, samples were transferred from the glovebox to the XPS chamber using a sample transfer vessel (ULVAC-PHI, INC.) Spectra were collected with a PHI 5000 VersaProbe II (ULVAC-PHI, INC.) using a monochromatized Al K_α source, a pass energy of 23.5 eV and a charge neutralizer. All spectra were calibrated with the C1s photoemission peak of adventitious carbon at 285 eV. Photoemission lines were fitted using combined Gaussian-Lorentzian functions after subtraction of a Shirley-type background.

6.3 Results and Discussion

The free-standing PEDOT films examined in this work were fabricated using an evaporative vapor-phase polymerization technique that generates the film directly from the substrate under conditions that yield fibrils of polymer film with nano- and microscale architectures.[161] Other fabrication methods such as in-situ deposition polymerization[162] or chemical vapor deposition (CVD)[37] can also yield PEDOT films with select architectures and high electronic conductivity. Furthermore, the examined PEDOT films lack the PSS polymer often used to acidically dope the polymer and aid its solubility in aqueous solutions and some organic emulsions. The use of a PEDOT-only electrode avoids addition of functionalities (such as PSS) that may complicate the understanding of PEDOT activity and the monitoring of changes induced by Li–O_2 reactions. The doped PEDOT films generated in this work have high electronic conductivity (130 S cm^{-1}), and have been fully characterized by D'Arcy *et al.*[161] The nanofibrillar architecture with high aspect ratio also makes it promising for Li–O_2 use because it will provide abundant nucleation sites for Li_2O_2 growth.

The ability of PEDOT to support crystalline Li_2O_2 formation after discharge without the addition of catalyst or other electron conducting media such as carbon was explored. Using lithium metal as the anode and a 0.1M $LiClO_4$ in DME electrolyte, PEDOT was able to support Li–O_2 discharge with a discharge plateau at 2.6 V reminiscent of the voltage at which oxygen reduction occurs with other Li–O_2 battery electrodes (Figure 6-1a).[34] Winter-Jensen *et al.*[163] have

previously shown that the PEDOT surface is capable of supporting oxygen reduction, albeit in aqueous media. In conventional Li–ion batteries where PEDOT was evaluated as the electrode, low discharge capacities were observed because of poor intercalation of lithium ions. However, for Li–O_2 batteries, PEDOT does not need to intercalate lithium, but provide an electronically conducting surface that can support the diffusion and adsorption of O_2 and its subsequent reduction. X-ray diffraction (XRD) of the discharged electrode (Figure 6-1b) shows that Li_2O_2 is the primary discharge product, as evident from the (100) and (101) crystalline peaks.[34,59] Furthermore, using scanning electron microscopy (SEM), one can observe the toroidal morphology associated with Li_2O_2 formation along the walls of the PEDOT electrode (Figure 6-1c).[34,59]

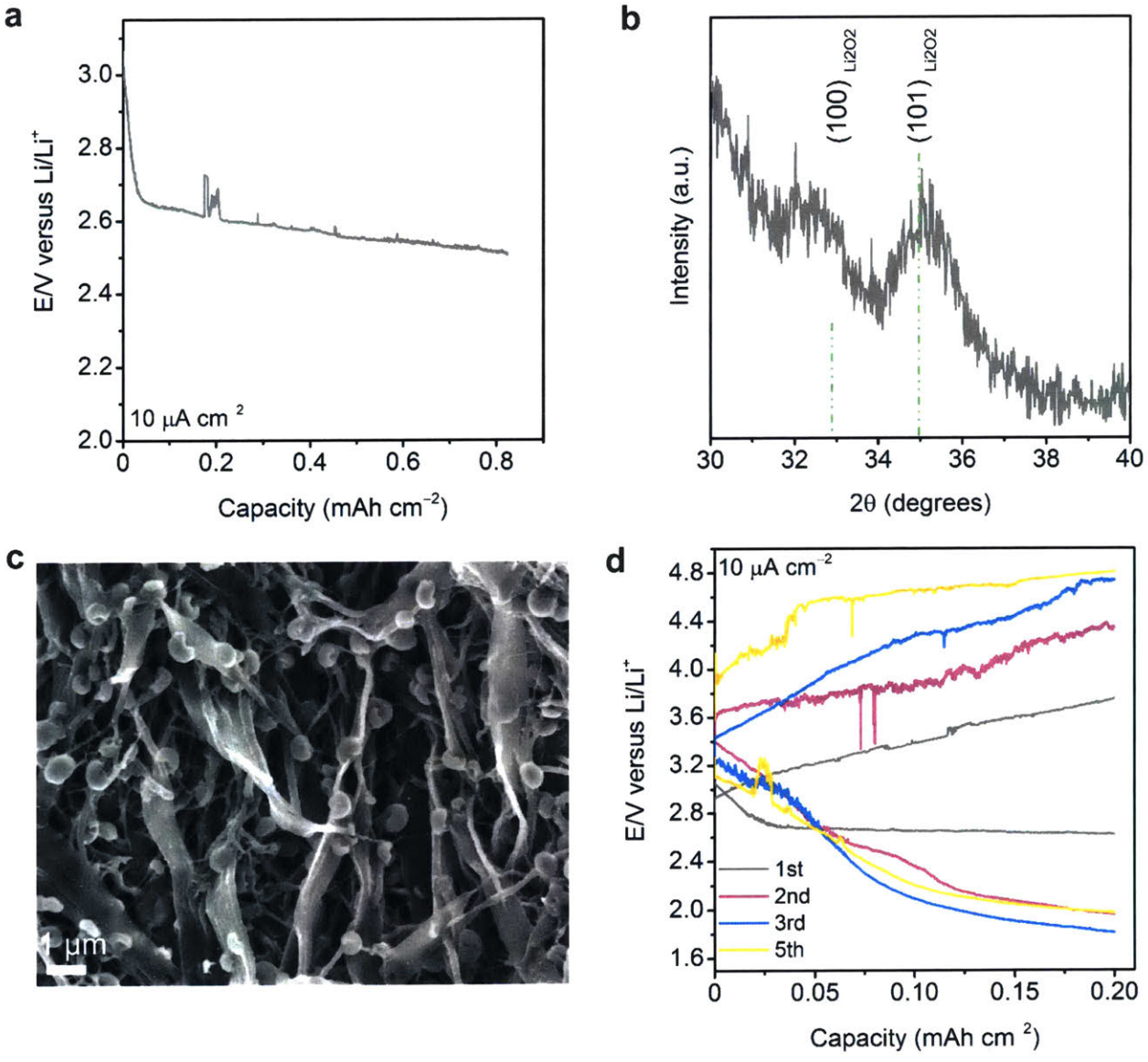

Figure 6-1 | Electrochemical and spectroscopic characterization of PEDOT electrodes in Li–O_2 batteries. (a), Discharge curve of a Li–O_2 cell in O_2 at 10 μA cm^{-2} using a free-standing PEDOT electrode; (b), x-ray diffraction (XRD) and (c), Scanning electron microscopy (SEM) image after one discharge with a free-standing PEDOT electrode; (d) Five cycles at 10 μA cm^{-2} in O_2 using a free-standing PEDOT electrode. Figure 6-2a shows an SEM image of a pristine PEDOT electrode. Electrolyte: 0.1M $LiClO_4$ in DME.

Next, the PEDOT Li–O_2 cell was cycled five times using a capacity-limited regime at 0.2 mAh cm^{-2} (Figure 6-1d). The first discharge is similar to that observed in Figure 6-1 with the 2.6 V discharge voltage. The first charge is completed below 4 V, which is promising because typical carbon-based electrodes have higher charging potentials above 4 V and low energy efficiencies. Although the charging overpotential in the first cycle is low, subsequent cycling leads to higher discharge and charge overpotentials. By the fifth cycle, the discharge plateau is at 1.6 V and the charge culminates at 4.8 V.

SEM (Figure 6-2) was used to track the changes in the PEDOT architecture that may explain the poor cycling in Figure 6-1d. Figures 6-2a and b show a pristine and discharged electrode, respectively. As expected, toroids are abundant along the PEDOT network. After the first charge, Figure 6-2c shows disappearance of the Li_2O_2 toroids, revealing the original PEDOT structure. Therefore, PEDOT can support Li_2O_2 formation and oxidation in at least one cycle. By the fifth cycle, agglomerates are observed (Figure 6-2d) that may be due to an accumulation of decomposition from DME and PEDOT. DME is known to be unstable during Li–O_2 cycling,[19,44,45] and prone to electrochemical oxidation above 4 V. The high charging voltages needed to complete charging on the PEDOT electrode may thus exacerbate the degradation of DME. Accumulation of insulating decomposition products such as Li_2CO_3 and acetates,[44] may then passivate the PEDOT surface, preventing oxygen reduction in subsequent cycles.

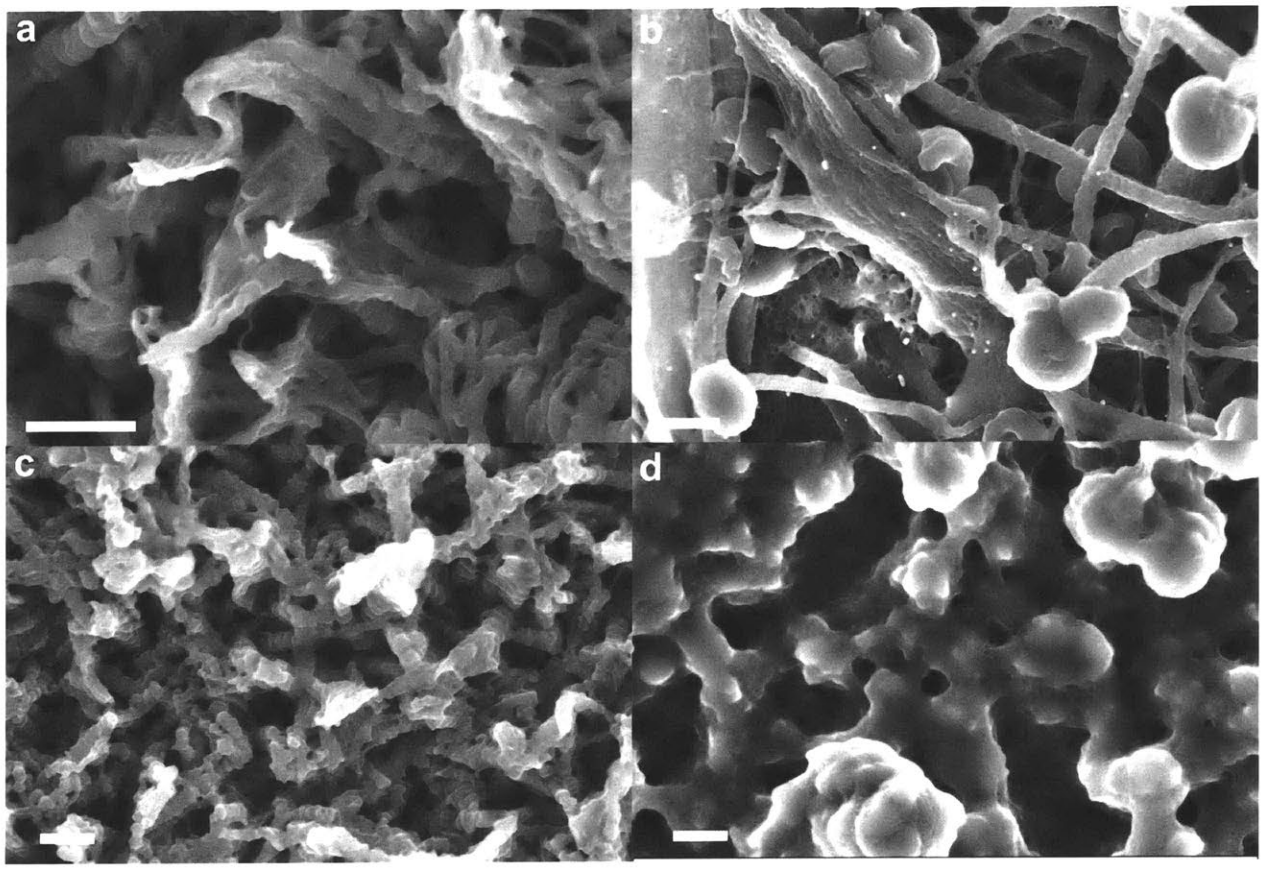

Figure 6-2 | SEM characterization of PEDOT films before and after Li–O_2 electrochemistry. SEM images of pristine PEDOT electrode before discharge (a), after one discharge (b), one cycle (c), and five cycles (d). The free-standing PEDOT electrodes were discharged and charged at 10 μA cm^{-2} in O_2 in a 0.1M $LiClO_4$ in DME electrolyte. Scale bar = 500 nm.

To understand the stability of PEDOT, X-ray photoelectron spectroscopy (XPS) was used. Although electrochemical reduction to superoxide and consequently peroxide can occur on the PEDOT surface, these species are highly nucleophilic and can chemically attack PEDOT. Figure 6-3 shows C (1s), S (2p), and O (1s) spectra of the pristine PEDOT electrode and the electrode after 1 discharge, 1 cycle (ending on charge), and 5 cycles (ending on charge). The S (2p) spectra in Figure 6-3 show significant changes in the chemical environment of the S atom in PEDOT. As cycle number increases, the fraction of the higher binding energy peaks at ~169 ($S2p_{3/2}$) and ~170 eV ($S2p_{1/2}$) (relative to the original PEDOT peaks) increases. The shift to higher binding

energy is due to sulfur atoms bound to a more electronegative atom like oxygen and those peaks have been attributed to sulfone.[164] Marciniak *et al.*[164] have shown that the PEDOT S atom can be attacked due to photooxidation and Verge *et al.*[165] have observed attack of the S atom in the presence of hydroxyl radicals.[165] Superoxide and peroxide anions are strong nucleophiles like hydroxyl, and may undergo similar reaction pathways with PEDOT (Figure 6-4).

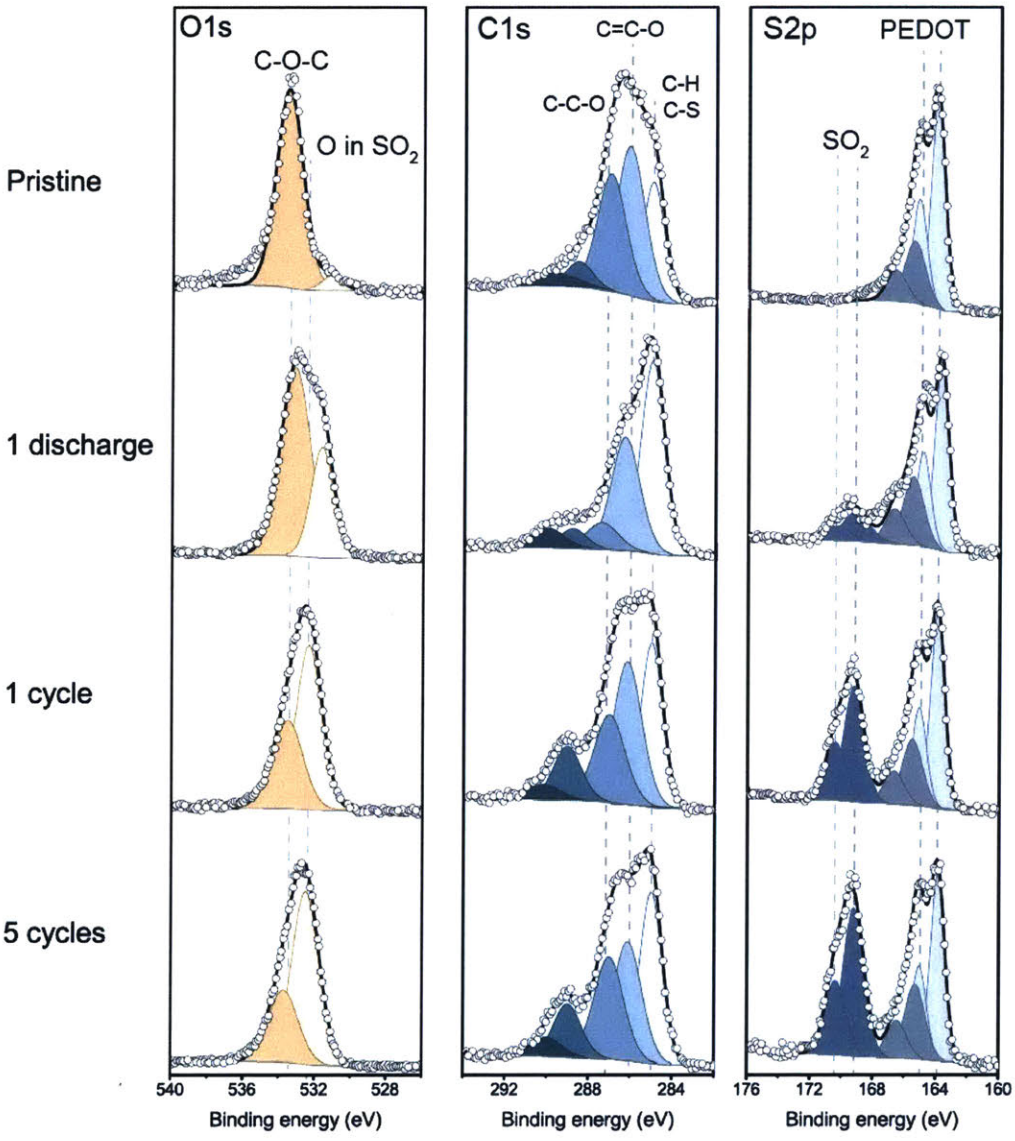

Figure 6-3 | XPS characterization of PEDOT films before and after Li–O_2 electrochemistry. X-ray photoelectron spectroscopy (XPS) at the C (1s), O (1s) and S (2p) of a pristine PEDOT electrode, after one discharge, one cycle (ending on charge), and five cycles (ending on charge).

The XPS spectra corresponds to the SEM images displayed in Figure 6-2. Details of the XPS deconvolution can be found in Table E-1.

The O (1s) spectra corroborate the observation in the S (2p) spectra. The fraction of the peak at 532 eV (compared to the total peak area) increases with cycling (Figure 6-5) and constitutes further evidence of the formation of a sulfone functionality. In addition, the O/S ratio provides a gauge of PEDOT oxidation because an increase in the ratio indicates oxygen external to PEDOT has been incorporated on the PEDOT surface or chemical structure. After the first discharge, Li_2O_2 is observed as expected at around 531 eV in the O (1s) spectra[166] in Figure 6-3, and may account for the high O/S ratio observed in Table E-2. However, with subsequent cycling that ends on charge, the O/S ratio is still higher than that observed in the pristine electrode and indicative of sulfone formation and oxygen-based DME decomposition species. The peak increase at 289 eV in the C (1s) spectra was postulated to be due to the formation of carbonyl/carboxyl groups on PEDOT or from DME oxidation or a shift due to the oxidized thiophene ring.[164] As Figure 6-5 shows, the fraction of oxidized products in the O (1s), C (1s), and S (2p) spectra increases with cycling.

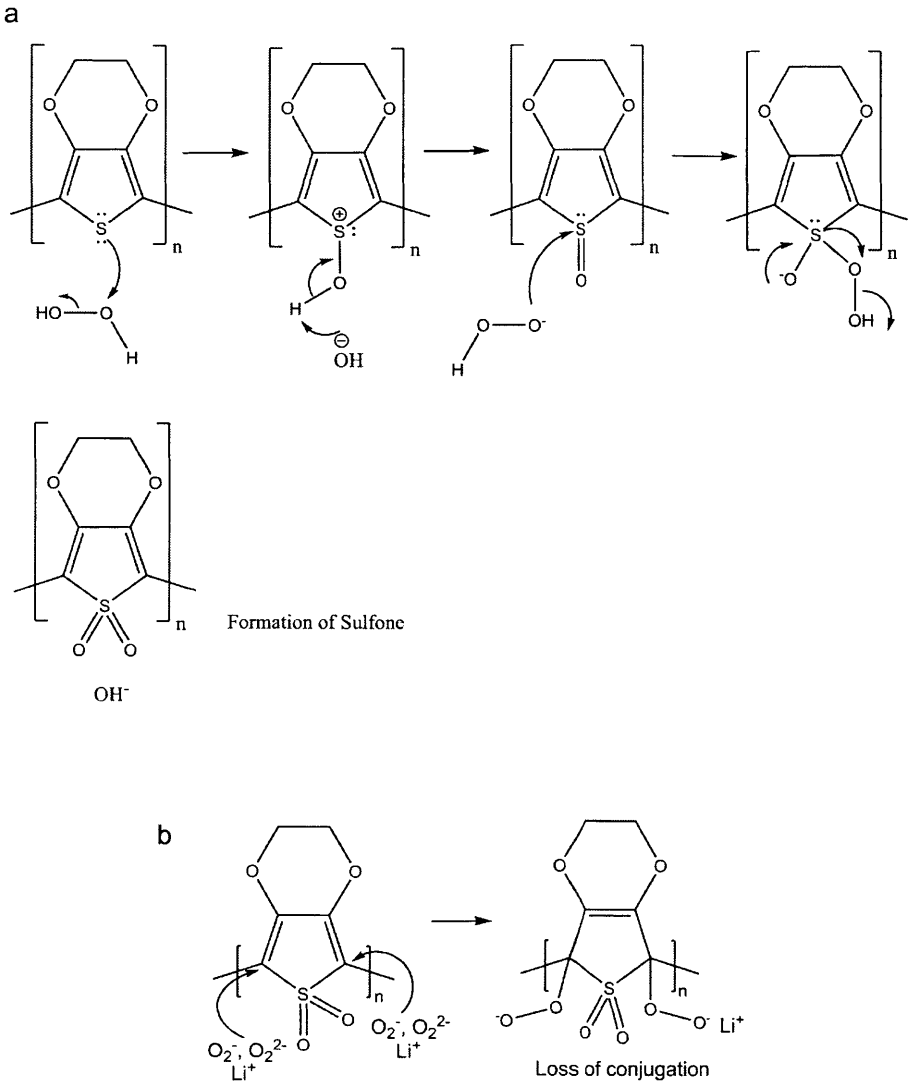

Figure 6-4 | Proposed Mechanism of PEDOT decomposition. Proposed mechanism for the reaction of H_2O_2 (through possible reaction of Li_2O_2 with ether electrolyte or residual water) with PEDOT that leads to formation of sulfone functionality. Although we show the mechanism with H_2O_2, Li_2O_2 can possibly react with the same pathway. (b) Further reaction of the sulfone that leads to loss of conjugation and diminished electron conductivity. The counter-ion for all the negatively charged species in the schematic is lithium.

In Figure 6-4, we propose a mechanism for PEDOT degradation where oxygen reduction products from discharge and charge attack the partially positive S atom on the thiophene ring. A sulfoxide unit results and further addition to the S atom leads to formation of sulfone. Other sites on the PEDOT chemical structure can also be attacked as Verge *et al.*[165] show that OH radicals can oxidize the C–S–C bond. The formation of the sulfone functionality on the PEDOT ring is an irreversible chemical change, and has been shown to lead to cleavage of the polymeric chain and a loss of conjugation.[164,165] Conjugation across the polymer backbone is responsible for electron conduction; therefore, the loss of conjugation decreases electronic conductivity, and may explain the inability of PEDOT to sustain further oxygen reduction after the first cycle (Figure 6-1d).[167,168]

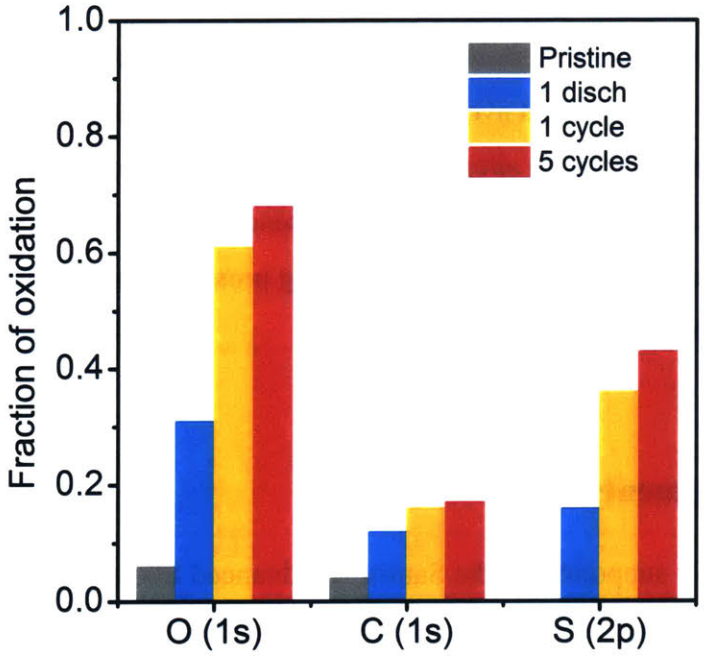

Figure 6-5 | Fraction of oxidation due to Li–O_2 cycling. Fraction of oxidation products in the XPS O (1s), C (1s), and S (2p) spectra for the pristine PEDOT electrode, electrode after 1 discharge, 1 cycle (ending on charge), and 5 cycles (ending on charge). These fractions correspond to the XPS data in Figure 6-3. O (1s) fraction of oxidation = (532 eV peak area/ total peak area); C (1s) fraction of oxidation = (289 and 290 eV peak area/ total peak area); S (2p)

fraction of oxidation = (169 and 170 eV peak area/ total peak area). The S (2p) spectra for the pristine has no peaks at 169 and 170 eV and has a "0" fraction.

6.4 Conclusions

In this work, we examined the performance of PEDOT as a stand-alone electrode in a Li–O_2 battery. We show that the conducting polymer PEDOT can initially support Li–O_2 discharge and charge with the formation and oxidation of Li_2O_2 respectively. However, after several discharges and charges, irreversible changes occur on PEDOT that lead to the oxidation of the thiophene ring and formation of sulfone, cleavage of segments of the polymer that lead to loss of conjugation and electronic conductivity; these changes result in poor cycling behavior. Therefore, the use of PEDOT is limited for binder or electrode use in Li–O_2 batteries. Knowledge gained from this work should galvanize the Li–O_2 community in developing new electronic conducting polymers that avoid the susceptibility of PEDOT S atom oxidation and loss of conjugation, and provide an alternative to the carbon and inorganic electrodes that have been heavily studied so far. These findings are important in the search for new Li–O_2 electrodes, of which electron-conducting polymers are an exciting prospect, and the physical insights related to PEDOT decomposition are significant and urgent.

6.5 Acknowledgments

This work was partially supported by the Samsung Advanced Institute of Technology (SAIT), and the facilities at the Koch Institute for Integrative Cancer Research. C.V.A is supported by the Department of Defense through the National Defense Science and Engineering Graduate (NDSEG) Fellowship, and the GEM Fellowship. T.B.P is supported by the Skoltech Electrochemical Center. SEM was performed at the Center for Nanoscale Systems (CNS) at Harvard University.

Chapter 7

Summary and Perspectives

7.1 Summary

In **Chapter 2**, we synthesized a silicon-tripodand solid state siloxane polymer and studied its thermal and ionic conductivity properties as a function of lithium salt type and content. Furthermore, mesoporous silica additive was added to reduce ion-ion interactions and modify the glass transition temperature (T_g) and ionic conductivity. The siloxane polymer film was incorporated into a Li–O_2 battery and shown to support discharge. However, we use nuclear magnetic resonance (NMR) spectroscopy to show that the Si–O–CH_2 bond is unstable. To understand what nucleophile is responsible for the instability, we make a chemical mixture of Li_2O_2 (the desired Li–O_2 battery discharge product) with the siloxane polymer and show that Li_2O_2 can react with Si–O–CH_2 in the same manner as observed electrochemically.

Therefore, the chemical mixture of Li_2O_2 with the polymer can serve as a proxy to understanding polymeric stability in actual Li–O_2 cells. Instead of fabricating Li–O_2 cells to understand stability, one could use chemical mixtures with commercial Li_2O_2. In **Chapter 3**, we selected a group of polymers that have been heavily studied for Li-ion and Li-air batteries. We showed that two parameters seem to govern the instability of the polymers studied: (i) the presence of highly electron-withdrawing/electrophilic functional groups on the polymer side chain, and (ii) the presence of hydrogen atoms that are adjacent to the aforementioned electron-withdrawing groups. Polymers such as poly(acrylonitrile) (PAN), poly(vinyl chloride) (PVC), poly(vinylidene fluoride) (PVDF), poly(vinylidene fluoride-co-hexafluoropropylene) (PVDF-HFP), and poly(vinyl pyrrolidone) (PVP) are reactive and unstable in the presence of Li_2O_2. On the other hand, the polymers poly(tetrafluoroethylene) (PTFE), Nafion®, and poly(methyl methacrylate) (PMMA) appear stable against nucleophilic Li_2O_2 attack. The lack of labile hydrogen atoms and the poor leaving nature of the fluoride group allows for the stability of PTFE and Nafion®, while the methyl and methoxy functionalities in PMMA reduce the number of potential reaction pathways for Li_2O_2 attack in PMMA.

Since PEO and other smaller molecule ethers have been shown to be susceptible to auto-oxidation and degradation in oxygen, the use of solid polymer electrolytes (SPEs) is limited. Almost all SPEs depend on the ether functionality for ionic conduction. Therefore, this necessitated a shift to gel polymer electrolytes (GPEs) that decouple mechanical stability and ionic conductivity. In **Chapter 4**, we fabricated GPEs where PMMA provides mechanical

stability, and an ionic liquid (IL)/lithium salt mixture provides ionic conductivity. We fabricate free-standing flexible GPE films and show that the lithium/ionic liquid cation molar ratio in the GPE modulates the thermal and ionic conductivity properties. Also, we show that when the Li/IL molar ratio is > 1, low ionic conductivity and low discharge capacities are obtained. When 0 < Li/IL molar ratio < 1, two discharge plateaus are observed where the first plateau at around 2.5 V is a function of lithium ion content, and the second plateau is a function of ionic liquid cation type. The first plateau is a 2 mol e^-/mol O_2 reduction process and the second a 1 mol e^-/mol O_2 process. Our work was the first time this switching behavior was shown, and was only observed using a GPE. When an ionic liquid/salt electrolyte is used without the polymer present, this switching process is not observed. We used UV-Vis, electron paramagnetic resonance (EPR), and X-ray photoelectron spectroscopy (XPS) to confirm the formation of ionic liquid-superoxide complexes as the discharge product. Scanning electron microscope (SEM) indicates that these complexes may be solid. To broaden the scope of the work, we fabricated non-aqueous cells that incorporate tetrabutylammonium (TBA) salt to mimic the ionic liquid behavior in the GPE. In **Chapter 5**, we show that TBA dissolved in ether or dimethyl sulfoxide (DMSO) with a lithium metal anode can be used to support discharge and charge in Li–O_2 batteries without a lithium salt present. Using X-ray diffraction (XRD) and Raman spectroscopy, we showed that Li_2O_2 is the discharge product despite the lack of dissolved lithium salt. Hence, the lithium ions originate from the oxidized lithium metal anode. During charge, we show that the TBA-ether electrolytes lead to a > 0.5 V reduction in charging overpotentials. In addition, we show that in contrast to lithium salts, TBA electrolytes support Li_2O_2 oxidation during charging. Finally, we use NMR and quadrupole time-of-flight (Q-TOF) mass spectrometry to understand the charging process. We show that during charging, electrochemical-induced transformation of TBA to tributylamine occurs at > 3.55 V, and reaction with O_2 or Li_2O_2 leads to a tributylamine oxide intermediate that reacts with and oxidizes Li_2O_2.

In **Chapter 6**, we used a free-standing PEDOT polymeric electrode as the cathode for Li–O_2 batteries, and show for the first time that PEDOT can support oxygen reduction in a non-aqueous setting to form Li_2O_2. Because we have free-standing PEDOT films that do not contain polystyrene sulfonate (PSS), we used XPS to show that sulfone functionalities form on the PEDOT backbone with increased cycling. PEDOT degradation may lead to chain cleavage that hampers electron conductivity and lead to poor cycling.

7.2 Perspectives

In **Chapter 3**, although we developed a screening procedure to understand the chemical stability of polymers by using chemical mixtures of polymer and Li_2O_2, more work could be done on understanding the effect of polymer molecular weight, polymer morphology (e.g., crosslinked network, block copolymer) on the rate of reaction with Li_2O_2. Could polymeric structures where vulnerable functional groups are hidden in a core-shell like morphology reduce side reactions? The work in **Chapter 3** was done at room temperature and in an inert atmosphere. The influence of temperature, oxygen, and superoxide (KO_2) was not explored, and can provide insight especially for polymers deemed to be stable. For example, poly(methyl methacrylate) (PMMA) was found to be stable in contact with Li_2O_2 at room temperature. However, we found that adding KO_2 to a PMMA/ Li_2O_2 mixture and performing the reaction at 60 °C leads to decomposition.

Furthermore, experimental screening procedures can be time consuming. Therefore, computational tools such as density functional theory (DFT) will be vital. DFT could be used to compute activation energy barriers, reaction free energies, deprotonation energies as a function of functional group type and molecules of interest that are attached to a polymeric chain. Knowledge/trends obtained using computational tools can then be verified experimentally. Some of the molecules determined to be stable may not be commercially available. Hence, more synthetic chemists are needed to join the Li–O_2 community to fabricate new compounds and polymers.

The gel polymer electrolyte (GPE) system discussed in **Chapter 4** showed the ability to use the electrolyte to control the discharge and charge process in Li–O_2 batteries. The ability to decouple mechanical stability from ionic conductivity in GPEs increases the number of polymers that can be studied. However, more stable ionic liquids (or small molecules) and polymers are needed. The oxygen solubility and lithium ion conductivity/diffusivity of ionic liquids also need to be improved. These improvements can lead to an increase in current rates and discharge capacities.

Despite the focus of my work on polymeric systems, the development of inorganic ionically-conductive ceramic membranes is vital. These membranes can be chemically stable against

peroxide and superoxide attack. However, their stability in contact with lithium metal needs to be improved; although an ionically conducting polymer can be used at the anode-ceramic interface. Deposition tools such as atomic layer deposition (ALD) and pulsed laser deposition (PLD) can also be used to reduce the interfacial resistance and improve kinetics and transport across the cell.

Knowledge gained from this thesis can be used in other battery chemistries. For example, the siloxane polymer studied in **Chapter 2** has room temperature ionic conductivities greater than the ubiquitous PEO at room temperature. Although, we show the siloxane polymer to be unstable in Li–O_2 because of the labile Si–O–CH_2 and ether linkages, the Si–O–CH_2 can easily be changed to Si–CH_2–O–CH_2, and the lack of mobile superoxide and peroxide species in lithium-metal, lithium-ion, and silicon-anode batteries etc. can lead to elimination of flammable and unsafe volatile electrolytes currently used.

My PhD thesis sought to accomplish two things: 1) Develop new materials (polymers, additives) for lithium-air batteries, and 2) Study the performance and reaction mechanisms of Li–O_2 devices incorporating these materials, and the degradation pathways the materials can undergo. Coupling fundamental understanding with material selection can empower the design of next generation Li–O_2 batteries.

Appendix A

Table A-1. Average ionic conductivity of the silicon tripodand films as a function of LiTFSI salt content and silica content. All the silica-containing films have 10 wt% LiTFSI.

	Average Ionic Conductivity (S/cm)				
LiTFSI salt wt%	80 °C	60 °C	50 °C	40 °C	25 °C
10	2.0E-04	1.3E-04	9.0E-05	7.3E-05	4.6E-05
15	2.7E-05	1.6E-05	1.2E-05	8.7E-06	5.8E-06
20	1.6E-05	9.6E-06	7.7E-06	5.2E-06	3.2E-06

	Average Ionic Conductivity (S/cm)				
Silica wt%	80 °C	60 °C	50 °C	40 °C	25 °C
0	2.0E-04	1.3E-04	9.0E-05	7.3E-05	4.6E-05
2	2.0E-05	1.1E-05	8.9E-06	6.5E-06	4.0E-06
8	3.0E-05	2.0E-05	1.4E-05	6.9E-06	6.5E-06

Table A-2. Glass transition temperatures obtained from Differential Scanning Calorimetry (DSC) measurements as a function of LiTFSI salt content and salt content. All the silica-containing films have 10 wt% LiTFSI.

LiTFSI salt wt %	Tg (°C)
10	<−90
15	−83
20	−74

Silica wt%	Tg (°C)
0	<−90
2	−74
4	−80
8	−84

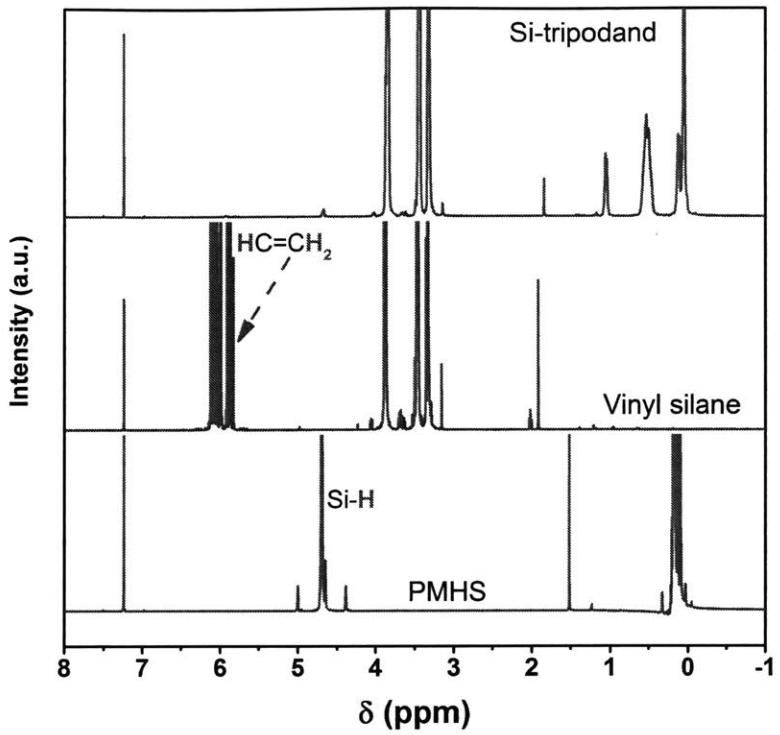

Figure A-1. ^{1}H NMR characterization of polymethylhydrosiloxane (PMHS), tris(2-methoxyethoxy)(vinyl)silane and the synthesized product (Si-tripodand). ^{1}H NMR (400 MHz; $CDCl_3$; residual $CHCl_3$ reference)

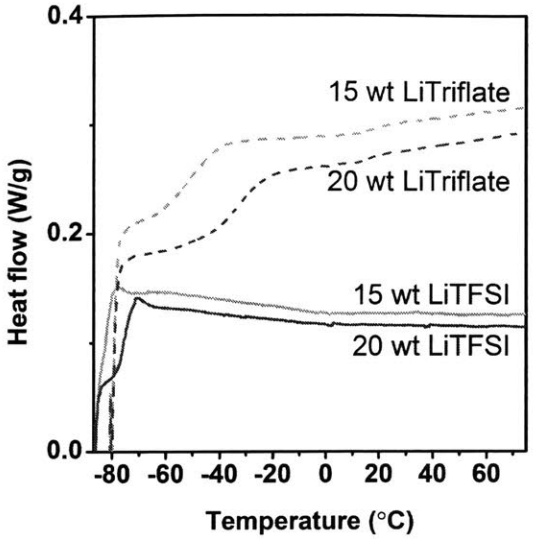

Figure A-2. DSC spectra of 15 and 20 wt% lithium triflate and LiTFSI where the Si-trip/triflate films lead to glass transition temperatures greater than the Si-trip/LiTFSI films at similar salt concentrations.

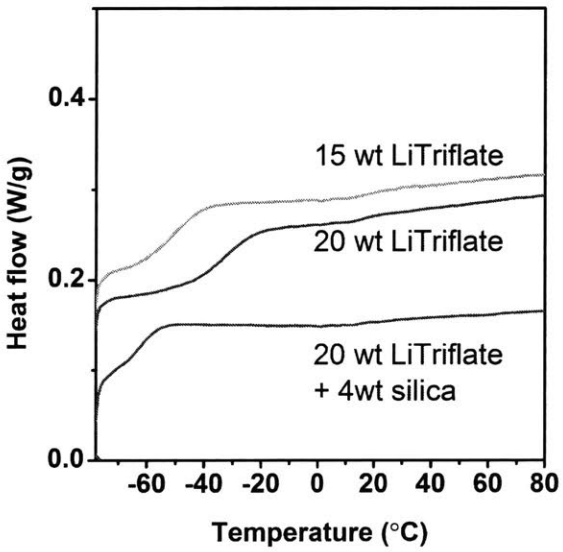

Figure A-3. Differential Scanning Calorimetry (DSC) spectra of siloxane/salt films as a function of lithium triflate content and silica content.

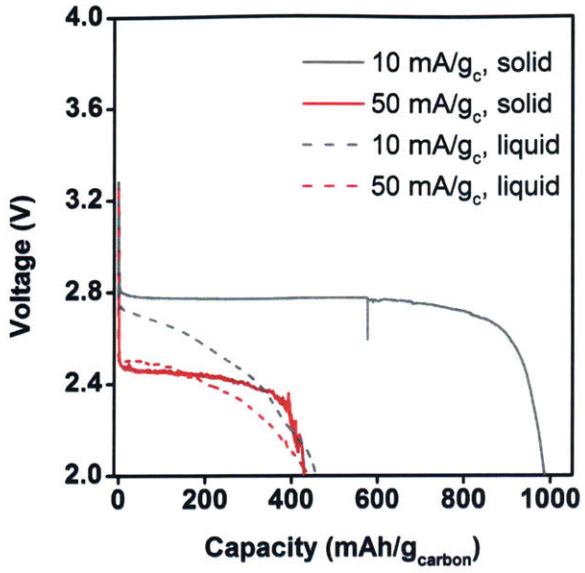

Figure A-4. Comparison of discharge capacities as a function of current rates for both solid-state Si-tripodand films, and for a 10 wt% lithium triflate salt dissolved in a Si-trip oligomer.

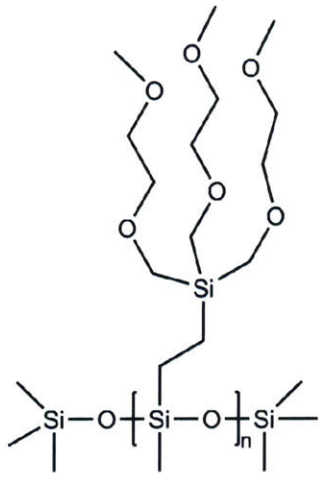

Modified silicon tripodand

Figure A-5. Modified silicon tripodand structure that avoids the labile Si–O–CH_2 bond and is replaced with a stronger Si–CH_2–O–CH_2 moiety.

Table A-3. Calculations used to determine reactant and catalyst amount needed for Si-tripodand synthesis.

PMHS repeating group	60	MW of vinyl silane	280.39
		Density of vinyl (g/mL)	1.034
Molar ratio	Vinyl_silane:PMHS	PMHS density (g/mL)	1.006
	1.2	Catalyst density (g/mL)	0.855
		Pt wt% in catalyst	0.02
Mass of PMHS (g)	**10**		
Moles of PMHS	0.166666667		
Moles of Vinyl	0.2		
Mass of vinyl (g)	56.078		
Volume of vinyl	**54.23404255**		
Volume PMHS (mL)	**9.940357853**		
Karstedt catalyst (uL)	**15**		
Catalyst amount in product (g)	0.0002565		
Catalyst amount (ppm)	**3.881776083**		

Appendix B

Table B-1. Properties of the polymers studied in this work.

Polymer	Abbreviation	M_w	T_g (°C) ref. [73])	T_m (°C) ref. [73]
Poly(acrylonitrile)	PAN	150,000	125	317
Poly(vinylidene fluoride)	PVDF	180,000	–40	171
Poly(vinylidene fluoride-co-hexafluoropropene)	PVDF-HFP	400,000	–90	135
Poly(vinyl chloride)	PVC	233,000	85	–
Poly(ethylene oxide)	PEO	100,000	–64	65
Poly(methyl methacrylate)	PMMA	120,000	105	–
Poly(vinyl pyrrolidone)	PVP	10,000		
Poly(tetrafluoroethylene)	PTFE	–		321
Nafion®	–	1100		

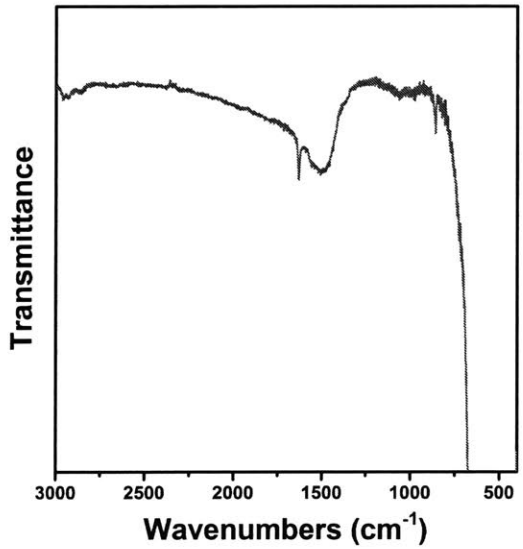

Figure B-1. FTIR plot of the mixture of Li_2O_2 and DMF. These peaks do not interfere with the polymeric peaks of interest.

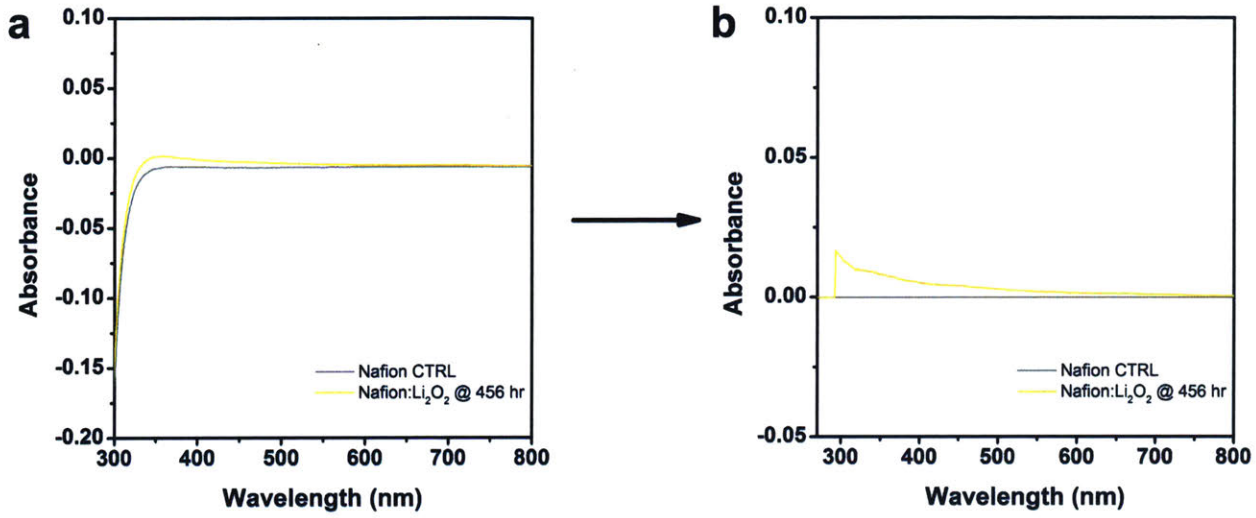

Figure B-2. UV-Vis spectra of the Nafion mixture with Li_2O_2 before (a) and after (b) the CTRL data was subtracted from the Nafion data. The (a) data was as obtained from the UV-Vis spectrophotometer. The Nafion:Li_2O_2 mixture was recorded after 456 hours of stirring. No peaks due to soluble decomposition species were present in the UV-Vis spectra (Figure B-2a) for Nafion at an even much longer time frame than that used to study the hydrohalogenated polymers (PVC, PVDF, and PVDF-HFP). The increase from ~300-500 nm in the Nafion:Li_2O_2 spectrum (Figure B-2b) is an artifact of the subtraction process because the Nafion CTRL data in Figure B-2a was below zero for that wavelength range. As described in the Experimental section, the Nafion:Li_2O_2 was filtered before performing UV-Vis to avoid interference from Li_2O_2 particles.

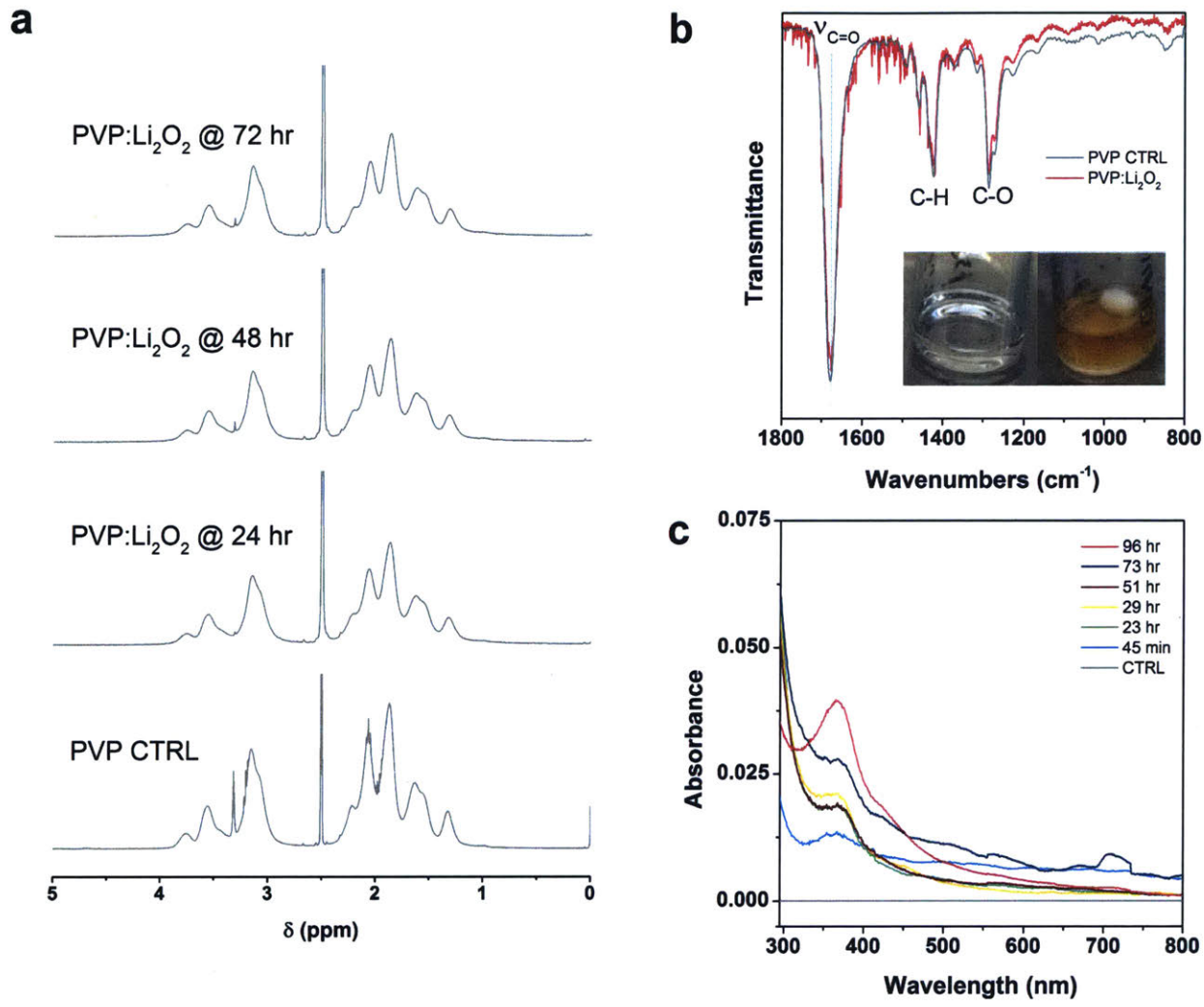

Figure B-3. (a) ^{1}H NMR (400 MHz; DMSO; Me_4Si), (b) FTIR, and (c) UV-Vis plot of the poly(vinyl pyrrolidone) (PVP) reaction with Li_2O_2. Inset in (b) shows the clear and transparent PVP solution, and the characteristic yellowish color of the PVP solution after mixture with Li_2O_2. The disappearance of the peak at δ=3.33 ppm (attributed to H_2O present in deuterated DMSO) is most likely due to a reaction between water and lithium peroxide.

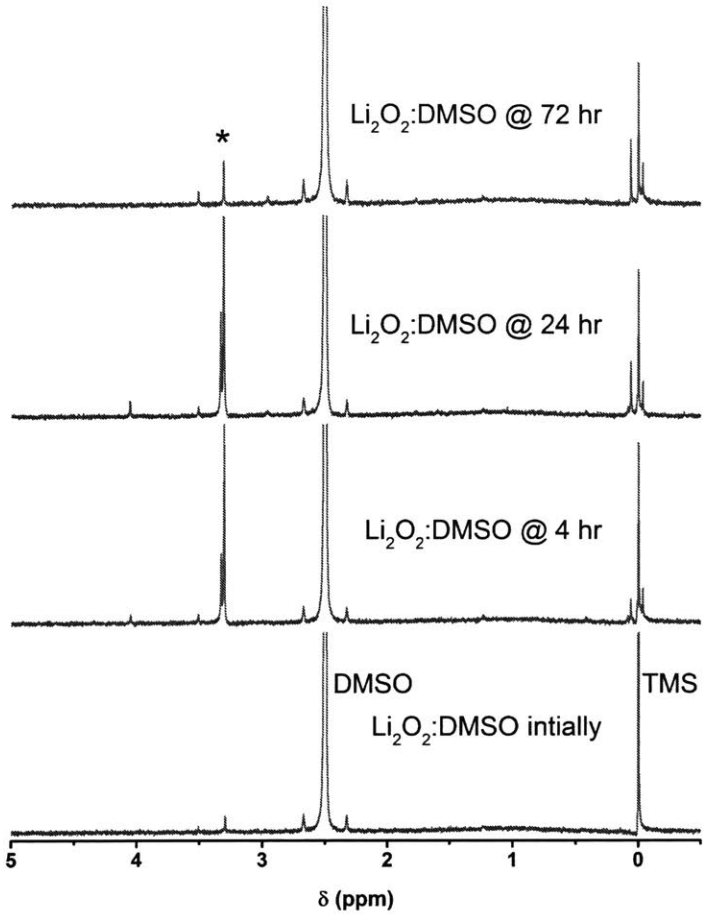

Figure B-4. ^{1}H NMR (400 MHz; DMSO; Me_4Si) spectra of the mixture of Li_2O_2 with DMSO. This was used as a control for the NMR experiments. *It does appear that Li_2O_2 reacts with DMSO, increasing the concentration of water (δ=3.33 ppm), an occurrence previously postulated by reference [69]. Also, the TMS appears to be affected by the presence of Li_2O_2, leading to satellite peaks at δ=0 ppm.

Appendix C

Discussion on Jung, K.-N., Lee, J.-I., Jung, J.-H., Shin, K.-H. & Lee, J.-W. A quasi-solid-state rechargeable lithium–oxygen battery based on a gel polymer electrolyte with an ionic liquid. *Chemical Communications* **50**, 5458-5461 (2014)

Jung *et al.* fabricated a PVDF-HFP/Pyr_{14}TFSI/LiTFSI gel polymer electrolyte by dissolving PVDF-HFP, LiTFSI, and Pyr_{14}TFSI in N-methyl pyrrolidone (NMP). The films were cast on a Teflon mold and vacuum-dried at 70 °C. NMP is a non-volatile solvent with a boiling point of 202 °C. As they report, PVDF-HFP is semi-crystalline, and it is known that crystallinity in polymer electrolytes hinders ionic transport. However, they report an ionic conductivity of PVDF-HFP-LiTFSI electrolyte (without ionic liquid) to be 1.6×10^{-4} S/cm at 30 °C. Conductivities as high as 10^{-4} at low temperatures for PVDF-HFP-based electrolytes have only been reported in the presence of small molecule solvents (refs [169] and [170]). Furthermore, for a PVDF-HFP polymer immersed in EC/DEC solvent, the ionic conductivity at low solution ratios approaches 10^{-8} S/cm at 10 % solution (ref. [171]). Therefore, NMP must be present in the PVDF-HFP-LiTFSI films studied by Jung *et al.* leading to high ionic conductivities (without ionic liquid). Since the same procedure is used for the fabrication of the PVDF-HFP/Pyr_{14}TFSI/LiTFSI films, we expect the NMP impurity to be present also. Therefore, NMP (in addition to Pyr_{14}TFSI) helps with ionic conduction, and may inadvertently affect the discharge and charge behavior of the reported Li–O_2 cells.

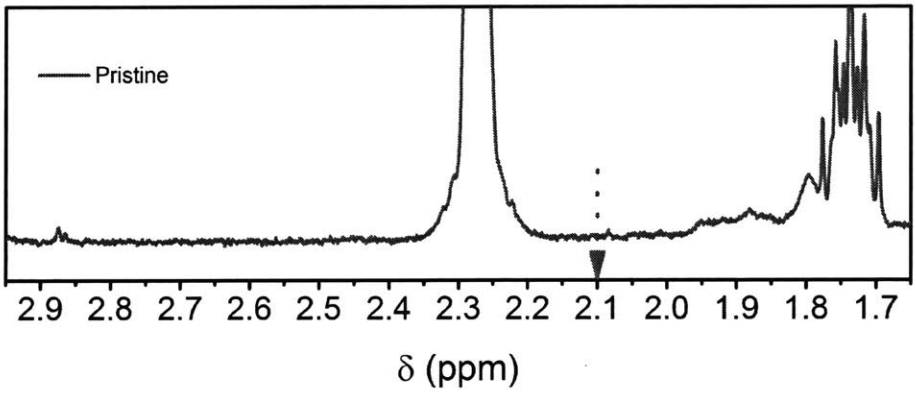

Figure C-1 | NMR of pristine GPE film. ^{1}H NMR (400 MHz, $CDCl_3$) spectra of a pristine GPE film ($Li^+/Pyr^+ = 0.6$) soaked in deuterated chloroform for at least one night. The liquid is then used for ^{1}H NMR. Chloroform and acetonitrile (solvent used for GPE film fabrication) are miscible. The lack of a peak at $\delta = 2.10$ ppm shows that no acetonitrile impurity is present in the GPE films studied in our work.

Ionic conductivity measurements

Ionic conductivity measurements were made by sandwiching the GPE between two 15 mm stainless steel disks (Stainless steel disk | GPE | Stainless steel disk). The setup was heated at 60 °C for 10 hours before electrochemical impedance spectroscopy (EIS) measurement was performed. This exact setup was allowed to rest at room temperature for 5 hours before the 25 °C data point was collected. The thickness of the GPE film was determined after the EIS measurements were completed. This is because the GPE film flows during heating, leading to a different thickness before and after heating. The thickness after heating is the true thickness contributing to ionic conductivity, and is used for the calculations. The thicknesses listed below are not the typical thickness of free-standing films which are 350–400 μm.

EIS measurements were performed in the frequency range of 1 MHz to 0.1 Hz with a signal level of 10 mV. 15 mm was used as the film diameter.

Table C-1. Ionic conductivity of different GPE formulation at 60 °C and 25 °C.

Li^+/Pyr^+ molar ratio	Thickness (mm)	Ionic conductivity (S/cm) @ 60 °C	Ionic Conductivity (S/cm) @ 25 °C
0	0.096	1.6×10^{-4}	1.0×10^{-5}
0.25	0.041	7.2×10^{-5}	1.2×10^{-5}
0.6	0.057	4.7×10^{-5}	2.3×10^{-6}
1.0	0.075	2.9×10^{-5}	1.4×10^{-6}
1.5	0.189	8.0×10^{-6}	2.4×10^{-7}

Table C-2. Typical GPE weight percentages for different Li salt/ionic liquid molar ratios.

Li^+/Pyr^+ molar ratio	PMMA (wt%)	LiTFSI (wt%)	$Pyr_{14}TFSI$ (wt%)
0	37.5	0	62.5
0.25	30	10	60
0.6	30	20	50
1.5	29.4	35.3	35.3
Li^+/EMI^+ molar ratio	PMMA (wt%)	LiTFSI (wt%)	EMITFSI (wt%)
0	37.5	0	62.5
0.6	28.4	21.9	49.7
1.5	28.4	34.0	37.5

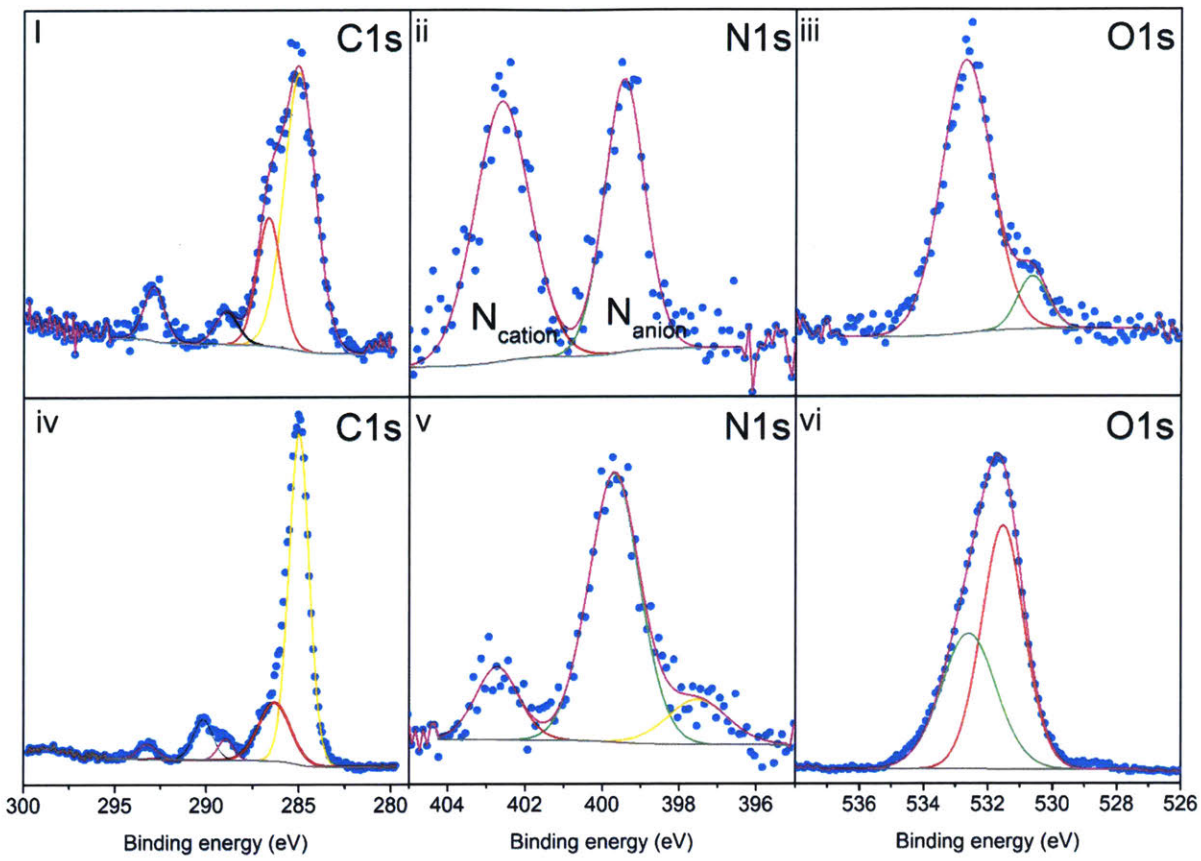

Figure C-2 | X-ray photoelectron spectroscopy (XPS) of pristine and after one discharge. XPS data chronicling the change in the C1s, N1s, and O1s in the pristine (i–iii) and after 1 discharge at 10 mA g^{-1} using a CNT electrode (iv–vi). This spectra corresponds to a different location of the same sample examined in the XPS figure in Chapter 4 (Figure 4-5). The pristine electrode involves sandwiching the CNT electrode with a GPE Li^+/Pyr^+ molar ratio = 0 and heating at 60 °C. When a chemical reaction occurs—and not a complexation—there is the rise of an alkene peak in the C1s spectra at B. E. = 291 eV and a reduction in the cationic N1s peak (compared to the TFSI anion N1s peak). The observed changes in the N1s spectra are different for a reaction versus a complexation. This XPS observation corroborates the work by Schwenke *et al.*[115] that reports alkene formation and opening of the Pyr^+ cation ring, which should lead to a reduction in the cation N1s peak.

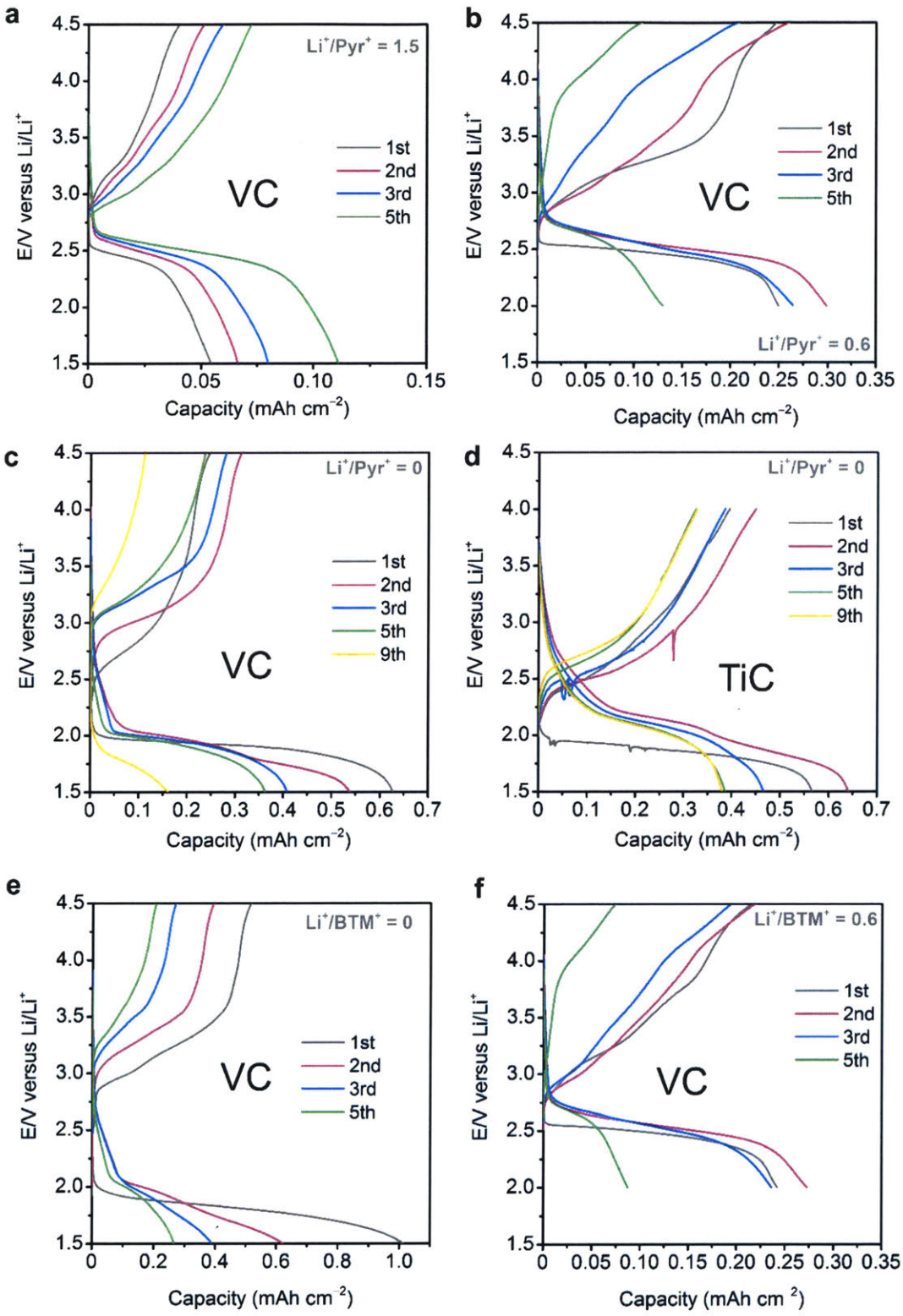

Figure C-3 | Cycling profiles using different GPE formulations (with Li^+/Pyr^+ and Li^+/BTM^+) with different electrodes. Cycling using a GPE Li^+/Pyr^+ molar ratio of 1.5 (**a**), GPE Li^+/Pyr^+ ratio of 0.6 with a discharge cutoff voltage of 2 V (**b**), and GPE Li^+/Pyr^+ ratio of 0 (**c**) with a Vulcan carbon/PMMA electrode (4:1 mass ratio) at 10 μA cm^{-2} ; **d,** Cycling using a GPE

Li^+/Pyr^+ molar ratio of 0 with a TiC electrode at 12.4 μA cm^{-2}. Cycling with a Vulcan carbon/PMMA electrode (4:1 mass ratio) at 10 μA cm^{-2} using a Li^+/BTM^+ molar ratio of 0 (**e**) and 0.6 (**f**). Cycling performed at 60 °C and current rates based on geometric surface area. The Vulcan carbon cycling behavior is similar across the different ionic liquid-based GPEs.

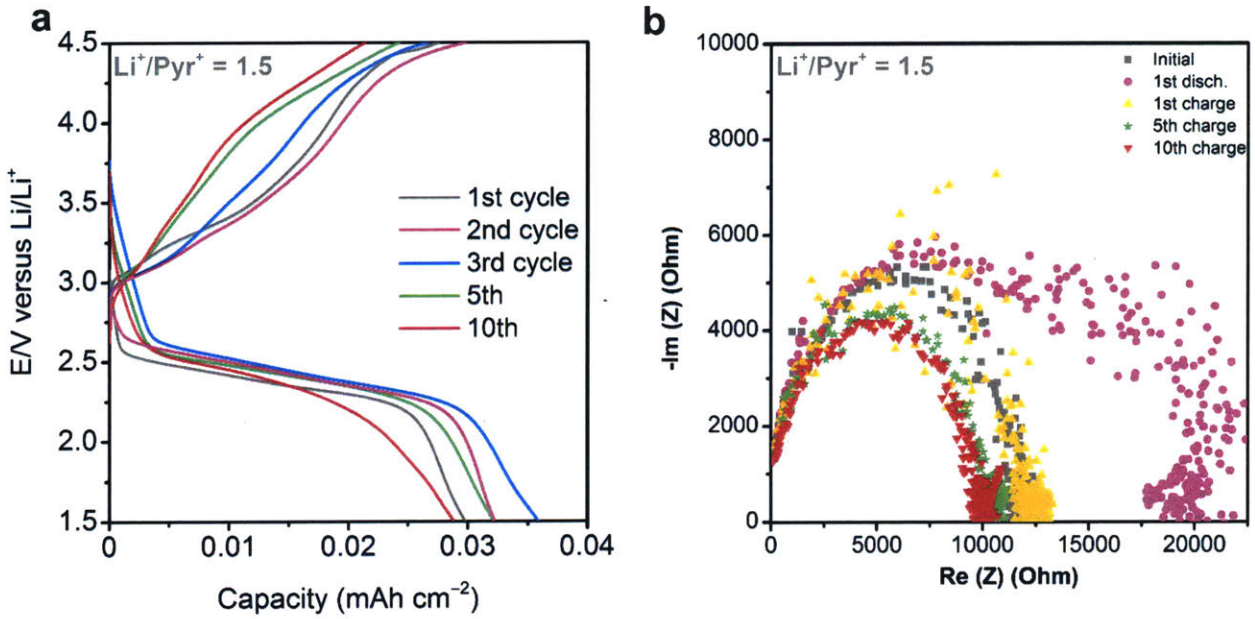

Figure C-4 | Electrochemical Impedance Spectroscopy (EIS) study of reversibility. a, Cycling using a GPE Li^+/Pyr^+ molar ratio of 1.5. **b**, EIS spectrum corresponding to the cycled cell in (**a**). Li_2O_2 is a known insulator with a 4.8 eV bandgap.[172] After the first discharge, the resistance increases, and is eliminated after first charge. The reversible formation and oxidation of these resistive species mirrors the reversible formation and oxidation of Li_2O_2.[173] Other resistive species such as Li_2CO_3 and LiOH require much higher oxidation potentials and show poor reversibility with longer cycling.[35,174] Electrode: 70wt% Vulcan carbon, 15wt% lithiated nafion, 7.5wt% LiTFSI, and 7.5wt% Pyr_{14}TFSI on carbon paper.

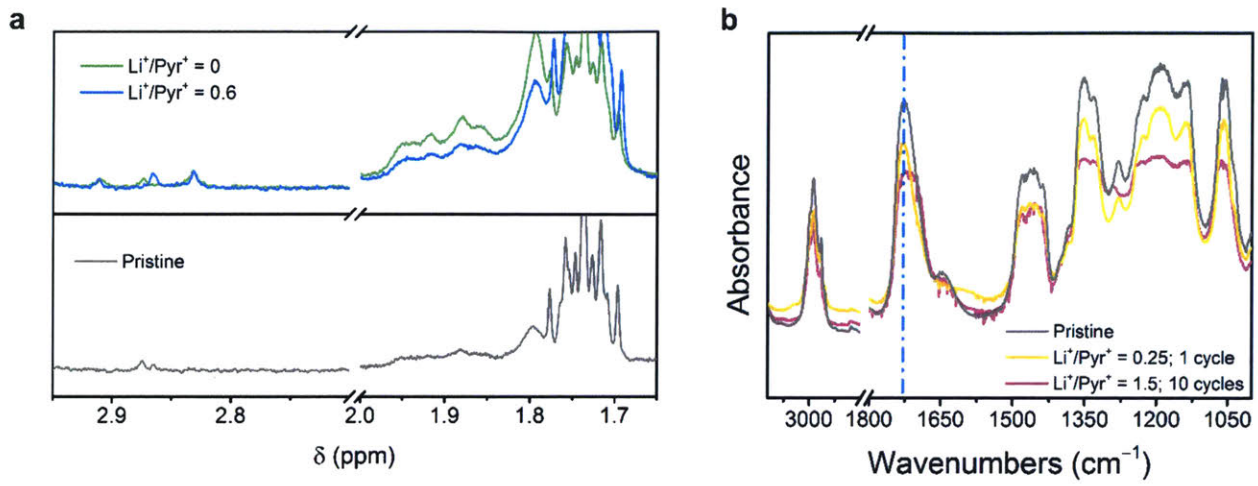

Figure C-5 | Spectroscopic characterization of GPEs after electrochemical analysis. a, ^{1}H NMR (400 MHz, $CDCl_3$) of different GPE films before and after cycling. The pristine spectra in the ^{1}H NMR corresponds to a GPE molar ratio of 0.6, the $Li^+/Pyr^+ = 0$ corresponds to the GPE film after cycling (Cycling spectra in Figure C-3d), and the $Li^+/Pyr^+ = 0.6$ corresponds to the GPE film after 3 cycles with a TiC electrode (All cycles are at 6.2 μA cm^{-2} except for the 1st charge at 3.1 μA cm^{-2}). The small peaks at $\delta = 2.8 - 2.9$ after cycling could be decomposition products or impurities; **b**, FTIR spectra corresponding to pristine (GPE Li^+/Pyr^+ molar ratio of 0.25) and cycled GPEs, where the cycling spectra for $Li^+/Pyr^+ = 0.25$ is in Figure 4-10 and the $Li^+/Pyr^+ = 1.5$ cycling spectra is in Figure C-4. The GPE films (before and after discharge) were soaked in $CDCl_3$ overnight. The solution was then taken for ^{1}H NMR.

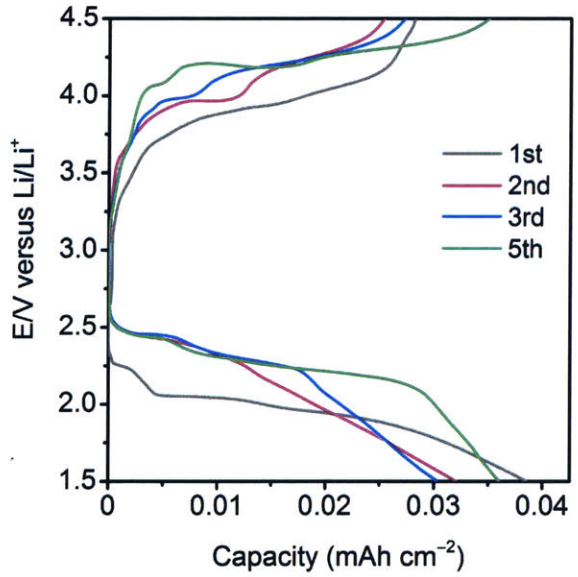

Figure C-6 | Cycling behavior of non-aqueous Li–O_2 cells to mimic GPE Li–O_2 behavior. Five cycles for a system containing 0.1M $TBAClO_4$ with an anion exchange membrane (AEM)

present at 3.94 μA cm^{-2} at room temperature. Current rates based on geometric surface area. The configuration of the Li–O_2 cell is in Figure 4-12a in Chapter 4.

Electrochemical analysis for Pyr-based GPEs

Assuming a 1:1 molar stoichiometry of Pyr^+–$O_2^{\bullet-}$, and utilizing the amount of capacity obtained at the plateau at 1.9 V, the average fraction of the Pyr^+ used in the cell is computed. To determine the amount of Li used in the cell, a 2 mol e^-/mol O_2 was utilized.

Li^+/Pyr^+ molar ratio	Average fraction of Li^+ used in cell	Average fraction of Pyr^+ used in cell	Mol superoxide
0	N/A	0.25	3.0×10^{-5}
0.25	0.21	0.24	4.1×10^{-5}
0.6	0.131	0.25	3.5×10^{-5}
1.5	0.0122	0.0018	1.7×10^{-7}

Within regimes where the ionic liquid-superoxide complex forms, the cell capacity should be dictated by the ionic liquid concentration in the electrolyte. Assuming a 1:1 molar stoichiometry of Pyr^+:$O_2^{\bullet-}$, only 25–30 % of the ionic liquid is utilized for complexation before 'sudden death' occurs in the cell. In conventional non-aqueous systems, 'sudden death' is a function of pore blockage due to Li_2O_2 accumulation and eventual electrical isolation of the electrode because of insulating Li_2O_2.[175] Formation of the cuboid ionic liquid-superoxide complexes appears responsible for the observed 'sudden death' when they clog the available pores. It is also possible that only 25–30 % of the ionic liquid is accessible to the electrode, and capacities could be limited by the diffusivity of superoxide into the ionic liquid.

Electrochemical analysis for TBA-based non-aqueous cells containing an anion-exchange membrane

The below acronyms explain the legend of Figure 4-12b in Chapter 4 and shows the configuration of the Li–O_2 cell. All salts were dissolved in diglyme. About 90 µL of electrolyte was used in the cells.

Li, no membrane = (Li metal | 0.1M $LiClO_4$ | Celgard C480 | 0.1M $LiClO_4$ | Carbon paper)

TBA, no membrane = (Li metal | 0.1M $TBAClO_4$ | Celgard C480 | 0.1M $TBAClO_4$ | Carbon paper)

Li, TBA, no membrane = (Li metal | 0.1M $LiClO_4$ | Celgard C480 | 0.1M $TBAClO_4$ | Carbon paper)

Li, membrane = (Li metal | 0.1M $LiClO_4$ | Celgard C480 | AEM | Celgard C480 | 0.1M $LiClO_4$ | Carbon paper)

TBA, membrane = (Li metal | 0.1M $TBAClO_4$ | Celgard C480 | AEM | Celgard C480 | 0.1M $TBAClO_4$ | Carbon paper)

Mol of TBA added	**Capacity (Ah)**	**Mol of superoxide**	**Fraction of TBA used**
6×10^{-6}	5×10^{-5}	1.9×10^{-6}	0.31

A 1:1 molar stoichiometry of TBA^+–$O_2^{\bullet-}$ was assumed, and the capacity used for the calculations was obtained from Figure 4-12b in Chapter 4. It is also assumed that the TBA available for complexation is the TBA added after the AEM and in contact with the electrode. Of the 90 µL electrolyte solution in the Li–O_2 cell, 60 µL was added after insertion of the AEM. Therefore, only 6×10^{-6} mol of TBA is available for complexation.

The fraction of TBA^+ used is very similar to the fraction of Pyr^+ utilized for superoxide complexation.

Appendix D

Table D-1. Theoretical calculations to determine how much TBA is consumed during each charge and how many cycles are needed to completely consume TBA. This assumes a 1 electron decomposition pathway as proposed by Finkelstein *et al.*[147]

$$0.05\,mAh * \frac{1A}{1000mA} * \frac{C}{1A \cdot s}\frac{3600s}{1h} * \frac{mol}{96485\,C} = 1.87 \cdot 10^{-6} mol\,TBA\,per\,charge\,step$$

TBA concentration	0.1 M
Volume in cell	120 µL
Amount of TBA present	1.20×10^{-5} mol
Charge capacity in one cycle (5 µA for 10 hours)	0.05 mAh
Amount TBA consumed	1.87×10^{-6} mol
Cycles needed to consume all TBA present	6.45

Table D-2. Integration of NMR data from Figure 5-7 in Chapter 5 detailing the changes in the TBA structure and the increase of decomposition species after cycling due to TBA oxidation at 3.55 V. The Argon cell was cycled five times while the O_2 cell was cycled fifteen times. 0.1 M TBA in DME was used as the electrolyte with a lithium metal anode and a carbon paper cathode.

Region	Pristine TBA	Cycled in Argon	Cycled in O_2
1.68 – 1.45 ppm	1.0	1.0	1.0
2.35 – 2.25 ppm	**0.01**	**0.18**	**0.16**
0.976 – 0.780 ppm	**1.45**	**1.75**	**2.25**

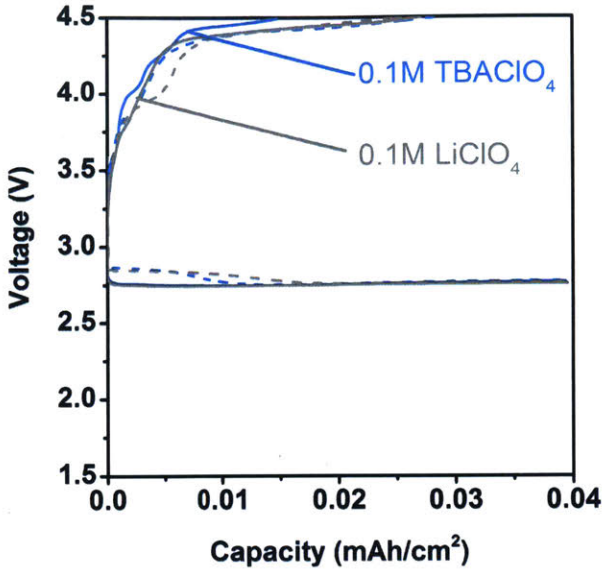

Figure D-1. Cycling performance of a Li–O_2 cell with a 0.1 M $TBAClO_4$ or a 0.1 M $LiClO_4$ in DMSO electrolyte in oxygen at 3.95 μA/cm^2 to a 0.0395 mAh/cm^2 cutoff. Li–O_2 cell setup: Li metal | 0.1 M $TBAClO_4$ or 0.1 M $LiClO_4$ in DMSO | carbon paper. (Bold lines) – First cycle; (Dashed lines) – Fifth cycle

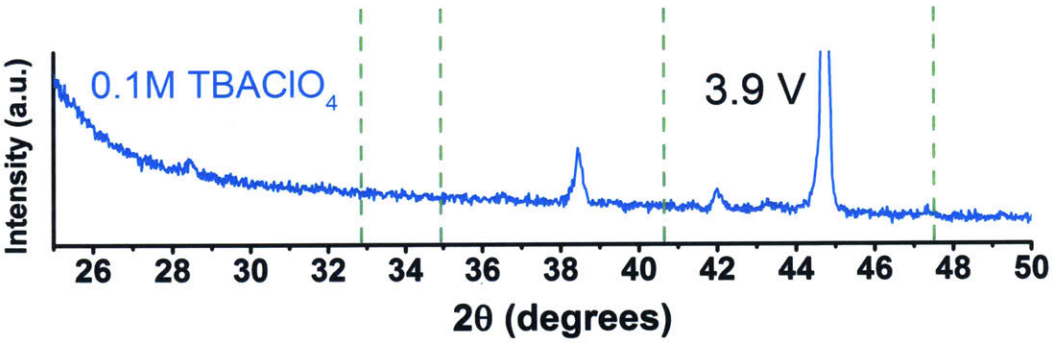

Figure D-2. XRD spectra after holding a Li_2O_2 preloaded electrode at 3.9 V for 100 hours in a 0.1 M $TBAClO_4$ in DMSO electrolyte. Dashed lines are where the (100), (101), (102), and (004) Li_2O_2 diffraction peaks should be (left to right). Li–O_2 cell set-up: Li metal | 0.1 M $TBAClO_4$ salt in DMSO | Vulcan carbon + Nafion + Li_2O_2 on aluminum foil.

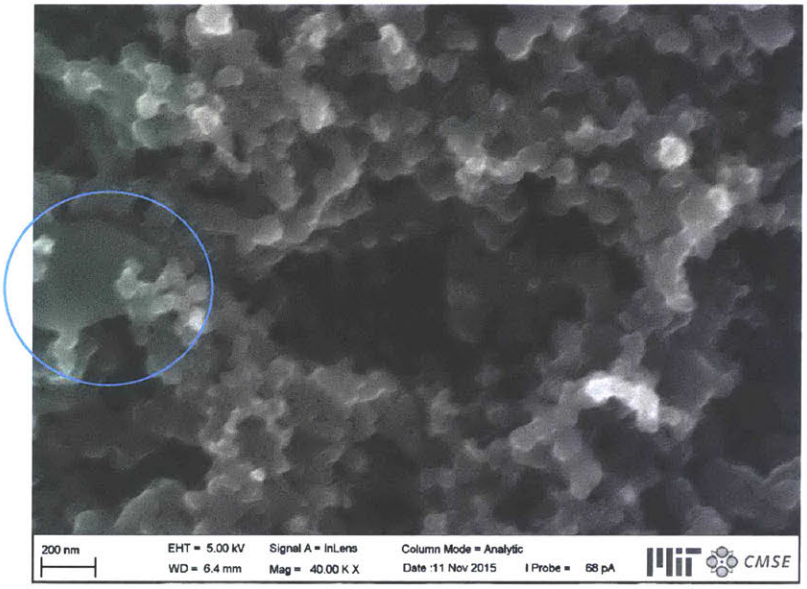

Figure D-3. Remnant of Li_2O_2 particles (circled) after a Li_2O_2-preloaded electrode was held at 3.9 V for 100 hours in a 0.1M $TBAClO_4$ in diglyme electrolyte. The electrochemistry is located in Figure 5-4. The large holes in the electrode are where Li_2O_2 particles used to be before their oxidation.

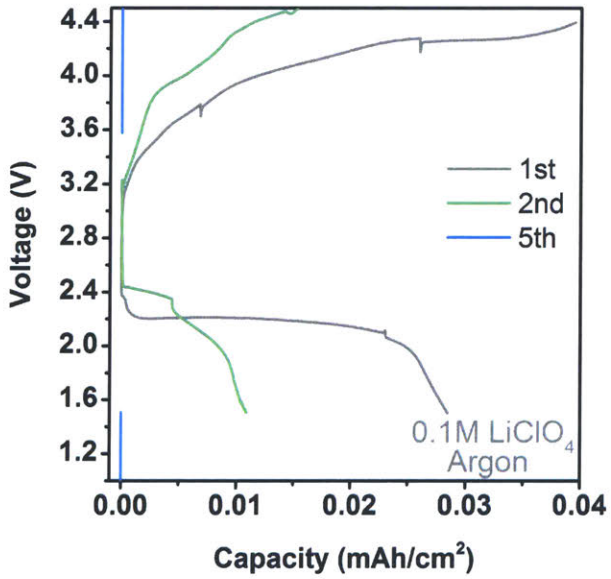

Figure D-4. Cycling using 0.1 M $LiClO_4$ in DME at 3.95 $\mu A/cm^2$ to 0.0395 mAh/cm^2 in argon. The observed reduction plateau may be due to dissolved oxygen in the solvent. However, the discharge capacity fades quickly with cycling. Li–O_2 cell setup: Li metal | 0.1 M $LiClO_4$ in DME | carbon paper.

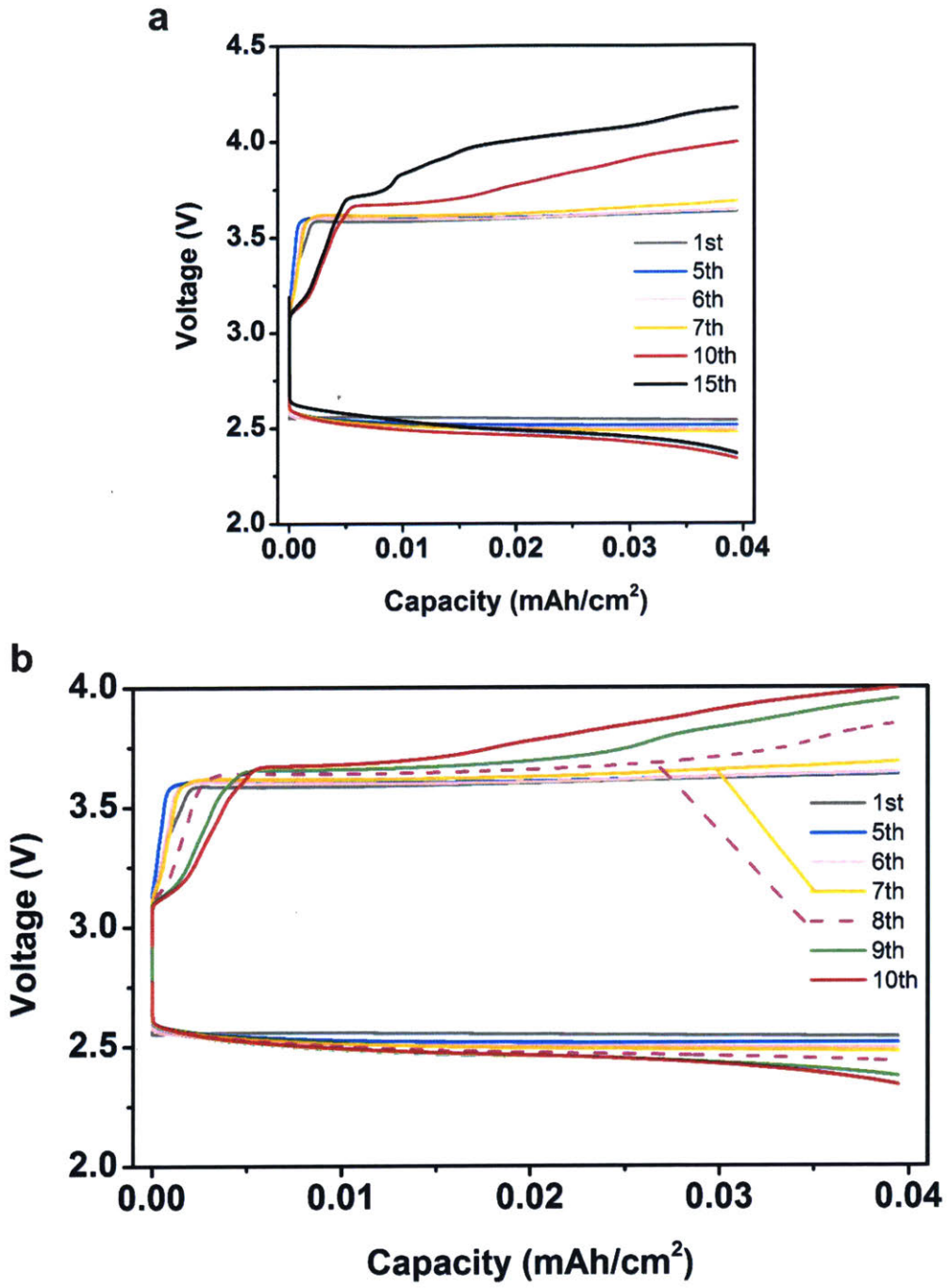

Figure D-5. (**a**) Cycling of a Li–O_2 cell in oxygen at 3.95 μA/cm^2 to a 0.0395 mAh/cm^2 cutoff using a 0.1 M $TBAClO_4$ in DME electrolyte. This cycling data corresponds to the NMR data shown in Figure 5-7. (**b**) Zoomed-in image of (**a**). Li–O_2 cell setup: Li metal | 0.1 M $TBAClO_4$ in DME | carbon paper.

Figure D-5b shows that the voltage begins to deviate from the rest by the 7th cycle. One cannot easily distinguish the 1st to 6th charge steps, but it is easy to see the 7th charge step. The voltage begins to increase by the 7th cycle, and is very close to the expected complete consumption of TBA by 6.45 cycles (Table D-1). More discussion can be found in Chapter 5.

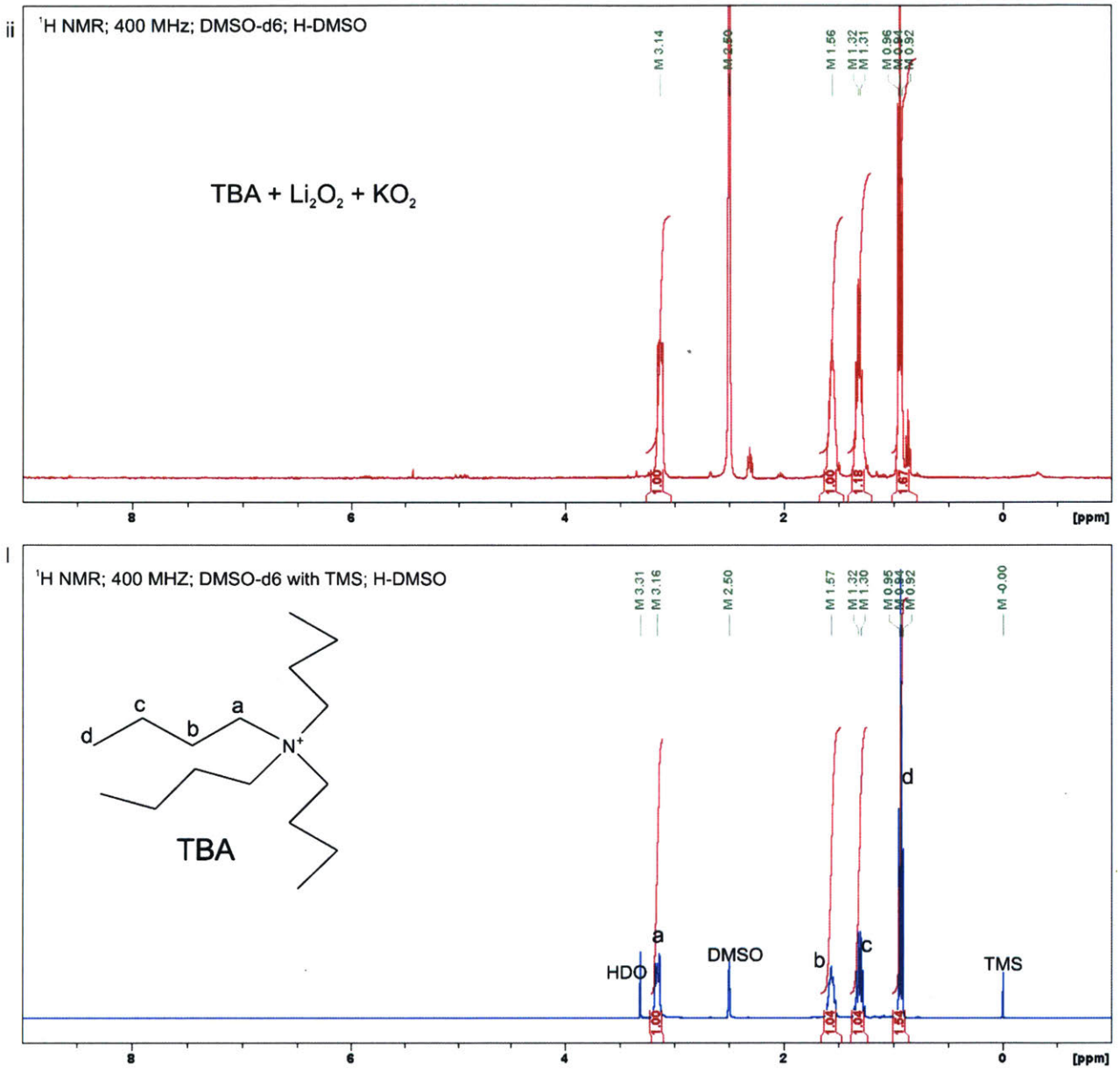

Figure D-6. ^{1}H NMR spectra of (i) a pristine tetrabutylammonium perchlorate sample and (ii) after mixture with Li_2O_2 and KO_2 for three days. DMSO-d6 was used as the NMR solvent with residual DMSO in DMSO-d6 ('H-DMSO') used for spectra calibration. HDO originates from the NMR solvent.

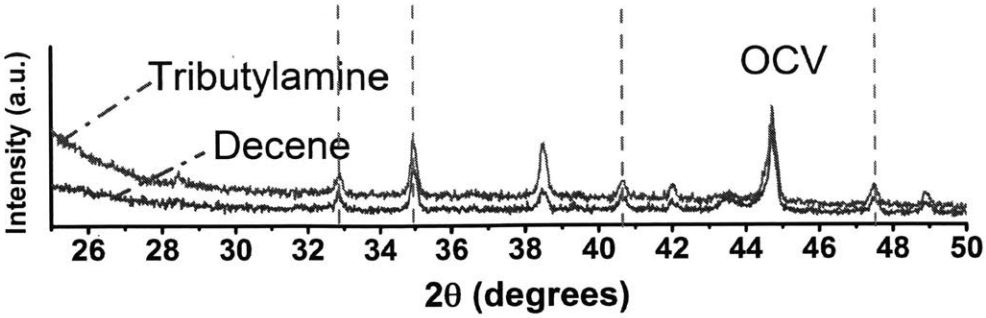

Figure D-7. XRD spectra of a Li_2O_2 preloaded electrode after being held in either pure tributylamine or decene at open-circuit potential for 200 hours. The dashed lines represent Li_2O_2 diffraction peaks, and this data shows that Li_2O_2 remains after prolonged exposure to these molecules.

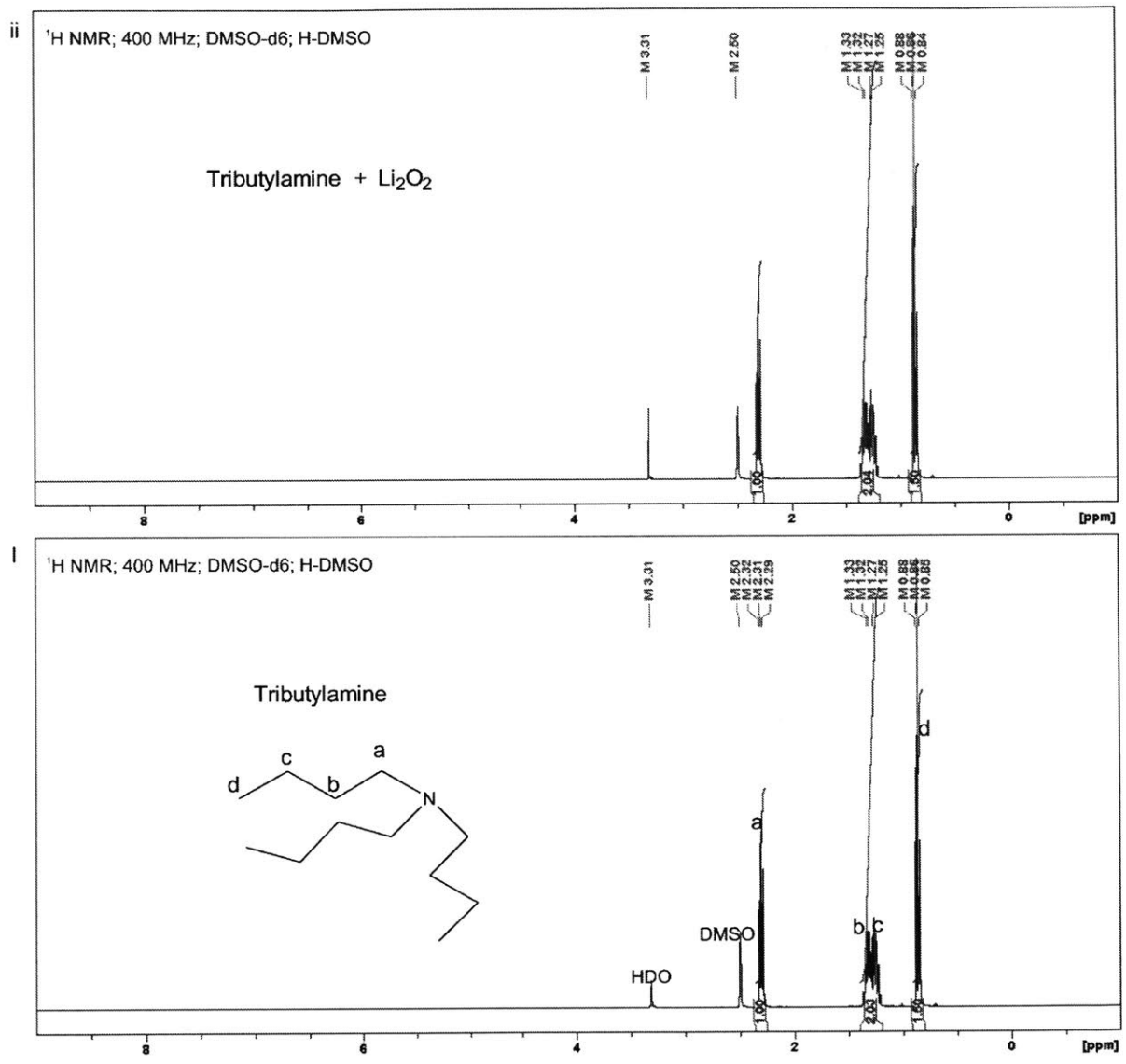

Figure D-8. ^1H NMR spectra of (i) a pristine tributylamine sample and (ii) after mixture with Li_2O_2 for three days. DMSO-d6 was used as the NMR solvent with residual DMSO in DMSO-d6 ('H-DMSO') used for spectra calibration. HDO originates from NMR solvent.

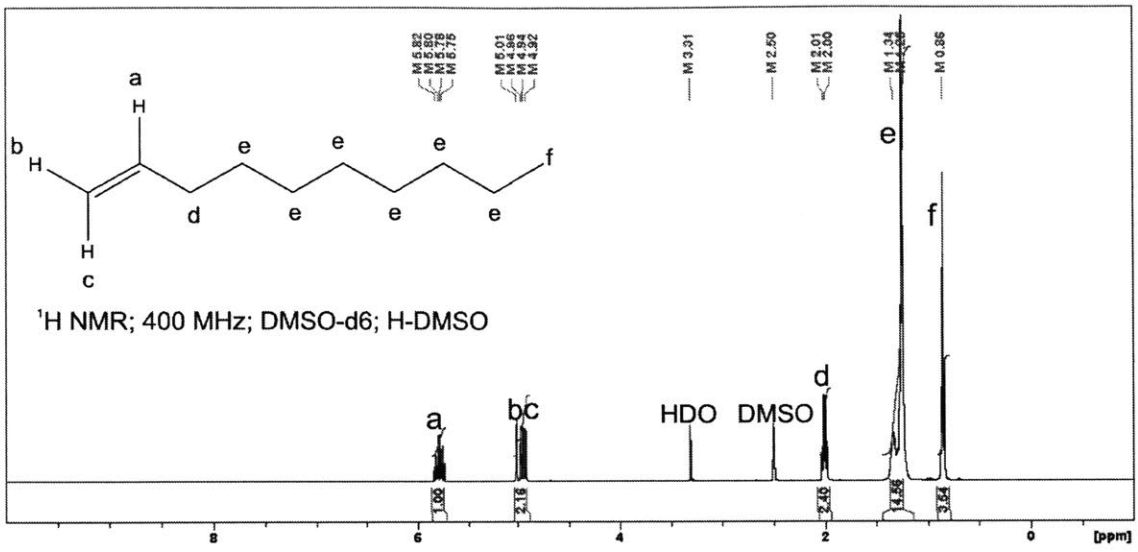

Figure D-9. ^{1}H NMR spectra after a mixture of decene with Li_2O_2 for three days. DMSO-d6 was used as the NMR solvent with residual DMSO in DMSO-d6 ('H-DMSO') used for spectra calibration.

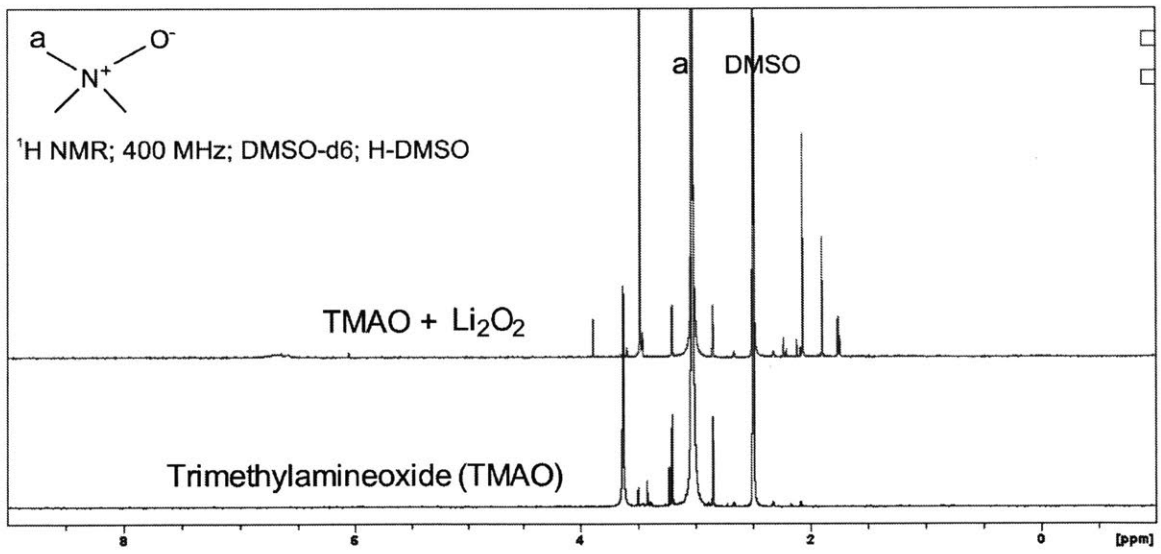

Figure D-10. ^{1}H NMR spectra of a pristine trimethylamineoxide (TMAO) sample and after mixture with Li_2O_2 for three days. DMSO-d6 was used as the NMR solvent with residual DMSO in DMSO-d6 ('H-DMSO') used for spectra calibration.

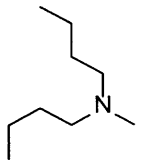

Chemical Formula: $C_9H_{21}N$
Molecular Weight: 143.27

Figure D-11. Possible molecule that may correspond to the unassigned m/z values obtained in Figure 5-9 in Chapter 5.

Appendix E

Table E-1. O (1s), C (1s), and S (2p) X-ray photoelectron spectroscopy (XPS) values obtained from pristine PEDOT films, after 1st discharge, after 1 cycle (ending on charge), and after 5 cycles (ending on charge).

O1s

	Position (eV)	FWHM	Area/(RSF*T*MFP)
Pristine	533.53	1.775	131.4
	531.11	1.368	7.9
1st discharge	533.15	2	218.2
	531.63	1.5	95.8
1st charge	533.51	2	102.1
	532.34	1.691	160.7
5th charge	533.73	2	84.0
	532.49	1.813	181.5

C1s

	Position (eV)	FWHM	Area/(RSF*T*MFP)
Pristine	285	1.2	377.0
	286.09	1.6	630.7
	287	1.641	508.2
	288.55	1.456	30.9
	289.72	2.48	27.2
1st discharge	285	1.29	608.9
	286.29	1.6	442.3
	287.4	1.8	115.1
	288.8	1.466	69.7
	290	1.849	87.4
1st charge	285	1.2	378.2
	286.14	1.6	437.1
	287	1.752	293.1
	289.02	1.573	161.5
	290.17	2	56.6
5th charge	285	1.235	392.
	286.11	1.597	352.1
	287	1.669	315.0
	288.99	1.538	150.0
	290	1.704	59.7

S2p

	Name	Position (eV)	FWHM	Area/(RSF*T*MFP)
Pristine	S 2p3/2	163.99	1.063	46.1
	S 2p1/2	165.15	1.063	23.0
	S 2p3/2 2	165.44	1.5	19.2
	S 2p1/2 2	166.6	1.5	9.6
1st discharge	S 2p3/2	163.7	1.066	21.1
	S 2p1/2	164.86	1.066	10.5
	S 2p3/2 2	165.48	1.5	10.7
	S 2p1/2 2	166.64	1.5	5.3
	S 2p	169.15	2	6.0
	S 2p	170.31	2	3.0
1st charge	S 2p3/2	163.91	1.066	22.0
	S 2p1/2	165.07	1.066	11.0
	S 2p3/2 2	165.5	1.5	10.3
	S 2p1/2 2	166.66	1.5	5.2
	S 2p	169.22	1.523	18.4
	S 2p	170.38	1.523	9.2
5th charge	S 2p3/2	163.86	1.072	18.5
	S 2p1/2	165.02	1.072	9.2
	S 2p3/2 2	165.29	1.5	10.3
	S 2p1/2 2	166.45	1.5	5.1
	S 2p	169.19	1.574	21.5
	S 2p	170.35	1.574	10.7

Table E-2. This table was used to make Figure 6-5 in Chapter 6. The values were obtained using the area values in Table E-1.

	C (1s)	O (1s)	S (2p)	O/S ratio
Pristine	0.04	0.06	0	1.4
1st discharge	0.12	0.31	0.16	5.5
1st charge	0.16	0.61	0.36	3.4
5th charge	0.17	0.68	0.43	3.5

The ratios in the table were obtained as follows: C (1s) = (Area at 288.9 + Area at 290 eV)/ total C (1s) area; O (1s) = Area at lower energy level (531 or 532 eV)/ Total area; S (2p) = (Area at 169 + area at 170 eV) / total S (2p) area; O/S ratio = total O (1s) area / total S (2p) area.

References

(1) Nations, U. *Framework Convention on Climate Change*, 2015.

(2) Tans, E. D. a. P. 2017; Vol. 2017.

(3) D'Alessandro, D. M.; Smit, B.; Long, J. R. Carbon Dioxide Capture: Prospects for New Materials. *Angew. Chem. Int. Ed.* **2010**, *49*, 6058-6082.

(4) Leung, D. Y.; Caramanna, G.; Maroto-Valer, M. M. An Overview of Current Status of Carbon Dioxide Capture and Storage Technologies. *Renewable and Sustainable Energy Reviews* **2014**, *39*, 426-443.

(5) Lewis, N. S. Toward Cost-Effective Solar Energy Use. *science* **2007**, *315*, 798-801.

(6) Lewis, N. S.; Nocera, D. G. Powering the Planet: Chemical Challenges in Solar Energy Utilization. *Proceedings of the National Academy of Sciences* **2006**, *103*, 15729-15735.

(7) Dunn, B.; Kamath, H.; Tarascon, J.-M. Electrical Energy Storage for the Grid: A Battery of Choices. *Science* **2011**, *334*, 928-935.

(8) Center, M. D. o. E. R. M. C. E. *State of Charge: Massachusetts Energy Storage Initiative*, 2016.

(9) Grey, C.; Tarascon, J. Sustainability and in Situ Monitoring in Battery Development. *Nat. Mater.* **2017**, *16*, 45-56.

(10) Tarascon, J.-M.; Armand, M. Issues and Challenges Facing Rechargeable Lithium Batteries. *Nature* **2001**, *414*, 359-367.

(11) Winter, M.; Besenhard, J. O.; Spahr, M. E.; Novák, P. Insertion Electrode Materials for Rechargeable Lithium Batteries. *Adv. Mater.* **1998**, *10*, 725-763.

(12) Bruce, P. G.; Freunberger, S. A.; Hardwick, L. J.; Tarascon, J.-M. Li-O2 and Li-S Batteries with High Energy Storage. *Nat. Mater.* **2011**, *11*, 19-29.

(13) Scrosati, B.; Hassoun, J.; Sun, Y.-K. Lithium-Ion Batteries. A Look into the Future. *Energy Envion. Sci.* **2011**, *4*, 3287-3295.

(14) Lu, Y.-C.; Gallant, B. M.; Kwabi, D. G.; Harding, J. R.; Mitchell, R. R.; Whittingham, M. S.; Shao-Horn, Y. Lithium–Oxygen Batteries: Bridging Mechanistic Understanding and Battery Performance. *Energy Envion. Sci.* **2013**, *6*, 750-768.

(15) Lin, D.; Liu, Y.; Cui, Y. Reviving the Lithium Metal Anode for High-Energy Batteries. *Nature Nanotechnology* **2017**, *12*, 194-206.

(16) Kwabi, D.; Ortiz-Vitoriano, N.; Freunberger, S.; Chen, Y.; Imanishi, N.; Bruce, P.; Shao-Horn, Y. Materials Challenges in Rechargeable Lithium-Air Batteries. *MRS Bull.* **2014**, *39*, 443-452.

(17) Xu, W.; Wang, J.; Ding, F.; Chen, X.; Nasybulin, E.; Zhang, Y.; Zhang, J.-G. Lithium Metal Anodes for Rechargeable Batteries. *Energy Envion. Sci.* **2014**, *7*, 513-537.

(18) Freunberger, S. A.; Chen, Y.; Peng, Z.; Griffin, J. M.; Hardwick, L. J.; Bardé, F.; Novák, P.; Bruce, P. G. Reactions in the Rechargeable Lithium–O2 Battery with Alkyl Carbonate Electrolytes. *J. Am. Chem. Soc.* **2011**, *133*, 8040-8047.

(19) Freunberger, S. A.; Chen, Y.; Drewett, N. E.; Hardwick, L. J.; Bardé, F.; Bruce, P. G. The Lithium–Oxygen Battery with Ether-Based Electrolytes. *Angew. Chem. Int. Ed.* **2011**, *50*, 8609-8613.

(20) Peng, Z.; Freunberger, S. A.; Chen, Y.; Bruce, P. G. A Reversible and Higher-Rate Li-O2 Battery. *Science* **2012**, *337*, 563-566.

(21) Meyer, W. H. Polymer Electrolytes for Lithium-Ion Batteries. *Adv. Mater.* **1998**, *10*, 439-448.

(22) Harding, J. R.; Amanchukwu, C. V.; Hammond, P. T.; Shao-Horn, Y. Instability of Poly (Ethylene Oxide) Upon Oxidation in Lithium–Air Batteries. *J. Phys. Chem. C* **2015**, *119*, 6947-6955.

(23) Balaish, M.; Peled, E.; Golodnitsky, D.; Ein-Eli, Y. Liquid-Free Lithium–Oxygen Batteries. *Angew. Chem. Int. Ed.* **2015**, *54*, 436-440.

(24) Kwabi, D. G.; Batcho, T. P.; Amanchukwu, C. V.; Ortiz-Vitoriano, N.; Hammond, P.; Thompson, C. V.; Shao-Horn, Y. Chemical Instability of Dimethyl Sulfoxide in Lithium–Air Batteries. *J. Phys. Chem. Lett.* **2014**, *5*, 2850-2856.

(25) Chen, Y.; Freunberger, S. A.; Peng, Z.; Bardé, F.; Bruce, P. G. Li–O2 Battery with a Dimethylformamide Electrolyte. *J. Am. Chem. Soc.* **2012**, *134*, 7952-7957.

(26) Black, R.; Oh, S. H.; Lee, J.-H.; Yim, T.; Adams, B.; Nazar, L. F. Screening for Superoxide Reactivity in Li-O2 Batteries: Effect on Li2o2/Lioh Crystallization. *J. Am. Chem. Soc.* **2012**, *134*, 2902-2905.

(27) Nasybulin, E.; Xu, W.; Engelhard, M. H.; Nie, Z.; Li, X. S.; Zhang, J.-G. Stability of Polymer Binders in Li–O 2 Batteries. *J. Power Sources* **2013**, *243*, 899-907.

(28) Amanchukwu, C. V.; Harding, J. R.; Shao-Horn, Y.; Hammond, P. T. Understanding the Chemical Stability of Polymers for Lithium–Air Batteries. *Chem. Mater.* **2015**, *27*, 550-561.

(29) Bohnke, O.; Frand, G.; Rezrazi, M.; Rousselot, C.; Truche, C. Fast Ion Transport in New Lithium Electrolytes Gelled with Pmma. 1. Influence of Polymer Concentration. *Solid State Ionics* **1993**, *66*, 97-104.

(30) Elia, G.; Hassoun, J.; Kwak, W.-J.; Sun, Y.-K.; Scrosati, B.; Mueller, F.; Bresser, D.; Passerini, S.; Oberhumer, P.; Tsiouvaras, N. An Advanced Lithium–Air Battery Exploiting an Ionic Liquid-Based Electrolyte. *Nano Lett.* **2014**, *14*, 6572-6577.

(31) Amanchukwu, C. V.; Chang, H.-H.; Gauthier, M.; Feng, S.; Batcho, T. P.; Hammond, P. T. One-Electron Mechanism in a Gel–Polymer Electrolyte Li–O2 Battery. *Chem. Mater.* **2016**, *28*, 7167-7177.

(32) Hartmann, P.; Bender, C. L.; Vračar, M.; Dürr, A. K.; Garsuch, A.; Janek, J.; Adelhelm, P. A Rechargeable Room-Temperature Sodium Superoxide (Nao2) Battery. *Nat. Mater.* **2013**, *12*, 228-232.

(33) Ren, X.; Wu, Y. A Low-Overpotential Potassium–Oxygen Battery Based on Potassium Superoxide. *J. Am. Chem. Soc.* **2013**, *135*, 2923-2926.

(34) Lu, Y.-C.; Kwabi, D. G.; Yao, K. P.; Harding, J. R.; Zhou, J.; Zuin, L.; Shao-Horn, Y. The Discharge Rate Capability of Rechargeable Li–O2 Batteries. *Energy Envion. Sci.* **2011**, *4*, 2999-3007.

(35) Ottakam Thotiyl, M. M.; Freunberger, S. A.; Peng, Z.; Bruce, P. G. The Carbon Electrode in Nonaqueous Li–O2 Cells. *J. Am. Chem. Soc.* **2012**, *135*, 494-500.

(36) MM, O. T.; Freunberger, S.; Peng, Z.; Chen, Y.; Liu, Z.; Bruce, P. A Stable Cathode for the Aprotic Li-O2 Battery. *Nat. Mater.* **2013**.

(37) Lock, J. P.; Im, S. G.; Gleason, K. K. Oxidative Chemical Vapor Deposition of Electrically Conducting Poly (3, 4-Ethylenedioxythiophene) Films. *Macromolecules* **2006**, *39*, 5326-5329.

(38) Cui, Y.; Wen, Z.; Liang, X.; Lu, Y.; Jin, J.; Wu, M.; Wu, X. A Tubular Polypyrrole Based Air Electrode with Improved O 2 Diffusivity for Li–O 2 Batteries. *Energy Envion. Sci.* **2012**, *5*, 7893-7897.

(39) Nasybulin, E.; Xu, W.; Engelhard, M. H.; Li, X. S.; Gu, M.; Hu, D.; Zhang, J.-G. Electrocatalytic Properties of Poly (3, 4-Ethylenedioxythiophene)(Pedot) in Li-O 2 Battery. *Electrochem. Commun.* **2013**, *29*, 63-66.

(40) Yoon, D. H.; Yoon, S. H.; Ryu, K.-S.; Park, Y. J. Pedot: Pss as Multi-Functional Composite Material for Enhanced Li-Air-Battery Air Electrodes. *Scientific Reports* **2016**, *6*.

(41) Amanchukwu, C. V.; Gauthier, M.; Batcho, T. P.; Symister, C.; Shao-Horn, Y.; D'Arcy, J. M.; Hammond, P. T. Evaluation and Stability of Pedot Polymer Electrodes for Li–O2 Batteries. *J. Phys. Chem. Lett.* **2016**, *7*, 3770-3775.

(42) Yao, K. P.; Risch, M.; Sayed, S. Y.; Lee, Y.-L.; Harding, J. R.; Grimaud, A.; Pour, N.; Xu, Z.; Zhou, J.; Mansour, A. Solid-State Activation of Li 2 O 2 Oxidation Kinetics and Implications for Li–O 2 Batteries. *Energy Envion. Sci.* **2015**, *8*, 2417-2426.

(43) Chen, Y.; Freunberger, S. A.; Peng, Z.; Fontaine, O.; Bruce, P. G. Charging a Li–O2 Battery Using a Redox Mediator. *Nat. Chem.* **2013**, *5*, 489-494.

(44) McCloskey, B.; Speidel, A.; Scheffler, R.; Miller, D.; Viswanathan, V.; Hummelshøj, J.; Nørskov, J.; Luntz, A. Twin Problems of Interfacial Carbonate Formation in Nonaqueous Li–O2 Batteries. *J. Phys. Chem. Lett.* **2012**, *3*, 997-1001.

(45) McCloskey, B.; Bethune, D.; Shelby, R.; Girishkumar, G.; Luntz, A. Solvents' Critical Role in Nonaqueous Lithium–Oxygen Battery Electrochemistry. *J. Phys. Chem. Lett.* **2011**, *2*, 1161-1166.

(46) Yi, J.; Guo, S.; He, P.; Zhou, H. Status and Prospects of Polymer Electrolytes for Solid-State Li–O 2 (Air) Batteries. *Energy Envion. Sci.* **2017**.

(47) Oh, B.; Vissers, D.; Zhang, Z.; West, R.; Tsukamoto, H.; Amine, K. New Interpenetrating Network Type Poly (Siloxane-< I> G</I>-Ethylene Oxide) Polymer Electrolyte for Lithium Battery. *J. Power Sources* **2003**, *119*, 442-447.

(48) Zhang, Z.; Sherlock, D.; West, R.; West, R.; Amine, K.; Lyons, L. J. Cross-Linked Network Polymer Electrolytes Based on a Polysiloxane Backbone with Oligo (Oxyethylene) Side Chains: Synthesis and Conductivity. *Macromolecules* **2003**, *36*, 9176-9180.

(49) Walkowiak, M.; Schroeder, G.; Gierczyk, B.; Waszak, D.; Osińska, M. New Lithium Ion Conducting Polymer Electrolytes Based on Polysiloxane Grafted with Si-Tripodand Centers. *Electrochem. Commun.* **2007**, *9*, 1558-1562.

(50) Rohan, R.; Pareek, K.; Chen, Z.; Cai, W.; Zhang, Y.; Xu, G.; Gao, Z.; Cheng, H. A High Performance Polysiloxane-Based Single Ion Conducting Polymeric Electrolyte Membrane for Application in Lithium Ion Batteries. *Journal of Materials Chemistry A* **2015**, *3*, 20267-20276.

(51) Zhang, Z.; Fang, S. Novel Network Polymer Electrolytes Based on Polysiloxane with Internal Plasticizer. *Electrochim. Acta* **2000**, *45*, 2131-2138.

(52) Linert, W.; Camard, A.; Armand, M.; Michot, C. Anions of Low Lewis Basicity for Ionic Solid State Electrolytes. *Coord. Chem. Rev.* **2002**, *226*, 137-141.

(53) Walls, H.; Zhou, J.; Yerian, J. A.; Fedkiw, P. S.; Khan, S. A.; Stowe, M. K.; Baker, G. L. Fumed Silica-Based Composite Polymer Electrolytes: Synthesis, Rheology, and Electrochemistry. *J. Power Sources* **2000**, *89*, 156-162.

(54) Capiglia, C.; Mustarelli, P.; Quartarone, E.; Tomasi, C.; Magistris, A. Effects of Nanoscale Sio 2 on the Thermal and Transport Properties of Solvent-Free, Poly (Ethylene Oxide)(Peo)-Based Polymer Electrolytes. *Solid State Ionics* **1999**, *118*, 73-79.

(55) Wang, X.-L.; Mei, A.; Li, M.; Lin, Y.; Nan, C.-W. Effect of Silane-Functionalized Mesoporous Silica Sba-15 on Performance of Peo-Based Composite Polymer Electrolytes. *Solid State Ionics* **2006**, *177*, 1287-1291.

(56) Weston, J.; Steele, B. Effects of Inert Fillers on the Mechanical and Electrochemical Properties of Lithium Salt-Poly (Ethylene Oxide) Polymer Electrolytes. *Solid State Ionics* **1982**, *7*, 75-79.

(57) Girishkumar, G.; McCloskey, B.; Luntz, A.; Swanson, S.; Wilcke, W. Lithium–Air Battery: Promise and Challenges. *J. Phys. Chem. Lett.* **2010**, *1*, 2193-2203.

(58) Lu, Y.-C.; Gasteiger, H. A.; Parent, M. C.; Chiloyan, V.; Shao-Horn, Y. The Influence of Catalysts on Discharge and Charge Voltages of Rechargeable Li–Oxygen Batteries. *Electrochem. Solid-State Lett.* **2010**, *13*, A69-A72.

(59) Mitchell, R. R.; Gallant, B. M.; Thompson, C. V.; Shao-Horn, Y. All-Carbon-Nanofiber Electrodes for High-Energy Rechargeable Li–O 2 Batteries. *Energy Envion. Sci.* **2011**, *4*, 2952-2958.

(60) Gallagher, K. G.; Goebel, S.; Greszler, T.; Mathias, M.; Oelerich, W.; Eroglu, D.; Srinivasan, V. Quantifying the Promise of Lithium–Air Batteries for Electric Vehicles. *Energy Envion. Sci.* **2014**, *7*, 1555-1563.

(61) Gallant, B. M.; Mitchell, R. R.; Kwabi, D. G.; Zhou, J.; Zuin, L.; Thompson, C. V.; Shao-Horn, Y. Chemical and Morphological Changes of Li–O2 Battery Electrodes Upon Cycling. *J. Phys. Chem. C* **2012**, *116*, 20800-20805.

(62) Jung, H.-G.; Hassoun, J.; Park, J.-B.; Sun, Y.-K.; Scrosati, B. An Improved High-Performance Lithium–Air Battery. *Nat. Chem.* **2012**, *4*, 579-585.

(63) Lu, Y.-C.; Gasteiger, H. A.; Crumlin, E.; McGuire, R.; Shao-Horn, Y. Electrocatalytic Activity Studies of Select Metal Surfaces and Implications in Li-Air Batteries. *J. Electrochem. Soc.* **2010**, *157*, A1016-A1025.

(64) Laoire, C. O.; Mukerjee, S.; Abraham, K.; Plichta, E. J.; Hendrickson, M. A. Influence of Nonaqueous Solvents on the Electrochemistry of Oxygen in the Rechargeable Lithium– Air Battery. *J. Phys. Chem. C* **2010**, *114*, 9178-9186.

(65) Sharon, D.; Etacheri, V.; Garsuch, A.; Afri, M.; Frimer, A. A.; Aurbach, D. On the Challenge of Electrolyte Solutions for Li–Air Batteries: Monitoring Oxygen Reduction and Related Reactions in Polyether Solutions by Spectroscopy and Eqcm. *J. Phys. Chem. Lett.* **2012**, *4*, 127-131.

(66) Bryantsev, V. S.; Giordani, V.; Walker, W.; Blanco, M.; Zecevic, S.; Sasaki, K.; Uddin, J.; Addison, D.; Chase, G. V. Predicting Solvent Stability in Aprotic Electrolyte Li–Air Batteries: Nucleophilic Substitution by the Superoxide Anion Radical (O2•–). *J. Phys. Chem. A* **2011**, *115*, 12399-12409.

(67) Hassoun, J.; Croce, F.; Armand, M.; Scrosati, B. Investigation of the O2 Electrochemistry in a Polymer Electrolyte Solid-State Cell. *Angew. Chem. Int. Ed.* **2011**, *50*, 2999-3002.

(68) Aurbach, D.; Daroux, M.; Faguy, P.; Yeager, E. The Electrochemistry of Noble Metal Electrodes in Aprotic Organic Solvents Containing Lithium Salts. *Journal of electroanalytical chemistry and interfacial electrochemistry* **1991**, *297*, 225-244.

(69) Sharon, D.; Afri, M.; Noked, M.; Garsuch, A.; Frimer, A. A.; Aurbach, D. Oxidation of Dimethyl Sulfoxide Solutions by Electrochemical Reduction of Oxygen. *J. Phys. Chem. Lett.* **2013**, *4*, 3115-3119.

(70) Kwabi, D. G.; Batcho, T. P.; Amanchukwu, C. V.; Ortiz-Vitoriano, N. P.; Hammond, P. T.; Thompson, C. V.; Shao-Horn, Y. Chemical Instability of Dimethyl Sulfoxide in Lithium-Air Batteries. *J. Phys. Chem. Lett.* **2014**.

(71) Li, F.; Kitaura, H.; Zhou, H. The Pursuit of Rechargeable Solid-State Li–Air Batteries. *Energy Envion. Sci.* **2013**, *6*, 2302-2311.

(72) Jung, K.-N.; Lee, J.-I.; Jung, J.-H.; Shin, K.-H.; Lee, J.-W. A Quasi-Solid-State Rechargeable Lithium–Oxygen Battery Based on a Gel Polymer Electrolyte with an Ionic Liquid. *Chem. Commun.* **2014**, *50*, 5458-5461.

(73) Manuel Stephan, A. Review on Gel Polymer Electrolytes for Lithium Batteries. *Eur. Polym. J.* **2006**, *42*, 21-42.

(74) Nasybulin, E.; Xu, W.; Engelhard, M. H.; Nie, Z.; Li, X. S.; Zhang, J.-G. Stability of Polymer Binders in Li–O2 Batteries. *J. Power Sources* **2013**, *243*, 899-907.

(75) Itkis, D. M.; Semenenko, D. A.; Kataev, E. Y.; Belova, A. I.; Neudachina, V. S.; Sirotina, A. P.; Hävecker, M.; Teschner, D.; Knop-Gericke, A.; Dudin, P. Reactivity of Carbon in Lithium–Oxygen Battery Positive Electrodes. *Nano Lett.* **2013**, *13*, 4697-4701.

(76) Manuel Stephan, A.; Nahm, K. Review on Composite Polymer Electrolytes for Lithium Batteries. *Polymer* **2006**, *47*, 5952-5964.

(77) Abraham, K.; Jiang, Z. A Polymer Electrolyte-Based Rechargeable Lithium/Oxygen Battery. *J. Electrochem. Soc.* **1996**, *143*, 1-5.

(78) Choe, H.; Carroll, B.; Pasquariello, D.; Abraham, K. Characterization of Some Polyacrylonitrile-Based Electrolytes. *Chem. Mater.* **1997**, *9*, 369-379.

(79) McMurry, J. *Organic Chemistry*; Brooks/Cole Cengage Learning, 2012.

(80) Coleman, M.; Petcavich, R. Fourier Transform Infrared Studies on the Thermal Degradation of Polyacrylonitrile. *Journal of Polymer Science: Polymer Physics Edition* **1978**, *16*, 821-832.

(81) Shimada, I.; Takahagi, T.; Fukuhara, M.; Morita, K.; Ishitani, A. Ft-Ir Study of the Stabilization Reaction of Polyacrylonitrile in the Production of Carbon Fibers. *J. Polym. Sci., Part A: Polym. Chem.* **1986**, *24*, 1989-1995.

(82) Varma, D. S.; Needles, H. L.; Cagliostro, D. E. Benzoic Acid Degradation of Polyacrylonitrile Fibers. *Industrial & Engineering Chemistry Product Research and Development* **1981**, *20*, 520-524.

(83) Verneker, V. P.; Shaha, B. On Coloration of Polyacrylonitrile: A Nmr Study. *Macromolecules* **1986**, *19*, 1851-1856.

(84) Mailhot, B.; Gardette, J.-L. Mechanism of Thermolysis, Thermooxidation and Photooxidation of Polyacrylonitrile. *Polym. Degrad. Stab.* **1994**, *44*, 223-235.

(85) Chen, J.; Harrison, I. Modification of Polyacrylonitrile (Pan) Carbon Fiber Precursor Via Post-Spinning Plasticization and Stretching in Dimethyl Formamide (Dmf). *Carbon* **2002**, *40*, 25-45.

(86) Xu, W.; Viswanathan, V. V.; Wang, D.; Towne, S. A.; Xiao, J.; Nie, Z.; Hu, D.; Zhang, J.-G. Investigation on the Charging Process of Li2o2-Based Air Electrodes in Li–O2 Batteries with Organic Carbonate Electrolytes. *J. Power Sources* **2011**, *196*, 3894-3899.

(87) Bowley, H. J.; Gerrard, D. L.; Maddams, W. F. The Chemical Dehydrochlorination of Poly (Vinyl Chloride), 2. Studies on N, N-Dimethylformamide Solutions. *Die Makromolekulare Chemie* **1985**, *186*, 707-714.

(88) Bowley, H. J.; Gerrard, D. L.; Maddams, W. F.; Paton, M. R. The Chemical Dehydrochlorination of Poly (Vinyl Chloride), 1. Studies on Tetrahydrofuran Solutions. *Die Makromolekulare Chemie* **1985**, *186*, 695-705.

(89) Kobayashi, M.; Tashiro, K.; Tadokoro, H. Molecular Vibrations of Three Crystal Forms of Poly (Vinylidene Fluoride). *Macromolecules* **1975**, *8*, 158-171.

(90) Krimm, S.; Folt, V.; Shipman, J.; Berens, A. Infrared Spectra and Assignments for Polyvinyl Chloride and Deuterated Analogs. *Journal of Polymer Science Part A: General Papers* **1963**, *1*, 2621-2650.

(91) Younesi, R.; Hahlin, M.; Treskow, M.; Scheers, J.; Johansson, P.; Edström, K. Ether Based Electrolyte, Lib (Cn) 4 Salt and Binder Degradation in the Li–O2 Battery Studied by Hard X-Ray Photoelectron Spectroscopy (Haxpes). *J. Phys. Chem. C* **2012**, *116*, 18597-18604.

(92) Mano, V.; Felisberti, M.; De Paoli, M.-A. Influence of Fecl3 on the Mechanical, Thermal, and Dynamic Mechanical Behavior of Pvc. *Macromolecules* **1997**, *30*, 3026-3030.

(93) Liang, Z.; Chen, W.; Liu, J.; Wang, S.; Zhou, Z.; Li, W.; Sun, G.; Xin, Q. Ft-Ir Study of the Microstructure of Nafion< Sup>®</Sup> Membrane. *Journal of membrane science* **2004**, *233*, 39-44.

(94) Abraham, K.; Alamgir, M. Li+-Conductive Solid Polymer Electrolytes with Liquid-Like Conductivity. *J. Electrochem. Soc.* **1990**, *137*, 1657-1658.

(95) Abraham, K.; Alamgir, M. Dimensionally Stable Meep-Based Polymer Electrolytes and Solid-State Lithium Batteries. *Chem. Mater.* **1991**, *3*, 339-348.

(96) Ghosh, G.; Kanti Naskar, M.; Patra, A.; Chatterjee, M. Synthesis and Characterization of Pvp-Encapsulated Zns Nanoparticles. *Opt. Mater.* **2006**, *28*, 1047-1053.

(97) Adebahr, J.; Byrne, N.; Forsyth, M.; MacFarlane, D.; Jacobsson, P. Enhancement of Ion Dynamics in Pmma-Based Gels with Addition of Tio< Sub> 2</Sub> Nano-Particles. *Electrochim. Acta* **2003**, *48*, 2099-2103.

(98) Susan, M. A. B. H.; Kaneko, T.; Noda, A.; Watanabe, M. Ion Gels Prepared by in Situ Radical Polymerization of Vinyl Monomers in an Ionic Liquid and Their Characterization as Polymer Electrolytes. *J. Am. Chem. Soc.* **2005**, *127*, 4976-4983.

(99) Brinkhuis, R.; Schouten, A. Thin-Film Behavior of Poly (Methyl Methacrylates). 2. An Ft-Ir Study of Langmuir-Blodgett Films of Isotactic Pmma. *Macromolecules* **1991**, *24*, 1496-1504.

(100) Nishioka, A.; Watanabe, H.; Yamaguchi, I.; Shimizu, H. High Resolution Nmr Spectra of Isotactic and Syndiotactic Polymethyl Methacrylate in Chloroform Solution. *Journal of Polymer Science* **1960**, *45*, 232-234.

(101) Yoshihara, T.; Tadokoro, H.; Murahashi, S. Normal Vibrations of the Polymer Molecules of Helical Conformation. Iv. Polyethylene Oxide and Polyethylene-D4 Oxide. *J. Chem. Phys.* **1964**, *41*, 2902-2911.

(102) Yao, K. P.; Lu, Y.-C.; Amanchukwu, C. V.; Kwabi, D. G.; Risch, M.; Zhou, J.; Grimaud, A.; Hammond, P. T.; Bardé, F.; Shao-Horn, Y. The Influence of Transition Metal Oxides on the Kinetics of Li 2 O 2 Oxidation in Li–O 2 Batteries: High Activity of Chromium Oxides. *PCCP* **2014**, *16*, 2297-2304.

(103) Schwenke, K. U.; Meini, S.; Wu, X.; Gasteiger, H. A.; Piana, M. Stability of Superoxide Radicals in Glyme Solvents for Non-Aqueous Li–O 2 Battery Electrolytes. *PCCP* **2013**, *15*, 11830-11839.

(104) Hansch, C.; Leo, A.; Taft, R. A Survey of Hammett Substituent Constants and Resonance and Field Parameters. *Chem. Rev.* **1991**, *91*, 165-195.

(105) Gallant, B. M.; Kwabi, D. G.; Mitchell, R. R.; Zhou, J.; Thompson, C. V.; Shao-Horn, Y. Influence of Li 2 O 2 Morphology on Oxygen Reduction and Evolution Kinetics in Li–O 2 Batteries. *Energy Envion. Sci.* **2013**, *6*, 2518-2528.

(106) Lim, H. D.; Song, H.; Kim, J.; Gwon, H.; Bae, Y.; Park, K. Y.; Hong, J.; Kim, H.; Kim, T.; Kim, Y. H. Superior Rechargeability and Efficiency of Lithium–Oxygen Batteries: Hierarchical Air Electrode Architecture Combined with a Soluble Catalyst. *Angew. Chem. Int. Ed.* **2014**, *53*, 3926-3931.

(107) Laoire, C.; Mukerjee, S.; Plichta, E. J.; Hendrickson, M. A.; Abraham, K. Rechargeable Lithium/Tegdme-Lipf6/O2 Battery. *J. Electrochem. Soc.* **2011**, *158*, A302-A308.

(108) Laoire, C. O.; Mukerjee, S.; Abraham, K.; Plichta, E. J.; Hendrickson, M. A. Elucidating the Mechanism of Oxygen Reduction for Lithium-Air Battery Applications. *J. Phys. Chem. C* **2009**, *113*, 20127-20134.

(109) Kwabi, D. G.; Bryantsev, V. S.; Batcho, T. P.; Itkis, D. M.; Thompson, C. V.; Shao-Horn, Y. Experimental and Computational Analysis of the Solvent-Dependent O2/Li+-O2– Redox Couple: Standard Potentials, Coupling Strength, and Implications for Lithium–Oxygen Batteries. *Angew. Chem.* **2016**, *128*, 3181-3186.

(110) Thotiyl, M. M. O.; Freunberger, S. A.; Peng, Z.; Chen, Y.; Liu, Z.; Bruce, P. G. A Stable Cathode for the Aprotic Li–O2 Battery. *Nat. Mater.* **2013**, *12*, 1050-1056.

(111) Johnson, L.; Li, C.; Liu, Z.; Chen, Y.; Freunberger, S. A.; Ashok, P. C.; Praveen, B. B.; Dholakia, K.; Tarascon, J.-M.; Bruce, P. G. The Role of Lio2 Solubility in O2 Reduction in Aprotic Solvents and Its Consequences for Li–O2 Batteries. *Nat. Chem.* **2014**, *6*, 1091-1099.

(112) Wang, Y.; Zheng, D.; Yang, X.-Q.; Qu, D. High Rate Oxygen Reduction in Non-Aqueous Electrolytes with the Addition of Perfluorinated Additives. *Energy Envion. Sci.* **2011**, *4*, 3697-3702.

(113) Lu, J.; Lee, Y. J.; Luo, X.; Lau, K. C.; Asadi, M.; Wang, H.-H.; Brombosz, S.; Wen, J.; Zhai, D.; Chen, Z. A Lithium–Oxygen Battery Based on Lithium Superoxide. *Nature* **2016**.

(114) Pearson, R. G. Hard and Soft Acids and Bases. *J. Am. Chem. Soc.* **1963**, *85*, 3533-3539.

(115) Schwenke, K. U.; Herranz, J.; Gasteiger, H. A.; Piana, M. Reactivity of the Ionic Liquid Pyr14tfsi with Superoxide Radicals Generated from Ko2 or by Contact of O2 with Li7ti5o12. *J. Electrochem. Soc.* **2015**, *162*, A905-A914.

(116) Katayama, Y.; Onodera, H.; Yamagata, M.; Miura, T. Electrochemical Reduction of Oxygen in Some Hydrophobic Room-Temperature Molten Salt Systems. *J. Electrochem. Soc.* **2004**, *151*, A59-A63.

(117) Branchini, B. R.; Behney, C. E.; Southworth, T. L.; Fontaine, D. M.; Gulick, A. M.; Vinyard, D. J.; Brudvig, G. W. Experimental Support for a Single Electron-Transfer Oxidation Mechanism in Firefly Bioluminescence. *J. Am. Chem. Soc.* **2015**, *137*, 7592-7595.

(118) Allen, C. J.; Hwang, J.; Kautz, R.; Mukerjee, S.; Plichta, E. J.; Hendrickson, M. A.; Abraham, K. Oxygen Reduction Reactions in Ionic Liquids and the Formulation of a General Orr Mechanism for Li–Air Batteries. *J. Phys. Chem. C* **2012**, *116*, 20755-20764.

(119) Egashira, M.; Todo, H.; Yoshimoto, N.; Morita, M. Lithium Ion Conduction in Ionic Liquid-Based Gel Polymer Electrolyte. *J. Power Sources* **2008**, *178*, 729-735.

(120) Castiglione, F.; Ragg, E.; Mele, A.; Appetecchi, G. B.; Montanino, M.; Passerini, S. Molecular Environment and Enhanced Diffusivity of Li+ Ions in Lithium-Salt-Doped Ionic Liquid Electrolytes. *J. Phys. Chem. Lett.* **2011**, *2*, 153-157.

(121) Paul, R.; Johar, S.; Banait, J.; Narula, S. Transference Number and Solvation Studies in Tetramethylurea. *J. Phys. Chem.* **1976**, *80*, 351-352.

(122) Fawcett, W. R.; Ryan, P. J. The Diffuse Double Layer in Ionic Liquids. *Collect. Czech. Chem. Commun.* **2010**, *74*, 1665-1674.

(123) Appetecchi, G. B.; Montanino, M.; Zane, D.; Carewska, M.; Alessandrini, F.; Passerini, S. Effect of the Alkyl Group on the Synthesis and the Electrochemical Properties of N-Alkyl-N-Methyl-Pyrrolidinium Bis (Trifluoromethanesulfonyl) Imide Ionic Liquids. *Electrochim. Acta* **2009**, *54*, 1325-1332.

(124) Yu, Q.; Ye, S. In Situ Study of Oxygen Reduction in Dimethyl Sulfoxide (Dmso) Solution: A Fundamental Study for Development of the Lithium–Oxygen Battery. *J. Phys. Chem. C* **2015**, *119*, 12236-12250.

(125) Dietzel, P. D.; Kremer, R. K.; Jansen, M. Tetraorganylammonium Superoxide Compounds: Close to Unperturbed Superoxide Ions in the Solid State. *J. Am. Chem. Soc.* **2004**, *126*, 4689-4696.

(126) Men, S.; Lovelock, K. R.; Licence, P. X-Ray Photoelectron Spectroscopy of Pyrrolidinium-Based Ionic Liquids: Cation–Anion Interactions and a Comparison to Imidazolium-Based Analogues. *PCCP* **2011**, *13*, 15244-15255.

(127) Ruckman, M.; Chen, J.; Qiu, S.; Kuiper, P.; Strongin, M.; Dunlap, B. Interpreting the near Edges of O 2 and O 2− in Alkali-Metal Superoxides. *Phys. Rev. Lett.* **1991**, *67*, 2533.

(128) Pedio, M.; Wu, Z.; Benfatto, M.; Mascaraque, A.; Michel, E.; Ottaviani, C.; Crotti, C.; Peloi, M.; Zacchigna, M.; Comicioli, C. Nexafs Experiment and Multiple Scattering Calculations on Ko 2: Effects on the Π Resonance in the Solid Phase. *Phys. Rev. B* **2002**, *66*, 144109.

(129) Kang, J.-S.; Kim, D.; Hwang, J.; Baik, J.; Shin, H.; Kim, M.; Jeong, Y.; Min, B. Soft X-Ray Absorption and Photoemission Spectroscopy Study of Superoxide Ko 2. *Phys. Rev. B* **2010**, *82*, 193102.

(130) Kozen, A. C.; Pearse, A. J.; Lin, C.-F.; Schroeder, M. A.; Noked, M.; Lee, S. B.; Rubloff, G. W. Atomic Layer Deposition and in Situ Characterization of Ultraclean Lithium Oxide and Lithium Hydroxide. *J. Phys. Chem. C* **2014**, *118*, 27749-27753.

(131) Lim, H.-K.; Lim, H.-D.; Park, K.-Y.; Seo, D.-H.; Gwon, H.; Hong, J.; Goddard III, W. A.; Kim, H.; Kang, K. Toward a Lithium–"Air" Battery: The Effect of Co2 on the Chemistry of a Lithium–Oxygen Cell. *J. Am. Chem. Soc.* **2013**, *135*, 9733-9742.

(132) Piana, M.; Wandt, J.; Meini, S.; Buchberger, I.; Tsiouvaras, N.; Gasteiger, H. A. Stability of a Pyrrolidinium-Based Ionic Liquid in Li-O2 Cells. *J. Electrochem. Soc.* **2014**, *161*, A1992-A2001.

(133) Radin, M. D.; Siegel, D. J. Charge Transport in Lithium Peroxide: Relevance for Rechargeable Metal–Air Batteries. *Energy Envion. Sci.* **2013**, *6*, 2370-2379.

(134) Yoshida, K.; Nakamura, M.; Kazue, Y.; Tachikawa, N.; Tsuzuki, S.; Seki, S.; Dokko, K.; Watanabe, M. Oxidative-Stability Enhancement and Charge Transport Mechanism in Glyme–Lithium Salt Equimolar Complexes. *J. Am. Chem. Soc.* **2011**, *133*, 13121-13129.

(135) Aetukuri, N. B.; McCloskey, B. D.; García, J. M.; Krupp, L. E.; Viswanathan, V.; Luntz, A. C. Solvating Additives Drive Solution-Mediated Electrochemistry and Enhance Toroid Growth in Non-Aqueous Li–O2 Batteries. *Nat. Chem.* **2015**, *7*, 50-56.

(136) Burke, C. M.; Pande, V.; Khetan, A.; Viswanathan, V.; McCloskey, B. D. Enhancing Electrochemical Intermediate Solvation through Electrolyte Anion Selection to Increase Nonaqueous Li–O2 Battery Capacity. *Proceedings of the National Academy of Sciences* **2015**, *112*, 9293-9298.

(137) Gao, X.; Chen, Y.; Johnson, L.; Bruce, P. G. Promoting Solution Phase Discharge in Li-O2 Batteries Containing Weakly Solvating Electrolyte Solutions. *Nat. Mater.* **2016**.

(138) Khetan, A.; Luntz, A.; Viswanathan, V. Trade-Offs in Capacity and Rechargeability in Nonaqueous Li–O2 Batteries: Solution-Driven Growth Versus Nucleophilic Stability. *J. Phys. Chem. Lett.* **2015**, *6*, 1254-1259.

(139) Schmeisser, M.; Illner, P.; Puchta, R.; Zahl, A.; van Eldik, R. Gutmann Donor and Acceptor Numbers for Ionic Liquids. *Chemistry–A European Journal* **2012**, *18*, 10969-10982.

(140) Jozwiuk, A.; Berkes, B. B.; Weiß, T.; Sommer, H.; Janek, J.; Brezesinski, T. The Critical Role of Lithium Nitrate in the Gas Evolution of Lithium–Sulfur Batteries. *Energy Envion. Sci.* **2016**, *9*, 2603-2608.

(141) Walker, W.; Giordani, V.; Uddin, J.; Bryantsev, V. S.; Chase, G. V.; Addison, D. A Rechargeable Li–O2 Battery Using a Lithium Nitrate/N, N-Dimethylacetamide Electrolyte. *J. Am. Chem. Soc.* **2013**, *135*, 2076-2079.

(142) Schwenke, K. U.; Metzger, M.; Restle, T.; Piana, M.; Gasteiger, H. A. The Influence of Water and Protons on Li2o2 Crystal Growth in Aprotic Li-O2 Cells. *J. Electrochem. Soc.* **2015**, *162*, A573-A584.

(143) Frith, J. T.; Russell, A. E.; Garcia-Araez, N.; Owen, J. R. An in-Situ Raman Study of the Oxygen Reduction Reaction in Ionic Liquids. *Electrochem. Commun.* **2014**, *46*, 33-35.

(144) Yang, L.; Frith, J.; Garcia-Araez, N.; Owen, J. R. A New Method to Prevent Degradation of Lithium–Oxygen Batteries: Reduction of Superoxide by Viologen. *Chem. Commun.* **2015**, *51*, 1705-1708.

(145) Gittleson, F. S.; Yao, K. P.; Kwabi, D. G.; Sayed, S. Y.; Ryu, W. H.; Shao-Horn, Y.; Taylor, A. D. Raman Spectroscopy in Lithium–Oxygen Battery Systems. *ChemElectroChem* **2015**, *2*, 1446-1457.

(146) Bergner, B. J.; Schürmann, A.; Peppler, K.; Garsuch, A.; Janek, J. r. Tempo: A Mobile Catalyst for Rechargeable Li-O2 Batteries. *J. Am. Chem. Soc.* **2014**, *136*, 15054-15064.

(147) Finkelstein, M.; Petersen, R. C.; Ross, S. D. The Electrochemical Degradation of Quaternary Ammonium Salts1. *J. Am. Chem. Soc.* **1959**, *81*, 2361-2364.

(148) Lu, Y.-C.; Shao-Horn, Y. Probing the Reaction Kinetics of the Charge Reactions of Nonaqueous Li–O2 Batteries. *J. Phys. Chem. Lett.* **2012**, *4*, 93-99.

(149) Cope, A. C.; LeBel, N. A.; Lee, H.-H.; Moore, W. R. Amine Oxides. Iii. Selective Formation of Olefins from Unsymmetrical Amine Oxides and Quaternary Ammonium Hydroxides1. *J. Am. Chem. Soc.* **1957**, *79*, 4720-4729.

(150) Hoh, G.; Barlow, D.; Chadwick, A.; Lake, D.; Sheeran, S. Hydrogen Peroxide Oxidation of Tertiary Amines. *Journal of the American Oil Chemists' Society* **1963**, *40*, 268-271.

(151) Slagle, I. R.; Dudich, J. F.; Gutman, D. Identification of Reactive Routes in the Reactions of Oxygen Atoms with Methylamine, Dimethylamine, Trimethylamine, Ethylamine, Diethylamine, and Triethylamine. *Journal of Physical Chemistry* **1979**, *83*, 3065-3070.

(152) Cullis, C.; Waddington, D. In *Proceedings of the Royal Society of London A: Mathematical, Physical and Engineering Sciences*; The Royal Society: 1958; Vol. 246, p 91-98.

(153) Cope, A. C.; Foster, T. T.; Towle, P. H. Thermal Decomposition of Amine Oxides to Olefins and Dialkylhydroxylamines. *J. Am. Chem. Soc.* **1949**, *71*, 3929-3934.

(154) Mousavi, M. P.; Kashefolgheta, S.; Stein, A.; Bühlmann, P. Electrochemical Stability of Quaternary Ammonium Cations: An Experimental and Computational Study. *J. Electrochem. Soc.* **2016**, *163*, H74-H80.

(155) Kundu, D.; Black, R.; Berg, E. J.; Nazar, L. F. A Highly Active Nanostructured Metallic Oxide Cathode for Aprotic Li–O 2 Batteries. *Energy Envion. Sci.* **2015**, *8*, 1292-1298.

(156) Yao, Y.; Liu, N.; McDowell, M. T.; Pasta, M.; Cui, Y. Improving the Cycling Stability of Silicon Nanowire Anodes with Conducting Polymer Coatings. *Energy Envion. Sci.* **2012**, *5*, 7927-7930.

(157) Kuwabata, S.; Masui, S.; Yoneyama, H. Charge–Discharge Properties of Composites of Limn 2 O 4 and Polypyrrole as Positive Electrode Materials for 4 V Class of Rechargeable Li Batteries. *Electrochim. Acta* **1999**, *44*, 4593-4600.

(158) Arbizzani, C.; Mastragostino, M.; Rossi, M. Preparation and Electrochemical Characterization of a Polymer Li 1.03 Mn 1.97 O 4/Pedot Composite Electrode. *Electrochem. Commun.* **2002**, *4*, 545-549.

(159) Her, L.-J.; Hong, J.-L.; Chang, C.-C. Preparation and Electrochemical Characterizations of Poly (3, 4-Dioxyethylenethiophene)/Licoo 2 Composite Cathode in Lithium-Ion Battery. *J. Power Sources* **2006**, *157*, 457-463.

(160) Fan, X.; Luo, C.; Lamb, J.; Zhu, Y.; Xu, K.; Wang, C. Pedot Encapsulated Feof Nanorod Cathodes for High Energy Lithium-Ion Batteries. *Nano Lett.* **2015**, *15*, 7650-7656.

(161) D'Arcy, J. M.; El-Kady, M. F.; Khine, P. P.; Zhang, L.; Lee, S. H.; Davis, N. R.; Liu, D. S.; Yeung, M. T.; Kim, S. Y.; Turner, C. L. Vapor-Phase Polymerization of Nanofibrillar Poly (3, 4-Ethylenedioxythiophene) for Supercapacitors. *ACS Nano* **2014**, *8*, 1500-1510.

(162) Hohnholz, D.; MacDiarmid, A. G.; Sarno, D. M.; Jones Jr, W. E. Uniform Thin Films of Poly-3, 4-Ethylenedioxythiophene (Pedot) Prepared by in-Situ Deposition. *Chem. Commun.* **2001**, 2444-2445.

(163) Winther-Jensen, B.; Winther-Jensen, O.; Forsyth, M.; MacFarlane, D. R. High Rates of Oxygen Reduction over a Vapor Phase–Polymerized Pedot Electrode. *Science* **2008**, *321*, 671-674.

(164) Marciniak, S.; Crispin, X.; Uvdal, K.; Trzcinski, M.; Birgerson, J.; Groenendaal, L.; Louwet, F.; Salaneck, W. R. Light Induced Damage in Poly (3, 4-Ethylenedioxythiophene) and Its Derivatives Studied by Photoelectron Spectroscopy. *Synth. Met.* **2004**, *141*, 67-73.

(165) Verge, P.; Vidal, F.; Aubert, P.-H.; Beouch, L.; Tran-Van, F.; Goubard, F.; Teyssié, D.; Chevrot, C. Thermal Ageing of Poly (Ethylene Oxide)/Poly (3, 4-Ethylenedioxythiophene) Semi-Ipns. *Eur. Polym. J.* **2008**, *44*, 3864-3870.

(166) Lu, Y.-C.; Crumlin, E. J.; Veith, G. M.; Harding, J. R.; Mutoro, E.; Baggetto, L.; Dudney, N. J.; Liu, Z.; Shao-Horn, Y. In Situ Ambient Pressure X-Ray Photoelectron Spectroscopy Studies of Lithium-Oxygen Redox Reactions. *Scientific Reports* **2012**, *2*.

(167) Dietz, K.; Beck, F. Positive Polyacetylene Electrodes in Aqueous Electrolytes. *J. Appl. Electrochem.* **1985**, *15*, 159-166.

(168) Vork, F.; Schuermans, B.; Barendrecht, E. Influence of Inserted Anions on the Properties of Polypyrrole. *Electrochim. Acta* **1990**, *35*, 567-575.

(169) Miao, R.; Liu, B.; Zhu, Z.; Liu, Y.; Li, J.; Wang, X.; Li, Q. Pvdf-Hfp-Based Porous Polymer Electrolyte Membranes for Lithium-Ion Batteries. *J. Power Sources* **2008**, *184*, 420-426.

(170) Ferrari, S.; Quartarone, E.; Mustarelli, P.; Magistris, A.; Fagnoni, M.; Protti, S.; Gerbaldi, C.; Spinella, A. Lithium Ion Conducting Pvdf-Hfp Composite Gel Electrolytes Based on N-Methoxyethyl-N-Methylpyrrolidinium Bis (Trifluoromethanesulfonyl)-Imide Ionic Liquid. *J. Power Sources* **2010**, *195*, 559-566.

(171) Saito, Y.; Kataoka, H.; Capiglia, C.; Yamamoto, H. Ionic Conduction Properties of Pvdf−Hfp Type Gel Polymer Electrolytes with Lithium Imide Salts. *J. Phys. Chem. B* **2000**, *104*, 2189-2192.

(172) Garcia-Lastra, J. M.; Bass, J.; Thygesen, K. S. Communication: Strong Excitonic and Vibronic Effects Determine the Optical Properties of Li2o2. *J. Chem. Phys.* **2011**, *135*, 121101.

(173) Zhang, G.; Zheng, J.; Liang, R.; Zhang, C.; Wang, B.; Au, M.; Hendrickson, M.; Plichta, E. A-Mno2/Carbon Nanotube/Carbon Nanofiber Composite Catalytic Air Electrodes for Rechargeable Lithium-Air Batteries. *J. Electrochem. Soc.* **2011**, *158*, A822-A827.

(174) Ling, C.; Zhang, R.; Takechi, K.; Mizuno, F. Intrinsic Barrier to Electrochemically Decompose Li2co3 and Lioh. *J. Phys. Chem. C* **2014**, *118*, 26591-26598.

(175) Luntz, A. C.; Viswanathan, V.; Voss, J.; Varley, J. B.; Nørskov, J. K.; Scheffler, R.; Speidel, A. Tunneling and Polaron Charge Transport through Li2o2 in Li–O2 Batteries. *J. Phys. Chem. Lett.* **2013**, *4*, 3494-3499.